A new RbYb ultracold mixture machine

—

from room temperature to

2-photon-photoassociation on the intercombination line

Inaugural-Dissertation

zur

Erlangung des Doktorgrades der

Mathematisch-Naturwissenschaftlichen Fakultät

der Heinrich-Heine-Universität Düsseldorf

vorgelegt von

Tobias Franzen

aus Viersen

Düsseldorf, Dezember 2022

Contents

1.

Introduction

Kicked off by the first magneto-optical trap in 1987 [1] and first demonstrations of Bose-Einstein condensation in 1995 [2, 3], the field of ultracold atoms has rapidly developed into an important part of atomic and molecular physics. A wide variety of quantum phases and systems [4, 5] have been realized and many applications in precision measurements have emerged [6–11]. An area of particular interest is quantum simulation [12, 13], where a Hamiltonian that is of interest in other systems can be implemented in a cold atom system. This often allows for observations and variation of parameters that is not possible in the original system and thus facilitates the study of the underlying physics.

While ultracold atoms can be used to implement many quantum systems requiring no interactions or short-range contact interactions, the engineering of long-range interactions remains challenging. These are however of considerable interest, as introducing long range correlations results in a variety of additional phenomena. In this context, dipole-dipole interactions are of particular interest, being both long-range and anisotropic [14–16] - indeed, dipole-dipole interactions are the only available long-range interaction mechanism in neutral atoms [14]. For some highly magnetic atom species, effects arising from interactions between magnetic dipole moments have been demonstrated [17–19], but interaction lengths remain much less than the typical particle spacing and thus too small to realize most systems of interest.

Polar molecules whose ground state exhibits a large electric dipole moment present a promising option for ultracold quantum simulation. Of particular interest are arrays of such molecules in an optical lattice. If this can be realized with a high filling fraction, it will open up the possibility to implement a wide variety of quantum systems, among them the implementation of lattice spin models [20] allowing the modeling of condensed matter systems, investigating topics such as quantum magnetism [21] or even quantum computing [20, 22, 23]. But even in bulk traps and at much lower filling fractions, an ultracold dipolar gas provides plenty of physics to explore, among them quantum chemistry [24, 25] and atom-molecule collisions which have recently received considerable interest [26, 27]. The use of polar molecules to implement synthetic dimensions [28] has also been proposed.

Even more possibilities arise when the molecular ground state has a magnetic as well as an electric dipole moment, as this gives an additional degree of freedom allowing for external control of the interactions mediated by the electric dipole moment. For example the magnetic moment enables further approaches to shielding against collisions [29], external control of collective spin excitations [30] and the combination of the large internal electric

field and the presence of a single unpaired electron also opens up the possibility of their use in the search for an electric dipole moment of the electron [31]. Quantum computing schemes relying on a $^2\Sigma$ ground state have also been proposed [32].

Until now, a majority of the work on ultracold atoms and molecules has concentrated on the alkali metals and their dimers. This can largely be attributed to the convenience provided by having a single valence electron and the relatively accessible transition wavelengths. However, bialkali dimers always have a diamagnetic ground state with the two electron spins cancelling out each other. In order to achieve a paramagnetic ground state in a diatomic molecule, the electron spins of the constituent atoms must not be equal. One way to achieve this is the combination of an alkali-atom – in our case rubidium (Rb) – with a closed shell atom with spin singlet ground state – in our case ytterbium (Yb).

1.1. Routes towards ultracold molecules

One approach towards the production of ultracold molecule is of course to apply the same techniques that have proven so successful for atoms to the cooling of molecules. However, their more complex structure makes it much more challenging to establish a closed transition. While such *direct laser cooling of molecules* is a rapidly growing field and has made considerable progress in recent years, [33–38] it has not yet caught up with the tremendously successful cooling of atoms.

This is the reason for the popularity and success of the *ultracold molecules from ultracold atoms* approach. Samples of ultracold atoms are prepared using the vast toolbox that has been developed over the years and the atoms are then assembled into molecules while preserving their temperature. This requires the controlled assembly of ultracold atoms into molecules, which can be achieved by two main methods.

An established technique is the creation of weakly bound molecules using a magnetically tunable Feshbach resonance [39]. By ramping over the resonance atom pairs can be converted to molecules (and vice versa) with very high efficiency. However, this *magnetoassociation* process is harder to implement for some classes of molecules than it is for others: While the interaction between electron spins in a bialkali ensures a conveniently strong coupling between channels and thus broad Feshbach resonances, the situation is less favorable in the combination of an alkali atom with a closed shell atom. While a variety of coupling mechanisms have been predicted [40–42] and observed [43, 44] here, their strength is orders of magnitude lower than in bialkalis, making their successful exploitation for the creation of molecules an outstanding challenge.

For this reason the path we will pursue is that of *photoassociation* [45], where the coupling from the scattering state to a bound state in the electronic ground state is provided by optical transitions to an electronically excited state. Efficient coherent transfer from a scattering state to a bound state by photoassociation is however notoriously difficult due to the small overlap between these states and the introduction of additional loss channels from coupling to excited states. Nonetheless in the case of an alkali-closed shell molecule, where efficient magnetoassociation has yet to be demonstrated, photoassociation is a promising
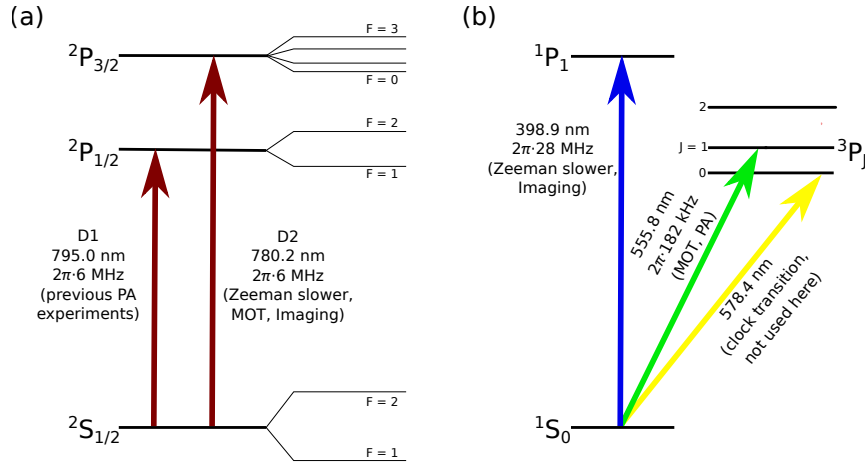
Figure 1.1.: Relevant energy levels for (a) ^{87}Rb and (b) Yb. The transitions are labeled with their wavelength, natural linewidth and their applications. Not to scale, data from [54, 55]

option.

With either approach (magnetoassociation or photoassociation) the result will be a weakly bound molecule in the electronic ground state. This weakly bound molecule then has to be transferred to the absolute (electronic, vibrational and rotational or *rovibronic*) ground state to both stabilize it against decay and make the permanent electric dipole moment (which has considerable magnitude in the ground state only) accessible. As the overlap between bound states is much larger than that to the scattering states, this stabilization step can be realized in a very efficient way by means of *stimulated raman adiabatic passage* (STIRAP) [46] using optical coupling to an electronically excited state [47, 48]. Using this process, the absolute ground state has been reached for the polar molecules KRb [49], RbCs [50, 51], NaK [52] and NaRb [53], with current work focusing on improvements in phase space density and lifetime of the samples.

1.2. Why RbYb?

If we want to achieve a paramagnetic ground state, our best option is the combination of an alkali metal with a closed shell atom. We have chosen the combination of the alkali atom Rb and the rare earth like Yb. The relevant levels and transitions for both species are shown in Figure 1.1 A main motivation for this choice is the fact that laser cooling and the production of degenerate quantum gases is well established for both species. The combination of Yb with its five stable bosonic and two stable fermionic isotopes with the two bosonic Rb isotopes provides the ability to create both fermionic and bosonic molecules with the full range of scattering lengths [56].

Another important feature introduced by the closed shell atom is the existence of narrow intercombination lines that prove useful for applications ranging from laser cooling to precision spectroscopy.

Other experiments are working towards similar goals with CsYb [44, 57] – where the large

mass of Cs leads to a high density of bound states, which combined with the large nuclear spin is promising for the study of magnetically tuneable Feshbach resonances [40] –, LiYb [58, 59] – which is particularly interesting due to its large mass ratio – and RbSr [60] – with Sr providing even narrower intercombination lines, but less choice of isotopes than Yb.

1.3. Previous work on RbYb

Ultracold mixtures of Rb and Yb have been investigated in Düsseldorf since 2004 [61], with the long-term goal being the creation of ground state molecules.

Meanwhile, the other experiments using this combination at the University of Maryland [62] and Universität Hamburg [63] have concentrated more on investigations of degenerate mixtures and Yb quantum gases, respectively.

Investigations of their thermalization [64, 65] behavior have uncovered - in addition to approximate scattering lengths - a striking phase separation for mixtures of ^{87}Rb and ^{174}Yb [66].

Extensive photoassociation spectroscopy has been performed on the Rb D1 asymptote [67–70]. This resulted in the measurement of binding energies for the excited $^2\Pi_{1/2}$ state down to a binding energy of $E_b = h \cdot 2.2\,\text{THz}$ [71] and 2-photon photoassociation of the $^2\Sigma_{1/2}$ ground state to a binding energy of $E_b = h \cdot 58\,\text{GHz}$ [69, 70, 72]. The later results also led to the precise determination of interspecies scattering lengths [56]. In preparation for future experiments aiming at the efficient production of molecules in the electronic ground state, Autler-Townes spectroscopy was used to determine the Franck-Condon factors for selected transitions between weakly bound states [73].

Following the prediction of magnetically tuneable Feshbach resonances [40], attempts at their experimental observation unfortunately were not successful [69, 74].

While all of these investigations provided valuable insights, experiments in the old apparatus suffered from poor optical access and conflicting requirements for the preparation of both species, ultimately leading to the conception of the apparatus described in this thesis.

1.4. Aims of this thesis

Here, we present a complete redesign of the Düsseldorf RbYb apparatus. The new setup features separate production chambers for each species, largely decoupling their preparation and allowing for more access to and less intrusive reconfiguration of the dedicated science chamber. Transfer of the ultracold samples to the science chamber is achieved by long distance transport in optical traps.

A critical part of the new apparatus is a novel fiber amplifier for $1112\,\text{nm}$ light, that is needed for the laser cooling of Yb and was developed in the scope of this thesis.

Working towards the goal of ground state molecules, the possibility of performing photoassociation using the narrow $^2S_{\frac{1}{2}} + {}^3P_1$ asymptote rather than the commonly used alkali D1 asymptote is explored. The narrow linewidth allows for a higher spectroscopic resolution and may enable an efficient free-bound STIRAP process in the future, particularly

for weakly bound states where off resonant excitation of the atomic line is otherwise an important issue.

In homonuclear experiments with Yb, Sr and Ca, intercombination line photoassociation has enabled precision spectroscopy [75–80] and the efficient creation of dimers by free-bound STIRAP from a Mott insulator [81]. Intercombination line photoassociation has also been reported in RbSr [82].

However, to the best of the authors knowledge, it has not been previously applied to any alkali-Yb dimer.

1.5. Structure of this thesis

This document is structured as follows: First basic concepts of the physics of diatomic molecules, the scattering behavior of ultracold atoms and photoassociation will be introduced in chapter 2, where we will also motivate the choice of isotopes for the experiments presented here. Then chapter 3 will give a short overview of optical trapping, fiber amplifiers and the concepts of synthesizers and beatnote frequency stabilization, all of which are used extensively in our apparatus. The new apparatus will be introduced in chapter 4, where the various subsystems required for our experiments will be described. In chapter 5 we will deal with the steps used in the preparation of our ultracold samples, culminating in Bose-Einstein condensates for each individual species and an ultracold mixture which will be the starting point for the following experiments.

We then turn towards the intercombination line photoassociation experiments: First we will briefly cover homonuclear photoassociation of Yb in chapter 6 as this presents a good test of our procedures[1]. Our search for RbYb photoassociation resonances and their characterization will be described in chapter 7, demonstrating intercombination line photoassociation in RbYb is indeed possible. In chapter 8 2-photon photoassociation spectroscopy on the two most weakly bound states of the electronic ground state will be described.

Finally, chapter 9 will suggest further improvements to the apparatus and sketch a path towards the long-term goal of the creation of RbYb molecules in the absolute ground state molecules.

---

[1] and of course we get a lot of the data for free during our scans for interspecies resonances

2.

Molecular Physics

The step from a single atom to a diatomic molecule introduces considerable additional complexity. While the electronic states of a single atom are known to high accuracy for most elements, their interaction at short distances and consequentially the molecular electronic states are often poorly understood. The relative motion of the two nuclei introduces vibrational and rotational states and coupling of angular momenta leads to new quantum numbers. This chapter introduces some concepts from molecular physics that are required to interpret the experimental results presented in chapters 6 to 8. A more thorough treatment can be found in the extensive literature on this subject [83–86].

2.1. Angular Momenta and Hund's cases

Assembling a molecular state from atomic states requires coupling of the angular momenta of the atomic states to come up with the appropriate quantities for the molecular states. The order in which the couplings have to be evaluated depends on the relative strengths of the interaction mechanisms, which depends not only on the atoms involved but also on their spatial separation.

A classification for these coupling schemes has been developed by Hund in 1926-27 and they are since known as *Hund's cases* [87]. A discussion of Hund's cases in general and their application to RbYb can be found in [67], though the case of the $^2S_{\frac{1}{2}} + {}^3P_1$ asymptote is not treated there. We will have a closer look at this in the context of the interpretation of 1-photon photoassociation spectra in subsection 7.6.1. Many real world scenarios are intermediate cases and will thus not be well described by any of the cases.

Here we will briefly introduce the two cases we will need for labelling of molecular potentials in RbYb. For us *Hund's case a*, where the electrostatic interaction between the atoms dominates over an intermediate spin-orbit coupling and a weak rotation, and *Hund's case c*, where spin-orbit coupling dominates, will be of interest.

2.1.1. Long range: Atomic states and Hund's case c

A pair of atoms at large separation is well described by the atomic wavefunctions, a scattering wavefunction characterized by its partial wave l and a small perturbation due to interactions between the two atoms. In this case, the electronic quantum numbers of both atoms remain valid, and combine to form a total electronic angular momentum J_a.

For smaller separations, the total electronic angular momentum ceases to be a good quantum number and its projection to the nuclear axis Ω takes its place. Such a state is designated in *Hund's case c* by

$$P \left|\Omega\right|^{\pm}_{g/u} \tag{2.1}$$

where P is the electronic excitation, counting molecular states for each value of Ω starting at 1 for the lowest excited state, with the ground state being denoted by X. The angular momentum coupling in this case is discussed in more detail in Appendix A.

In the case of the $\Omega = 0$ states, the designation $\pm$ indicates the parity for reflections of the wavefunction at a plane containing the molecular axis. For homonuclear molecules, the parity for reflections of the wavefunction at a plane normal to the molecular axis is given by the subscript u/g.

2.1.2. Short range: Hund's case a

At even shorter range, the interaction between the two atoms will exceed the spin-orbit coupling within each atom, so rather than orbital and spin angular momentum of each atom coupling to each other, they will first couple to the internuclear axis resulting in the projection quantum numbers Λ and Σ. These then couple to form $\Omega = |\Lambda + \Sigma|$. Such states are denoted by

$$P^{(2S+1)} \left|\Lambda\right|^{\pm}_{\Omega,g/u} \tag{2.2}$$

where in analogy to atomic orbital momentum $|\Lambda|$ is given by the greek letters $\Sigma, \Pi, \Delta, \dots$ and again the subscript $\pm$ and the superscript g/u only apply to certain cases. As this work will only deal with very weakly bound states, these term symbols will only occasionally appear in cases where there exists only a single short-range potential corresponding to a particular threshold and the mapping is thus unambiguous.

2.2. Molecular Potential Energy Curves

Each electronic state will support a (usually large) number of vibrational states or bound states. To determine their energies, we require knowledge of the potential energy of the atom pair as a function of their separation, the *potential energy curve* (PEC) [86]. This section will describe ways to calculate and represent (an approximation of) the potential energy curve. We will also deal with both numerical methods and analytical approximations to calculate the vibrational energies from the PEC, thus connecting it to our photoassociation measurements. Figure 2.1 shows an example of a model for a potential energy curve and the associated bound states.

2.2.1. Computational solutions

The proper way to calculate the interaction between two atoms of course would be to solve the Schrödinger equation for all of its constituents while including all interaction terms.
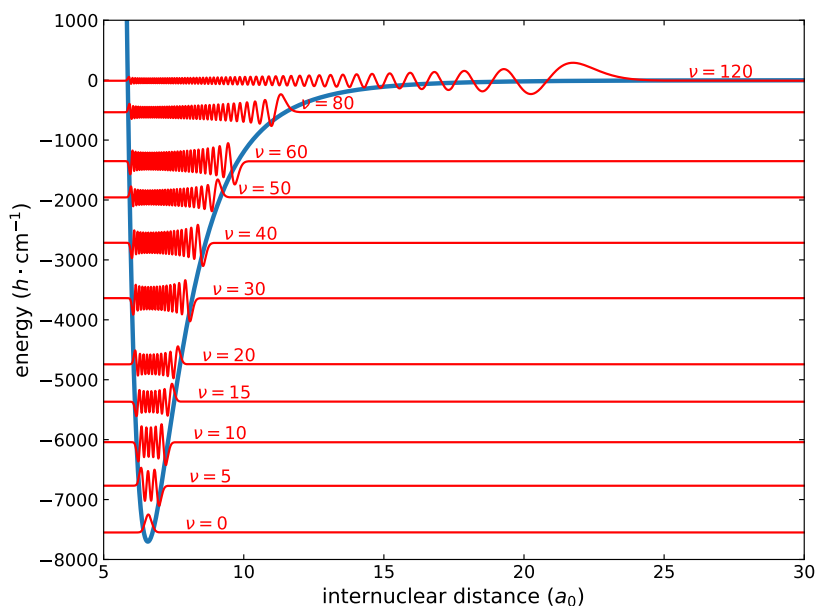
Figure 2.1.: An example of a (toy model of a) potential energy curve: Lennard-Jones potential (with $J = 0$). Vibrational wavefunctions for selected bound states are shown.

Unfortunately this approach is computationally prohibitive for even the smallest of systems, not to speak of RbYb with 107 electrons. The development of methods that allow for reasonable approximations to the solution is at the heart of the field of computational chemistry [88]. An approachable introduction to the methods used can be found in [89]. While these methods themselves are well beyond the scope of this thesis, their results are relevant. Such ab-initio methods are often not as accurate as we would like them to be, but still provide valuable guidance and can be refined by fitting them to experimental data.

2.2.2. Short range potential

For performing analytic calculations, it is desirable to have an expression for the potential energy that is easily parameterizable yet still closely matches the actual curve. Many potential energy curves can be reasonably approximated by a Morse potential of the form

$$V(r) = T_E + D_E \cdot \left(1 - e^{-\omega_E \sqrt{\frac{\mu}{2D_E}}(r - r_E)}\right)^2 \tag{2.3}$$

parameterized by the equilibrium distance between the two nuclei r_E, the harmonic oscillation frequency at this point ω_E, the potential depth D_E and the term energy T_E. This approximation is useful for deeply bound states, as the functional form allows precise control over this region of the potential. For this reason Morse potential parameters are often published with *ab initio* calculations. However these potential functions do not usually reproduce the long range part in a satisfactory way.

2.2.3. Long range expansions

The long range part of the interatomic potential can usually be well approximated by a power law $V(r) = \frac{C_n}{r^n}$, where C_n is a constant, which can be motivated by the interaction mechanism in question.

The leading term is usually the *van der Waals interaction* or *London dispersion force* with $n = 6$. This arises from the interaction between induced dipoles in both atoms. The coefficient C_6 is related to the static polarizabilities and excitation energies of the atoms involved.

In the case of two identical atoms in different states which are connected by an electric dipole transition, the *resonant dipole-dipole interaction* with $n = 3$ arises. Here the excitation is shared between both atoms, leading to a different scaling of the resulting interaction. As this interaction depends on the dipole matrix element between the two states involved, just as the optical transition between the two states does, its strength is related to the transition wavelength λ and the lifetime of the upper atomic state τ by [90]

$$C_3 = \frac{3\hbar}{2\tau} \left(\frac{\lambda}{2\pi} \right)^3.$$
(2.4)

In fact this enables the use of photoassociation of homonuclear molecules for the precision measurement of atomic state lifetimes [91, 92]. Unfortunately as we will see in section 7.2 there is no such straightforward way to predict the C_6 coefficient which is the leading term in heteronuclear photoassociation.

By taking a sum over multiple orders $n, m, \ldots$, effects beyond the leading order can be included in a long range expansion, further improving the approximation. A commonly used case is the Lennard-Jones potential

$$V(r) = -\frac{C_6}{r^6} + \frac{C_{12}}{r^{12}}$$
(2.5)

where the long range attraction is described by the term with $n = 6$ and a repulsion at short range is modelled by the second term with $m = 12$.

2.2.4. Combined approaches

In practice, the described approaches for the short and long range parts of the potential are often combined. For example a Morse potential can be combined with a long range expansion or a computational solution may be combined with an analytic long range expansion using a switching function [56] in order to accurately describe the potential at a wider range of binding energies.

2.2.5. Vibrational states

Given an interaction potential $V(r)$, the relative motion of the two nuclei is described by the Schrödinger equation

$$\left(-\frac{\hbar^2}{2\mu} \frac{\mathrm{d}^2}{\mathrm{d}r^2} + V(r) + \frac{\hbar^2}{2\mu r^2} \left(J(J+1) \right) \right) \Psi(r) = E\Psi(r),$$
(2.6)

where μ is the reduced mass and J is the rotational quantum number (see subsection 2.2.6

A few of the resulting vibrational wavefunctions for a Lennard-Jones type potential are shown in Figure 2.1

Although nowadays this equation can be numerically solved with relative ease, it is instructive to consider a semi-classical description of this problem. This will lead to some expressions that are particularly useful when dealing with limited data restricted to levels close to dissociation, as is typically the case in photoassociation experiments

This section will closely follow the treatment in [86]. First we apply the Wentzel-Kramers-Brillouin (WKB) approximation, which assumes that the potential does not vary significantly on the scale of a wavelength. Although this approximation is not well justified in our case, the resulting expressions have stood the test of time. We consider the *Bohr-Sommerfeld quantization condition* which is given by

$$\pi \left(\nu + \frac{1}{2} \right) = \Phi = \int_{R_1(E)}^{R_2(E)} \sqrt{\frac{2\mu \left(E - V(r) \right)}{\hbar^2}} \, \mathrm{d}r, \tag{2.7}$$

where ν is the vibrational level index, $R_1(E)$ and $R_2(E)$ are the inner and outer classical turning point respectively and μ is the reduced mass.

Mass scaling

When applied to the dissociation threshold, Equation 2.7 yields the relation

$$\pi \left(\nu_D + \frac{1}{2} \right) = \int_{R_0}^{\infty} \sqrt{-\frac{2\mu V(r)}{\hbar^2}} \, \mathrm{d}r, \tag{2.8}$$

where ν_D is the fractional vibrational level index associated with the dissociation threshold and the integration goes from the classical inner turning point to infinity.

As a change in isotopologue affects only the reduced mass μ and the potential $V(r)$ is independent of isotope within the Born-Oppenheimer approximation it follows that $(\nu_D + \frac{1}{2}) \propto \sqrt{\mu}$, allowing us to establish a relationship between the binding energies of weakly bound vibrational levels of different isotopologues by so called *mass scaling*.

Near-Dissociation theory: the LeRoy-Bernstein formula

The semi-classical approach can also be used to derive an analytic expression for the binding energies of vibrational levels close to the dissociation threshold, often referred to as *Near-Dissociation theory*. Such an analytical expression is particularly useful to predict the position of further states from measured data.

Consider the derivative of Equation 2.7 with respect to the level energy E_ν, yielding the density of bound states

$$\frac{\mathrm{d}\nu}{\mathrm{d}E_\nu} = \frac{1}{2\pi} \sqrt{\frac{2\mu}{\hbar^2}} \int_{R_1(E)}^{R_2(E)} \frac{\mathrm{d}r}{\sqrt{E_\nu - V(r)}}. \tag{2.9}$$

As the value of the integral is dominated by the long range tail of the potential, a good approximation is obtained by replacing the potential with its long range form $-\frac{C_n}{r^n}$ and

setting the lower integration bound to zero, since the new integrand vanishes at short range, giving

$$
\frac{\mathrm{d}\nu}{\mathrm{d}E_\nu} \approx \frac{1}{2\pi}\sqrt{\frac{2\mu}{\hbar^2}}\int_0^{R_2(E)}\frac{\mathrm{d}r}{\sqrt{E_\nu+\frac{C_n}{r^n}}}
\tag{2.10}
$$

using $E_\nu = -\frac{C_n}{R_2(E_\nu)^n}$ and substituting $y = r/R_2(E_\nu)$ we obtain

$$
\frac{\mathrm{d}\nu}{\mathrm{d}E_\nu} \approx \frac{1}{2\pi}\sqrt{\frac{2\mu}{\hbar^2}}\frac{C_n^{1/n}}{E_\nu^{(n+2)/(2n)}}\int_0^1\frac{\mathrm{d}y}{\sqrt{y^{-n}-1}}
\tag{2.11}
$$

where the integral is given by

$$
\int_0^1\frac{\mathrm{d}y}{\sqrt{y^{-n}-1}} = \frac{\sqrt{\pi}}{n}\frac{\Gamma\left(\frac{1}{2}+\frac{1}{n}\right)}{\Gamma\left(1+\frac{1}{n}\right)}.
\tag{2.12}
$$

. After inversion and integration we arrive at the final result

$$
E_\nu = D - \left[\frac{(n-2)\sqrt{\pi}}{C_n^{1/n}}\sqrt{\frac{\hbar^2}{2\mu}}\frac{\Gamma\left(1+\frac{1}{n}\right)}{\Gamma\left(\frac{1}{2}+\frac{1}{n}\right)}\right]^{2n/(n-2)}(\nu_D-\nu)^{2n/(n-2)}
\tag{2.13}
$$

where ν_D denotes the fractional vibrational state index at dissociation and D is the energy at dissociation. This expression is commonly known as the *LeRoy-Bernstein formula*.

While the *LeRoy-Bernstein formula* formula only allows for a single C_n term, this is often not enough to reproduce the relevant aspects of the real potential energy curves. An improved version was developed by Comparat [93], which allows for an additional C_m term as well as introducing a parameter affecting the short range behavior.

Vibrational quantum number

The vibrational quantum number ν counts the vibrational levels from the bottom up, with $\nu = 0$ corresponding to the vibrational ground state. While this is straightforward in theory and in experiments dealing with deeply bound molecules, it poses some problems in photoassociation experiments, where the number of bound states is often unknown and the only accessible reference is the dissociation threshold. The bound states thus have to be counted from dissociation rather than from the bottom of the potential. To make this obvious negative numbers will be used with $\Delta\nu = -1$ denoting the least bound state.

2.2.6. Rotation

The remaining degree of freedom for a diatomic molecule is the rotation. Due to its symmetry, the molecule can only rotate about an axis perpendicular to the molecular axis and only a single quantum number is required to describe this. The rotational energy is given by

$$
E_\text{rot} = B_\nu\,J(J+1)
\tag{2.14}
$$
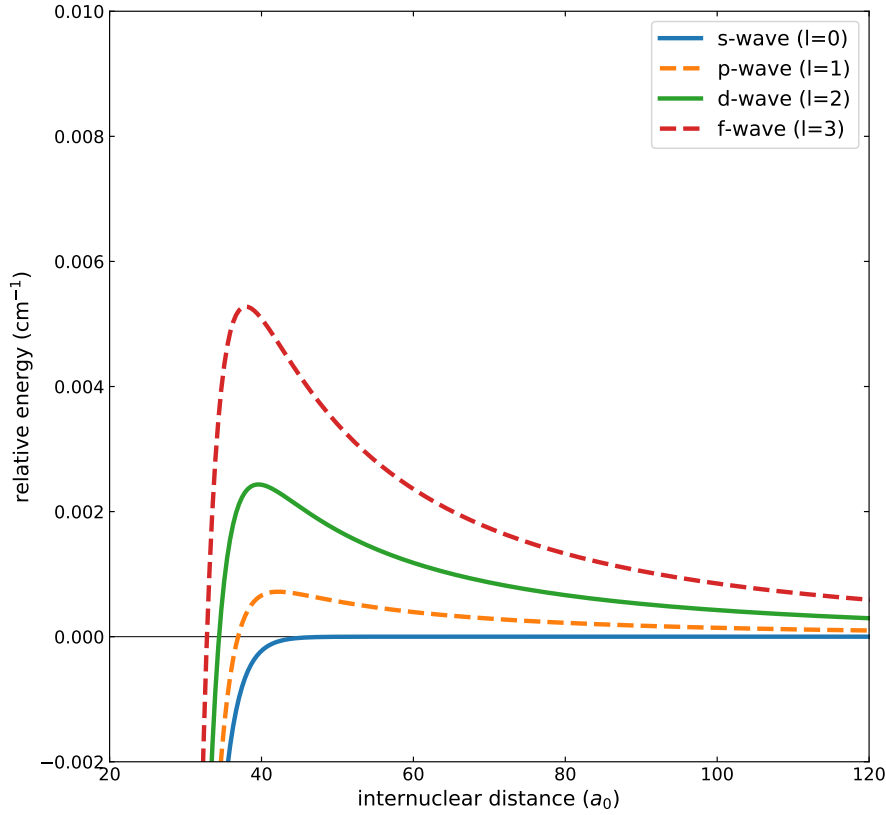
Figure 2.2.: Illustration of the centrifugal barrier for Yb^2, showing the effective potential for the first four partial waves.

where B_ν is the rotational constant – where the subscript ν indicates that this in principle depends on the vibrational level, but most importantly serves to distinguish it from the magnetic field B. Assuming a rigid rotor, the rotational constant is given by

$$B_\nu = \frac{\hbar^2}{2\mu r_{\text{eff}}^2}$$

(2.15)

where r_{eff} denotes the bond length. This will correspond to the expectation value of r^{-2} and for weakly bound states as covered in this thesis will be slightly smaller than the classical outer turning point.

The rotation term also gives rise to the centrifugal barrier, which is illustrated in Figure 2.2 and leads to the suppression of collisions with $l > 0$ for ultracold atoms.

2.3. The scattering length

Closely related to the vibrational states is the scattering behaviour of a pair of free atoms. A thorough treatment of this problem may be found in [94], some key results of which will be reproduced here.

In the low energy limit the scattering behaviour is fully described by the s-wave scattering length a. The scattered wavefunction will be a spherical wave and the scattering length is defined by

$$a = -\lim_{k \to 0} \frac{\tan \delta_0(k)}{k} \tag{2.16}$$

where k is the wavenumber and $\delta_0(k)$ is the energy dependent phase shift of the scattered spherical wave.

The scattering cross section is given in the low energy limit by $\sigma = 4\pi a^2$ for distinguishable particles and $\sigma = 8\pi a^2$ for indistinguishable bosons, and is thus independent of the sign of the scattering length. The sign is however important for the stability of a BEC or for miscibility.

For indistinguishable fermions, the low energy scattering cross section vanishes as the s-wave scattering process cannot be made anti-symmetric. A pure spin polarized fermionic sample will thus not thermalize and cannot be cooled evaporatively.

In practice the scattering cross section can exhibit a strong energy dependence over the range of energies sampled in a typical cold atom experiment. This can be troublesome if a minimum is experienced in the course of evaporative cooling (see subsection 5.1.2,subsection 5.1.4 and subsection 5.2.3), which can severely degrade the efficiency. In general, and especially for the final stage of the experiment where we are dealing with either ultracold or quantum degenerate samples, the scattering behaviour is well characterized by the single low energy s-wave scattering length.

A negative (positive) value of the scattering length a corresponds to attractive (repulsive) interaction. The scattering length is directly related to the position of the least bound state in the scattering potential and thus the reduced mass of the molecule. It exhibits a pole when a new bound state appears and will be large and positive when there is a bound state just below the threshold. This relationship allows for the precise determination of scattering lengths from photoassociation data, while the more arguably more direct determination from measurements of their interaction, e.g. thermalization rates or interactions in a BEC, is notoriously hard to calibrate.

2.4. Choice of isotopes

The seven stable isotopes of Yb combined with the two stable isotopes of Rb, all of which are listed in Table 2.1, lead to a total of 14 isotopologues for RbYb.

The main difference between these isotopologues will be in their differerent scattering behaviour characterised by the scattering lengths a. All of them are well known from previous photoassociation measurements [56, 96] and are compiled in Table 2.2.

The interspecies scattering lengths of all combinations are shown in Figure 2.3 and span a full cycle offering everything from strong repulsion to strong attraction as well as very low scattering cross sections. Ideally, the choice of isotopes would be determined solely by these interspecies interactions and isotopes could be switched at will to explore the full range of mass scaling.

	Isotope	M (amu)	Abundance
Rb	85	84.912	72.2 %
	87	86.909	27.8 %
Yb	168	167.934	0.1 %
	170	169.935	3.0 %
	171 ($I = \frac{1}{2}$)	170.936	14.3 %
	172	171.936	21.8 %
	173 ($I = \frac{5}{2}$)	172.938	16.1 %
	174	173.939	31.8 %
	176	175.943	12.8 %

Table 2.1.: Atomic masses M and natural abundance of the stable isotopes of Rb and Yb. [95]

In practice, technical considerations play a considerable role in the selection of the isotopes to be used. The preparation of large samples of each species with a reasonable cycle time requires a certain natural abundance of the isotope in question as well as intraspecies scattering properties that allow for efficient evaporative cooling.

Rubidium

The large attractive intraspecies interaction of ^{85}Rb causes BECs to collapse in a so called *bosenova* [98–100] once they reach a critical atom number (which is impractically low under typical trapping conditions). In addition, the large magnitude of the scattering length
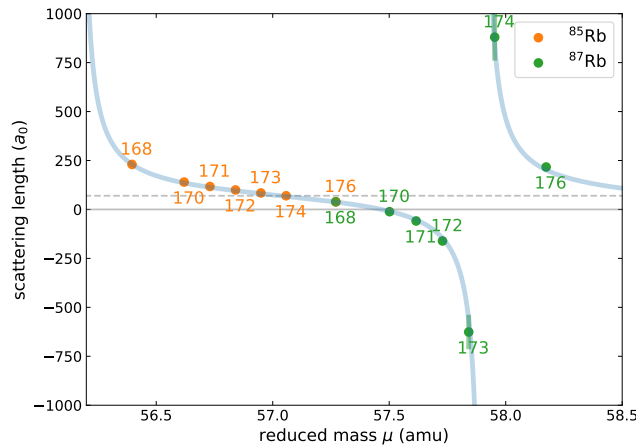
Figure 2.3.: Variation of the interspecies scattering length a with reduced mass μ. The dashed line denotes the mean scattering length of Gribakin and Flambaum [97]. Data from [56].

leads to a large three-body-loss rate. However, the existence of a broad ($\sim 10\,\mathrm{G}$) magnetic Feshbach resonance at an accessible field of $156\,\mathrm{G}$ allows the scattering length too be widely tuned, allowing the creation of stable condensates [101].

The other stable isotope of Rb, ^{87}Rb on the other hand has a much more convenient scattering length of $100\,a_0$, providing a repulsive interaction with a good balance between thermalization rates and three-body-losses. On the flipside, the scattering length of this isotope cannot be tuned as easily, as the Feshbach resonances are much narrower and located at considerable field strengths, the most practical candidate being located at $1000\,\mathrm{G}$ and having an elastic width of only $0.2\,\mathrm{G}$ [1][102], making its use experimentally challenging.

To reduce experimental complexity, the apparatus is thus initially designed for operation with ^{87}Rb only. Conversion for use with ^{85}Rb at a later date is however possible by upgrading the magnetic coils in the science chamber to be able to apply the required bias field and replacing the microwave systems with one designed to operate at the frequency corresponding to the hyperfine splitting of ^{85}Rb ($3.8\,\mathrm{GHz}$).

Ytterbium

As the ground state of Yb lacks any magnetic structure, no magnetic Feshbach resonances are possible here. In principle, the scattering length could be tuned using optical Feshbach resonances [103], however due to the large losses involved, this is impractical for the optimization of thermalization, where relatively long holding times are required.

As in ^{85}Rb, ^{172}Yb exhibits a large negative scattering rate, causing inelastic loss and thus making evaporation relatively inefficient.

On the other hand, the scattering length of ^{176}Yb is relatively low, leading to slow thermalization. This is worsened further by the existence of a Ramsauer-Townsend minimum around $25\,\mu\mathrm{K}$ [96], causing the scattering cross section to go to zero at a temperature corresponding to the transfer from our optical tweezer to the crossed dipole trap, making this step very inefficient.

The fermionic isotopes ^{171}Yb and ^{173}Yb would additionally complicate the analysis of spectra due to their hyperfine structure and pose additional complications during evaporative cooling due to the need to maintain a spin mixture. Even then, the scattering length of ^{171}Yb is extremely low, preventing efficient evaporative cooling.

Working with ^{168}Yb is impractical due to the low natural abundance of $0.1\,\%$, requiring extremely long MOT loading times.

From the single species properties, ^{87}Rb, ^{174}Yb would seem to be the ideal combination, with both exhibiting moderate repulsive intraspecies interaction and thus good thermalization behaviour allowing the production of large condensates of both. However for this combination the repulsive interspecies interaction is so large, that phase separation occurs already at modest temperatures of a few $\mu\mathrm{K}$ [66]. While this phenomenon is interesting in its own right, two clouds that only touch on their surface are not a good starting point for photoassociation experiments. On the other hand, the existence of a very weakly bound

---

[1]The small width compared to the other resonances is due to the fact that in ^{87}Rb the singlet and triplet potentials have nearly equal scattering phase shifts [102]

state may provide possibilities not accessible in the other systems, for example the possibility of association using a microwave rather than an optical photon [104].

Taking into account these aspects, the experiments carried out in the course of this thesis were conducted using ^{87}Rb and ^{170}Yb. With a scattering length of $a_{\mathrm{Rb,Yb}} = -11\,a_0$, this combination has a weakly attractive interspecies interaction. On the one hand this means that interspecies thermalization is slow, making sympathetic cooling impractical and impeding the use of thermalization as a tool to quantify overlap of both species. On the other hand, the attractive interaction, combined with a moderate repulsive intraspecies interactions, ensures miscibility and the existence of a mixed Mott insulator state, which is highly desirable as a starting point for photoassociation. Both intraspecies scattering cross section and abundance are lower for ^{170}Yb than for ^{174}Yb, making it harder to obtain large condensates.

Another promising combination for future use is that of ^{85}Rb and ^{174}Yb. If the intraspecies interaction of Rb can be tuned to be repulsive using a Feshbach resonance, the higher atom numbers and better thermalization of ^{174}Yb and the moderate interspecies scattering length of $a_{\mathrm{Rb,Yb}} = 70\,a_0$ would allow efficient sympathetic cooling of Rb by Yb. As only a small number of Rb atoms would be required in this case, this might even be possible without the microwave[2] evaporation step (see subsection 5.1.2), thus needing no modifications to the setup except for the magnetic field.

		Rb	**Yb**						
isotope			168	170	171	172	173	174	176
Yb			252	64	-3	-599	-200	105	-24
Rb	85	-443[a]	230	140	117	100	84	70	39
	87	100[b]	39	-11	-59	-161	-626	880	217

Table 2.2.: Inter- [56] and intraspecies [96] scattering lengths in units of a_0.

[a]Can be widely tuned via broad magnetic Feshbach resonance at $156\,\mathrm{G}$ [105]

[b]Tuning by Feshbach resonance possible in principle, but resonances are narrow and located at relatively high fields [102, 106]

[2]Adapting the microwave system is of course possible, but will require replacement of the VCO, the amplifier and the antenna as these all are narrow band designs.

2.5. Photoassociation

In photoassociation (PA) a pair of colliding atoms is transferred to an electronically excited, (weakly) bound state by absorption of a photon with an energy corresponding to the difference between these two states, or

$$A + B + \gamma \rightarrow (AB)^* \tag{2.17}$$

where A and B denote the two atoms, which may or may not be of the same species, γ is the photon and $*$ denotes the electronic excitation. This is illustrated in Figure 2.4.

This process has been studied extensively and has proven its use both as a spectroscopic tool for the investigation of molecular potentials and for the production of ultracold molecules from a sample of ultracold atoms. An exhaustive review may be found in [45].

After excitation the molecule will decay into either a bound state in the electronic ground
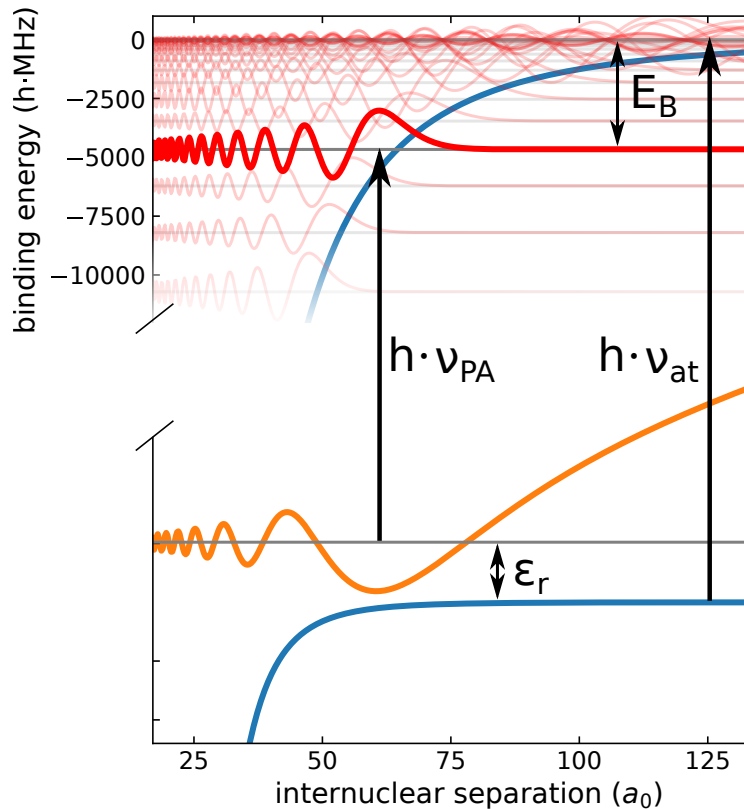
Figure 2.4.: Schematic depiction of the PA process from a scattering state with energy ϵ_r (greatly exaggerated in the figure) in the electronic groundstate to a vibrational state bound by E_B in the electronically excited state.

state or a pair of separated atoms[3]. In a typical ultracold atom experiment, both of these processes lead to a loss in the detectable atom number – either due to the bound state not being resonant with the imaging light or due to the atom pair being too energetic to remain trapped.

The rate of this process is given by [45, 77]

$$K(\Delta, I, \vec{p}_c, \vec{p}_r) = \frac{\hbar\pi}{k_r \mu} \sum_{e,g} (2l+1) \frac{\Gamma_{pe}\Gamma_{eg}(I, \epsilon_r)}{[\Delta_{\mathrm{FB}}(\Delta, I, \vec{p}_c, \vec{p}_r)]^2 + [\Gamma_e(I, \epsilon_r)/2]^2} \tag{2.18}$$

where k_r, ϵ_r and p_r are the wavenumber, energy and momentum of the relative motion, p_c is the center of mass momentum, Δ_{FB} is the detuning from the photoassociation resonance accounting for all relevant shifts including Doppler shift, recoil shift and light induced shift of the transition and ϵ_r is the energy of the scattering state.

Several loss rates or linewidths appear in the expression: Γ_{pe} is the loss rate from the excited state. When radiative losses are dominant, this is the natural lifetime of this state. The light induced width between the e and g states is given by *Fermi's Golden Rule*:

$$\Gamma_{eg} = 2\pi \left| \langle \Psi_e | \hat{V}_{\mathrm{laser}}(I) | \Psi_g(\epsilon_r) \rangle \right|^2, \tag{2.19}$$

where the operator $\hat{V}_{\mathrm{laser}}(I)$ represents the optical coupling by the PA laser and $|\Psi_e\rangle$ and $|\Psi_g(\epsilon_r)\rangle$ are the bound state and energy normalized wavefunction of the scattering state respectively. Finally $\Gamma_e = \Gamma_{pe} + \sum_g \Gamma_{eg}$ is the total width.

For weakly bound states, where the transition dipole moment does not appreciably change between vibrational states, it is possible to separate the matrix element into a part corresponding to the atomic transition and the overlap between the vibrational wavefunctions. We can then write [77]

$$\Gamma_{eg} = \Gamma_{\mathrm{A}} \frac{3}{4\pi} \frac{I\lambda_{\mathrm{A}}^3}{c} f_{eg}^{\mathrm{rot}} f_{eg}^{\mathrm{FC}} \tag{2.20}$$

where Γ_{A} and λ_{A} are the natural linewidth and wavelength of the atomic transition, f_{eg}^{rot} contains the factors relating to the angular momenta of both states and

$$f_{eg}^{\mathrm{FC}} = \left| \int_0^\infty \psi_e(r)\, \psi_g(r, \epsilon_r)\, \mathrm{d}r \right|^2 \tag{2.21}$$

is the free-bound Franck-Condon factor defined as the overlap integral between the vibrational wavefunctions $\psi_e(r)$ and $\psi_g(r, \epsilon_r)$.

As weakly bound excited states will have the amplitude of their vibrational wavefunction concentrated near their classical outer turning point, while the scattering wavefunction rapidly falls off with decreasing separation, the Franck-Condon factor is approximately proportional to the squared value of the scattering wavefunction at the Condon point r_C, defined as the outer point where the local wavenumber is equal for both states.

---

[3]Although we will see that the overlap between the scattering state of a particular energy and the excited bound state is usually extremely small, the integration over all energies may lead to an appreciable probability for this process.

Within the reflection approximation [107], the Condon point is approximately equal to the classical outer turning point and we can approximate the Franck-Condon factor by

$$f_{eg}^{\mathrm{FC}} \approx \frac{\delta E_e}{\delta n} \frac{1}{D_C} \left| \psi_g(r_C, \epsilon_r) \right|^2 , \tag{2.22}$$

where $\frac{\delta E_e}{\delta n}$ is the vibrational level spacing in the excited state and D_C is the difference in slope between ground and excited state potentials evaluated at the Condon point. For cases where the reflection approximation is not valid, that is the difference between the Condon point and the classical outer turning point is significant, modified expressions are available [108].

Experimentally, photoassociation is usually detected by trap loss spectroscopy. Even if the excited states decays into a bound ground state molecule that remains trapped, it will be invisible to the absorption or fluorescence detection schemes used for the atoms. From Equation 2.19 we expect the PA resonance to have a Lorentzian lineshape. In practice we will often perform PA on a sample with a (thermal) continuum of energies rather than a discrete energy. In this case the actual lineshape is obtained by integrating over the energy distribution. As the prefactor, the detuning and the light induced width all have an energy dependence, this will lead to a broadening and modification of the lineshape particularly for narrow resonances [77].
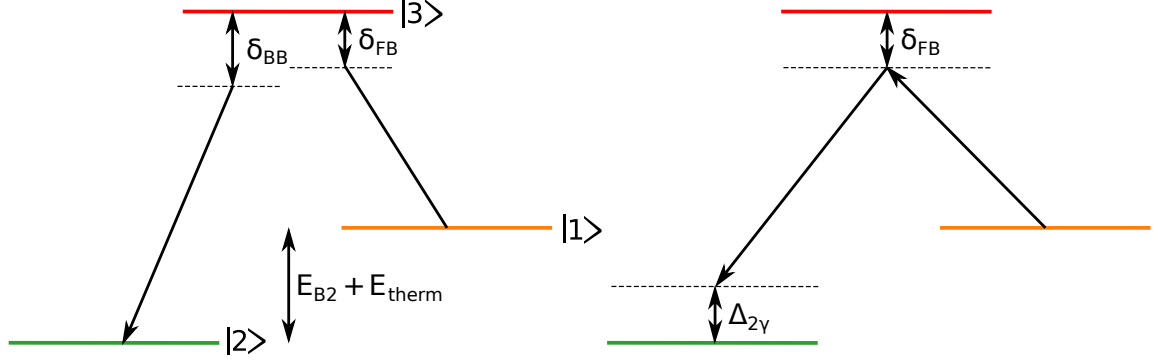
2.6. 2-photon-photoassociation

In 2-photon photoassociation [109], the bound state in the electronically excited potential is coupled to a bound state of the electronic ground state by an additional laser, which we will call the bound-bound laser.

Figure 2.5 shows a simplified diagram of the 2-photon photoassociation level scheme. The scattering state and the bound levels of the electronically excited and ground state form a Λ-type three level system with the couplings Ω_{BB} and Ω_{FB} created by the bound-bound and free-bound laser respectively. The energy separation between the lower two levels is the sum of the binding energy of the final bound state E_{B2} and the thermal energy of the scattering state E_{therm}. Such three level systems have been analyzed extensively and offer a wealth of possibilities for coherent manipulation, including *Electromagnetically Induced Transparency* (EIT) [110, 111] and *Stimulated Raman Adiabatic Passage* (STIRAP) [112, 113].

In the following, we will take the bound-bound laser frequency $\tilde{\nu}_{\mathrm{BB}}$ to be defined relative to the free-bound laser frequency. When analyzing a specific transition the laser frequencies are parameterized using either the individual detunings δ_{FB} and δ_{BB} of the free-bound and bound-bound laser from their respective transition, or the free-bound detuning δ_{FB} and the two-photon detuning $\Delta_{2\gamma} = \delta_{\mathrm{FB}} - \delta_{\mathrm{BB}}$.

In the simplest type of experiment, the free-bound laser frequency ν_{FB} is kept on resonance with the unperturbed photoassociation transition, while the frequency of the bound-bound laser $\tilde{\nu}_{\mathrm{BB}}$ is scanned. When the bound-bound laser comes close to resonance with a vibrational level of the ground state, this transition exerts a light shift on the excited state. As the bound-bound Franck-Condon factor is generally orders of magnitude larger than the

Figure 2.5.: Level scheme for the 2-photon photoassociation measurement showing the different parameterizations using either the individual detunings δ_{FB} and δ_{BB}, or δ_{FB} and the two-photon detuning $\Delta_{2\gamma}$

free-bound Franck-Condon factor, for comparable intensities of both lasers this shift will easily be large enough to prevent the (1-photon) photoassociation process by shifting the free-bound transition out of resonance, leading to an increase in the remaining atom number compared to that without the bound-bound laser.

When the bound-bound laser is weak and the resulting light shift is less than the linewidth of the free-bound transition and the relative linewidth between both lasers, it is more appropriate to think of the effect in terms of interference rather than light shifts. In this case the possible paths from the free state $|1\rangle$ to the excited bound state $|3\rangle$ are either $|1\rangle \to |3\rangle$ or $|1\rangle \to |3\rangle \to |2\rangle \to |3\rangle$. On resonance, they interfere destructively, preventing the population of state $|3\rangle$ [110]. Another way to conceptualize this is in the dressed state picture, where a so called dark state emerges (see section 9.5).

In either case, when the free bound laser is kept on the unpertubed 1-photon resonance, resonance of the bound-bound laser with a bound level of the ground state $|2\rangle$ leads to a suppression of photoassociation loss and is thus easily detectable as an increase in atom number.

The atom loss rate due to photoassociation is given by the solution to the optical Bloch equations. For $\Omega_{\mathrm{BB}} \gg \Omega_{\mathrm{FB}}$ – which is generally easily fulfilled since the free-bound FCFs are much smaller that the bound-bound FCFs – the loss rate is given by [110]

$$\frac{\dot{N}}{N} = \frac{\Omega_{\mathrm{FB}}^2 \left[4\Gamma\Delta_{2\gamma}^2 + \Gamma_{\mathrm{eff}}\left(\Omega_{\mathrm{BB}}^2 + \Gamma_{\mathrm{eff}}\Gamma\right)\right]}{\left|\Omega_{\mathrm{BB}}^2 + \left(\Gamma + 2i\delta_{\mathrm{FB}}\right)\left(\Gamma_{\mathrm{eff}} + 2i\Delta_{2\gamma}\right)\right|^2} \tag{2.23}$$

with the free-bound and bound-bound Rabi frequencies Ω_{FB} and Ω_{BB}, the decay rate of the excited state Γ and the effective decay rate Γ_{eff} accounting for decoherence of the dark state.

In the case of zero free-bound detuning δ_{FB}, this expression reduces to a Lorentzian lineshape as a function of the two photon detuning $\Delta_{2\Gamma}$.

On the other hand, when keeping the bound-bound laser on resonance ($\Delta_{\mathrm{BB}} = 0$) and scanning the free-bound detuning δ_{FB}, the well known EIT or dark resonance lineshape emerges [110].

To obtain the actual lineshape in the presence of thermal broadening (see subsection 8.6.2), the lineshape is again integrated over the distribution of detunings corresponding to the thermal distribution of collision energies.

3.

Optical Traps, Fiber amplifiers, synthesizers and beatnotes

This chapter introduces a number of technologies that play a crucial role in our apparatus. All our photoassociation experiments will be performed with the atoms held in optical traps, which also play a large role in the preparation of the samples. The first part of this chapter thus aims to give an introduction to optical trapping in general (section 3.1) and the application and development of fiber amplifiers for this purpose. We will also discuss the development of a novel fiber amplifier, which was crucial for the success of this thesis (section 3.3). We will then give an introduction to the concept of synthesizers (section 3.4), especially their application to laser frequency stabilization using beatnotes (section 3.5). This technology will later allow us to stabilize our photoassociation laser at a tunable offset from the atomic transition and is also used to stabilize the repumper and microwave sources in the Rb system.

3.1. Optical Dipole Traps

As in most modern ultracold atom experiments, the majority of our experiment takes place with the atoms held in various optical dipole traps (ODT). I will thus give a short overview of these traps, following the exhaustive treatment of [114].

In a semi-classical picture dipole trapping arises due to the atom being polarized by the rapidly oscillating electric field of the light, with the relationship between the electric field and the polarization given by the complex polarizability $\alpha(\omega_L)$, depending on the frequency relative to the atomic transition frequency.

A light field of intensity $I(\vec{r})$ thus creates a potential

$$U_{\text{dip}}(\vec{r}) = -\frac{1}{2}\left\langle \vec{p}\cdot\vec{E}\right\rangle = -\frac{1}{2\epsilon_0 c}\text{Re}(\alpha)\cdot I(\vec{r}) \tag{3.1}$$

which will be attractive when the light frequency is red detuned with respect to the dominant atomic transition and repulsive for blue detuning.

On the other hand, the photon scattering rate, which leads to unwanted heating of the trapped atoms, is given by

$$\Gamma_{\text{sc}}(\vec{r}) = -\frac{1}{\hbar\epsilon_0 c}\text{Im}(\alpha)\cdot I(\vec{r}). \tag{3.2}$$
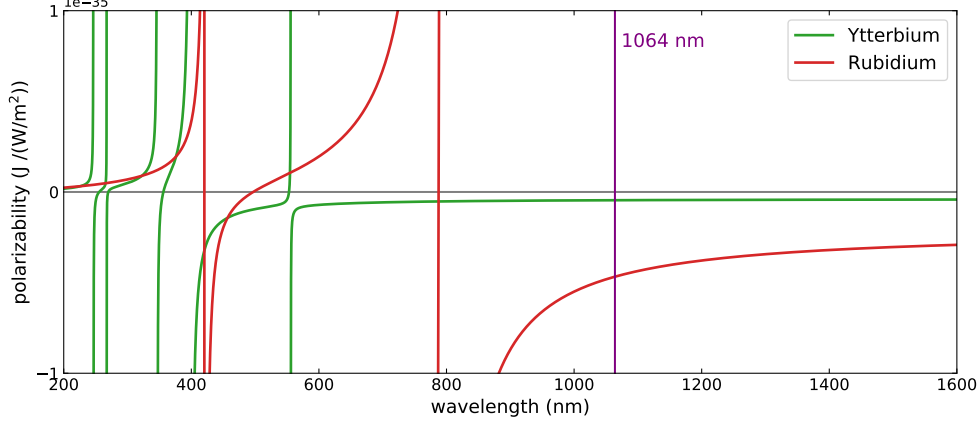
Figure 3.1.: Plot of the trap depth per intensity for both species as a function of trap wavelength. The wavelength of 1064 nm, which is used for most optical traps in this experiment, is marked by a vertical line.

It turns out that this scattering rate scales as $\frac{1}{\Delta^2}$, while the trap depth scales as $\frac{1}{\Delta}$. It is thus favorable to operate a trap at large detuning δ, where the scattering rate for a given trap depth is lower.

The polarizability $\alpha_a(\omega)$ for a state $|a\rangle$ is given by

$$\alpha_a(\omega) = \sum_b \frac{|\langle a|\vec{D}\cdot\hat{\epsilon}|b\rangle|^2}{E_b - E_a - \hbar\omega} + \sum_b \frac{|\langle a|\vec{D}\cdot\hat{\epsilon}|b\rangle|^2}{E_b - E_a + \hbar\omega} \tag{3.3}$$

with the sum going over (in principle) the complete set of electronic states, and is thus straight forward to calculate from published data on atomic transitions. The results of such a calculation for Rb and Yb, based on data from [54], are shown in Figure 3.1. For our experiments it is desirable for a dipole trap to be attractive and of similar trap depth for both Rb and Yb. However this can only be realized relatively close to atomic resonances, where the traps lifetime will be strongly limited by photon scattering and high power laser systems are not always straightforward. A common approach which we follow here is thus to chose a wavelength that is sufficiently red detuned from all atomic transitions of either species and easy to work with. In our case this is 1064 nm, which is marked by a vertical line in this figure. At this wavelength, traps will be about ten times deeper for Rb than for Yb, which poses certain challenges (see subsection 5.3.1). The setup may later be augmented by additional traps compensating for this difference.

3.1.1. Trap geometry

Optical dipole traps are commonly realized in several different geometries, the most common of which are illustrated in Figure 3.2 and will be introduced here.
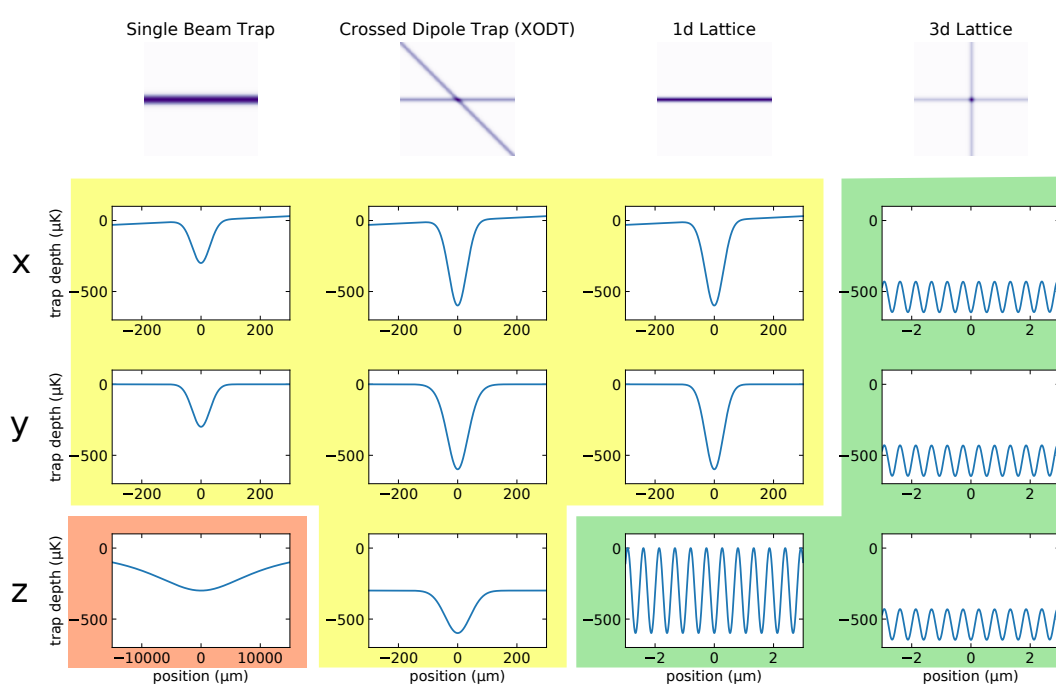
Figure 3.2.: Overview of the various geometries of optical traps and their different degrees of confinement, showing a false color representation of the beam intensities in the horizontal plane and plots of the trap depth along each axis. Note that the x-axis scaling and confinement length scales differ by several orders of magnitude, which is reflected in the color coded background. The color coding reflects the degree of confinement along each axis, from red for extremely weak to green for strong confinement.

The most basic geometry consists of the focus of a single gaussian beam. This configuration provides tight confinement along the two transverse axes with a length scale corresponding to the beam waist ω_0, but only very weak confinement along the propagation direction of the beam, where the length scale corresponds to the much larger Rayleigh length $z_R = \frac{\omega_0^2 \pi}{\lambda}$.

This can be improved by crossing two gaussian beams, leading to a much tighter trap providing strong confinement in all three directions. This is the trap of choice for evaporative cooling [115], which is a crucial technique in ultracold atom experiments, as confinement is strong enough to maintain a sufficient collision rate even when reducing the trap depth.

Finally, even stronger confinement on a length scale corresponding to half the optical wavelength can be achieved in standing wave traps, where in the simplest case the trapping beam is retroreflected, leading to a standing wave along the beam direction, provided the coherence length of the laser is sufficient. This again can be extended to more dimensions by crossing multiple pairs of beams, providing tight confinement along all directions.

Due to their periodic potential these traps are referred to as optical lattices [114]. In general, the atomic cloud will not be restricted to a single site in these lattices, but spread out over many sites, with tunneling between the sites playing an important role. This gives rise to rich physics on its own, which we will briefly explore in subsection 5.1.6 and section 9.3. On the other hand, the large number of sites supresses collisions to a high degree, making these traps unsuitable for evaporative cooling.

3.1.2. Trap wavelength

In order to achieve strong confinement in a far detuned optical dipole trap in either single beam or crossed geometry, a small beamwaist is required. This means the used lasers should be spatially single moded. For practical beam waists and trap depths, a relatively high power of several Watts is required. The exact wavelength on the other hand is not tightly constrained, as long as it is sufficiently red detuned from the relevant atomic transitions.

A major consideration is thus the availability and price of spatially single mode lasers with high output power. In this regard the $1\,\mu$m-region is particularly attractive, with both Nd:YAG lasers and Yb doped fiber lasers widely available. These systems can deliver tens of Watts of power while maintaining single mode operation both spatially and (if desired) spectrally.

Particularly Yb fiber amplifiers are a convenient and economical solution with practically maintenance free all-fiber setups that are relatively easy to assemble from off-the-shelf components.

With both signal and pump light being guided inside the fiber, long interaction lengths are possible, allowing high gains, while the spreading of the thermal load along the fiber allows high operating powers. Pump light can be efficiently provided by fiber coupled diode lasers, which are readily available with powers of tens of Watts in a typical $105\,\mu$m multimode fiber.

While high power Yb fiber lasers are commonly available between $1030\,$nm and $1070\,$nm, the wavelength $1064\,$nm is frequently used. This is in part due to widespread availability

of optics for this wavelength due to the popularity of Nd:YAG lasers. Indeed, Nd:YAG lasers with a non-planar ring oscillator (NPRO) geometry present an attractive seed laser for single-frequency fiber laser systems. Due to the monolithic resonator and the low intracavity losses, this laser type offers exceptionally low linewidths and excellent stability [116, 117] and is thus ideally suited for standing wave traps.

A drawback is the existence of bound-bound transitions in this spectral region that may have an impact on the production of and experiments with molecules if the wavelength is not carefully chosen. However, for most applications this is outweighed by the far better availability of high power lasers compared to the alternative wavelengths of $1.5\,\mu m$ (Erbium doped fiber), $2\,\mu m$ (Thulium doped fiber) or even $10.6\,\mu m$ (CO_2).

3.1.3. Spectral considerations

If a standing wave trap is desired, the need for a stable, high-contrast interference pattern – possibly in the presence of appreciable path length difference, as is the case for a backreflected optical lattice – dictates the need for single-frequency laser.

In the case of travelling wave traps, the exact spectral properties of the laser appear to be less important, provided the light is sufficiently far detuned from all relevant atomic and molecular transitions. There are however a few more or less subtle effects influencing the choice between a single-frequency and a multimoded laser, which are discussed in this section.

Stimulated Brillouin Scattering from single frequency lasers

Due to the small mode area and large interaction length found in single mode fiber systems, non-linear effects come into play already at relatively modest powers.

An effect that is particularly troublesome in this context is Brillouin scattering, where electrostriction introduces a coupling between photons and phonons propagating in the fiber. This leads to a process where a photon is converted into a phonon and a backward propagating photon with a frequency reduced by the Brillouin shift (determined by the phase matching condition and typically tens of GHz). In the presence of a strong monochromatic light field, this effect contributes appreciably to the phonon population in the medium, giving rise to *Stimulated Brillouin Scattering* (SBS) [118, 119].

This is illustrated by the backward propagating signal power measured in the fiber amplifier (see section 3.2) used for the optical lattice, which is shown in Figure 3.3d, rising exponentially with increasing output power. While the measurement was stopped in a range that is still safe for the amplifier, SBS would eventually lead to the majority of the power propagating in the backward direction.

This effect not only leads to a loss of available output power, but leads to a substantial amount of backward propagating power and induces an instability, both of which potentially lead to the destruction of the device.

The straightforward approach to counter this effect is to reduce the intensity, which can be achieved by increasing the mode area of the fiber. Fibers with a core diameter of $10\,\mu m$ instead of the typical $6\,\mu m$ for $1064\,nm$ fiber still only support a single transversal mode
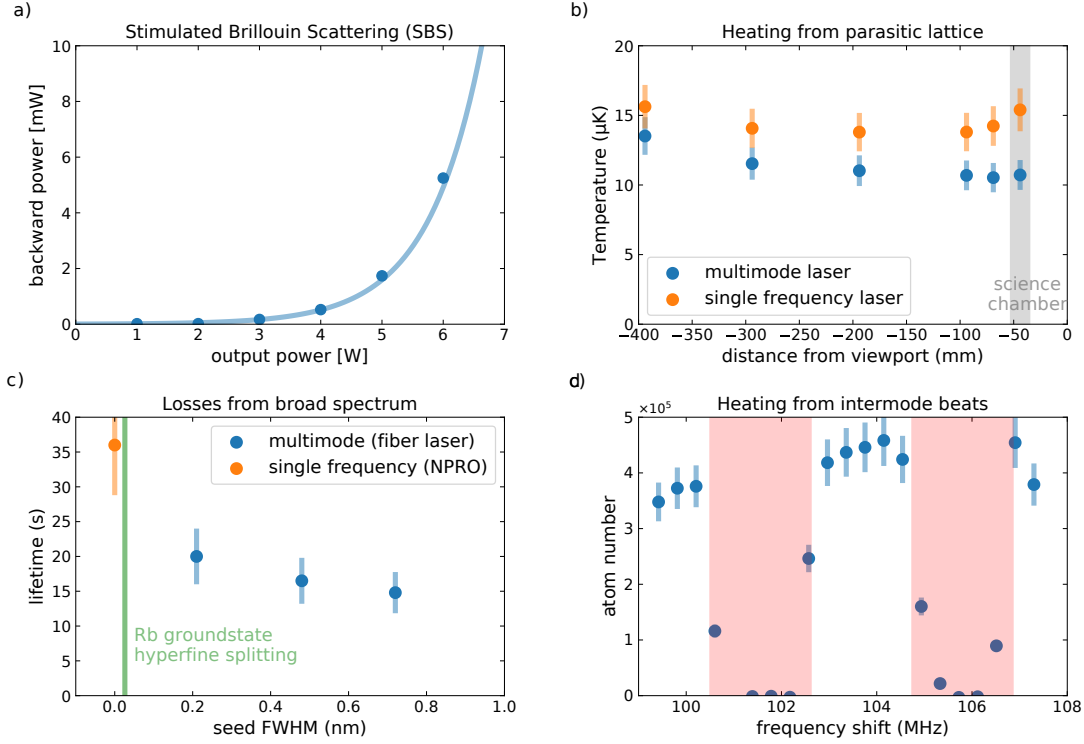
Figure 3.3.: Several effects influencing the choice of laser bandwidth: **(a)** SBS causing an exponential increase in the backward propagating light in a fiber amplifier, leading to increased danger of parasitic pulsing and eventually limiting the output power. **(b)** Heating of atoms transported in the optical tweezer when approaching the viewport, caused by the formation of parasitic lattice, compared to a multimode laser with short coherence length. Note the temperature in the last datapoints for the single frequency laser is limited by evaporation from the trap. **(c)** Decrease of the lifetime of a cloud of Rb with increasing spectral width of the seed laser, attributed to driving of Raman and photoassociation transitions. The green vertical line indicates the width corresponding to the hyperfine splitting of the Rb ground state **(d)** Atom number after evaporation in an XODT for different frequencies of the crossing AOM, showing loss when the frequency is close to a multiple of the laser mode spacing.

and can thus be used to increase the mode area without incurring further complications. Note that mixing $10\,\mu m$ and $6\,\mu m$ fiber in a system is possible, but will lead to an excess splice loss of ~ 0.7 dB for each transition[1]. Further increase of the mode area leads to the fiber supporting higher transversal modes, and special measures will have to be taken to ensure single spatial mode operation. Another approach to suppress SBS is by keeping different fiber sections at different temperatures and thus thermally shifting the Brillouin scattering resonance out of resonance between these sections [120].

If the laser bandwidth is much larger than the Brillouin bandwidth, which is given by the phonon lifetime in the medium and typically is on the order of $0.1\,GHz$, stimulated Brillouin scattering becomes inefficient. This is typically the case in multimode fiber lasers which have linewidths of tens of GHz.

Stimulated Brillouin Scattering thus imposes a limit on the output power of a fiber amplifier seeded with a narrow linewidth, but on the power scales dealt with here can be neglected for broad seeds.

Parasitic lattices from single frequency lasers

If parasitic reflections from optical surfaces reach the trap, they can give rise to unwanted standing waves, leading to corrugated potentials. This is particularly worrisome in the case of our optical tweezers, where the trap is translated by axial movement of the laser beam focus. As the confinement in this direction is relatively weak, even a weak standing wave is enough to introduce a relevant perturbation. This is demonstrated by the Rb tweezer setup, where as shown in Figure 3.3b even small translation cause strong heating when the amplifier is seeded by a single frequency laser, while no heating related to transport is observed when a multimoded seed laser with a coherence length[2] of $\sim 2\,mm$ is used. We attribute this to the reflection from the viewport where the tweezer beam exits the vacuum chamber (see chapter 4) being unfortunately well aligned to the axis of the tweezer —which in turn is tightly constrained by the orientation of the differential pumping tube. The corrugation caused by this stays stationary when the tweezer is moved, causing the atom cloud to be dragged through a series of bumps and heated in the process.

Photoassociation and Raman transitions driven by multimode lasers

The issues described in the previous sections can easily be avoided through the use of a laser operating on a large number of longitudinal modes simultaneously. A typical multimode fiber laser such as the one used in our setup has a spectrum consisting of thousands of modes, spaced by the free spectral range of the laser cavity. With typical fiber laser cavities being several meters in length, the mode spacing will be a few MHz and thus on the order of a typical atomic linewidth. It is thus almost guaranteed that any transition located within

---

[1]This excess loss can be eliminated by including a tapered fiber section, a so called Mode Field Adapter. In principle, these can be easily manufactured by drawing out a heated fiber – for example using a translation stage and the authors camping stove – In practice it is a much better, if less fun, idea to buy one of the readily available commercial models.

[2]defined as the distance after which the the value of the coherence function drops to $1/e$

the laser spectrum is resonantly driven by one laser mode. Even if the laser is far detuned from any atomic transition, photoassociation transitions may exist in the relevant spectral range.

This is the case for Rb, where the 1064 nm trap laser is red detuned from all atomic transitions originating from the ground state, but the well depth of the 0_u^+ potential formed by spin-orbit mixing of the $A^1\Sigma_u^+$ and $b^3\Pi_u$ potentials exceeds the detuning from the $^2S_{1/2} \rightarrow {}^2P_{3/2}$ transition [121]. Photoassociation transitions are thus possible in the spectral region in question and have been observed to cause trap loss [122, 123].

Another consequence of the dense array of laser modes is the possibility of driving stimulated Raman transitions [124]. If the atom exhibits any structure on the scale of the width of the laser spectrum, there will exist many pairs of modes with a difference frequency corresponding to the atomic splitting and it is possible for these mode pairs to drive stimulated Raman transitions and thus cause changes to the internal state of the atoms.

Such population transfer has been observed to occur between the hyperfine states of the Rb ground state with trapping wavelengths in the 1 μm-region. In addition to polluting the prepared hyperfine state, this leads to heating and trap loss by two-body decay [124].

In Yb, Raman transitions are not an issue due to the lack of structure in the ground state and there exist no molecular potentials reachable from the ground state by a single 1064 nm photon, so no short range photoassociation is possible either.

XODT beats caused by multimode lasers

When forming a crossed dipole trap from two beams derived from the same laser (see subsection 4.6.1), interference effects between both beams need to be avoided, particularly as they depend sensitively on the path length difference between both beams on a sub-wavelength scale, which will usually not be stable.

A common approach is to introduce a frequency shift between the two beams, causing the interference to oscillate at the difference frequency between the beams, which is typically orders of magnitudes larger than the trap frequencies involved, and thus will be averaged out. When a multimode laser is used, however, this approach fails when the difference frequency is close to an integer multiple of the lasers mode spacing. In this case, beats between pairs of laser modes give rise to intensity fluctuations at much lower frequencies – in particular close to the trap frequencies –, leading in turn to heating and trap loss.

This effect is illustrated in Figure 3.3c, where evaporative cooling of Rb (see section 5.1) has been performed with varying frequency differences between the two beams. It is immediately evident that there are frequency regions where heating is so strong that no atoms survive the evaporation ramp. These regions are spaced by about 4 MHz in this case, corresponding to the free spectral range of the laser cavity. Similar behaviour is observed for Yb.

One approach to reduce this effect is to ensure orthogonal polarizations between the two beams. In the Rb system, this is achieved by using a $\lambda/2$-plate to rotate the linear polarization by 90° when the beam is folded. Due to imperfections in this waveplate and

the remaining optical elements, non-orthogonal polarization components remain even after careful alignment. Thus care is taken to keep the difference frequency outside the identified zones, except for short times during the translation of the XODT. In the Yb setup we have to rely on choice of frequency alone as the polarization of the tweezer beam is not well defined and there is thus no straightforward way to generate the orthogonal polarization for the crossing beam.

3.2. Fiber amplifiers

The apparatus presented here makes heavy use of homebuilt fiber amplifiers for optical trapping and cooling and a large portion of the work presented here consists of the development of such systems. For this reason a brief overview of the topic is given here, with more extensive treatment to be found in [125, 126]. In a fiber amplifier the gain medium consists of doped optical fiber. The guiding of the light in the fiber allows the interaction length to be orders of magnitude higher than in bulk gain media, which is particularly beneficial for high power devices as the removal of excess heat is significantly improved.

By way of example, a schematic of the home-built fiber amplifier used for the Yb tweezer is shown in Figure 3.4 and will be used to briefly explain a typical fiber amplifier setup. This system was built in the scope of and will be described in detail in [127].

The seed laser first passes an isolator to prevent backreflections into the seed laser, and a fused coupler sampling $\sim 1\%$ of the light propagating in each direction for monitoring on photodiodes. It is then combined with the light from two multimode pump diodes using a commercial pump-signal-combiner. The double clad output fiber of the combiner is spliced to a double clad active fiber with the splice being enclosed in epoxy with a refractive index corresponding to that of the double clad fiber coating in order to prevent the loss of pump light.

The length of the active fiber is typically chosen so that $95\,\%$ of the pump light is absorbed and converted into signal light with high efficiency.

The active fiber is then again spliced to a passive (single-clad) fiber. In order to get rid of the remaining unabsorbed pump light this splice, denoted cladding power stripper in the figure, is coated with an refractive index close to that of the fiber cladding, allowing all light guided in the cladding to escape. In order to monitor the output power, the stray light coming from the losses in a further splice is detected using a photodiode. It would also be possible to utilize another fused coupler, but the largest commonly available coupling ratio of 99:1 leads to an impractically high power at the monitor port for high power amplifiers. Finally, an output isolator protects the amplifier from backreflections. In this case, an isolator with a free-space output is used, combining isolator and collimator and thus reducing losses.

The fiber amplifier shown here reliably provides an output power of $30\,\mathrm{W}$, starting from a seed power of $\sim 0.8\,\mathrm{W}$. It is however restricted to operating with spectrally broad seed lasers, as SBS would otherwise limit the usable output power to much lower values (see section 3.1.3 and section 4.4).
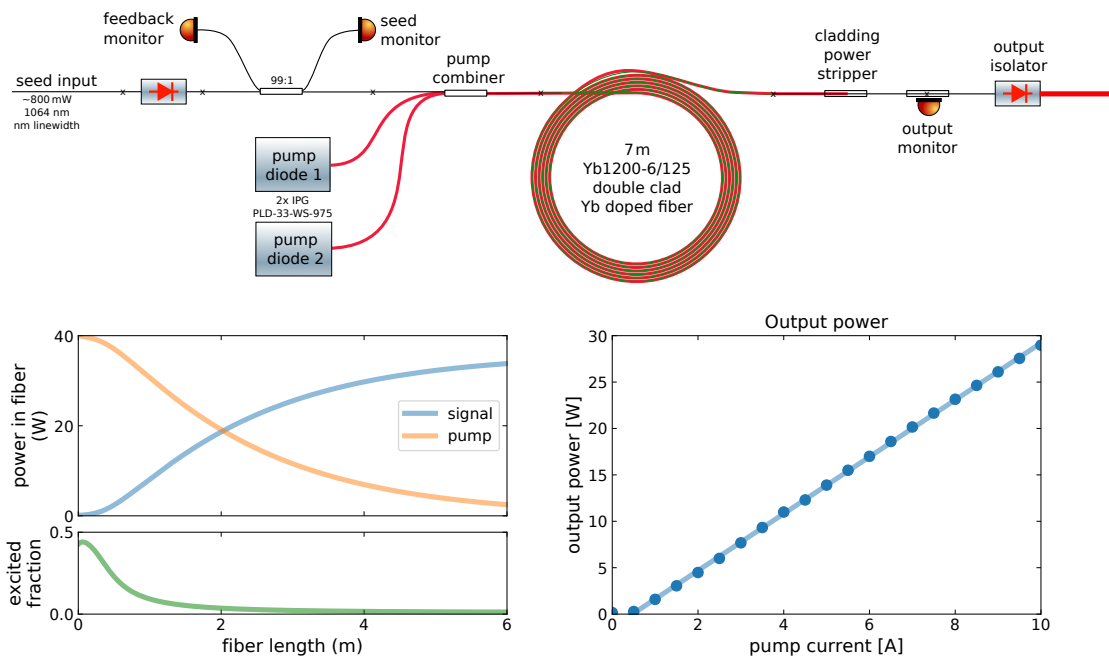
Figure 3.4.: Schematic of the fiber amplifier used for the Yb tweezer. The lower left panel shows a simulation (created using [128]) of the power evolution of pump and signal beam as well as the fraction of excited ions along the fiber length. The lower right shows the measured output power as a function of the pump current.

## 3.3. Yb Fiber amplifier at the edge of the gain spectrum

While light at 556 nm can be directly produced by dye lasers, frequency doubling of an infrared source at 1112 nm has become the standard technique to generate the light for laser cooling.

Commercially available distributed feedback (DFB) Yb fiber lasers with an output power in the 10 mW range and a linewidth of several 10 kHz in this spectral region are readily available. However, for laser cooling of Yb power levels of a few hundred mW in the green are desirable. Using modern waveguide PPLN devices, this requires $0.5 - 1$ W at 1112 nm. Therefore, the DFB fiber lasers can only be used as a seed source and an amplification of > 20 dB is required.

While semiconductor gain chips and tapered amplifier chips are commercially available and have been used in Yb experiments [130], they have limited output power and typically low beam quality. Recently, optically pumped vertical external-cavity surface-emitting lasers (VCSEL) have been shown to overcome these limitations [131]. Another route is the use of Raman amplifiers, which require very long fibers for moderate pump powers and potentially lead to significant linewidth broadening [132].

A natural choice for the amplifier is an Yb doped fiber amplifier. Such systems with output powers of 1 W were commercially available and commonly used for the cooling of Yb [133, 134], but proved to be not reliable enough and were discontinued. These commercial devices were pumped in the spectral region from the broad absorption feature at 915 nm to the narrow absorption peak at 976 nm of Yb doped fiber [125]. The gain profile of Yb doped fiber pumped at these wavelengths exhibits a peak between 1000 nm and 1060 nm and decreases for higher wavelengths. At 1112 nm, the gain is reduced to a fraction of its peak value [135]. This leads to pronounced amplified spontaneous emission (ASE) in the spectral region between 1000 nm and 1060 nm, necessitating the use of several amplification stages with low gain, separated by isolators and filtering stages (e. g. using unpumped sections of active fiber [136]) which contribute significant insertion losses and thus reduce the system's net gain. Additionally the required strong pumping combined with the low cross section at the signal wavelength leads to a high excitation fraction, strongly enhancing photodarkening of the doped fiber [137]. These disadvantages of a short wavelength pump can be partially remedied by heating of the active fiber as has recently been demonstrated for a high power fiber amplifier at 1120 nm [138].

Our approach to increase the single stage gain of an Yb fiber amplifier and reduce its vulnerability to photo-darkening, parasitic lasing and self-pulsing is to use a pump
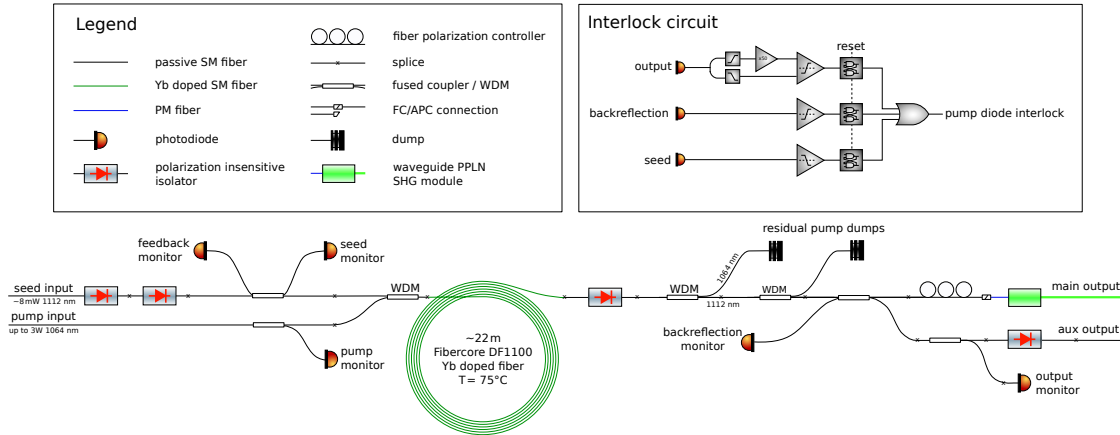
Figure 3.5.: Schematic of the fiber amplifier at 1112 nm. The setup is described in detail in the text (see 3.3.1). The main panel shows the optical fiber setup starting with the inputs for seed and pump laser source on the left to the frequency-doubled free space output on the right. The inset on the top right shows the interlock circuit described in section 3.3.3

wavelength which is longer than the wavelength of the gain peak. By pumping at 1064 nm, the wavelength range where unwanted gain is available is considerably restricted. The ratio between the gain at the signal wavelength and the gain peak is thus significantly increased [125]. Since high-power sources with single-mode fiber output are standard at 1064 nm, it is possible to guide both pump and signal light in the core of an active Yb doped single-mode fiber instead of using cladding-pumped fibers, which are used in most conventional fiber amplifiers. Thus, the fiber length required to achieve the desired gain of > 20 dB is still reasonable although the absorption cross section of Yb doped fiber at 1064 nm is more than two orders of magnitude lower than in the range around 976 nm. The absorption cross section can be increased by heating the fiber to moderate temperatures [135, 138, 139], which further reduces the required length of the active fiber.

The general approach for a fiber amplifier described here has previously been used to realize fiber lasers at wavelengths above 1150 nm [139–141], but to our knowledge has not yet been utilized for amplification in the 1110 nm region, where it is relevant for laser cooling of Yb.

3.3.1. Setup

The complete laser system (see Fig. 3.5) including the seed laser, the fiber amplifier and the second harmonic generation (SHG) module is built using fiber components. Though intended to be a lab setup for which compactness was not a primary goal, the complete amplifier fits inside a 3U 19in rack enclosure with just the SHG module located on the optical table due to its free space output.

Where possible, we use off-the-shelf components designed for 1064 nm, such as fused couplers and isolators. For fused couplers specified as 99:1 at 1064 nm we typically find

coupling ratios between 99:1 and 98:2 at 1112 nm. While polarization insensitive fiber isolators with a specified isolation of 30 dB at 1064 nm show no increase in insertion loss (typ. 1 dB), their isolation is naturally reduced to typically 22 dB at 1112 nm. However, the fiber amplifier has to be protected primarily from backreflections near the gain maximum around 1080 nm, where the isolation is still close to its design value, rather than at the signal wavelength. Custom wavelength division multiplexers (WDM), the only components that have to be tailored to the exact wavelengths used, are commonly available for reasonable prices in small manufacturing runs. The passive fibers included in the setup are either *Corning HI1060* or *Nufern 1060-XP*.

Pump source

The pump light at 1064 nm can be efficiently generated using cladding pumped Yb fiber lasers [142], which are readily available and are used for dipole trapping in many cold atom experiments. In our setup we use a commercial fiber laser module (*BKTel MFL-1370*) with a nominal output power of 5 W.

Seed laser

As a seed source we use a DFB fiber laser module removed from a retired commercial fiber amplifier system (*Koheras Boostik*), delivering 8 mW in a single mode fiber.

We characterize the spectral properties of the seed laser by analyzing the beatnotes with two similar fiber lasers in a three-cornered hat [143] configuration. For the spectral lineshape of the seed laser we obtain a Voigt profile with a Lorentzian FWHM of (12 ± 2) kHz and a Gaussian FWHM of (74 ± 2) kHz at an integration time of 3.4 ms.

When the seed laser is exposed to an optical feedback power larger than a few µW without additional isolation, we observe that the laser frequency becomes unstable and exhibits excursions of several 100 kHz (see Figure 3.9), consequently extra care has to be taken to prevent feedback from the amplifier to the seed laser by the insertion of additional optical isolators.

Fiber Amplifier

As depicted in Fig. 3.5, both the seed and the pump inputs of the fiber amplifier are connected to fused couplers with a coupling ratio of 99:1, which are used to monitor the respective input powers. While backward ASE levels are low in our design and we neither expect nor observe stimulated Brillouin scattering (SBS) to occur under the present conditions, the backward ports of these couplers are monitored for backward propagating waves. Since we observe that even low power feedback to the seed laser (e.g. Rayleigh scattering or reflections from index mismatch in fusion splices that are amplified in the active fiber) leads to frequency instabilities, the seed input is protected by two polarization insensitive isolators (*Thorlabs IO-H-1064B*) with a nominal isolation of 30 dB at 1064 nm.

Signal and pump radiation are combined using a custom made wavelength division multiplexer (WDM, *Lightcomm HPWDM-X-1*2-1064/1112*) with a typical insertion loss

of 0.3 dB and isolation of 15 dB.

The active Yb doped fiber (*Fibercore DF1100*, which was selected because of its relatively high doping concentration) has a nominal peak absorption of 1500 dB/m at 975 nm. A coil ($d = 10$ cm) of 22 m active fiber is placed inside a heated aluminium block. Using resistive heaters, the temperature is kept at 348 K under standard operating conditions. The maximum operating temperature of the fiber is specified as 358 K, limited by its low temperature acrylate coating. Heating of the active fiber increases the thermal population of the higher Stark levels (see Fig. 3.6) of the $^2F_{7/2}$ manifold. Since the absorption in the relevant region is dominated by the $d \rightarrow f$ transition with a central wavelength of ~ 1052 nm, this leads to an increased absorption cross section at the pump as well as the signal wavelength. Specifically, heating the fiber to 353 K increases the population of the d-state and thus the effective absorption cross section at these wavelengths by a factor of 2.4. As a positive side effect, reabsorption of the dominant ASE component around 1080 nm is also increased.

After the active fiber, the residual pump light is separated from the amplified signal using two additional WDMs in order to protect the SHG module (see subsection 3.3.2) from pump
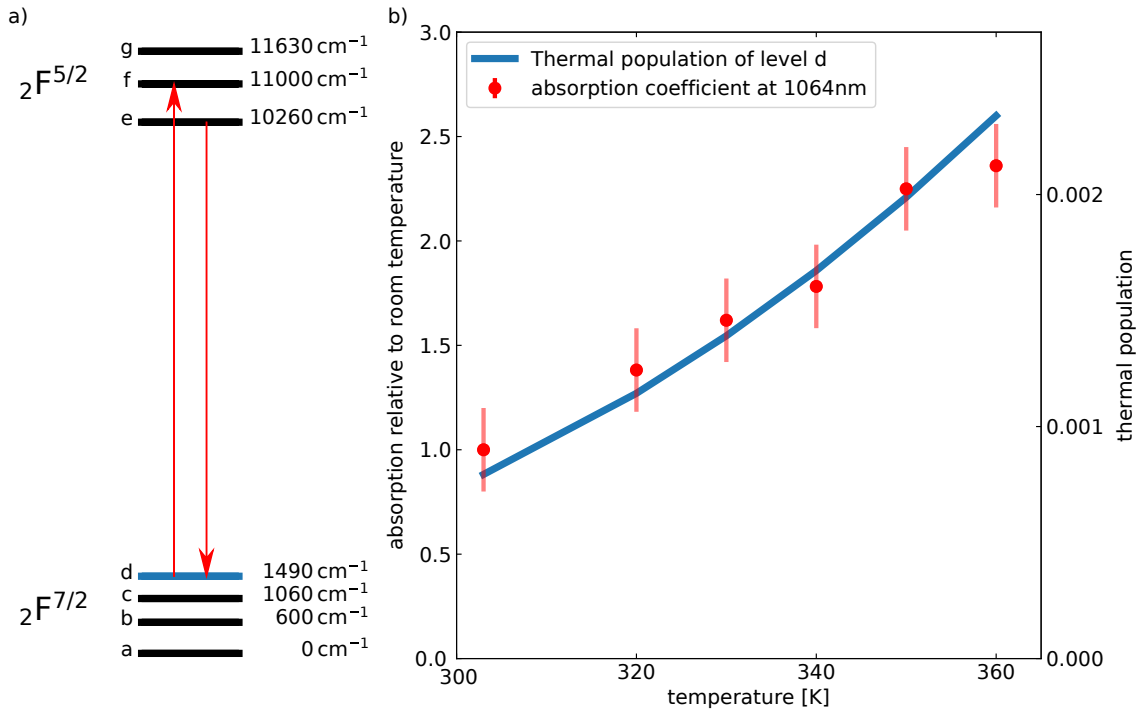
Figure 3.6.: (a) Relevant states of Yb^{3+}:germanosilicate, showing the pump and lasing transitions [135]. When pumping at 1064 nm, absorption is dominated by the transition from Stark levels d to f. From level f, non-radiative decay populates level e and lasing at 1112 nm occurs on the e-d transition. (b) Pump absorption at 1064 nm extracted from our measurements (see section 3.3.4) as a function of the fiber temperature. The blue curve shows the thermal population of level d expected from a Boltzmann distribution.

light. Since we have observed that the SHG module is becoming slightly reflective at the fundamental wavelength when its temperature is tuned to the phase matching temperature, we also insert a polarization independent isolator (*AFR MHI-06-10-N-B-1-P*) in the output path in front of the WDMs to protect the fiber amplifier as well as the seed laser. If a resonant free space setup for frequency doubling would be used, the isolator and both WDMs could be omitted. Behind the WDMs a fused coupler (coupling ratio nom. 99:1) is inserted in the signal path whose low-power output is again split between a photodiode (10%) to monitor the output power and an auxiliary output. The auxiliary output is protected by a polarization insensitive isolator and can be used for diagnostics and frequency stabilization (e.g. using a reference cavity or beatnotes with other laser systems). The fused coupler is also used to detect backreflections from the SHG module.

3.3.2. SHG

The output of the fiber amplifier is frequency-doubled to $556\,\mathrm{nm}$ using a commercial module (*NTT Electronics WH-0556-000-A-B-C*) based on a fiber coupled periodically poled lithium niobate (PPLN) waveguide. Since we have opted to use non-polarization maintaining single-mode optical fibers to circumvent the additional complications and insertion losses associated with polarization maintaining components and splices, the polarization of the fiber amplifier output has to be actively matched to the waveguide. The output of the fiber amplifier settles to a well-defined polarization state after a warm-up time of ~ 20 minutes. This polarization state is transformed into the linear polarization needed for phase matched SHG in the waveguide using a three paddle polarization controller. We obtain a polarization extinction ratio (PER) of $> 23\,\mathrm{dB}$ at the output, which is comparable to that of the seed laser. As long as the fibers are not mechanically disturbed, this polarization state is sufficiently stable to maintain high SHG efficiency for months without readjustment of the polarization controller.

The amplifier output is connected to the module's PM fiber using an FC/APC mating sleeve, preserving the modules connectorized pigtail and keeping the system modular. Operating the amplifier at an output power of $440\,\mathrm{mW}$, $200\,\mathrm{mW}$ output power at $556\,\mathrm{nm}$ are obtained, limited by the recommended optical operating power of the SHG module.

3.3.3. Electronics

Reliable operation of the fiber amplifier requires only a limited electronic control system. In order to keep the output power constant, the temperature of the active fiber spool is stabilized by a PID controller. To aid diagnostics, the amplifier is equipped with several photodiodes monitoring the power levels at key locations (see Fig. 3.5). An electronic interlock ensures that the pump is switched off in case of a) loss of seed power, b) high frequency components indicative of pulsing in the output power, or c) backreflections from the SHG stage to the amplifier output. For the detection of pulsing, we compare a high pass filtered copy of the output monitor signal with its DC component [144]. Additionally, the pump input power and optical feedback to pump and seed lasers are monitored. All

monitor photodiodes are equipped with AD converters (*TI ADS1115*) which are connected to a microcontroller via an I2C bus for display and logging of all important parameters.

3.3.4. Performance

Finally we evaluate the performance of our amplifier system with respect to its output power as well as the spectral characteristics of the output.

Characterization of the laser system

Figure 3.7 shows the dependence of the output power on the temperature of the active fiber. The seed power for these measurements was 5 mW, measured at the input end of the active fiber. At room temperature, pump absorption saturates at around 1 W and the resulting output power of the fiber amplifier is only around 100 mW. Thus, a substantially longer active fiber would be required to obtain the desired output power of several 100 mW. Heating the fiber considerably increases the pump absorption and thus the output power which reaches 800 mW at 353 K, the highest temperature in our characterization measurements, for a coupled pump power of 3 W.

The data is analyzed using a simple analytical model [145]. Integration of the rate equations for a general four-level system yields two coupled equations relating the in- and output powers for pump and signal. We fit our data using these equations, shown as solid lines in Figure 3.7. Figure 3.6 b shows the temperature dependence of the pump absorption coefficient extracted from this fit which agrees well with the expected increase in the thermal population of Stark level d.

The fiber length required in order to achieve the optimum pump absorption depends on both the operation temperature of the fiber, which determines the absorption coefficient, and the pump power, as significant saturation of pump absorption occurs at the power levels of interest.

A pump absorption of 13 dB is commonly taken to offer a good compromise between efficient use of the available pump power and reabsorption at the signal wavelength in weakly pumped sections of the fiber. Figure 3.7b shows that for an operating temperature of 348 K this value is reached at a pump power of ~ 1.5 W. At higher (lower) pump powers, a longer (shorter) fiber or a higher (lower) operating temperature would be beneficial.

The optical spectrum of the output obtained using an optical spectrum analyzer (*ANDO AQ-6315*) is depicted in figure 3.8. Although the amplifier is pumped colinearly in the core, the residual pump light at the output is more than 50 dB below the signal level. It is important to note that the amplified spontaneous emission component in the output is only 0.25 % of the total output power, which is an order of magnitude lower than that of commercial systems pumped at shorter wavelengths.

The linewidth of the amplifier output is determined in the same way as that of the seed laser (3.3.1) by taking the beatnote with two reference lasers. Figure 3.9 shows the beatnotes for each condition with one of the reference lasers. For the lineshape of the amplifier output a Voigt profile with a Lorentzian FWHM of (12 ± 2) kHz and a Gaussian FWHM of (76 ± 2) kHz is obtained. This is in good agreement with the results for the seed
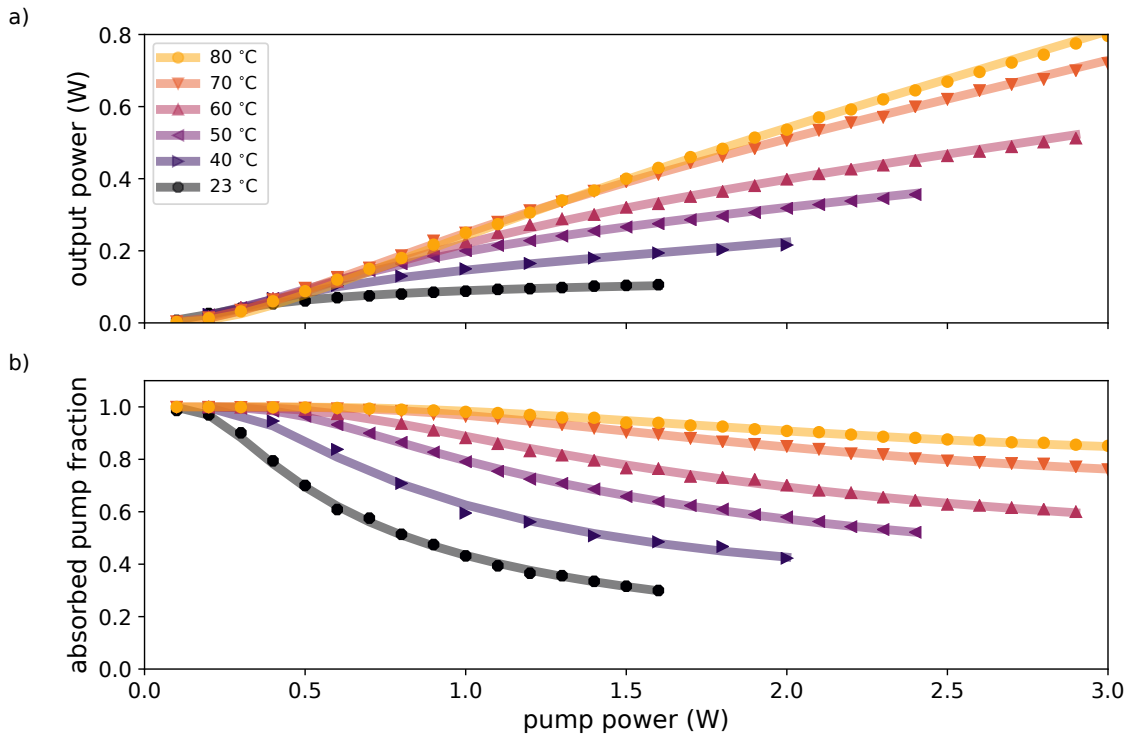
Figure 3.7.: (a) Output power of the fiber amplifier and (b) fraction of absorbed pump power as a function of coupled pump power for different temperatures of the active fiber. Solid lines are fitted analytical models.
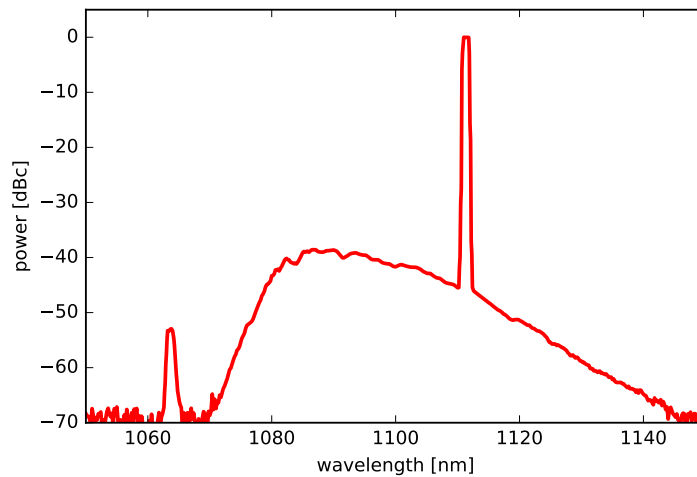
Figure 3.8.: Optical spectrum at the amplifier output operating at $80\,°C$ fiber temperature and $0.8\,W$ output power (resolution bandwidth $1\,nm$).

laser, confirming that there are no non-linear processes present in the amplifier which can lead to a significant increase of the linewidth [146].
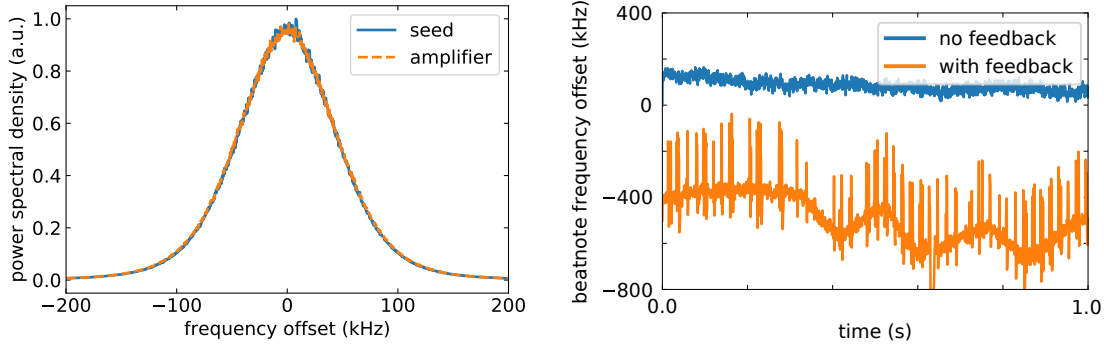
Figure 3.9.: a) Power density spectra of the beatnote between a reference fiber laser and the seed laser and the amplifier output, respectively. The curves are generated by slicing the recorded beatnote signal into 3.4 ms segments, computing their power spectral density, centering the peak and averaging the individual spectra. b) Time resolved beatnote center frequency of the individual slices for the seed laser, showing the fluctuations introduced by optical feedback to the seed laser. The traces are offset for clarity.

The observed output power stability of $\pm 1\%$ over a day is dominated by the stability of the coupled pump power and could thus be improved by a servo loop acting on the pump source.

While heating of the active fiber leads to a significant increase of the output power of our amplifier, it may compromise its reliability. Despite the coating being rated for temperatures up to 358 K, after several years of continuous heating at 348 K and regular laser operation in our ultracold atom experiment, we observe some discoloration and loss of elasticity, making the fiber more susceptible to mechanical stress. We do not, however, observe a degradation in output power. Fiber coatings with extended temperature range are commercially available, particularly in double-clad fibers meant for high power amplifiers, and could be used to improve reliability.

3.4. Synthesizer

While in the previous sections we have mostly been concerned with achieving high powers, another critical ingredient for our experiments are stable, precise frequencies, in the optical as well as in the radio frequency (RF) or microwave spectrum. This section aims to give an introduction to the concept of synthesizers and phase locked loops, a powerful tool to achieve this goal. A more thorough treatment may be found in [147].

A synthesizer is a system that takes a reference frequency and provides an output frequency that is related to this frequency by a certain configurable ratio, by controlling a tunable RF oscillator.

This tunable oscillator may be as simple as a voltage controlled oscillator (VCO) directly producing a radio or microwave frequency or as complex as a laser system with an optical beatnote to a reference laser as the RF output.

The following sections will introduce the building blocks of a synthesizer.

3.4.1. Prescaler

Prescalers are commonly found on both inputs of the synthesizer. The reference frequency is divided by R. The (output) RF frequency may simply be divided by an integer N, yielding the aptly named *Integer-N-Synthesizer*. In this case, the output frequencies are limited to multiples of the *channel spacing* $\frac{f_{\text{ref}}}{R}$. This leads to an undesired coupling between the frequency resolution and lock bandwidth, which is also limited by this frequency, and the resulting channel spacing is not sufficient for many applications.

A solution is the *Fractional-N-Synthesizer*. Here a so called $\Sigma\Delta$-Modulator – a building block that generates a stream of bits which appear random, but have a certain, configurable ratio between ones and zeros – rapidly switches the divider between N and $N + 1$. If for F out of M cycles, the divider is switched to $N + 1$, the effective average divider will be
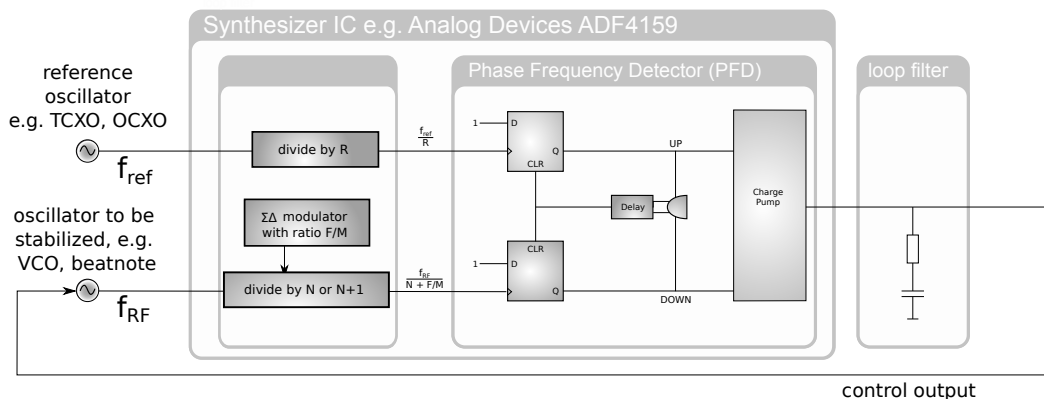
Figure 3.10.: Schematic diagram of a fractional N synthesizer. Both the reference and the oscillator to be stabilized pass through divider stages before they enter the PFD block. The output of the PFD is fed into the loop filter, symbolized by a simple PI filter here, which in turn generates the control signal for the oscillator, closing the loop.

$N + \frac{F}{M}$. This technique allows the combination of very high frequency resolution (referred to as channel spacing in a telecom context) and high loop bandwidths.

3.4.2. Phase Frequency Detector (PFD)

In order to generate an error signal for the control loop, the prescaled input and reference frequencies have to be compared. This is accomplished by a so called phase frequency detector (PFD). Here each input signal – after being divided – is fed to the clock input of a flip-flop. When an edge occurs on one of the input signals, the corresponding output signal goes high. Once both outputs are high, the flip-flops are reset and the cycle starts again.

If the input signals differ in frequency, the phase between the edges will be random. However, as edges occur more frequently on the higher frequency signal, the corresponding output will be triggered more frequently. This results in an averaged output signal proportional to the difference in frequency.

For signals of equal frequency, the PFD will be triggered by the input leading in phase, and remain turned until the edge occurs on the lagging signal. This leads to an output signal proportional to the phase difference between the inputs.

While in principle a synthesizer can be realized with a simpler phase only detector, the ability of the PFD to detect frequency errors allows the operation as a frequency locked loop in cases where a phase lock is not desired or not feasible, e.g. if no actuator of sufficient bandwidth is available, which is the case in most of our beatnote locks. In case of a phase locked loop, lock acquisition is improved by the addition of frequency detection.

It has to be noted that when switching from frequency detection to phase detection an additional integrator is introduced into the system ($\phi = \int \omega(t) \mathrm{d}t$), which may complicate design of the control loop.

3.4.3. Charge pump and loop filter

The PFD provides two digital outputs ("up" and "down") with the difference between their pulse rates proportional to the error signal. These signals are then converted to a bipolar current output by the charge pump, which sources or sinks a set charge on each pulse.

This signal is fed to the loop filter to generate the desired control signal (which in most cases is a voltage). Countless active and passive loop filter topologies exist and may be used to achieve the desired frequency response.

3.4.4. Realization

Highly integrated synthesizer circuits are commercially available with input bandwidths in the tens of GHz. These contain all necessary dividers, the PFD and charge pump and allow their configuration using a serial interface. Often additional features like ramp generators are also present.

In this work the *Analog Devices ADF4159* is used for the microwave synthesizers as well as the beatnote locks. This chip implements a fractional-N synthesizer with an input
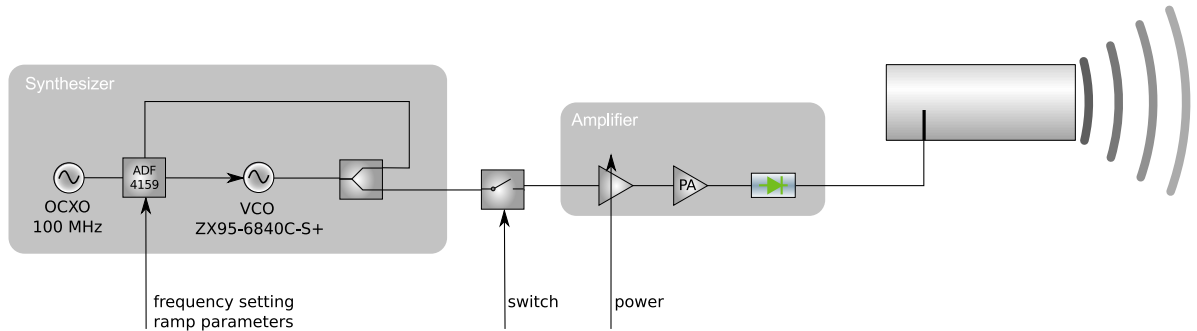
Figure 3.11.: Schematic diagram of the microwave systems employed for evaporative cooling and state preparation of Rb, consisting of the synthesizer circuit, a switch allowing for the generation of fast pulses, the power amplifier module including gain adjustment and an isolator for protection from backreflections, and the antenna.

frequency range of 0.5 to 13 GHz and capabilities for frequency and phase modulation as well as triggered frequency ramps.

3.4.5. Microwave

The hyperfine transition of the ^{87}Rb ground state near 6.8 GHz provides a convenient means for the manipulation of the internal state of Rb atoms (see subsection 5.1.5). Both the Rb production chamber (see subsection 4.1.3) and the science chamber (subsection 4.1.4) are equipped with a microwave system to address this transition. In the production chamber this is used for the forced evaporation from the quadrupole trap, while the science chamber system allows preparation of the atoms in the desired hyperfine and Zeemaan states as well as spectroscopic investigations.

For these applications, the microwave source needs to be tunable over a frequency range corresponding to the Zeeman shifts encountered in the experiment (typically ~ 100 MHz), able to perform frequency ramps in this range as well as deliver controlled short pulses and deliver sufficient output power (typically several Watts) to generate Rabi frequencies on the order of kHz. While commercial systems are available, an economical homebrew solution is presented here.

Synthesizer

The microwave signal is provided by a (internally frequency doubled) voltage controlled oscillator (VCO, *Minicircuits ZX95-6840C-S+*), which is phase locked to a crystal oscillator. While the standard temperature compensated crystal (TCXO) mounted on the evaluation board for the *Analog Devices ADF4159* synthesizer chip is sufficient for the microwave system used in the production chamber, which is mainly needed for forced evaporation, the microwave system for the science chamber is equipped with an oven controlled oscillator

(OCXO) for improved frequency stability in anticipation of applications requiring higher resolution.

A solid-state switch (*HMC1118*) allows the application of well defined pulses and prevents leakage through the disabled amplifier.

Amplifier

A *TERRASAT ED-0278-4* power amplifier module - originally intended for use in point-to-point communication - provides up to 6 W of output power. The module contains a variable gain amplifier for output power adjustment as well as a digital muting input. The output is protected against backreflections from the antenna by an integrated microwave isolator.

Antenna

Efficient coupling of the microwave radiation to the atoms is ensured by directional antennas. The antennas used here are of the *sawed-off waveguide* type, a primitive type of horn antenna [148]. Each antenna consists of a length of copper tubing acting as a circular waveguide. The signal is coupled into the waveguide by a stub of $\frac{\lambda}{4}$ length. One end is closed at a distance of $\frac{\lambda_{\mathrm{WG}}}{4}$ from the feed, while the other end is open and extends $\frac{\lambda_{\mathrm{WG}}}{2}$ from the feed, where λ_{WG} denotes the wavelength inside the waveguide. This geometry ensures optimal coupling, as confirmed by measurements of the reflection coefficient S_{11} [104].

In free space, the radiation propagates with a divergence angle of $\sim 40°$ due to diffraction at the aperture. This could be reduced by adding a conical horn, but in practice this would require the antenna to be mounted at a greater distance from the viewport to maintain optical access, negating the increase in field strength due to improved collimation.

3.5. Beatnote lock

Especially when performing photoassociation, the need to stabilize a laser at a frequency that does not coincide with any absolute reference —such as a transition accessible in a spectroscopy setup —often arises.

A so called optical beatnote between two lasers generates an RF signal with a frequency equal to the difference frequency between the two lasers.

This enables us to stabilize a laser at an arbitrary and widely tunable offset frequency with respect to another laser [149–151]. This is particularly advantageous if the reference laser can be locked to an absolute reference like atomic spectroscopy.

In the apparatus described here this technique is employed for locking the repumper lasers for Rb without the need for additional spectroscopy setups, as well as for the locking of the photoassociation lasers.

3.5.1. Beatnote

We start by having a short look at how the beatnote is generated. When light of two single frequency lasers at frequencies ω_1 and ω_2 is combined, the resulting electric field (at a single

point in space and neglecting differences in phase) is given by

$$E(t) = \frac{1}{2} \left(E_1 \cdot e^{i\omega_1 t} + E_2 \cdot e^{i\omega_2 t} + \text{c.c.} \right) \tag{3.4}$$

where c.c. denotes the complex conjugate. The photocurrent $i_{\text{photo}}(t)$ that occurs when detecting this light field on a photodiode is proportional to the incident power rather than the field strength, so we obtain

$$\begin{aligned}
i_{\text{photo}}(t) \quad &\propto \quad P_{\text{opt}}(t) \quad \propto \quad E(t)^2 \\[4pt]
&\propto \quad 2 \cdot E_1 E_2 \\[4pt]
&\quad + E_1 E_2 \cdot e^{i(\omega_1 + \omega_2)t} + E_1^2 \cdot e^{i2\omega_1 t} + E_2^2 \cdot e^{i2\omega_2 t} \\[4pt]
&\quad + E_1 E_2 \cdot e^{i(\omega_2 - \omega_1)t} \\[4pt]
&\quad + \text{c.c.}
\end{aligned}$$

All terms oscillating at optical frequencies ($2\omega_1$, $2\omega_2$, $\omega_1 + \omega_2$) will be averaged out, leaving only a DC current and the component oscillating at the difference frequency $\omega_2 - \omega_1$ at the photodiode output. We thus obtain an RF signal whose frequency is equal to the difference frequency between the two lasers, which is called the beatnote between those lasers.

Note that the beatnote amplitude scales with $E_1 E_2 \propto \sqrt{P_1 P_2}$, indicating that a lack of available power in one laser may be overcome by additional power in the second laser (heterodyne detection).

3.5.2. Combining

Detecting the beatnote with a good signal to noise ratio requires the wavefronts of both beams to be well matched across the surface of the detector. This can be easily ensured by combining both lasers in a single-mode fiber and thus forcing good spatial overlap.

The use of fibers is also advantageous because it provides a convenient way to couple to the detector and often the signal source is already available in a fiber (e.g. the monitor output of a fiber laser).

The beams can be combined by using a free space beamsplitter and carefully overlapping both beams and coupling them into the same fiber, or by independently coupling the lasers into separate fibers, which are then combined using fused fiber couplers.

3.5.3. Photodiode

The offset frequency range accessible by a beatnote setup is often limited by the bandwidth of the photodiode.

The bandwidth of a photodiode frontend [152] is typically limited by the low pass effect of the diode capacitance and the load resistance. A common technique to overcome this is the transimpedance amplifer, where an operational amplifier keeps the voltage across the photodiode constant, such that the photodiode capacitance is eliminated. This requires

a)   b)
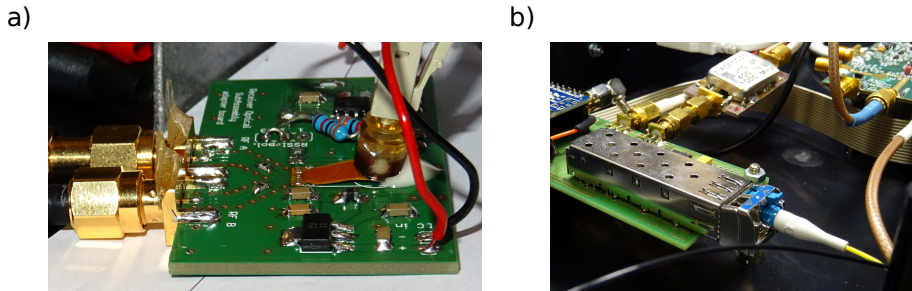
Figure 3.12.: Different types of photodiode assembly used for the beatnotes: **(a)** a 800 nm ROSA mounted on a custom PCB containing supply filters and regulators and connecting the output signal to SMA sockets using coplanar waveguides. These are used in the Rb repumper beatnotes. **(b)** A 1300 nm SFP+ module mounted on a custom PCB with similar functions to the one in (a), but additionally containing a microcontroller for configuration and monitoring of the module via the I2C interface. A home-built RF amplifier and filter circuit can be seen in the background. These modules are used in the Yb intercombination line beatnotes.

an operational amplifier bandwidth that is orders of magnitude larger than the signal bandwidth. While the construction and design of such photodiode frontends up to tens of MHz is routine in most labs, it becomes infeasible in the GHz range.

A common solution is to connect a high bandwidth photodiode (or metal-semiconductor-metal detector [153]) directly to a standard $50 \, \Omega$ amplifiers, which is readily available with bandwidths up to tens of GHz. However, the impedance mismatch between the diode and the amplifier leads to a large loss and thus to poor signal to noise ratio and high susceptibilities to external RF disturbance.

Fortunately, optical telecommunication has led to the availability of highly integrated components for high bandwidth optical detection. So called receiver optical sub-assemblies (ROSA) comprise a receptable for a fiber ferrule, a focusing lens, a photodiode and a transimpedance amplifier. The electrical interface to these is provided on a somewhat flimsy but readily solderable flex connector and consists of the differential RF output signal - which has to be AC coupled by the user - and the supply voltage. The supply for photodiode biasing is provided on a separate pin, allowing the insertion of a shunt resistor for measuring the DC photocurrent.

The next step up, the so called small formfactor pluggable (SFP) module, adds - in addition to a laser for transmission of signals, which we will completely ignore here - a proper locking fiber connector socket (typically using LC connectors, which are an unfamiliar sight in a atomic physics lab, but readily available) and most importantly a limiting amplifier. This further boosts the signal level for small signals, and due to its limiting action prevents fluctuations in the beatnote strength, e.g. due to changing polarization in non-PM fibers from influencing the locking electronics.

A digital interface allows reading of the DC photocurrent and in some models switching of the receiver bandwidth. The differential signal outputs are already AC coupled inside

the module and can thus be directly connected to the next component in the signal chain.

Both types of detectors are typically available either as short range versions with GaAs detectors, designed for operation with multimode fibers at 850nm, or as long range versions with InGaAs detectors, intended for singlemode fibers carrying signals in either the 1.3 or $1.5\,\mu$m range. We use the former type for our beatnote locks at $780\,$nm and the latter type for those at $1112\,$nm.

While these modules provide a differential output designed for termination with $100\,\Omega$, this is electrically identical to single ended termination of both outputs with $50\,\Omega$, so standard RF devices can be connected to each output independently.

As the evaluation boards we use for our beatnote locks only provide a single ended input, the second output can be used as a monitor output.

3.5.4. Error signal generation

In order to use the beatnote for laser stabilization, the frequency of the beatnote signal has to be converted into a dispersive error signal, representing the sign – and to a limited degree the magnitude – of the deviation from the desired frequency.

This is often done by means of a delayed RF interferometer [154], where the signal is split and recombined after experiencing different path lengths. The resulting interference fringes – whose frequency spacing depends on the path length difference between the arms and thus has to be calibrated and is susceptible to thermal drifts – allow the generation of an output signal by measuring the RF power at the interferometer output. To achieve tunability the signal is downmixed using a tuneable microwave source before entering the interferometer.

Another approach is to feed the beatnote and a microwave signal with the desired beatnote frequency to a phase detector (or phase and frequency detector) – in the simplest case an analog mixer.

Here we use the *Analog Devices ADF4159* fractional-N PLL (see section 3.4) chip to lock the beatnote signal to an arbitrary frequency using a $100\,$MHz RF reference. This approach has the advantage that no expensive microwave source is required and we can still control the beatnote frequency with the precision and convenience of a synthesized source by digitally setting the desired frequency.

3.5.5. Frequency range

Using the hardware presented here, offset frequencies up to about $13\,$GHz can be realized. In the case of the photoassociation laser, this figure is essentially doubled by taking the beatnote of the infrared lasers instead of the frequency doubled green light.

An increase of the possible beatnote frequency to $\sim 30\,$GHz could be realized using specialized photodetectors and high end PLL chips. In case an additional laser source is available, this could be used as a transfer oscillator, giving another doubling of the accessible frequency range.

Practically arbitrary offset frequencies could be achieved by using a frequency comb [155] instead of a single frequency laser as the reference. In this case the maximum beatnote

frequency would be given by half the repetition rate of the comb and typically be in the tens of MHz.

3.5.6. Beatnote analysis

A common technique to quantify the performance of a laser system and its stabilization, is by analyzing its beatnote with another – ideally identical – laser is often analyzed. The most straightforward method to evaluate a beatnote between two lasers is to measure the signal on an RF spectrum analyzer. However, the sweeping nature of their measurement means that frequency fluctuations occuring on a timescale comparable to or faster than the sweep time (typically tens of ms to hundreds of seconds, depending on the frequency span and resolution bandwidth) are hard to analyze. In these cases it is advantageous to instead digitize (a down-mixed version of) the beatnote and analyze it using a FFT technique [156].

While the down mixing and recording can of course be realized using standard laboratory equipment such as synthesizers, mixers and digital oscilloscopes, a convenient low-cost option is again provided by mass produced electronics. A line of USB sticks designed for the reception of DVB-T television signals known as RLT-SDR features a debug mode allowing for the digitization of a downmixed IQ-signal with a bandwidth of up to $3\,\mathrm{MHz}$ from the spectral region of $30 - 1800\,\mathrm{MHz}$ depending on the exact chip used [157, 158].

This allows resolving short-term frequency fluctuations such as those shown in Figure 3.9 or the resolution of bandwidths lower than those provided by affordable RF spectrum analyzer as in the measurements shown in Figure 4.17b[3].

---

[3]Note that the quality of the local oscillator included in the device may start to play a significant role here.

4.

The Apparatus

*"... always buying strange instruments of glass and metal
and combining them into instruments yet stranger ..."*
— H.P. Lovecraft, *Nyarlathotep*

This thesis involved the setup of a new RbYb mixture experiment starting from scratch, including the development of numerous laser systems needed for the experiment. This chapter gives an overview of the various optical and electronic systems required. The experimental apparatus is mainly divided into the optical table with the vacuum chambers and setups immediately required for the experiment, the *science table*, and a separate part of the room where all laser systems except for the high power trap lasers are located, the *laser room*. Light from all other lasers is brought from the *Laser room* to the *science table* by optical fibres.

After a brief overview of the vacuum system, we start with the laser systems required for the cooling of each species and work towards those required to perform the actual
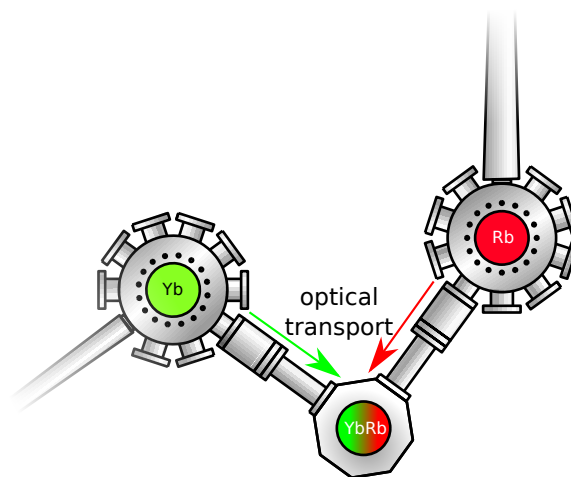
Figure 4.1.: Schematic diagram of the layout of the vacuum system showing the division into two production chambers for the individual species and optical transport into the science chamber.

experiments.

4.1. Vacuum chambers

The vacuum system is divided into two production chambers, where ultracold samples of the respective species are prepared, and a science chamber where they are brought together using optical tweezers and the main experiments are performed. Each production chamber in turn is connected by a Zeeman slower to the respective oven. All these chambers are separated by pneumatic gate valves, allowing them to be independently vented for upgrades.

4.1.1. Ovens

The preparation of both atom species starts with beams originating from samples of elemental metal heated in ovens.

The oven chambers are equipped with ion pumps, viewports to allow monitoring of the beam fluorescence, and rotary beamshutters, preventing the atom beams from interfering with the later cooling steps.

Rb oven

The Rb oven consists of a reservoir, which we fill with a Rb ampoule (broken under air and then quickly placed into the oven and pumped down, which we find to work well). This reservoir is heated to a temperature of $125\,°C$, so it fills with Rb vapor. The beam is formed by a nozzle which is kept at $140\,°C$. Behind the nozzle, a cold trap cooled to $\sim -5\,°C$ captures atoms leaving the nozzle at large angles and prevents them from depositing at the chamber walls. There is substantial radiative heat transfer between the cold trap and the heated nozzle, so substantial cooling power is needed. The thermal feedthrough is realized by a piece of copper which is clamped in a CF flange instead of the gasket and serves as a mounting point for the cold trap on the vacuum side, while the air side is cooled by a water cooled peltier element.

Yb oven

Due to the lower vapor pressure of Yb, considerably higher temperatures are needed in this oven. This simplifies the oven design, as no cold trap is needed because the atoms readily stick to room temperature surfaces. For operation with ^{170}Yb a relatively high atom flux is needed due to the low abundance of this isotope. We typically operate the oven at a temperature of 440°C.

Depending on the source of the Yb (our regular supply is specified as $> 99.9\,\%$ *metals basis* – note this does not give information about possible non-metal contaminants), we observe a grayish, powdery residual after evaporation, which can cover the remaining Yb metal and thus block it from entering the gas phase. This makes relatively frequent maintenance of the oven necessary, even when the oven filling has not been used up yet.

An additional issue is presented by the viewport opposite the Yb oven, through which the Zeeman slower beam needs to enter (see Figure 4.8). Because of the low vapor pressure of Yb at room temperature, the atoms deposited on the glass surface tend to build up over time, which is not an issue for Rb, where atoms will readily sublimate from a surface at room temperature.

When starting with a new viewport, at first a whitish, translucent coating is observed where the atom beam hits the window. This coating does not significantly degrade the performance of our Zeeman slower, apart from the transmitted slower power – and thus the fluorescence measured at the oven end of the slower – sinusoidally varying with time and thus coating thickness due to thin film interference. Similar behaviour has been observed in Sr [159] and this is likely due to the Yb atoms deposited on the surface reducing the SiO_2 substrate, creating a dielectric layer of Yb oxide. After a certain layer thickness has been reached, this reaction is stopped and an opaque spot starts to form. This spot leads to substantial power loss in the slower beam.

If the deposits get too bad for continued operation, we have found the Yb chamber can reach its operational pressure of 10^{-10} mbar after a couple of days when the viewport is exchanged, provided both the viewport and the gasket have been prebaked under vacuum and the exchange is carried out under a glovebag with a continous flow of high-purity nitrogen being maintained through both the vacuum chamber and the glovebag.

Currently, we keep the window heated to a temperature of 230°C, which we find to partially clear away existing deposits and prevent new deposits from forming. While the high temperature initially degrades the vacuum, it does not negatively impact the operation of the apparatus, as most steps requiring a long background lifetime are carried out in the science chamber rather than the production chamber.

4.1.2. Zeeman slowers

Both species are initially slowed using Zeeman slowers in increasing field geometry. The Yb slower consists of a double walled pipe, with the interstitial space filled with cooling water. This tube is wrapped with insulated wire to form the coil. The Rb slower on the other hand is single-walled, and wound with copper tubing insulated by a fiberglass sleeve, which conducts the cooling water as well as forming the coil. This design also features an additional coil operated at a higher current to create the necessary increase in magnetic field at the end of the slower. The detailed designs are described in [160] for Yb and - with some modifications - [61] for Rb.

4.1.3. Production chambers

The production chambers are cylindrical upright stainless steel chambers spanning two levels, the upper one of which is illustrated in Figure 4.2 and used to perform the experiment. On the upper level eight CF35 viewports in the horizontal plane provide access for the MOT and slower beams, imaging, and the optical tweezer beams. On the lower level ion getter pumps and titanium sublimation pumps are connected to each chamber.

The magnetic field gradients for the magneto-optical traps (MOTs) and the quadrupole trap are provided by two coils wound from watercooled copper tubing oriented along the vertical direction. The lower coil is wound around the outside of the vacuum chamber in order to preserve the large aperture for optical access and vacuum pumping, while the smaller upper coils is located inside a recessed flange to allow for the production of a large gradient with moderate currents. Additional smaller bias coils are located along each axis and allow nulling of the magnetic field or shifting of the magnetic zero.

The Rb production chamber also features a microwave system (see subsection 3.4.5) which is primarily used for forced evaporation in the quadrupole trap. The antenna is mounted below the chamber, where the large viewport allows direct line-of-sight to the atoms.

The production chambers are connected to the science chamber by conical differential pumping tubes with a length of 150 mm and diameters of 14 mm and 8 mm at the production chamber and science chamber respectively. Pneumatically actuated gate valves allow sealing off of the individual vacuum chambers, in particular to be able to perform upgrades on the science chamber without affecting the production chambers.
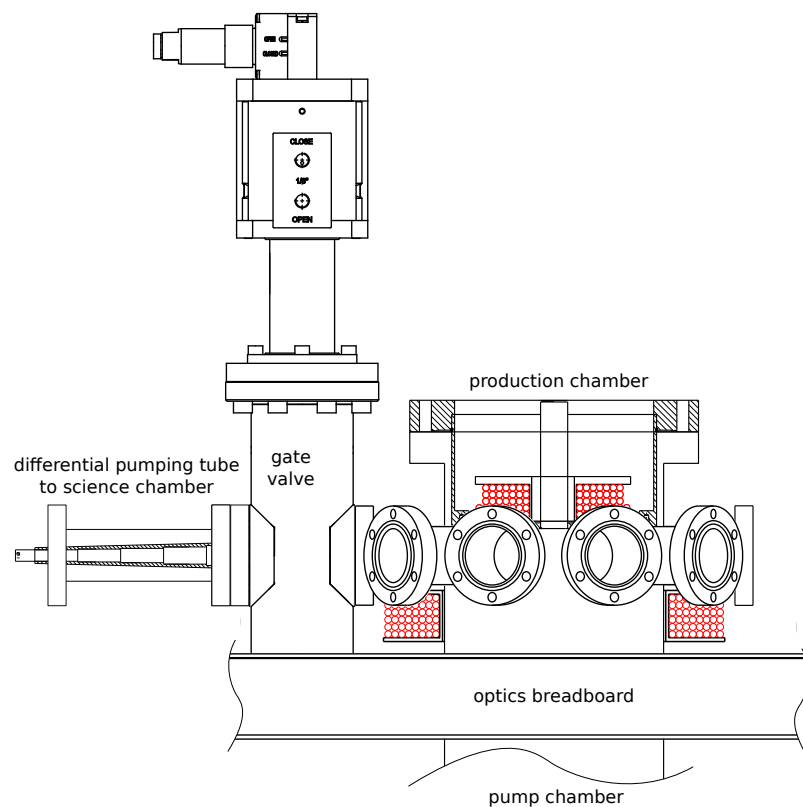
4.1.4. Science chamber

The science chamber consists of a stainless steel *spherical octagon* (*Kimball MCF600-SphOct-F2C8*), providing optical access on six horizontal and two vertical viewports with the remaining two horizontal ports being used for the connection to the production chambers.

Like the production chambers, this chamber is pumped by an ion pump and a titanium sublimation pump, which only requires firing a few times a year to maintain our target pressure.

Magnetic coils mounted on the top and bottom of the science chamber allow the application of uniform magnetic bias fields or gradients. Currently these are cooled passively, allowing for the application of modest fields of some tens of Gauss, but may eventually be replaced by more powerful watercooled versions, capable of accessing magnetic Feshbach resonances in either Rb or RbYb.

4.1.5. Pressure

The pressure in the Rb production chamber and the science chamber is well below the measurement limit of our ion pump controllers (1×10^{-11} mbar). This is confirmed by the fact that the measured lifetimes are consistent with expected Majorana loss rates for the quadrupole trap and photon scattering for the optical traps. Pressure in the Yb production chamber is significantly higher due to the need to heat the viewport for the Zeeman slower (see section 4.1.1). However, as no evaporative cooling is performed in this chamber the atoms are only held in the optical trap for a short time and lifetime is thus not critical.

Figure 4.2.: Schematic drawing of one of the production chambers and its connection to the science chamber. The cross sections of the coils generating the magnetic quadrupole field are shown in red. On the left the cross section of the differential pumping tube leading to the science chamber is shown.
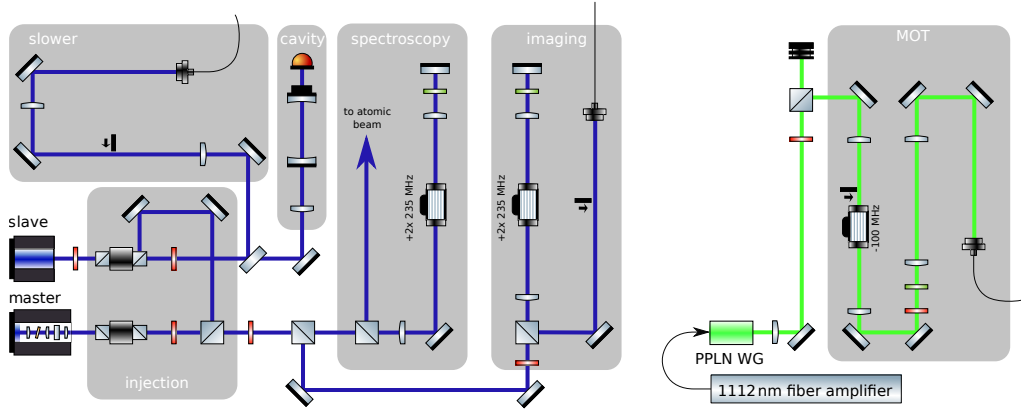
Figure 4.3.: Schematic setup of the lasers at a) 399 nm and b) 556 nm required for the cooling of Yb.

4.2. Yb cooling and imaging laser system

For the preparation of ultracold Yb, we require light to drive the broad $^1S_0 \rightarrow {}^1P_1$-transition at 399 nm for the Zeeman slower and absorption imaging (see section 4.8) and the narrow $^1S_0 \rightarrow {}^3P_1$ intercombination line at 556 nm, which we use for the MOT (see section 5.2) and for photoassociation (see chapter 6, 7 and 8). Both of these wavelengths present certain challenges, and the laser systems developed to address them will be presented in the following.

4.2.1. 399 nm laser system

Light at 399 nm is generated using home-built diode lasers. This system has been setup in the scope of the bachelor thesis of Bastian Pollklesener and is described in detail there [161]. The optical setup is shown in Figure 4.3a. In order to achieve the output power required for the Zeeman slower, a master-slave setup is employed. Both master and slave laser operate at the frequency required for the Zeeman slower, with resonant beams for spectroscopy and absorption imaging being generated by AOMs in double-pass configuration.

Master laser

The master laser is an interference filter stabilized external cavity diode laser [162, 163] based on the AR-coated *Nichia NDUA116T* diode with an output power of $\sim 10\,\text{mW}$.

Light from this laser is used to directly inject the slave laser, as well as frequency shifted by double pass AOMs and used for absorption imaging and spectroscopy stabilization, respectively.

Slave laser

The slave laser is based on a *Nichia NDV4313E* diode with a free running center wavelength of 401 nm. A small portion of this lasers output is coupled into a cavity for monitoring injection quality. As neither power control nor frequency changes are required for the Zeeman slower, and the requirements on the switching speed are very modest, the main output is switched only by a mechanical shutter and then directly coupled into the fiber leading to the Zeeman slower.

Despite the relatively low power of ~ 40 mW incident on the slower fiber face, we have observed substantial degradation of both coupling efficiency and output beam quality over time, suggesting endface damage at both fiber ends. Such effects have been reported at comparable power and wavelength and been attributed to the formation of wavelength-scale ripples on the fiber endface surface [164].

For this reason we have recently exchanged this fiber for one with coreless endcaps, which allow the beam to expand inside the fiber bulk and thus significantly reduce its intensity before hitting the glass-air interface where the damage occurs. Since this change has been implemented, we have not observed fiber damage at levels relevant for the operation of the Zeeman slower.

Frequency stabilization

In order to keep the 399 nm light in resonance with the atomic transition, the master laser is stabilized to fluorescence spectroscopy using a lock-in technique. Both lasers are operated at the detuning required for the Zeeman slower and other frequencies are generated using AOMs.

Light from the master laser is frequency shifted and modulated using a double pass AOM before being sent to the spectroscopy setup shown in figure 4.4. The beam is retroreflected by a concave mirror in order to cancel doppler shifts arising from misalignment and increase the signal level. The fluorescence signal is detected using a photodiode along the direction perpendicular to the plane spanned by atom and laser beam. The detected signal is further increased by another concave mirror opposite the photodiode, effectively doubling the solid angle from which fluorescence is collected.

Note that if the polarization is chosen to be along the axis of the photodiode, due to the radiation characteristics of a Hertzian dipole, no light will be detected by the photodiode. This however does not hold true in the presence of nuclear spin, such that in this case only fluorescence from the isotopes with nonzero nuclear spin, in the case of Yb all the fermionic isotopes, is observed.

A magnetic bias field is created using permanent neodymium magnets in order to split the transitions Zeeman components. This improves separation between our isotope of interest ^{170}Yb and ^{171}Yb by spreading the linestrength of the ^{171}Yb peak over a larger frequency range, thus leaving the unshifted ^{170}Yb peak as shown in the inset in Figure 4.4.

A 556 nm beam also enters the spectroscopy setup. When on resonance with the $^1S_0 \rightarrow$ $^3P_1$ transition this depletes the ground state population and thus reduces the fluorescence

signal observed at 399 nm. This provides a convenient way to locate the correct laser frequency, where the laser is then stabilized using the scheme described in subsection 4.2.3.

4.2.2. MOT laser system

The 556 nm light required for the Yb MOT is produced by the frequency doubled fiber laser system described in detail in section 3.3.

The subsequent free space section for the frequency doubled light contains a shutter and an AOM to allow switching. The AOM additionally serves as an actuator for stabilizing the power measured by a logarithmic photodiode located at the fiber output. While the laser output power is very stable on its own, this control loop compensates for fluctuations in fiber coupling and is particularly important for the low intensities required to reach low MOT temperatures at the end of the cooling cycle (see subsection 5.2.1).

Finally, a set of waveplates allows compensation for polarization rotations that will be introduced by the fiber and the light is coupled into the (non-PM) fiber leading to the science table.

### 4.2.3. Intercombination line laser stabilization

Due to the relatively narrow linewidth of the Yb intercombination line and the resulting low scattering rate as well as the required accuracy, direct stabilization to spectroscopy is challenging. Instead the lasers used for this transition are stabilized to a reference cavity in our setup. However, this cavity exhibits significant drift, which is corrected using an active stabilization system detecting the vertical position of the MOT. Both systems are described in this section.

Cavity stabilization

Part of the infrared monitor output of the fiber amplifier (see section 3.3) is frequency shifted to match the TEM00 mode of the reference cavity using a double pass AOM and sent to the cavity setup shown in figure 4.5.

The cavity consists of a rectangular Zerodur spacer with a coefficient of thermal expansion of $< 1.5 \cdot 10^{-7}$ and a length of 105 mm. The mirrors have a radius of curvature of -250 mm and a low loss coating with a nominal reflectivity of 99.995 %, yielding a theoretical finesse of $\mathcal{F} = 60 \cdot 10^3$. This corresponds to a linewidth significantly lower than that of the fiber laser used.

The cavity is mounted on a temperature stabilised copper block in a UHV chamber. However, most likely due to radiative coupling to the environment, we still observe a change in cavity frequency correlating with ambient temperature changes. For this reason we separately measure the temperature at the top of the spacer and find a linear relationship with a slope of 15 MHz/K. This corresponds to a coefficient of thermal expansion of $3 \cdot 10^{-8}$, which is a factor of 5 better than specified by the manufacturer, but may be influenced by the mean cavity temperature tracking the stabilized value more closely than our additional sensor.
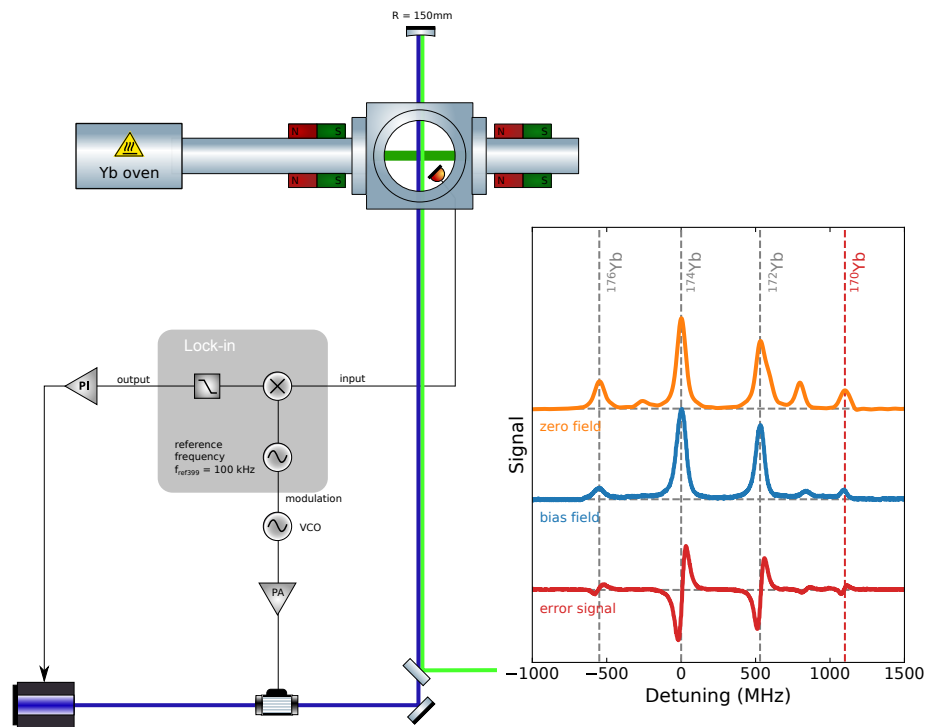
Figure 4.4.: Schematic drawing of the fluorescence spectroscopy setup for the stabilization of the 399 nm laser system, including the lock-in setup for the generation of the error signal. The setup includes a path for 556 nm light that can be used for diagnostics. The laser system is greatly simplified, more detailed depictions can be found in Figure 4.3. The graph shows the fluorescence signals with and without magnetic bias field and the generated error signal. The curves are offset for readability and the transition frequencies of the bosonic isotopes are labelled. Peaks belonging to the hyperfine states of the two fermionic isotopes are not labeled and partially overlap with the bosonic peaks.
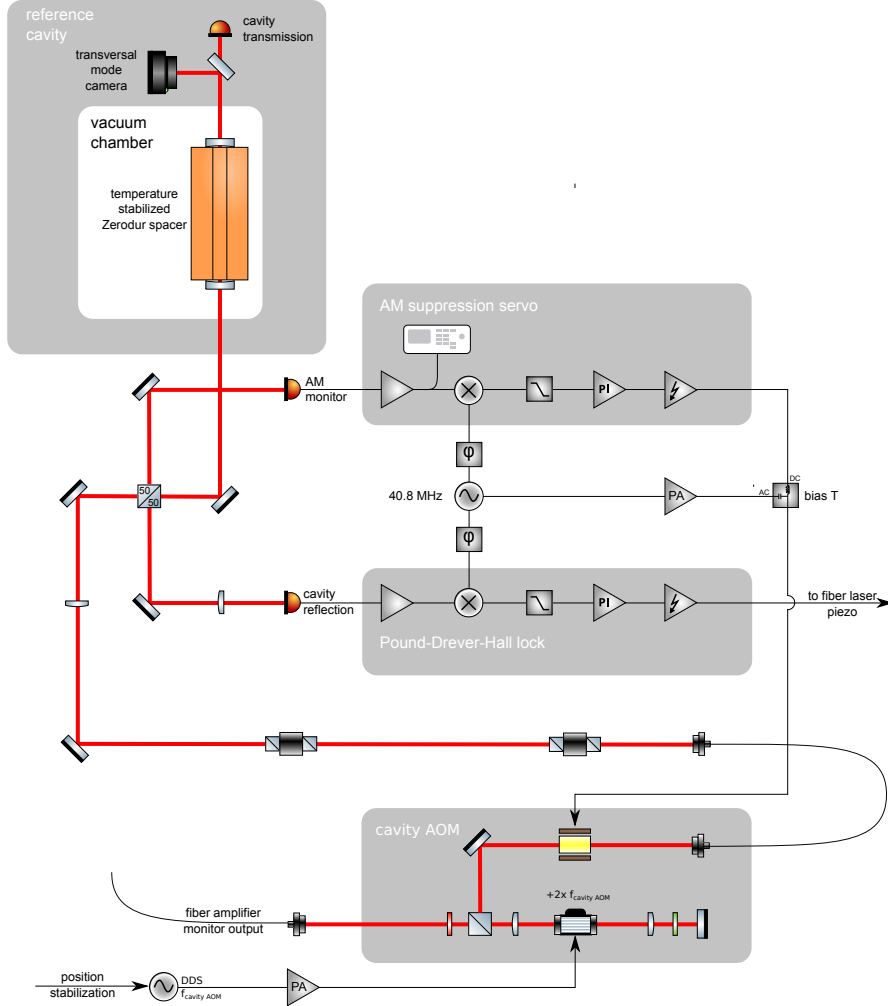
Figure 4.5.: Schematic of the Zerodur cavity setup used to stabilize the intercombination line lasers, including the Pound-Drever-Hall setup and the extra control loop for suppression of amplitude modulation.

We further observe a linear drift of $\sim 5\,\text{Hz/s}$, which we attribute to aging of the Zerodur spacer. The corresponding Zerodur contraction rate of $\frac{\Delta l}{l} = -3 \cdot 10^{-7}/\text{a}$ is in good agreement with the results reported in the literature [165].

Transmission through the cavity is monitored using a photodiode and a camera, which allows identification of the transversal mode, while the reflection is used for error signal generation using the Pound-Drever-Hall technique. Sidebands at a frequency of 40.8 MHz are generated using a homemade EOM consisting of a z-cut lithium niobate crystal driven by an RF amplifier.

As this device exhibits significant residual amplitude modulation (RAM) due to etalon effects between the flat end faces, in addition to the standard PDH circuitry we implement
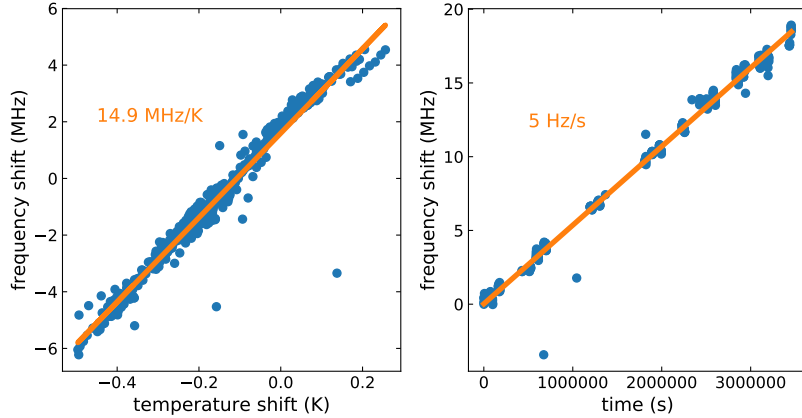
Figure 4.6.: Frequency shift of the Zerodur cavity as a function of a) measured spacer temperature and b) time with linear fits. Data was collected over several weeks and the datapoints in each plot have been compensated for the other variable using the respective fits.

a servo loop actively suppressing amplitude modulation by applying a bias voltage to the crystal [166] and thus stabilizing the optical path length of the crystal. For this purpose, part of the phase modulated beam is split off and detected on an additional photodiode before it reaches the cavity. Similarly to the generation of the PDH signal, this signal is mixed with a phase shifted reference signal in order to generate an error signal. This is then fed back to the EOM via an integrator, a high voltage amplifier and a bias-T combining it with the RF modulation. Due to the finite range of bias voltage, continuous drifts eventually cause this loop to fall out of lock, in which case the polarity is automatically inverted in order to move the lock point to the next available zero crossing of the RAM.

MOT position stabilization

While the stabilization to the Zerodur cavity provides good short term stability, the long term stability is not sufficient for stable loading of the optical traps from the intercombination line MOT for more than about twenty experimental cycles[1], because the vertical position of the MOT depends strongly on the exact laser detuning (see subsection 5.2.1).

For this reason we have opted to add an additional feedback loop where we detect the MOT position during the cooling phase and adjust the laser frequency to achieve the desired position for optimal loading of the optical trap. This has been published in [167].

A *Raspberry Pi* single board computer is used to implement this loop. It receives a digital trigger signal from the experiment control system, upon which a picture of the MOT fluorescence is recorded using the *Raspberry Pi*s camera. The center of gravity of

---

[1]On this timescale, the instability is dominated by the fluctuations in the actual temperature of the cavity spacer.
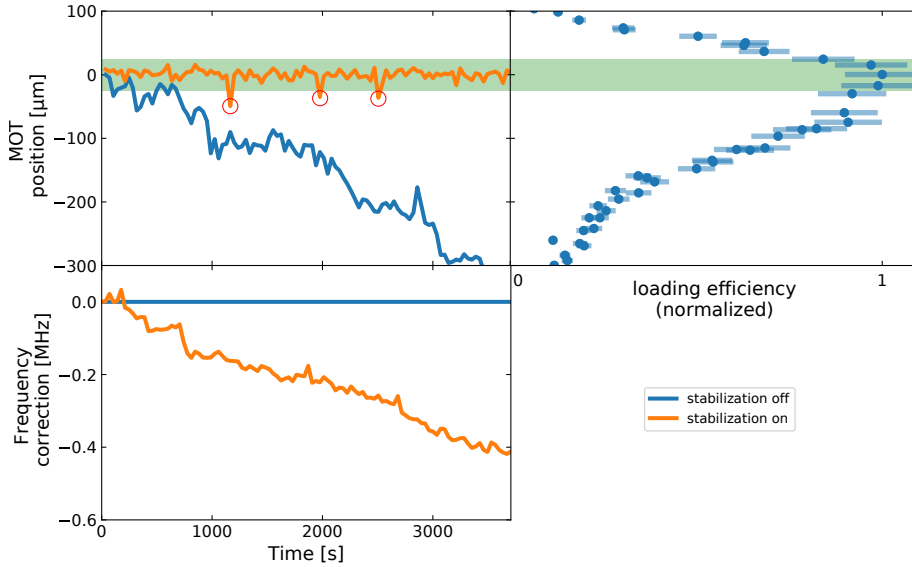
Figure 4.7.: Vertical position of the compressed MOT (see subsection 5.2.1) with the position stabilization turned off (blue) and on (orange) over time. The right panel shows the change in loading efficiency of the optical trap depending on the MOT position. The green area stretching across both panels indicates the target range where efficient loading of the optical trap occurs. The bottom panel shows the detuning of the cavity AOM corresponding to the position data.

the fluorescence data is compared to the position setpoint. The required frequency change, which is proportional to the measured position error, is then calculated and the frequency of the direct digital synthesizer (DDS) driving the cavity AOM is adjusted accordingly. An adjustable fraction of this frequency correction is also applied to the starting value for the next shot, effectively implementing a slow PI controller.

This loop successfully keeps the laser frequency in the range providing optimal loading of the dipole trap (see section 5.2), as is illustrated by the comparison of the MOT position with and without this stabilization in Figure 4.7. The occasional outliers (red circles) in the stabilized MOT position have since been identified as caused by a timing problem and have been eliminated.

4.2.4. Yb MOT setup

On the science table, light from the fibers for MOT (556 nm) and slower (399 nm) is collimated using homebuilt collimators and distributed as shown in Figure 4.8. The collimators are based on achromatic doublets to reduce spherical abberation, which otherwise leads to visible fringes at the relatively long focal lengths required to achieve the desired beam sizes. The MOT collimator is followed by a polarizing beam splitter cube in order to clean up the polarization and ensure the stability of the relative powers of the three MOT beams. A
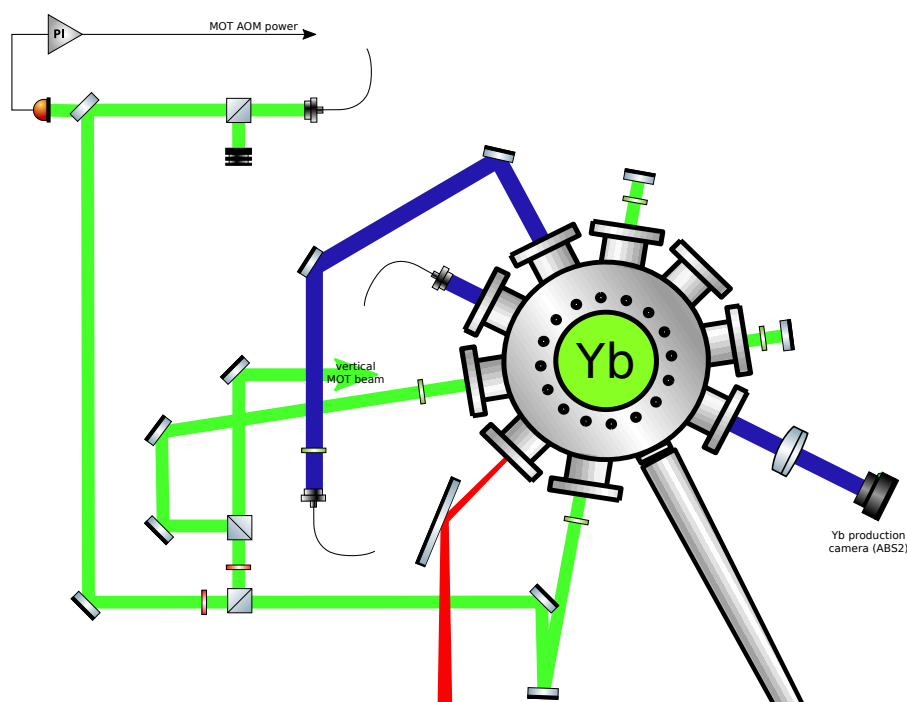
Figure 4.8.: Schematic diagram of the Yb production chamber, showing the MOT beams including the power stabilization setup, the slower beam and the absorption imaging setup. Also shown is the Yb tweezer beam entering the chamber. The connection to the Yb production chamber at the top right (opposite the viewport where the tweezer enters) is not shown.

logarithmic photodiode monitoring the transmission through one of the mirrors is used for intensity stabilization.

As the green MOT only reaches a low optical density and in its final stage only the effect of the upward beam is critical for its performance, the MOT beams are retroreflected in this setup. The light is thus split into three MOT beams and sent into the Yb production chamber with the appropriate polarisations.

The slower is directly focussed onto the oven aperture by the collimator. As the operation of the Yb slower only weakly depends on polarization, no measures to clean or fix the polarization are taken here. A single $\lambda/4$ waveplate allows for rough adjustment of the polarization.

4.2.5. Tweezer laser system

A large part of the optical setup at the science table consists of the various optical traps. The setup for the Yb tweezer beam is shown in Figure 4.9.

A home-built fiber amplifier (see Figure 3.4) seeded by a commercial multi-mode fiber laser (*IPG PYL-20M-LP*) is used to generate $\sim 30\,\text{W}$ of spectrally multimode light at

1064 nm in a single mode fiber. A polarization-insensitive fiber to free-space isolator couples the light out of the fiber and serves to protect the amplifier from backreflections.

In this setup the beam shape and thus the trap shape can be modified by modulating the RF frequency of an AOM. A change in frequency leads to a change in angle of the first diffraction order of the AOM and thus a change in position at the location of the focus[2]. If the drive frequency is modulated at a frequency that is fast relative to the trap frequencies, the atoms see only a time averaged potential. In this case we use a modulation designed to produce an ideal harmonic trap [168] (under the assumption of a point shaped beam; as the unmodulated beam size in our case is already about half of the target beam size, the actual beam shape is the convolution of a harmonic potential with a Gaussian). This waveform, which is shown in the inset of Figure 4.9, is output by an arbitrary waveform generator and serves as tuning voltage for the voltage controlled oscillator driving the AOM. In addition to shaping the trap, it can also be translated transversally by a few hundred micrometers by changing the DC offset.

This AOM also serves as a switch and as the actuator for the tweezers power stabilization loop, with the transmission through a mirror being measured by a logarithmic photodiode.

The beam is then magnified in order to reach the desired spot size after focussing by the final lens. This lens is mounted on an air-bearing translation stage (*Aerotech ABL1500*), allowing the focus to be translated from the production chamber into the science chamber. Due to the requirement to translate the focus inside the vacuum system by ~ 450 mm, the focussing lens has to have a relatively large focal length ($f = 1000$ mm) leading to a large required incident beam on the lens for the tight focusing required for the trap.

---

[2]Note this does not work if the AOM is located at a beam focus, as is often the case. In this case the location of the focus used for the trap – being an image of the beam in the AOM – would remain stationary while the beam tilts around this point.
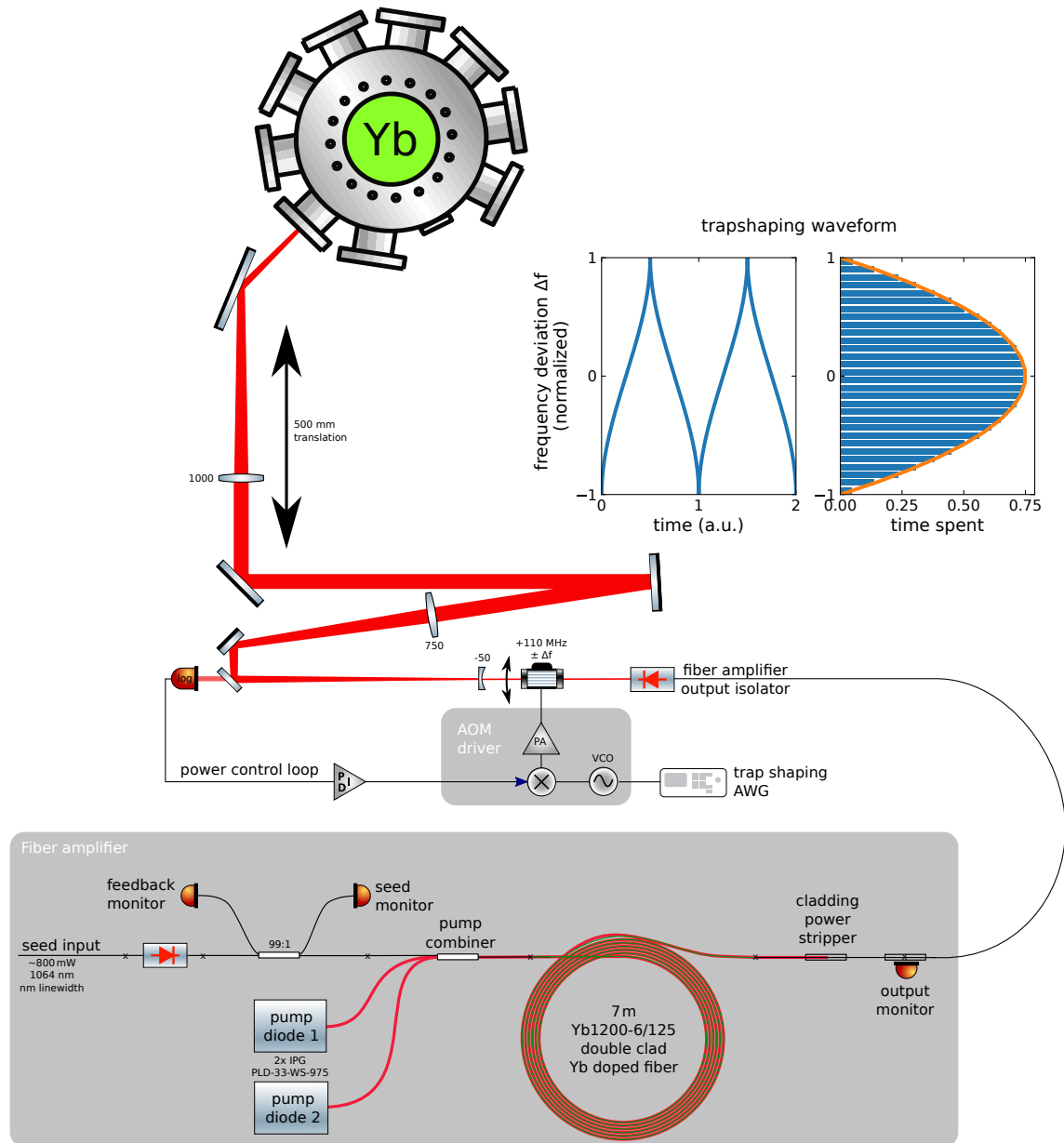
Figure 4.9.: Schematic diagram of the Yb tweezer setup including the fiber amplifier, the setup for power stabilisation and trapshaping, beam expansion through a Galilean telescope and the translation stage with the final focusing lens. The inset shows the signal used for frequency modulation of the tweezer AOM in the left panel, while the right panel is a histogram of the frequency deviations in this signal, showing the time averaged beam shape as it would appear for a pointlike input beam with a parabola for comparison.
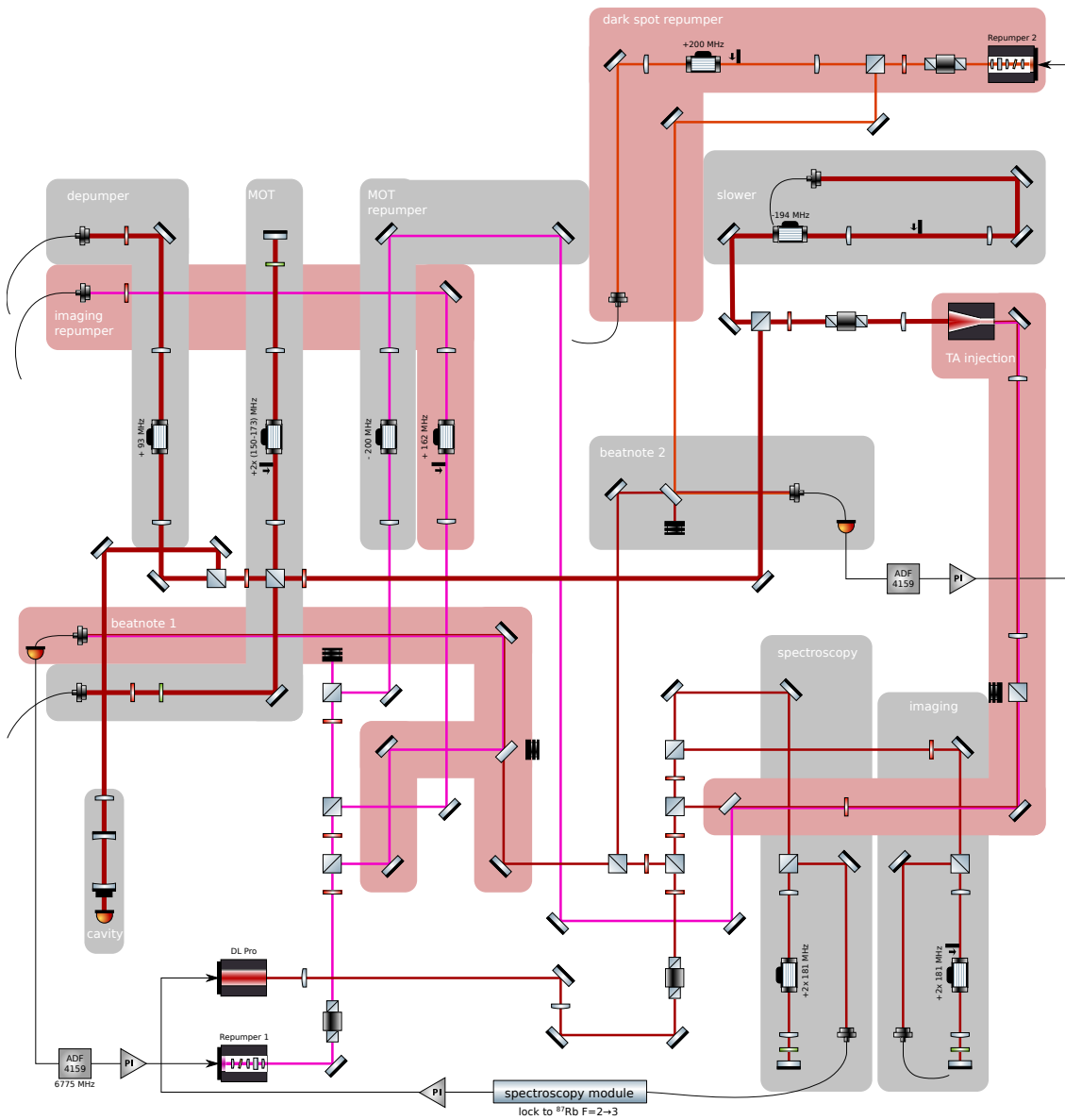
Figure 4.10.: Schematic diagram of the rubidum laser system, showing the master laser, the two repumpers and the tapered amplifier, as well as the AOMs, mechanical shutters and fiber couplings needed for the various beams.

4.3. Rb laser system

For the cooling of Rb, laser light driving the D2 line at 780 nm is required. The setup to generate the required beams is shown in Figure 4.10 and is briefly described here. As the hyperfine splitting of 6.8 GHz for ^{87}Rb cannot be easily bridged by AOMs, we employ separate lasers adressing the $F = 2$ and $F = 1$ manifold respectively, which will be refered to as the master – used to drive the cycling $F = 2 \rightarrow F' = 3$ transition for slowing, cooling and imaging – and the repumper – used to return atoms transferred to the $F = 1$ manifold

either intentionally, as for magnetic trapping, or due to off resonant excitation to $F' < 3$ states –, respectively.

The master laser light is produced by a commercial grating based ECDL system (*Toptica DL Pro*). Small portions are split off for absorption imaging as well as the spectroscopy beatnote setups used for frequency stabilization (see subsection 4.3.1), while the main part is seeding a tapered amplifier (TA, *DILAS TA-0780-1000*).

The output of the TA is split into the MOT and slower beams, frequency shifted and switched by AOMs and mechanical shutters and coupled into the respective fibers to the experiment.

Repumping light is generated by two interference filter based ECDL based on inexpensive *Sharp GH0781JA2C* laser diodes, denoted Repumper 1 and Repumper 2. Repumper 1 is amplified in the TA together with the master laser and provides repumping for the MOT and slower beams. Additionally a small portion is split off and switched using an AOM and a shutter and serves as imaging repumper.

As repumper 1 illuminates the complete MOT volume, it has to be turned off during the dark spot phase (see section 5.1.1). Here, repumper 2, which is switched using an AOM and a shutter and coupled into a separate fiber and only selectively illuminates the outer part of the MOT volume is employed.

4.3.1. Frequency stabilisation

The Rb master laser is stabilized to a frequency $360\,\mathrm{MHz}$ red detuned from the $^{87}\mathrm{Rb}$ D2 $F = 2 \to F' = 3$ transition using a compact saturated absorption spectroscopy setup which was developed as part of this thesis and is shown in figure 4.11.

The input beam is frequency shifted and modulated using a double pass AOM (see figure 4.10) before being coupled into a polarization maintaining fiber to the spectroscopy module. Here, the light is collimated and split into a strong pump beam and two weak probe beams, designated signal and reference. The pump is overlapped with the signal beam using a polarisation beam splitter, giving rise to a saturated absorption signal, while the reference beam gives a Doppler broadened signal.

The signal and reference beams are detected using a noise cancelling photodiode circuit [169]. One output corresponds to the logarithm of the ratio of signal and reference power and thus gives a Doppler free absorption spectrum with very good suppression of the Doppler broadened background. The other signal is the AC coupled difference between the (electronically balanced) photocurrents and is used as input for the lock-in amplifier producing the error signal.

Repumper beatnote locks

The two repumper lasers have to address the $^{87}\mathrm{Rb}$ $F = 1 \to F = 2$ transition, which as shown in Figure 4.12 requires them to be detuned from the master laser by about $6.8\,\mathrm{GHz}$. Rather than using additional spectroscopy setups for their stabilization, these lasers are offset locked to the master laser using low bandwidth beatnote locks (see section 3.5).
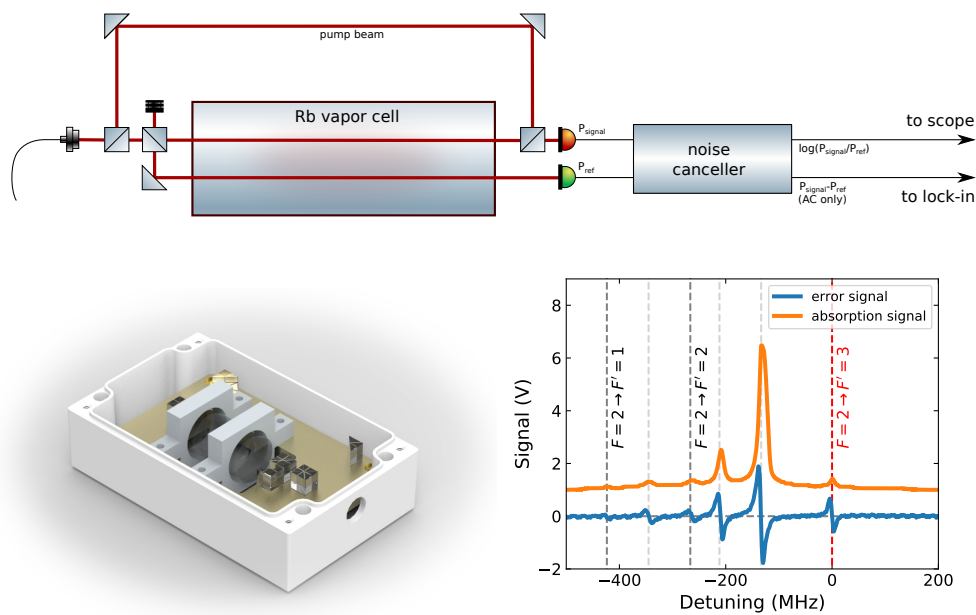
Figure 4.11.: Schematic drawing of the fiber coupled Rb saturated absorption spectroscopy module. The bottom row shows a CAD rendering of the setup and a graph of the generated output signals, including the dispersive error signal generated using the lock-in technique, for the ^{87}Rb $F = 2 \rightarrow F' = 1, 2, 3$ line. The atomic transitions are indicated using vertical dashed lines, with the ^{87}Rb $F = 2 \rightarrow F' = 3$ transition being highlighted in red. Gray lines represent crossover transitions arising from the saturated absorption spectroscopy technique.
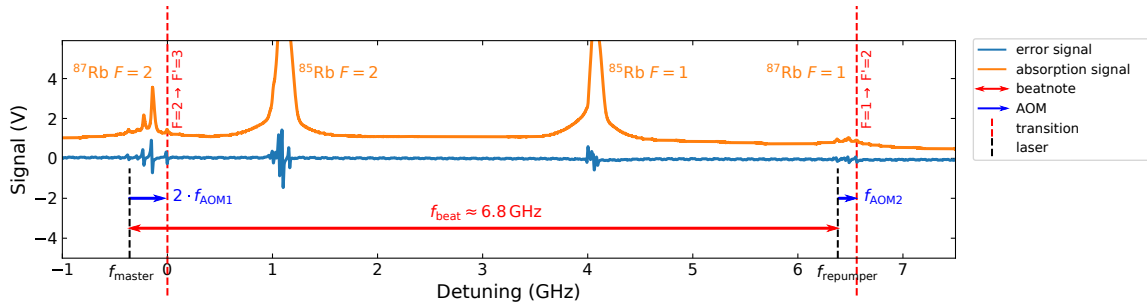
Figure 4.12.: Diagram of the frequencies and lockpoints for the Rb laser system. The master laser (indicated by the left dashed black line) is shifted by an AOM in double pass configuration (blue arrow) and locked to the ^{87}Rb $F = 2 \rightarrow F' = 3$ (left dashed red line) using the spectroscopy and corresponding error signals shown. The repump lasers need to address the ^{87}Rb $F = 1 \rightarrow F' = 2$ line (right dashed red line) after a frequency shift by an AOM required for fast switching. To achieve this, they are stabilized relative to the master laser using a beatnote lock (red arrow).

Both lasers are combined with beams from the master laser in free space and then coupled into single-mode fibers (see boxes *beatnote 1* and *beatnote 2* in Figure 4.10) . The beatnote signals are detected using GaAs ROSAs (see subsection 3.5.3) without further amplification and fed into the ADF4159 board (see section section 3.4).

While the diode lasers employed would in principle be suitable for a high bandwidth lock acting on the laser current and achieving a tight phase lock, a frequency lock is by far sufficient for the application as repumpers, so a simple PI controller acting on the laser piezo is used to achieve a robust frequency lock.

Slow drifts in environmental conditions cause the diode current required for the repumpper lasers to change over the day, causing them to fall out of lock eventually. For this reason, an automatic relocking system consisting of a *Raspberry Pi* single board computer constantly monitors the beatnote frequency and reacquires lock by scanning the laser current whenever necessary.

4.3.2. Rb tweezer

The Rb tweezer beam is produced by a commercial polarization-maintaining fiber amplifier (*Nufern NUA-1064-PB-0050-D0*) with a nominal output power of 50 W, seeded by the same spectrally multimode fiber laser seeding the Yb tweezer (*IPG PYL-20M-LP*).

As the amplifier does not incorporate an output isolator, the collimator is followed by a free space isolator (*Thorlabs IO-5-1064-VHP*). We note a substantial loss of isolation due to thermal effects [170] in this terbium gallium granate (TGG) based isolator, but together with the amplifiers backreflection interlock, it is still sufficient to protect from accidental backreflections.

The setup for the Rb tweezer is illustrated in Figure 4.13 and is similar to the one for Yb (see subsection 4.2.5): An AOM (*Crystal Technology 3110-191*) allows fast switching of the trap and acts as actuator for intensity stabilization using a logarithmic photodiode detecting the transmission through a mirror. Here it is not used for beam shaping though.

As in the Yb system, the beam is magnified before being focussed to a waist of 40 μm by the final lens mounted on an air-bearing translation stage (*Aerotech ABL1500*), which allows the focus to be translated from the production chamber into the science chamber.

4.3.3. Rb MOT setup

On the science table, light from the fibers for MOT and slower is collimated using homebuilt collimators based on achromatic doublets to reduce spherical abberation at the relatively long focal lengths required to achieve the desired beam sizes. Each collimator is followed by a polarizing beam splitter cube in order to clean up the polarization and a monitor photodiode – which in this case are not used for active stabilization as the experiment is insensitive to the relatively small power fluctuations ocurring in these beams.

The slower beam is directly focussed onto the oven aperture by the collimator. The MOT beam is split up into the required beams and distributed around the chamber by free space optics. Due to the high optical density reached in a Rb MOT, in this case six beams instead of three retroreflected beams as in the Yb setup are used.

4.3.4. Rb imaging and dark spot repumper

Imaging light and imaging repumping light is combined into a single fiber using a fused fiber coupler. This has the advantage of ensuring good spatial overlap between the imaging and repumper light and does not negatively impact image quality on our cameras when the repumping pulse occurs ~ 0.5 ms before the camera exposure. One output of the fiber splitter is used for the vertical imaging system in the science chamber while the other output is collimated at the production chamber and used for absorption imaging there. A polarization cleaning cube serves to divide the beam between the production chamber and the horizontal imaging system in the science chamber (see subsection 4.8.4).

This cube is also used to overlap the imaging beams and the dark spot repumper. This beam differs from the imaging repumper beam by its central dark spot, created using a gold mask deposited on an AR-coated glass substrate.
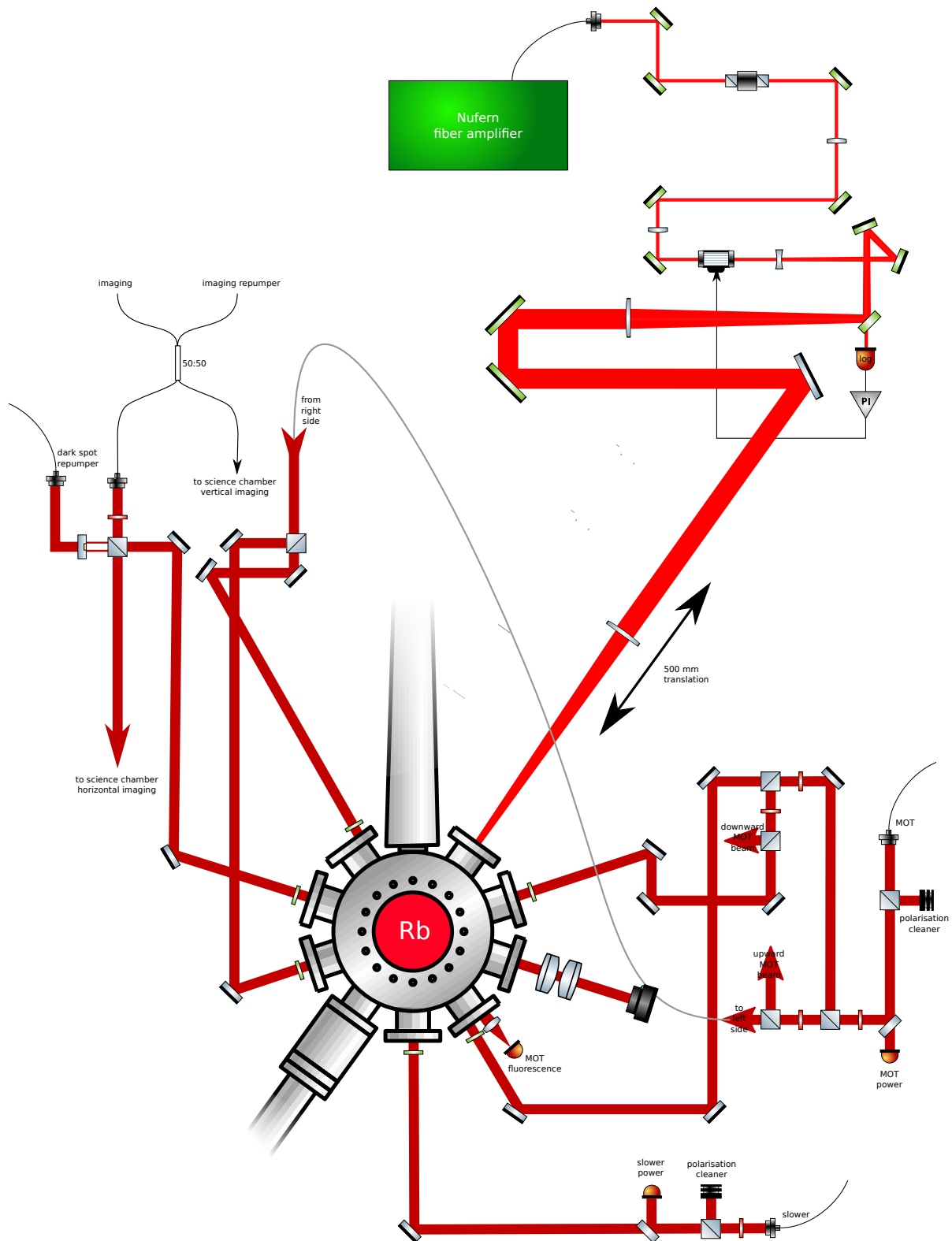
Figure 4.13.: Schematic diagram of the optics surrounding the Rb production chamber, including the optical tweezer setup on the top right, the horizontal MOT beams, the imaging setup and the dark spot repumper.

A quarter wave plate together with a magnetic bias field applied along the laser beam during imaging ensures either σ_+ or σ_- polarization in order to maximize the effective cross section for imaging.

4.4. Lattice laser system

The laser system for the optical lattice (see subsection 5.1.6) is shown in Figure 4.14. The light for the optical lattice is derived from an *Innolight Mephisto* Nd:Yag non-planar ring oscillator (NPRO) laser. This type of laser is characterized by good frequency stability and small linewidth, making it ideal for the creation of a stable lattice. A built in noise killer reduces amplitude noise.

The NPRO output is sent through a double stage isolator and is then fiber coupled. A home built fiber amplifier [171] yields an output power of 6 W, limited by SBS (see section 3.1.3) in the amplifier and output pigtail, both shown in the insets. Unlike in the other fiber amplifiers used in this apparatus, output light is sent through two stages of isolation, as the operation of a retroreflected optical lattice requires the light to be reflected back into the amplifier. The second isolator is fitted with a free space output onto a distribution breadboard.

In the free space section, the light is split into three beams for the individual lattice axes and their power is individually controlled by AOMs. In order to avoid interference effects between the beams, care is taken to ensure the individual AOM frequencies and thus the optical frequencies of the resulting lattice beams are separated by at least 2 MHz, so any interference between beams will average out on a time scale that is fast compared to the trap dynamics. The beams are then coupled into single mode fibers, leading to the lattice axes shown in Figure 4.18.
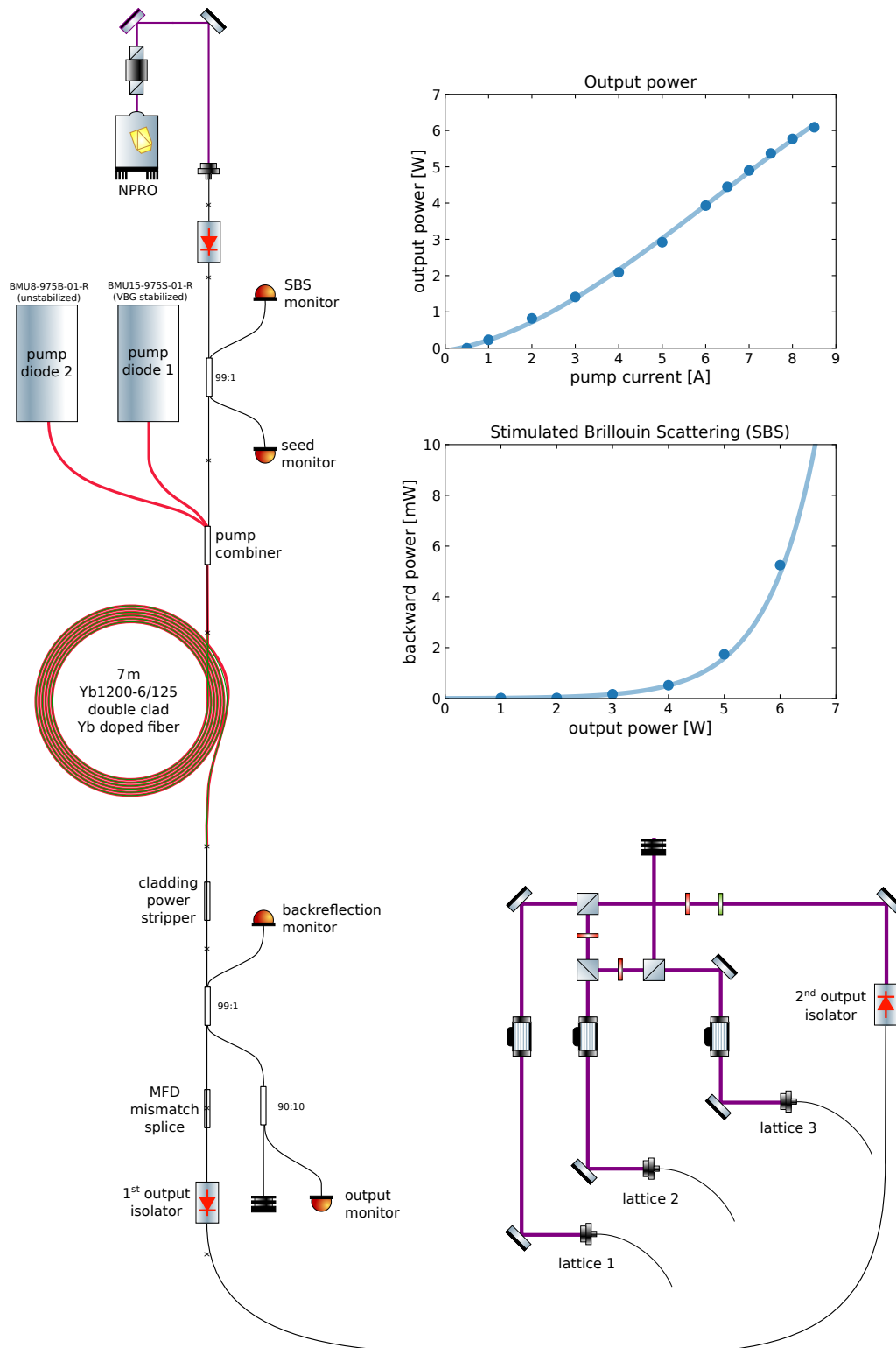
Figure 4.14.: Schematic diagram of the lattice laser system, including the NPRO seed laser, the fiber amplifier and the beam distribution and switching breadboard generating the three independently AOM controlled lattice beams. The insets show the amplifier output power (this shows non-linear behaviour because pump diode 1 is not wavelength stabilized and pump absorption thus changes with power) and SBS as a function of pump current (lines to guide the eye).

4.5. Photoassociation laser systems

In addition to the lasers required for preparing the ultracold atoms, several laser sources are required to perform the actual photoassociation experiments, which will be introduced in this section.

4.5.1. Free-bound laser

The light required for driving free-bound transitions near the $^2S_{\frac{1}{2}}+^3P_1$ asymptote is provided by a commercial frequency doubled fiber laser system [172], providing up to $16\,\mathrm{mW}$ output power at $556\,\mathrm{nm}$, tunable using a fiber stretching piezo.

   This laser has been integrated into our apparatus in the scope of [173]. The optical setup is shown in the upper half of Figure 4.15. The frequency doubled output of the laser is sent through an AOM and a shutter for fast and high contrast switching respectively and coupled into a fiber to the experiment.

Frequency stabilization

As the MOT laser is already stabilized to the $^2S_{\frac{1}{2}} + ^3P_1$ transition, it is an ideal frequency reference for photoassociation near the corresponding asymptote. The free-bound laser is stabilized by a beatnote between the (fundamental) monitor outputs of both lasers. To allow spectroscopy of and near the atomic resonance despite the synthesizer chips minimum frequency of $500\,\mathrm{MHz}$, the beam coming from the MOT laser is optionally frequency shifted by an AOM to increase the frequency difference, before the beams are overlapped using a fused coupler and detected using a SFP module (see subsection 3.5.3).

   Unfortunately the output of the fiber amplifier for the MOT exhibits amplitude noise peaks at multiples of $10\,\mathrm{MHz}$, originating from the free spectral range of its spectrally multimoded pump laser. These peaks appear in the beatnote signal and interfere with the frequency stabilization especially for small beatnote frequencies. To limit their influence, we use band pass filters with passbands of $\sim 1\,\mathrm{GHz}$, selected according to the beatnote frequency of interest, between photodiode module and amplifier. This also has the disadvantage of limiting the capture range of the lock – which nonetheless remains much larger than with other locks based on atomic spectroscopy or reference cavities.

   As control bandwidth is not a concern in this case, the phase frequency detector is operated at a reduced frequency of $10\,\mathrm{MHz}$ in this setup which we found to give a more stable lock. The error signal generated by the synthesizer chip is converted to a voltage with a series RC combination and then fed to a simple PI controller, thus effectively achieving a PI^2 controller.

   The output voltage is amplified and sent to the lasers fiber stretching Piezo. As the bandwidth of this actuator is limited to a couple of kHz, it is only suitable to stabilize the laser frequency and to narrow the lasers linewidth. The free-bound lasers linewidth thus remains unchanged at $\sim 120\,\mathrm{kHz}$ in the green.
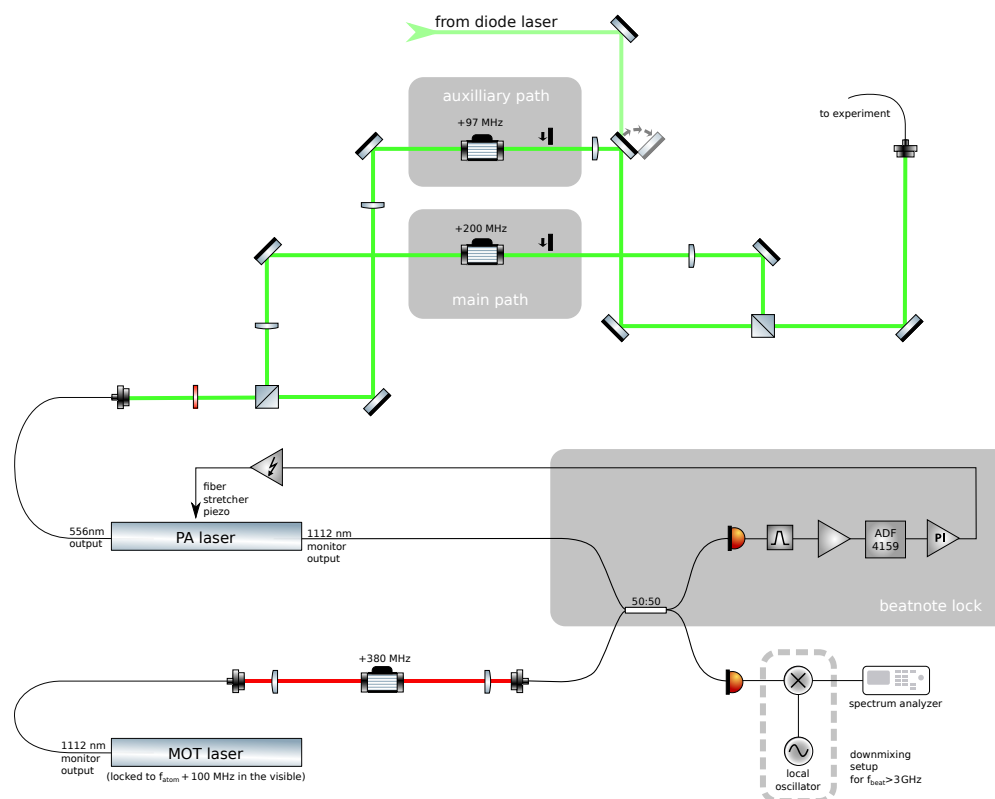
Figure 4.15.: Schematic diagram of the setup for the free-bound PA laser including the beatnote setup for frequency stabilization and the AOM intensity control setup. This includes an optional second path for bound-bound transitions with low binding energy of $\sim h \cdot 0.1\,\mathrm{GHz}$ (see section 4.5.2). As an alternative, an EOM may be placed into the *main path* to generate sidebands at additional frequencies in the GHz range (see section 4.5.2). An input for coupling light from the diode laser setup (see section 4.5.2) is also provided for use with more strongly bound levels.

4.5.2. Bound-bound laser

To access bound-bound transitions, we require a second light source that is blue detuned of the free-bound laser by the binding energy (plus the thermal energy of the unbound atoms) of the ground state vibrational level to be accessed.

For driving coherent processes such as STIRAP, it is desirable for the relative linewidth between the free-bound and the bound-bound laser to be as small as possible. Depending on the frequency separation required, this can be achieved by various means which will be described in this section.
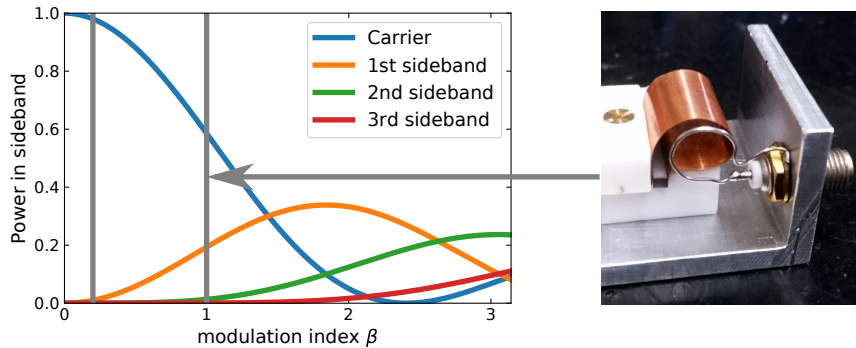
Figure 4.16.: Power of the sidebands generated in an EOM as function of the modulation index β. The vertical lines indicate the modulation depth achieved for an RF power of $1\,\mathrm{W}$ without resonant enhancement - but very generously assuming perfect impedance matching - and with the split ring resonator shown on the right.

AOM

For the most weakly bound levels, e.g. the least bound level of ${}^{87}\mathrm{Rb}{}^{170}\mathrm{Yb}$ with $E_B = h \cdot 102\,\mathrm{MHz}$, an auxiliary path in the free-bound laser setup allows the generation of a bound-bound beam. For this purpose a portion of the output light is split off as shown in the upper part of Figure 4.15 and sent through a second AOM, with the difference in frequency shifts corresponding to the binding energy. Note that for the frequency shift directions shown, in this case the main path will drive the bound-bound transition while the auxiliary path takes over the role of the free-bound coupling. This scheme has the advantage that the relative linewidth is limited only by that of the RF sources driving the AOMs and can thus be made very small. However, achieving the required AOM frequencies is only feasible for the most weakly bound levels of each isotopologue.

EOM

An alternative approach is the generation of sidebands using an electro-optic modulator (EOM). In contrast to an AOM, where different modulation orders are spatially separated due to their different diffraction angles, the output of an EOM driven by a single frequency will contain the input optical frequency as well as sidebands of various orders, with the amplitude of the nth sideband given by the Bessel function of the first kind $J_n(\beta)$ of the phase modulation amplitude β as shown in Figure 4.16. The unwanted sidebands not only cause a loss of power, but can also interfere with the experiment if one gets close to another transition. Furthermore, the carrier cannot be independently turned off, so implementation of e.g. a STIRAP scheme (section 9.5) would not be possible when using the carrier as one of the driving fields.

The unwanted frequencies could be reduced by the implementation of so called serrodyne modulation [174, 175], where the modulator is driven by a sawtooth ramp, requiring much

higher bandwidths than when using sinewave modulation and still typically giving considerable residual sidebands, or by the use of filtering cavities [176, 177] introducing considerable experimental complexity. None of these are implemented here, as the sole purpose of the EOM setup is performing spectroscopy on the one or two states that are hard to reach using a beatnote lock due to their low beatnote frequency[3] and to provide a benchmark that results achieved with the phaselocked laser can be compared against.

While broadband fiber optic modulators with bandwidths of tens of GHz are commercially available, their high cost also makes them unattractive for this *one trick pony* application. We thus use a homebuilt phase modulator based on z-cut lithium niobate crystal of dimensions $2\,\text{mm} \times 2\,\text{mm} \times 25\,\text{mm}$. In order to generate the electric field necessary to reach the maximum amplitude of the first sideband at a wavelength of $556\,\text{nm}$, corresponding to $\beta = 1.84$, a voltage of $100\,\text{V}$ is needed for this crystal, corresponding to an impractically high drive power of $100\,\text{W}$ into $50\,\Omega$ - which is bound to be the output impedance of practically every amplifier operating at these frequencies. The solution is to build a circuit resonantly enhancing the voltage over the crystal using a so called tank circuit. While at frequencies up to a few hundred MHz this circuit can be constructed from discrete components, this becomes impractical in the GHz region due to increasing parasitic effects. A better solution [178] at these frequencies is the implementation of a so called split-ring resonator, where a conductive hollow cylinder – or an approximation thereof, in our case a thin copper sheet whose ends are clamped to either side of the crystal as shown in Figure 4.16 – is split lengthwise and the crystal is inserted into the gap. Now the cylinder acts as an inductance, forming a resonant circuit together with the capacitance of the crystal filled gap. The input signal can be coupled into the resonator using a small wire loop, with the distance determining the coupling strength. The resonance frequency is determined by the radius of the cylinder and can be fine tuned by inserting either magnetic or dielectric elements into its bore - increasing the inductance or the capacitance respectively.

With the setup shown in Figure 4.16, a modulation of $\beta = 1$ - corresponding to $\sim 20\,\%$ of the power in each 1st sideband - is achieved with a modest drive power of $\sim 1\,\text{W}$ at frequencies tunable over a range of roughly $60\,\text{MHz}$ around the target frequency of $1018\,\text{MHz}$.

Diode PA-laser

In order to perform two-photon photoassociation to the vast majority of bound levels, an independent laser source is required. As fiber lasers such as the ones used for the MOT and first PA laser do not provide an actuator with sufficient bandwidth for linewidth narrowing, a diode laser is chosen for this task. An AR-coated gain chip (*Innolume GC-1113-TO-250*) is set up in a grating based external cavity diode laser and its output again frequency doubled in a PPLN waveguide. The output is switchable by a shutter and an AOM and can then be combined with the fiber PA laser instead of the auxilliary path (see Figure 4.15).

The diode based photoassociation laser is stabilized to its beatnote with the free-bound fiber laser. This has the advantage of the beatnote frequency (up to well defined shifts by

---

[3]Note that for frequencies from a couple of 100 MHz up this can also be circumvented by upmixing of the beatnote to a higher RF frequency
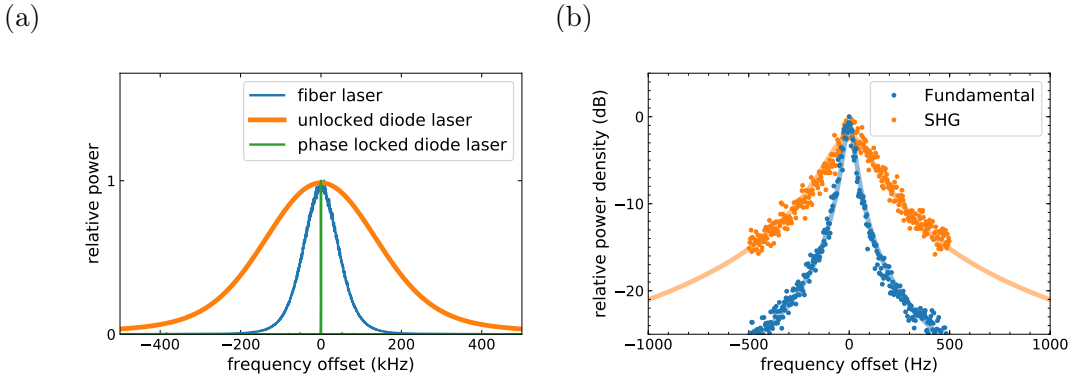
Figure 4.17.: (a) Comparison of the beatnote spectra – normalized to their peak value – between a fiber laser and a second independent fiber laser (blue), the weakly locked diode laser (orange, simulated) and the phase locked diode laser (green). (b) Beatnote spectra showing the carrier as measured at the infrared beatnote photodiode used for the lock and at a photodiode placed in the combined frequency doubled beams before they are coupled into the fiber.

AOMs) directly corresponding to the binding energy of the adressed vibrational state in the electronic ground state and allows control of the relative linewidth by acting on the diode laser only, instead of having to minimize the individual linewidth of two independent lasers. Additionally, the technical complications introduced by the pump laser noise in the MOT laser beatnote signal are avoided.

The beatnote is again realized using a fiber splitter, an SFP module as wideband photodiode (see subsection 3.5.3, and an ADF4159 snythesizer board (see section 3.4 – this time operating at the full phase detector frequency of $100\,\text{MHz}$ to maximize bandwidth – to generate the error signal. Due to the clean beatnote signal generated by this combination of lasers, no amplification or filtering of the beatnote is needed.

The error signal is again fed to a PI^2 controller, which in this case has been designed with special attention to high bandwidth through careful choice of operational amplifiers and component values. The controller output acts on the laser diode current through the modulation input of the well known Libbrecht-Hall current controller design [179].

An additional slower (pure integrator) servo loop gets the first loops output as input and acts on the laser piezo to keep the current near the center of the adjustment range. A lock bandwidth of $\sim 350\,\text{kHz}$ is achieved by this system, limited by the large capacitance of the gain chip and relatively long fiber and cable lengths in the current setup. This bandwidth exceeds the free-running laser bandwidth and thus allows the lock to actually narrow the laser bandwidth as illustrated in Figure 4.17a, where the dramatic difference in relative linewidth compared to using a fiber laser becomes apparent.

As the fundamental laser is stabilized before frequency doubling, and in the case of the free-bound laser amplification, some noise is introduced outside of the loop. This leads to a broadening of the relative linewidth of the PA lasers (FWHM $\sim 230\,\text{Hz}$) compared

to the in-loop measurement at the infrared photodiode (FWHM $\sim 53\,\mathrm{Hz}$) as shown in Figure 4.17b.

4.6. Science chamber

The setup at the science chamber mainly consists of the optics needed to create the crossed dipole traps from the tweezer beams transmitted through the science chamber, the setup for the optical lattice, the optics needed to perform the photoassociation experiments and of course the imaging systems needed for alignment and to detection of the atoms. A schematic overview of the layout is shown in Figure 4.18.

4.6.1. XODT

For each species a separate crossed optical dipole trap is formed by folding of the respective tweezer beam. The beam is recollimated after exiting the vacuum chamber and passes through an AOM, allowing the relative intensity of the crossing beam to be controlled. As translation of the tweezer causes the beam size at the AOM to exceed its aperture, an electrically controlled flip mirror is installed to deflect the beam into a beam block when the tweezer is not in the science chamber in order to prevent thermal damage to the AOM and uncontrolled stray light.

In the case of Rb the crossing beams polarization is rotated to be perpendicular to that of the tweezer beam in order to prevent interference between these beams (see section 3.1.3). The beam is then refocussed into the science chamber and aligned to intersect with the tweezer beam near the center of the chamber.

By changing the frequency and thus the deflection of the AOM controlling the crossed beam, either XODT can be translated along the tweezer beam by $\sim 1\,\mathrm{mm}$.

Alternatively a XODT for Yb can be formed by aligning the Rb tweezer beam to intersect with the Yb tweezer. Due to the higher available power in the Rb beam compared to the Yb XODT beam, this provides slightly better performance, but is less suitable for the creation of mixtures as the evaporation of both species cannot be separated nor can they be evaporated simultaneously due to the large difference in trap depths experienced by both species.

4.6.2. Optical lattice

The optical lattice provides an additional trap for the final steps of the preparation of ultracold mixtures in the science chamber, which will become important at a later stage for optimising the photoassociation protocol. The system has been developed and described in [171, 180] and will be briefly summarized here.

The lattice light arrives at the science chamber in individual polarization-maintaining fibers (see section 4.4). Each is collimated using a homebuilt fiber collimator [180] and focussed to the location of the atoms with a beam waist of $100\,\mu\mathrm{m}$. After exiting the chamber, the beams are recollimated and then retroreflected. The retroreflectors are set up
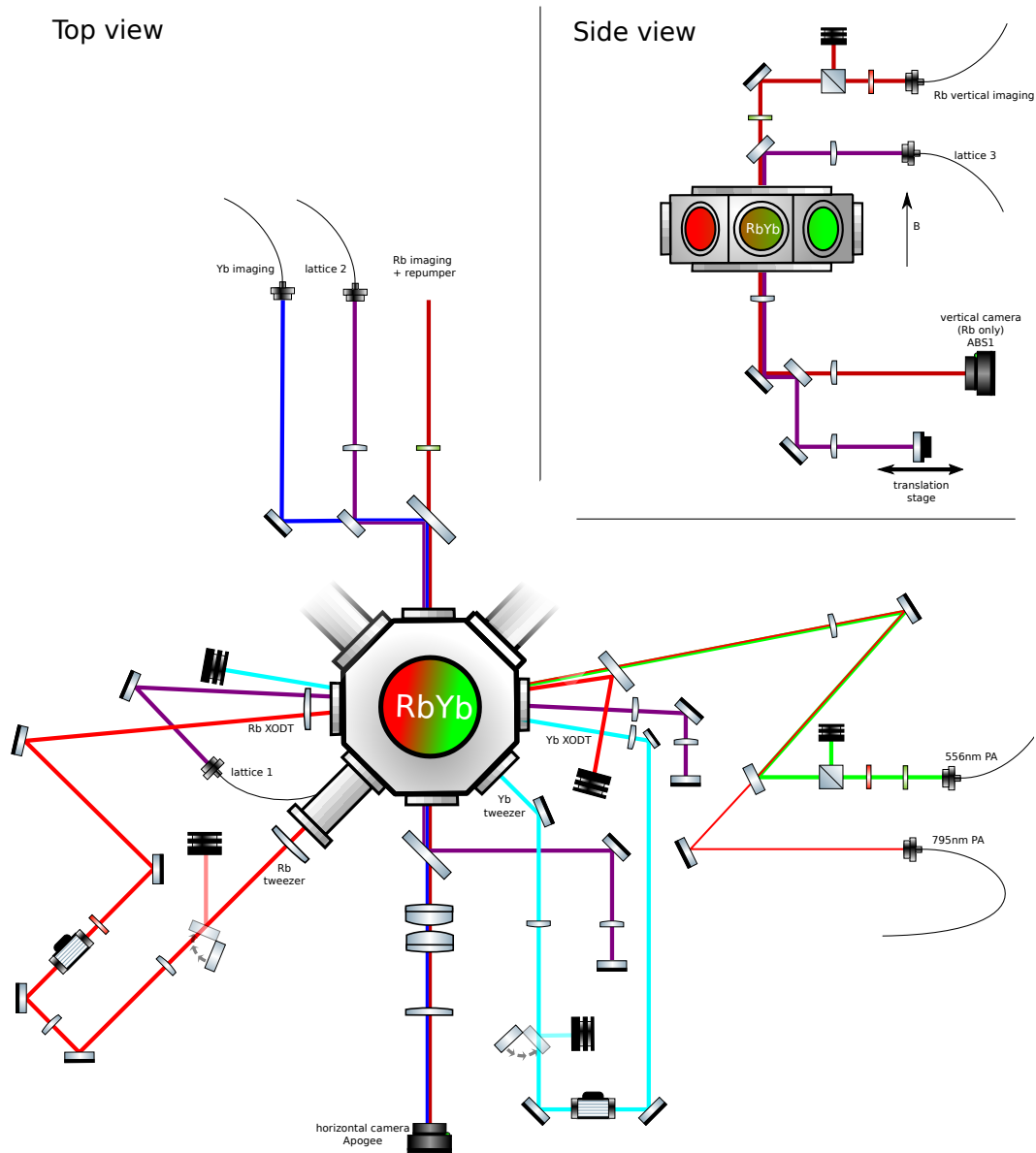
Figure 4.18.: Schematic diagram of the optical setup surrounding the science chamber, showing the trapping, imaging and photoassociation beams.
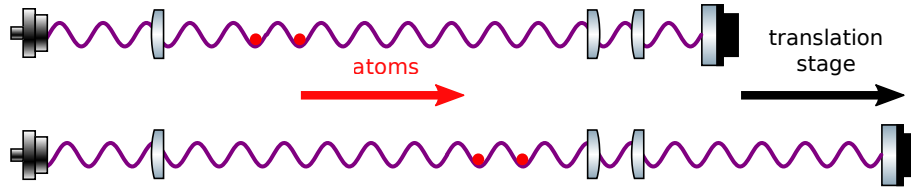
Figure 4.19.: Schematic representations of the lattice elevator with the standing wave trapping potential shown in purple. By translating the retroreflecting mirror along the beam direction, the standing wave antinodes and thus the atoms trapped inside them are moved. Note the translation distance and the optical wavelength are greatly exaggerated and the setup is shown horizontally for compactness of the figure.

as cat-eyes in order to reduce alignment sensitivity. Photodiodes behind the retroreflector allow monitoring of the optical powers.

Due to space constraints, Lattice 3 shares the focussing lens with the Rb XODT, while Lattice 1 and 2 are overlapped with the vertical and horizontal imaging path respectively using dichroic mirrors. Lattice 1 shares the recollimation lens with the imaging system.

Lattice elevator

The vertical beam (Lattice 1) has an additional function as elevator, allowing the transport of atoms between the planes of the Rb and Yb traps as illustrated in Figure 4.19.

The retroreflector for this beam is mounted on a DC servo driven translation stage (*Thorlabs DDSM100*), allowing it to be translated by up to 100 mm. When the retroreflector is translated, the standing wave and thus the trapping sites move with it, allowing us to vertically translate the atom cloud. As in our setup only the mirror is translated while all lenses are stationary, this leads to a mismatch of the reflected beam waist. However, for the small translations on the order of a mm used here, this does not cause a relevant change in trap parameters.

Due to the large longitudinal trapping frequencies achieved in the optical lattice, in contrast to the optical tweezers, the atoms adiabatically follow the translation for any reasonable motion profile.

4.6.3. Microwave

Similarly to the Rb production chamber, a microwave system for driving the Rb hyperfine transition is also installed in the science chamber [104]. The difference between both systems is that the system for the science chamber features an oven-controlled crystal oscillator (OCXO) as a more stable reference oscillator and the science chamber antenna is equipped with tuning screws, allowing for better impedance matching as well as slight tuning of the center frequency according to the application.

Due to space constraints, the antenna does not in fact have a direct line of sight to the location of the atoms. However, due to the relatively small size of the viewport compared

to the microwave wavelength and associated diffraction, as well as reflection by the chamber walls, we still get more than sufficient field strength at the location of the atoms for most applications.

4.6.4. PA beams

To allow for photoassociation both near the Rb D1 asymptote (see subsection 7.1.1) – mostly for diagnostic purposes – and the Yb intercombination line, the setup features beampaths for both 556 nm and 795 nm light. Both arrive in single mode fibers, with the polarization being adjusted and cleaned up by waveplates and a polarizer. They are then overlapped and focussed into the vacuum chamber such that they are close to counter-propagating to the Rb XODT beam. The $1/e^2$ beam radii at the location of the atoms are 0.11 mm for 556 nm and 0.7 mm for 795 nm.

As the magnetic bias field in the science chamber is oriented vertically, the horizontal PA beam allows for either π or a superposition of σ_+ and σ_- polarization to be selected by changing the light polarization.

4.7. Control system

Experiment control is based on a modified version of the *Cicero Word Generator* system [181]. A schematic overview is shown in Figure 4.20. The *Cicero* graphical interface allows the creation of experimental sequences, which are then executed by multiple synchronized *Atticus* servers.

The bulk of control tasks is realized using digital (TTL) and analog (13-bit -10 to $10\,\mathrm{V}$) signals from the one computer system located in the laser room and an additional system located at the science table. These signals are realized using *National Instruments PCI-6229* and *National Instruments PCI-6723* IO-boards respectively. The *PCI-6229* board also provides analog inputs, that can be recorded during the sequence. Both systems share a 20 kHz clock signal generated by one of the analog cards.

In addition to these hardware control signals, commands are sent to various devices using TCP/IP, USB and GPIB connections. In contrast to the digital and analog signals, these commands are generated in software and do not have guaranteed timing. Devices like cameras and microwave sweeps are thus triggered using digital outputs where possible. For applications with low timing requirements (or devices lacking a hardware trigger input like the translation stage controllers), timing is realized purely in software.

The cameras are controlled using legacy *LabView* programs and online image analysis – usually consisting of pixelsums over one or multiple areas as well as Gaussian or bimodal fitting– is performed in python.

Information about the individual runs and results of image analysis are written to a database on the data storage and analysis server *uefa*. A web interface allows immediate plotting of the results and simple fits such as lifetimes and time-of-flight measurements, while more elaborate analysis can be conducted using python notebooks.
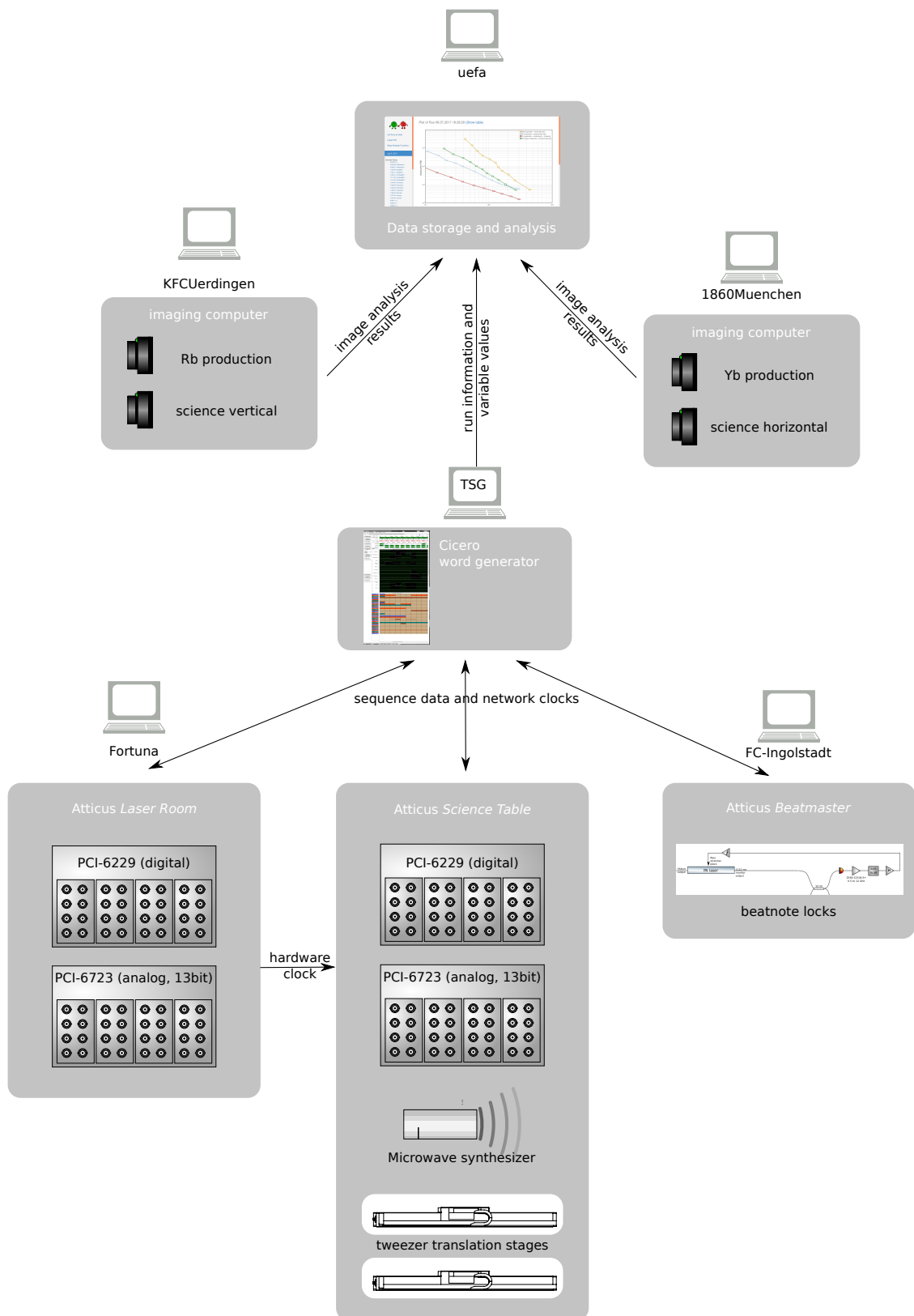
Figure 4.20.: Schematic overview of the experiment control system as well as the computers used for imaging and data analysis.

4.8. Absorption imaging

The main method to acquire experimental data in our apparatus is the direct detection of the atomic samples by absorption imaging. The sample is illuminated by a laser beam with a large diameter which is resonant with a cycling transition of the species to be detected. This beam is then detected by a camera, with the plane where the atoms are located imaged onto the camera chip.

Images are recorded with the atoms present and the imaging light turned on ($\vec{I}_{\mathrm{abs}}$), with the light turned on but without any atoms ($\vec{I}_{\mathrm{bright}}$) and with neither atoms nor light ($\vec{I}_{\mathrm{dark}}$). The dark image is subtracted from both other images to remove stray light and sensor dark current. The pixelwise ratio between $\vec{I}_{\mathrm{abs}} - \vec{I}_{\mathrm{dark}}$ and $\vec{I}_{\mathrm{bright}} - \vec{I}_{\mathrm{dark}}$ gives the transmission through the sample. Knowing the absorption cross section $\sigma_{\mathrm{abs}} = 3\lambda^2/(2\pi)$ of an atom, the column density $\tilde{n}(x, y)$ (integrated along the imaging axis z) can be reconstructed.

$$\tilde{n}(x,y) = \int n(x,y,z)\mathrm{d}z = -\frac{1}{\sigma_{\mathrm{abs}}} \ln \frac{\vec{I}_{\mathrm{abs}} - \vec{I}_{\mathrm{dark}}}{\vec{I}_{\mathrm{bright}} - \vec{I}_{\mathrm{dark}}} \tag{4.1}$$

Images are commonly taken after a *time-of-flight* (tof), that is with a delay of typically $1 - 10\,\mathrm{ms}$ after turning off the trap in which the atoms are held. During this time the atomic cloud is allowed to expand freely. After a sufficient tof, the measured density distribution reflects the initial distribution in momentum space rather than the spatial distribution of the atoms.

In situ imaging of all but the most dilute atomic clouds on the other hand is challenging because of the high optical densities involved and the limits of dynamic range of cameras as well as spectral purity of the imaging light. In cases where this is desired, special techniques like phase-contrast imaging are usually employed. This is not required in the experiments presented in this thesis though.

4.8.1. Atom Numbers

If only the atom number is required, it is sufficient to integrate the determined density over the remaining two dimensions within a region of interest by summing the values of all pixels. This can be done either for the whole sample or for several clouds that have been spatially separated, e.g. in the case of a Stern-Gerlach type experiment (see section 5.1.5) or Kapitza-Dirac scattering (see section 5.1.6).

4.8.2. Fitting

Further information can be extracted by nonlinear fitting of the expected density profiles to the density distribution. In the case of thermal clouds, this is a Gaussian and the quantity of interest is the cloud with. With either knowledge of the trap frequency (or the assumption that the tof is sufficient for the contribution of the clouds spatial extent to be negligible) or from a series of images with different tofs, the temperature of the sample can then be determined.

At the onset of quantum degeneracy, a bimodal momentum distribution emerges [182]. Here fitting the sum of a Gaussian distribution for the thermal fraction and a Thomas-Fermi distribution for the condensate fraction allows the determination of the condensate fraction and the temperature of the thermal fraction (if any).

4.8.3. Defringing

In practice, imperfections in the imaging beam path usually lead to the presence of interference fringes in the image. As long as neither the perturbing scatterers in the imaging beam path nor the laser frequency change between the absorption image and the bright reference image, these will cancel when calculating the optical density. If the fringes change between the two pictures, they will show up in the calculated optical density and degrade image quality. To minimize this effect, the principal component analysis can be used to reduce the contribution of fringes to the final image [183, 184].

We assemble a large collection of reference images into the matrix $\mathbf{M}$, with each row containing all pixel values of one reference image. Singular value decomposition – in our case performed by the python function *scipy.linalg.eigh* – of this matrix

$$\mathbf{M} = \mathbf{U}\mathbf{\Sigma}\mathbf{V}^{\dagger} \tag{4.2}$$

yields the left and right singular vectors $\mathbf{U}$ and $\mathbf{V}$ as well as the diagonal matrix Σ containing the corresponding eigenvalues.

The left singular vectors $\mathbf{U}$ form an orthonormal basis of the vector space spanned by the available background images. For each independently shifting set of fringes, this basis will contain a pair of images with a phase shift of $\frac{\pi}{2}$ between them. Other images may contain sources of incoherent stray light. Remaining images consist of noise and can be discarded. The dimension of the resulting vector space is much lower than of that spanned by all possible images - it only spans the variations of the laser beam and background light and we do not risk modifying the actual absorption signal.

Using the projection operator $\mathbf{U}\mathbf{U}^{\dagger}$ each absorption image $\vec{I}_{\text{abs}}$ is now projected onto this vector space to create the image

$$\tilde{\vec{I}}_{\text{bright}} = \mathbf{U}\mathbf{U}^{\dagger}\vec{I}_{\text{abs}}, \tag{4.3}$$

which contains only those features from image $\vec{I}_{\text{abs}}$ which can be described using the available reference images. If a suitable set of reference images is chosen, this image reproduces all fringes with the phases and amplitudes matching the absorption image and thus serves as the optimal reference image for this image.

4.8.4. Imaging systems

The science chamber is equipped with two imaging systems used for absorption imaging. A schematic representation of the views provided by the two cameras is shown in Figure 4.21.

In the horizontal plane either species can be imaged with an effective pixel size of $7.2\,\mu\text{m}$ and a field of view of $10\,\text{mm} \times 8\text{mm}$ (with the longer axis oriented vertically to allow for long times of flight) on a cooled CCD camera (*Apogee Ascent A285*).
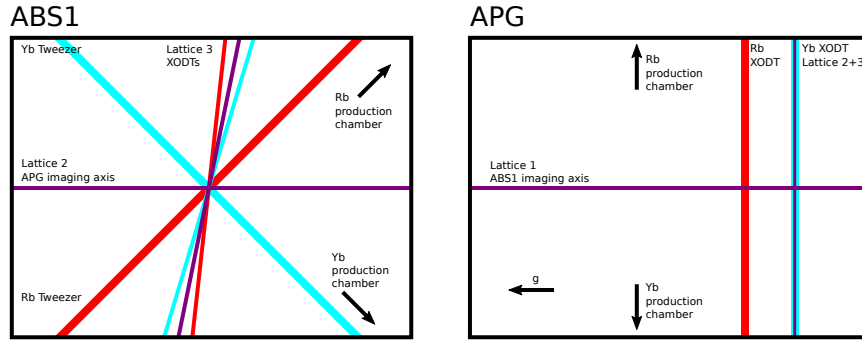
Figure 4.21.: Schematic representations of the field of view for the *ABS1* camera in the vertical imaging system and the *Apogee* camera in the horizontal imaging system, as shown by the camera program (i.e. mirrored and rotated with respect to the actual view from the camera locations) and the rough location of the relevant trapping beams.

In order to be able to image both Rb and Yb without the need to refocus, this lens system is specially designed to compensate for chromatic aberration between 400 nm and 780 nm. The system is based on two achromatic doublets (N-BK7 and N-SF5, *Edmund Optics VIS-NIR*) with a broadband AR coating covering both wavelengths. However, as the lenses are designed to minimize chromatic aberration over the visible range, and our wavelengths are located at its edges, a substantial focal length shift remains. An additional N-BK7 singlet is placed on the image side of the system, correcting for the residual difference in focal length. The optical axis is also vertically offset with respect to the CCD chip center, to allow the best imaging performance for in-situ imaging while also extending the field of view as far down as possible, allowing for imaging after long times of flight.

A second imaging system (which is normally only used for imaging of Rb, but still performs well enough for Yb to be very useful for the alignment of optical traps) is installed along the vertical axis. In addition to allowing the simultaneous detection of Rb and Yb on separate cameras, this extra angle is very useful for the alignment of optical traps. This setup uses a simple industrial CCD camera (*ABS UK1117*) and has an effective pixel size of 11 μm and a field of view of 8 mm × 6 mm.

5.

Preparation

This chapter deals with the preparation of ultracold samples of Rb and Yb. The individual steps for the preparation are described in section 5.1 for Rb and in section 5.2 for Yb, each culminating in the production of a Bose-Einstein-condensate.

Finally, section 5.3 will discuss how these sequences can be combined and extended by a merging step, producing an ultracold Rb-Yb mixture, which serves as a starting point for the experiments described in the following chapters.

5.1. Rubidium

After being emitted by the oven, Rb atoms are decelerated in a Zeeman slower and then accumulated in the MOT in the Rb production chamber. Once a sufficient number of atoms has accumulated in the MOT a dark spot phase is used to efficiently transfer the atoms to the magnetic quadrupole trap, where forced microwave evaporation is performed. Finally, the atoms are transferred into the optical tweezer and moved to the science chamber, where final evaporative cooling is performed in a crossed dipole trap. The phase space trajectory for the entire preparation cycle of Rb is plotted in Figure 5.1.

5.1.1. Magnteo-optical trap

At the start of the sequence, the MOT is loaded at a magnetic field gradient of $\mathrm{d}B/\mathrm{d}z = 15\,\mathrm{G/cm}$ and a laser detuning of $\Delta = -3\,\Gamma$. After a loading time of $8\,\mathrm{s}$, several 10^9 atoms have accumulated and the slower beam is switched off.

Compression and Dark Spot phase

In order to reach a higher density and improve mode matching to the magnetic trap, the magnetic gradient is then linearly ramped up to $44\,\mathrm{G/cm}$ over $30\,\mathrm{ms}$. Due to light assisted collisions and the high opacity of a compressed MOT, this compression alone would lead to substantial heating [185, 186]. Therefore, the laser detuning is ramped to $-9\,\Gamma$ at the same time. This reduces the scattering rate and enables sub-Doppler Sisyphus cooling [187], where the relevant energy scale is given by the light shift induced by the laser and thus temperature decreases with increased detuning magnitude. During this step, the repumper component of the MOT beams is switched off and the *dark spot repumper* is turned on. In
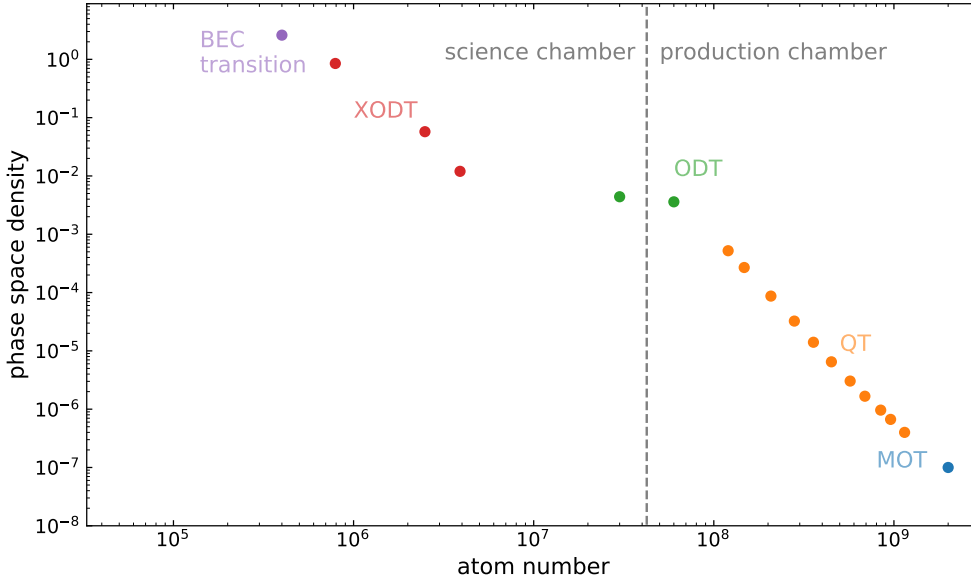
Figure 5.1.: Phase space trajectory for the preparation of a Rb BEC. The corresponding figure for Yb is Figure 5.9.

the dark spot configuration [188, 189], atoms near the trap center are not illuminated by repumping light. They enter the *dark* $F = 1$ manifold – which happens by off-resonant excitation to other F' states roughly every two thousand scattered photons – and remain there. Only once they diffuse out of the dark spot volume, they are pumped back to the $F = 2$ manifold and experience cooling and trapping forces again.

This approach dramatically reduces the scattering rate as well as light induced collisions and the opacity of the MOT, leading to lower temperatures and higher densities than those achievable in a bright MOT.

5.1.2. Quadrupole trap and microwave evaporation

The dark spot stage marks the last stage of dissipative cooling in the experimental cycle. In the following steps, atoms are held in conservative traps and any further cooling occurs by evaporation [115]. For Rb, efficient evaporative cooling can be performed in a magnetic trap. In this case we employ the most basic magnetic trap geometry, consisting of a quadrupole field just like the one needed for the MOT, the quadrupole trap (QT) [190].

As the magnetic trap gradient at the end of the dark spot phase exceeds the gradient required to hold the atoms against gravity, and they are already prepared in the desired $F = 1$ manifold, the magnetic trap can be loaded by simply turning off the MOT beams. The atoms in the $|F = 1, m_F = -1\rangle$ state are now trapped in the QT, while those in other substates are lost.
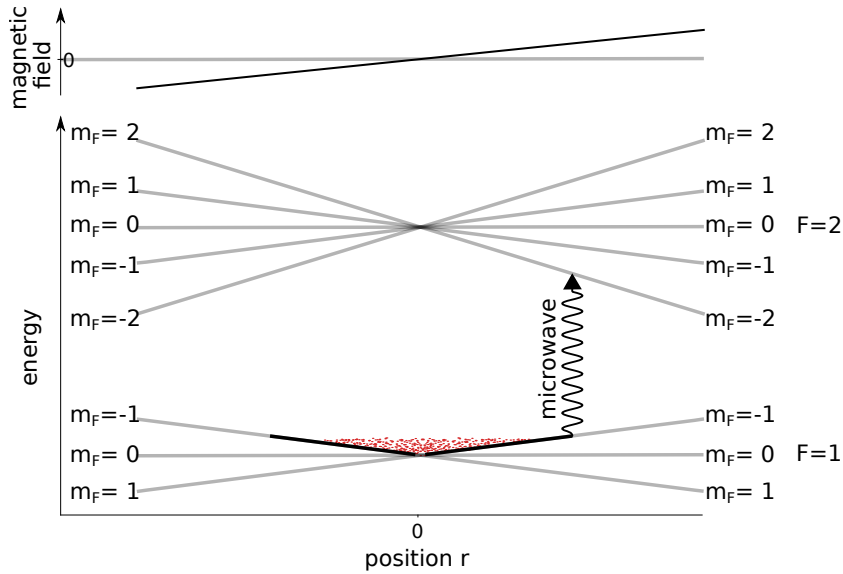
Figure 5.2.: Schematic representation of microwave driven evaporation from the quadrupole trap in the $|F = 1, m_F = -1\rangle$ state. The hyperfine splitting is not to scale.

The magnetic field gradient is then ramped up to its maximum value of $290\,\mathrm{G/cm}$ in $1\,\mathrm{s}$ in order to increase the collision rate by adiabatic compression [115]. At the end of this ramp, the QT contains 10^9 atoms at a temperature of $0.5\,\mathrm{mK}$.

Forced evaporation is performed by using microwave radiation [191] to drive the transition from the trapped $|F = 1, m_F = -1\rangle$ state to the anti-trapped $|F = 2, m_F = -2\rangle$ state as illustrated in Figure 5.2. In contrast to RF evaporation, where atoms are first transferred to the magnetically insensitive $|F = 1, m_F = 0\rangle$ state, this actively removes the hot atoms from the trap volume after absorbing a single microwave photon. The microwave detuning is linearly ramped from $120\,\mathrm{MHz}$ corresponding to an effective trap depth of $k_B \cdot 2\,\mathrm{mK}$ to $20\,\mathrm{MHz}$ corresponding to a trap depth of $k_B \cdot 0.3\,\mathrm{mK}$ in $5.3\,\mathrm{s}$.

During the microwave evaporation the tweezer beam is already on at a reduced power of $8\,\mathrm{W}$. At higher powers the optical trap would be deep enough to keep some $|F = 2, m_F = -2\rangle$ atoms trapped and thus prevent efficient evaporative cooling. After a final holding step of $0.5\,\mathrm{s}$, the quadrupole trap contains $1.8 \cdot 10^8$ atoms at a temperature of $44\,\mathrm{\mu K}$. Further evaporative cooling in the quadrupole trap is limited by the onset of Majorana flips [185]. Although this could be avoided through a hybrid trap [192], an optical plug [193] or a different magnetic trap geometry [194, 195], we transfer the atoms to optical traps at this point in preparation for their transport to the science chamber.

5.1.3. Optical dipole trap and transport

The atoms are transferred from the magnetic trap to the optical trap by ramping the quadrupole field to zero over $1\,\mathrm{s}$. This expands the atom cloud adiabatically and improves
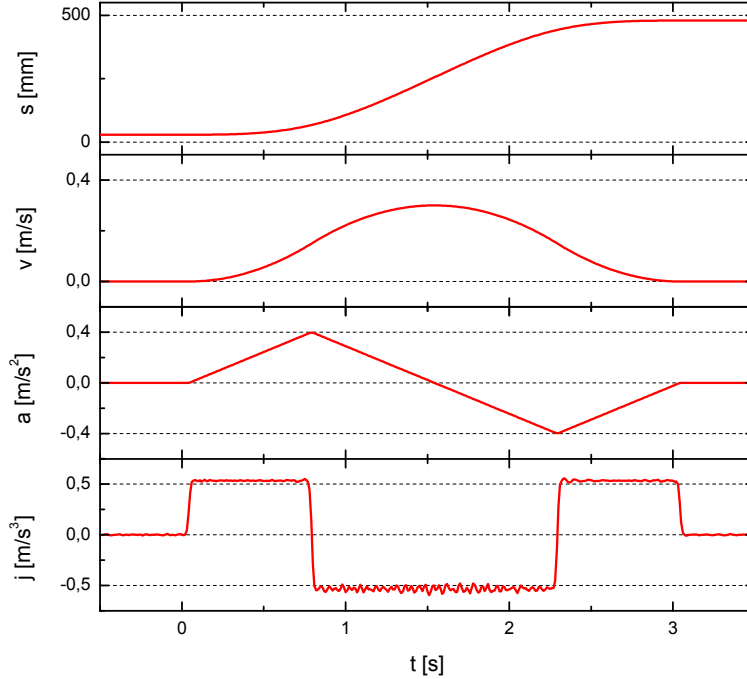
Figure 5.3.: Typical minimum-jerk motion profile used for the Rb tweezer translation stage. A very similar profile with slightly different parameters is used for Yb. Position and its derivatives are obtained from in-loop measurements of the stage controller.

mode matching to the optical trap while performing further evaporative cooling at the same time. Simultaneously the tweezer power is increased to 16 W. We typically obtain $7 \cdot 10^7$ atoms at $30\,\mu$K in the optical trap with a lifetime of $30(1)\,$s.

At this point the atoms are transferred from the production chamber to the science chamber by axially translating the optical trap. The distance of 450 mm is covered in 3 s following a minimum-jerk trajectory with a peak acceleration of $0.3\,$m/s², as shown in Figure 5.3. The transport speed is limited by the relatively low axial trap frequency of $\omega_z \approx 2\pi \cdot 4\,$Hz. The initial acceleration [1] of the trap causes a small additional loss of atoms, after which we experience no additional losses beyound the trap lifetime during the transport. Care has to be taken to maintain a sufficient magnetic bias field throughout the transport to maintain the sample polarised in the $|F = 1, m_F = -1\rangle$ state.

While the transport is straightforward in principle, a number of pitfalls were encountered

---

[1]Earlier we observed large losses when passing the weld of the reentrant viewport. While the chamber is made from 316L steel with very low magnetism, this is not necessarily preserved during the welding process and it may have become magnetized. Curiously the situation improved after an (accidental) overheating of the nearby coil.

during its realization. At first the use of a single frequency laser led to the formation of a parasitic lattice by reflection from a viewport (see section 3.1.3). In response to this the laser was replaced by a multimoded laser, which led to issues with the atom lifetime likely caused by accidental driving of photoassociation and Raman transitions (see section 3.1.3), which we found to be significantly reduced by choosing the polarization of the trapping light parallel to the magnetic field direction and operating the laser at a pump current where its spectral width is still relatively small.

5.1.4. Crossed optical dipole trap and Bose-Einstein condensation

Once the atoms arrive in the science chamber, they are transferred to the crossed optical dipole trap (XODT). Because of the weak axial confinement, evaporation in a single beam optical trap is rather inefficient due to the rapid further loss of confinement and the resulting decrease in collision rate when reducing the trap depth. While a crossed dipole trap, unlike a magnetic trap, still suffers from a reduction of confinement during evaporation, it provides strong initial confinement in all directions and thus allows for efficient evaporative cooling [196].

The transition from the single beam trap to the XODT is performed by ramping up the power of the crossing beam over 0.2 s using a cubic ramp function, while simultaneously reducing the tweezer power to 10 W.

Forced evaporation is then performed by ramping down the power of the tweezer beam, leading to a proportional reduction in the crossed beam power. The evaporation ramp follows the function

$$P(t) = P_i \left(1 + \frac{t}{\tau} \right)^{-3.5}, \tag{5.1}$$

which is designed to keep the truncation parameter $\eta = \frac{\hat{U}}{k_B T}$ constant during evaporation [197]. The time constant τ is optimized experimentally, with the typical value being $\tau = 6$ s. Note that the derivation for this ramp does not hold for low powers, where gravity significantly changes the trapping potential and the trap depth is thus not proportional to the beam power anymore. The ramp time depends on the desired final Rb temperature.

A final holding time of 0.5 s allows the sample to reach thermal equilibrium at the end of the evaporation ramp. Absorption images of a Rb cloud for various final trap powers and the corresponding density profiles illustrating the formation of a Bose-Einstein condensate (BEC) are shown in Figure 5.4. Starting from a thermal cloud with a gaussian density distribution, a bimodal distribution with a dense central peak emerges, until in the end only the Thomas-Fermi distribution of the condensate is discernible. Another telltale sign of a BEC is the – in this case slight – anisotropy of the resulting cloud, stemming from the fact that the expansion of a BEC is driven by interactions, leading to anisotropic expansion from an anisotropic trap, unlike the thermal cloud where expansion is driven by the isotropic thermal momentum distribution.

Using this procedure, we routinely produce Rb BEC of $3 \cdot 10^5$ atoms with no discernible thermal fraction in the $|F = 1, m_F = -1\rangle$ state.
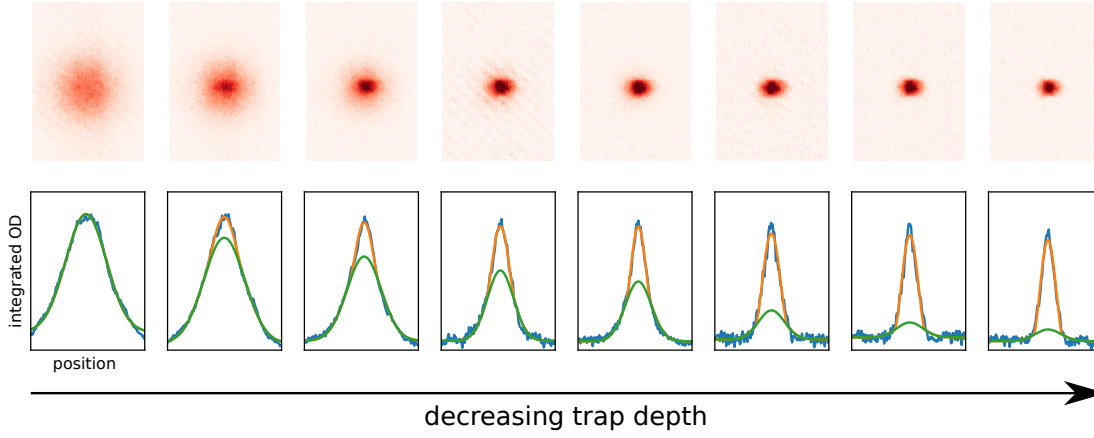
Figure 5.4.: False color absorption images of the Rb cloud at different stages of evaporation, showing the transition from an almost purely thermal cloud to a BEC of $3 \cdot 10^5$ atoms with no discernible thermal fraction. The lower row shows the extracted density profile with bimodal fit, showing the gaussian component in green and the sum in orange.

5.1.5. Hyperfine state manipulation

An additional degree of freedom for the Rb atoms is given by the hyperfine and Zeeman states of its ground state. By our magnetic trap loading process the atoms are prepared almost exclusively in the $|F = 1, m_F = -1\rangle$ state, which is conserved in the optical traps by application of a magnetic bias field. Transitions into other states can be driven by the application of microwave fields, and the resulting distribution can be analyzed by Stern-Gerlach type experiments, as will be described in the following.

Rabi pulses

A straightforward way to change the hyperfine state is to apply a microwave pulse resonant with the desired transition. This leads to Rabi oscillations [198] between the states involved, as shown in Figure 5.5a. The Rabi frequency Ω_R is given by

$$\Omega_R = \frac{2\mu_B}{\hbar} \left\langle F, m_F \right| \hat{J} \cdot \hat{B} \left| F', m_F' \right\rangle, \tag{5.2}$$

with the electron spin operator $\hat{J}$ and the magnetic field $\hat{B}$. Typical Rabi frequencies in our system are in the range $\Omega_R = 2\pi \cdot 1...6\,\text{kHz}$.

This technique has the advantage of allowing the preparation of arbitrary superpositions, however it is quite sensitive to external influences, particularly the background magnetic field. For example pulses need to be synchronized to the 50 Hz line cycle as background fields in the lab have a significant component at this frequency.
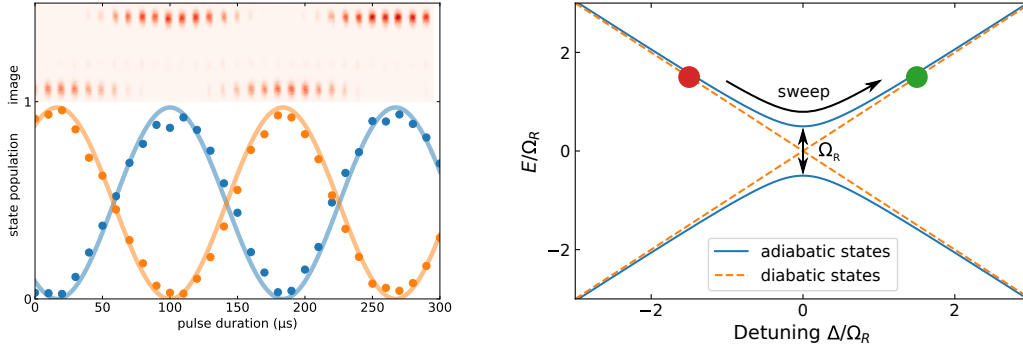
Figure 5.5.: Transfer between Rb hyperfine states using the microwave system: **(a)** Microwave driven Rabi oscillations between the $|F=1, m_F=-1\rangle$ and $|F=2, m_F=-2\rangle$ states in Rb, with a Rabi frequency of $\Omega_R = 6$ kHz. The top panel shows a composite image of the absorption images for each timestep, with the hyperfine states being spatially separated using the Stern-Gerlach technique. Below the extracted population of each state is plotted together with sinusoidal fits. **(b)** Schematic representation of a Landau-Zener sweep, achieving complete population transfer from an origin state (red) to a target state (green) by sweeping over the resonance while applying a coupling of strength $\hbar\Omega_R$.

Landau Zener sweep

A more robust way of transferring atoms to a different hyperfine state is to perform a Landau Zener sweep [199, 200], also known as rapid adiabatic passage (RAP), illustrated in Figure 5.5b. Here, the system is slowly ramped over the resonance, while the microwave couples origin and target state and thus induces an avoided crossing.

For two states which are connected by the perturbation Hamiltonian H', in our case the microwave coupling, the probability [200] of adiabatic following from state 1 to state 2 is then given by

$$P = 1 - e^{-2\pi\Gamma}, \qquad \text{with } \Gamma = \frac{|\langle 1| H' |2\rangle|^2}{\hbar \frac{\mathrm{d}E}{\mathrm{d}t}} = \frac{\hbar\Omega_R^2}{\frac{\mathrm{d}E}{\mathrm{d}t}} . \tag{5.3}$$

Provided the ramp characterized by $\frac{\mathrm{d}E}{\mathrm{d}t}$ is slow with respect to the coupling strength given by the Rabi frequency Ω_R, which is easily achievable in this case, this leads to practically complete transfer to the target state.

For technical reasons we typically realize this by ramping the magnetic bias field while keeping the microwave frequency constant. As the amplitude of this ramp is significantly larger than that of the line related magnetic field, this scheme does not require synchronization to the mains cycle and is much more robust than Rabi pulses.

Stern-Gerlach

The distribution of Zeeman states can be detected by performing a Stern-Gerlach type experiment. Here a magnetic gradient is applied during the *time of flight* phase, leading

to a state dependent force $F_{\mathrm{SG}} = m_F g_F \mu_B \nabla B$ and thus – after some time – a spatial separation of the different states. This allows the population of different hyperfine states to be imaged independently, as is shown in Figure 5.5a. Note that the $F = 1$ and $F = 2$ states of ^{87}Rb have gyromagnetic ratios g_F of the same absolute value, but opposite sign [55], and are thus deflected in opposite directions for the same value of m_F.

The hyperfine state can be determined by the imaging sequence: As our imaging scheme is based on a cycling transition originating from the $F = 2$ manifold, atoms in the $F = 1$ can only be detected if a repumping pulse – either optical or microwave [2] – is applied prior to the imaging pulse.

Magnetic Field Calibration

In addition to allowing the preparation of Rb in the desired internal state, the microwave system also provides a convenient means to precisely calibrate the magnetic field at the location of the atoms. By measuring the transition frequency of a transition and comparing to the well known [55, 201, 202] splittings and magnetic shifts of the states involved, the actual magnetic field can be determined to high precision.

5.1.6. Optical Lattice

After the atoms have been prepared in the XODT, they can be transferred to the optical lattice for further experiments if desired. While optical lattices offer rich dynamics of their own [5] they will be used here as just another type of optical trap. We will therefore only give a very brief introduction to the world of optical lattices at this point.

The Hamiltonian for a 1D lattice of potential depth V_0 – neglecting interactions which will be introduced in Equation 9.1– is given by

$$\left(-\frac{\hbar^2}{2m} \frac{\mathrm{d}^2}{\mathrm{d}x^2} + \frac{V_0}{2} \cos\left(2kx\right) \right) \psi(x) = E\psi(x) . \tag{5.4}$$

The energy scale of an optical lattice is given by the recoil energy $E_R = \frac{\hbar^2 k^2}{2m}$ and the lattice depth is commonly expressed by the dimensionless parameter $s = V_0/E_R$.

For a shallow lattice, the appropriate eigenfunctions are given by the Bloch waves [203], fulfilling the relationship

$$\Psi_{n,q}\left(x + \lambda/2\right) = \exp\left(\frac{i\lambda q}{2\hbar}\right) \Psi_{n,q}\left(x\right), \tag{5.5}$$

where $-\hbar k < q \leq \hbar k$ is the quasi-momentum and n the band index. The emerging bandstructure is shown in Figure 5.6. Starting from the parabolic dispersion relation of a free particle, band gaps develop and eventually the discrete spectrum of (approximately) a harmonic oscillator emerges.

---

[2]Note that these two approaches have different outcomes: an optical repumper will transfer all atoms to the $F = 2$ manifold, while a microwave sweep will swap populations between states of the $F = 1$ and $F = 2$ manifolds.
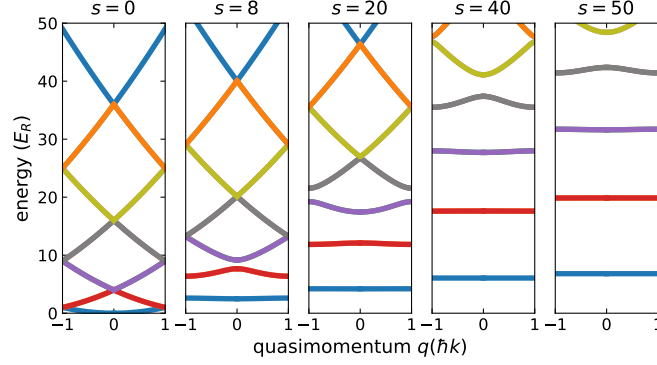
Figure 5.6.: Bandstructure for different lattice depths $s = V_0/E_R$ showing the evolution from a free particle to bound states approaching the energies of an harmonic oscillator. Bandstructures are obtained from the characteristic value of the Mathieu equation [204].

In the tight binding model [205] corresponding to large lattice depths atoms are localized to individual lattice sites, with their wavefunctions given by the Wannier functions [206]. Movement between the lattice sites is possible by tunneling. The tunneling amplitude t_1 for the lowest band is given by

$$|t_1| = \frac{J}{E_R} = \frac{4}{\sqrt{\pi}} s^{\frac{3}{4}} \exp\left(-2\sqrt{s}\right). \tag{5.6}$$

When an external acceleration a such as gravity is applied to atoms trapped in the lowest band of an optical lattice, they are not accelerated out of the lattice but remain trapped and undergo so called Bloch oscillations with $\omega_B = \frac{ma\lambda}{2h}$.

There is however a probability r for them to tunnel into a higher band and eventually leave the trap at the turning points of this oscillation, which for a shallow lattice is given by [5, 199]

$$r = \exp\left(-\frac{V_0^2 d}{16\hbar^2 a}\right), \tag{5.7}$$

where $d = \frac{\lambda}{2}$ is the lattice period. This process is however strongly suppressed even at modest lattice depths.

Kapitza-Dirac scattering

When the lattice is pulsed on for a short time t we obtain so called Kapitza-Dirac scattering [207], which can be imagined as the diffraction of the atomic matter wave at the grating created by the optical lattice.

Kapitza-Dirac scattering is often used to calibrate lattice depths [208], as it gives a direct connection between the lattice depth in units of E_R and the time evolution of the populations of the momentum states, which is easily accessible in the experiment by measuring atom numbers in different regions after a time-of-flight as shown in Figure 5.7.
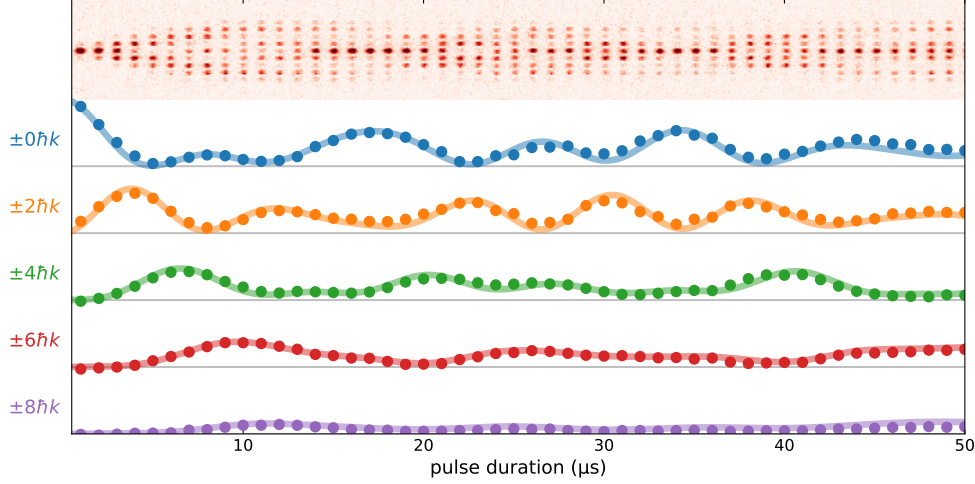
Figure 5.7.: Kapitza-Dirac scattering at a lattice depth of $s = 75$. The top row shows the sequence of absorption images taken at different pulse lengths. Below, the relative population of each momentum component is plotted. Points are experimental data extracted from the image on top, while the lines represent a numerical solution to Equation 5.8.

Applying Equation 5.4 to discrete states with momentum $2n\hbar k$ and complex amplitudes $c_n(t)$ where $n = -n_{\max}..n_{\max}$ we obtain a set of coupled differential equations [208]

$$i\frac{\mathrm{d}c_n}{\mathrm{d}t} = \frac{n^2\,4\,E_R}{\hbar}c_n + \frac{V_0}{4\hbar}\left(c_{n-1} + 2\,c_n + c_{n+1}\right) \tag{5.8}$$

which can be solved numerically and compared to the measured populations $p_n = |c_n|^2$.

Conservation of energy dictates that the highest populated momentum state is $n_{\max} = \sqrt{\frac{V_0}{4\,E_R}}$ [208], where the potential energy corresponding to the lattice depth is completely converted into kinetic energy, already giving a rough estimate of the lattice depth from a Kapitza-Dirac sequence at a first glance.

An example of Kapitza-Dirac scattering is given by the measurement shown in Figure 5.7, where a lattice with a depth of $V_0 = 75E_R$ has been pulsed on for varying durations and the momentum distribution was measured by imaging after a time-of-flight. The complex time evolution of the populations of the individual momentum states is obviously well explained by the numerical solution to Equation 5.8.

Note that for lattice depth calibration one would often use a much shorter sequence, where the Raman-Nath approximation can be applied and Equation 5.8 is solved by the Bessel functions of the first kind.
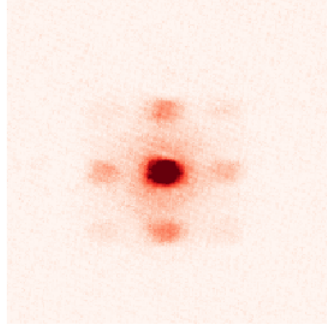
Figure 5.8.: Absorption image of the diffraction patten created by releasing atoms from a 2-dimensional optical lattice.

Adiabatic loading

If the atoms are to be trapped in the optical lattice for the purpose of further experiments, a distribution over many bands as is caused by the sudden turn on in Kapitza Dirac scattering is usually highly undesirable. Instead the goal is usually to load the atoms into the lowest band. This can be achieved either by evaporating the atoms into the lattice [209] – in which case the possibility of the lattice preventing the collisions needed for evaporation has to be considered –, or by first completing evaporative cooling and then adiabatically turning on the lattice.

The criterion for adiabatic loading into the lowest band can be shown [210] to be $\frac{\mathrm{d}V_0}{\mathrm{d}t} \ll \frac{16\,E_R^2}{\hbar}$. While this is usually easy to fulfill, it only ensures adiabacity with respect to the lattice band structure. If the lattice is not applied in all three dimensions, adiabacity with respect to the change in confinement in the other directions has to be considered. If for example a Mott insulator is to be created, the ramp also has to be adiabatic with respect to the timescale of the interactions [210].

When a BEC is adiabatically loaded into a lattice and then released, a diffraction pattern like that shown in Figure 5.8 for a 2D lattice forms due to the interference between the matter waves from each individual lattice site.

5.2. Ytterbium

The preparation of Yb atoms follows a similiar path to that of Rb, with the main difference being that trapping and evaporation in a magnetic trap is not feasible due to the small magnetic moment of its $^1S_0$ ground state. Instead, the narrow intercombination line allows the Yb MOT to reach a similar phase space density to that reached for Rb using microwave evaporation. The resulting phase space trajectory is shown in Figure 5.9.

5.2.1. MOT

The first and longest step in the preparation of Yb is the loading of the intercombination line MOT. While the narrow linewidth of $2\pi \cdot 182\,\text{kHz}$ allows achieving high phase space densities in the MOT, this is paid for by a low capture velocity and consequently long loading times.

Loading of the Yb MOT is performed at a magnetic gradient of $3\,\text{G/cm}$ and a detuning of $-10\,\Gamma$ for typically $25\,\text{s}$. Even though the slower beam is far detuned from atoms at rest at the MOT position, it exerts a significant pushing force in the MOT, which is partially compensated by offsetting the magnetic field.

After a sufficient number of atoms – typically $3 \cdot 10^7$ atoms for ^{170}Yb – has accumulated, the slower beam is turned off and the resulting MOT shift is compensated by a corresponding change in offset fields. A wait time of $0.4\,\text{s}$ prevents interference with the following steps.
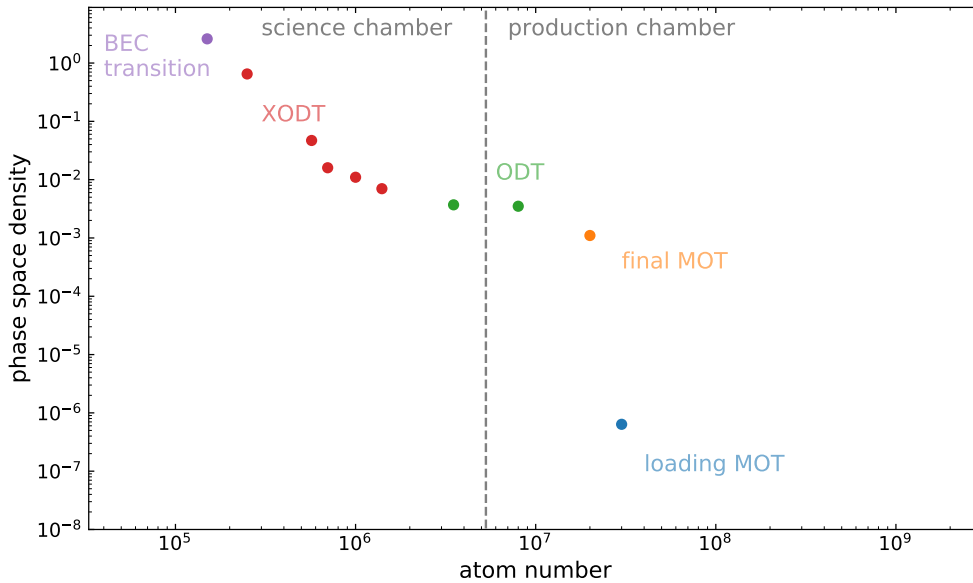
Figure 5.9.: Phase space trajectory for the preparation of an Yb BEC. Note the scale is the same as used in the corresponding figure for Rb (Figure 5.1).
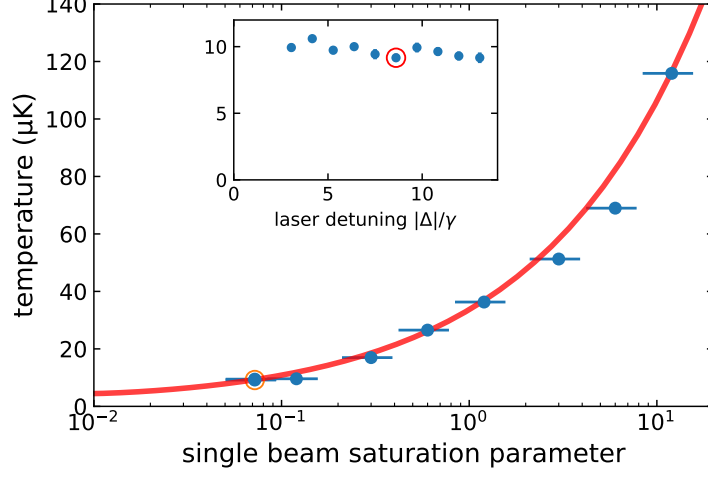
Figure 5.10.: Measured dependence of the Yb MOT temperature on the intensity and on the laser detuning (inset). The solid line shows the expected behavior from Equation 5.10 up to a horizontal scaling factor of $\frac{1}{2}$. This figure has previously appeared in [129].

After the initial loading MOT, which is optimized for the highest possible loading rate, but neither particularly dense nor particularly cold, parameters are changed to realize a compressed MOT, which reaches a high phase space density but would not be able to capture any atoms from the Zeeman slower. First, the magnetic gradient is linearly increased over $0.1\,\mathrm{s}$ to $19\,\mathrm{G/cm}$ in order to spatially compress the MOT. This limits the temperatures reachable in the following steps, but is nonetheless beneficial because it leads to better mode matching between the MOT and the optical trap.

The intensity is then linearly ramped down from $\sim 90\,I_{\mathrm{sat}}$ to $\sim 0.5\,I_{\mathrm{sat}}$ (per beam) over $0.5\,\mathrm{s}$. This leads to a reduction in temperature and to a change in MOT shape as illustrated in Figure 5.11. For $^{170}\mathrm{Yb}$, $2 \cdot 10^7$ atoms at $21\,\mathrm{\mu K}$ are typically achieved at this stage.

The narrow linewidth also has consequences for the dynamics of the MOT [133, 211]. As the ratio between the optical and gravitational forces $R = \frac{\hbar k \Gamma}{2mg} \approx 478$ is comparatively small, gravity plays a significant role when operating the MOT at low intensities. The MOT then sags until the light forces are sufficient to hold the atoms against gravity, leading to an effective detuning [211] of

$$\frac{\Delta_{\mathrm{eff}}}{\Gamma} = -\frac{\sqrt{Rs - s' - 1}}{2}, \tag{5.9}$$

where $s = \frac{I}{I_s}$ [3] is the saturation parameter and $s' > s$ accounts for saturation induced by the beams along the other two axes. Applying standard Doppler cooling theory the resulting

---

[3]The saturation parameter s used in this section is not to be confused with the lattice depth in units of recoil energies used elsewhere in this thesis and also denoted by s.
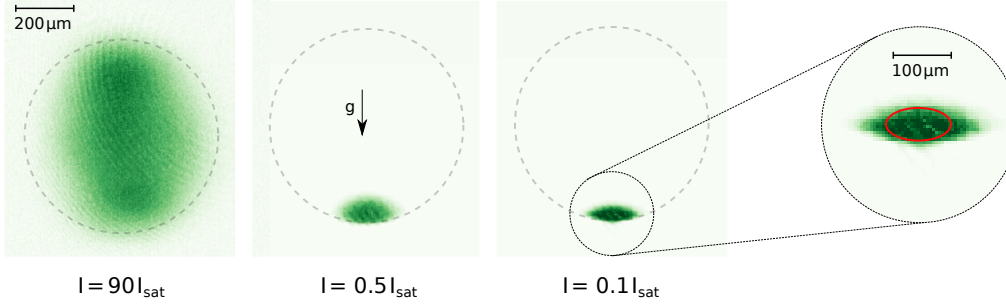
Figure 5.11.: False color absorption images of the Yb MOT operated at three different intensities. The dashed circle indicates a contour of constant magnetic field. While this volume is roughly filled with atoms at high intensity, they sink to the bottom at lower intensities. The detail shows the MOT shape around the time where transfer to the optical trap occurs, with the optical trapping beam indicated by the red contour.

temperature is

$$
T = \frac{\hbar\Gamma}{2k_B} \cdot \frac{R\sqrt{s}}{2\sqrt{R - s'/s - 1/s}},
\tag{5.10}
$$

which depends on the intensity only and is independent of the laser detuning over a wide range.

Figure 5.10 shows that the achieved temperatures follow this behavior up to a scaling factor of $\frac{1}{2}$ in the intensity, which can be explained by polarization imperfections and the fact that the laser linewidth is not negligible compared to the atomic linewidth in our case.

Finally, the transfer to the optical trap is achieved by reducing the MOT intensity to zero over $0.3\,\mathrm{s}$, providing a smooth loading of the optical trap.

Aside: Momentum Crystals

When the MOT laser is stepped to a blue detuned frequency after compression of the MOT, a peculiar phenomenon shown in Figure 5.12 can be observed: instead of being cooled to a velocity distribution centered around zero momentum, the atoms are concentrated into *momentum packets* or bunches with a velocity of

$$
v = \frac{1}{k}\left(\Delta + \frac{\Gamma}{2}\sqrt{s(R-1)-1}\right)
\tag{5.11}
$$

along each axis [211]. In images taken after a time of flight, as shown in the figure, this results in atom clouds situated at the corners of a cube. The bunches in the upper layer appear more compact in the images and indeed, these are effectively cooled in the process [211].

While this effect is not of much use for our purposes, it may be used as a diagnostic tool to determine the laser detuning.

Δ=-1Γ   Δ=4Γ

increasing detuning Δ
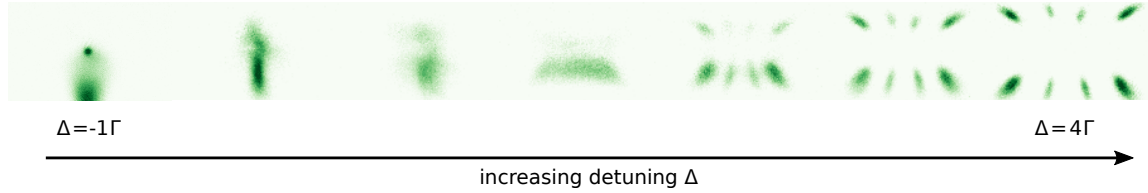
Figure 5.12.: Absorption images of the Yb cloud as the crystallisation pulse is tuned over the resonance, showing the progression from a MOT (with a falling cloud of uncaptured atoms) to the formation of a momentum crystal where the atoms are concentrated into eight distinct momentum packages.

5.2.2. Optical trap and transport

In order to obtain a good starting point for evaporative cooling in the science chamber, the initial atom number is of great importance. It is thus worth some effort to optimize the transfer from the compressed MOT to the optical trap.

A further increase in the MOT atom number, e.g. by increasing the MOT loading time unfortunately does not significantly lead to more atoms in the ODT, as the MOT is density limited at this point and only the increase in MOT cloud size along the axial direction translates into more atoms in the capture volume.

As illustrated in the last panel of Figure 5.11, the MOT assumes an oblate shape when sagging under gravity during the last phase while the optical trapping beam has a round cross section. In order to improve transfer efficiency to the ODT, the tweezer beam shape is matched to the MOT shape using the trap painting setup described in subsection 4.2.5. As shown in Figure 5.13, this doubles transfer efficiency compared to the unshaped round beam. For large modulation amplitudes the transfer efficiency decreases again due to the finite available laser power resulting in decreasing trap depth.

Due to the weak confinement provided by the optical trap in axial direction, mode matching between MOT and ODT is not feasible for this axis. However, the slow turn off of the MOT beams allows the atoms to slowly expand along the beam. Using these measures, we typically achieve a transfer efficiency of $50\,\%$ between the compressed MOT and the optical trap, yielding $1 \cdot 10^7$ atoms at $30\,\mu K$. In order to maximize the axial trap frequency during transport to the science chamber, trap shaping is then adiabatically turned off over $0.1\,s$.

The transfer to the science chamber happens in a similar way to Rb here. Due to the lower polarizability of Yb at the trap wavelength and the resulting difficulty achieving a high axial trap frequency, some loss has to be accepted here, with only $\sim 4 \cdot 10^6$ atoms arriving in the science chamber.

5.2.3. Crossed Dipole Trap (XODT) and Bose-Einstein condensation

As for Rb, once the atoms have arrived in the science chamber, they are transferred to a crossed dipole trap in order to facilitate further evaporative cooling. For the data presented
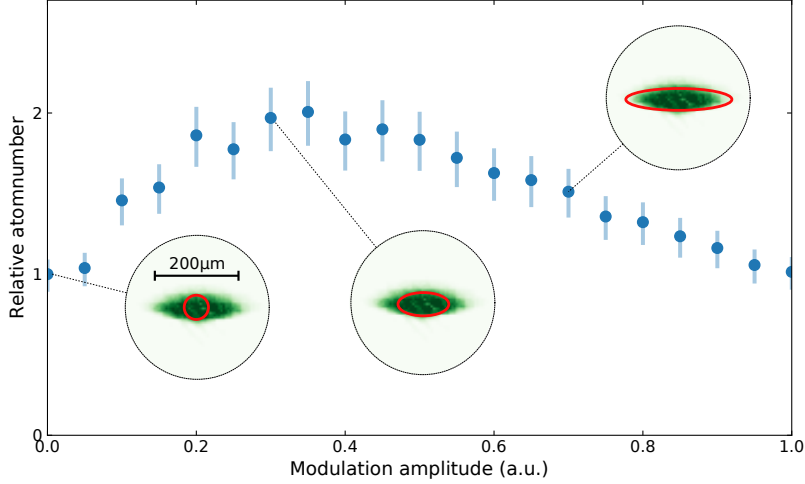
Figure 5.13.: Dependence of the atomnumber loaded into the optical trap on the modulation amplitude and thus horizontal trap size. The insets show absorption images of the Yb MOT shortly before transfer, with the respective beam shapes indicated in red.

in this section, the crossing is formed between the Yb and Rb tweezer beams. For the experiments in subsection 5.3.1 and the following chapters, the dedicated Yb crossing beam described in subsection 4.6.1 will be used instead. Again, all evaporation ramps follow Equation 5.1, with a typical time constant of $\tau = 10\,\mathrm{s}$ which is significantly longer than for Rb due to the slower thermalization rate caused by lower trap frequencies and the smaller intra-species scattering length of $64\,a_0$ for ^{170}Yb, compared to $100\,a_0$ for ^{87}Rb. Particularly the onset of evaporation, where the atoms first need to be collected from the wings of the trap into the crossing, is slower than in the case of Rb. To achieve this as quickly as possible, in the first evaporation step only the power of the Yb tweezer is ramped down to $6\,\mathrm{W}$ in $3\,\mathrm{s}$ while the Rb tweezer is held at full power. Note this is only possible when using the Rb tweezer as an independent crossing beam, while in the usual setup the crossing beam always has less power than the first beam. At the end of this initial evaporation ramp, 10^6 atoms are trapped in the crossing with the wings mostly empty. From here on, the power of the Rb tweezer is ramped down proportionally to that of the Yb tweezer. Absorption images taken from the last portion of this evaporation at decreasing trap depth are shown in Figure 5.14.

Starting with a circular thermal cloud in the first image, the formation of a Bose-Einstein condensate can be clearly seen as the formation of a dense, elliptical cloud in its center. In this case, unlike previous attempts to condense ^{174}Yb in the old machine [74], both the bimodal distribution and anisotropic expansion provide clear evidence of Bose-Einstein condensation. As evaporation progresses, the thermal fraction shrinks and the condensate grows, finally resulting in a BEC of $2 \cdot 10^4$ atoms with no discernible thermal fraction.
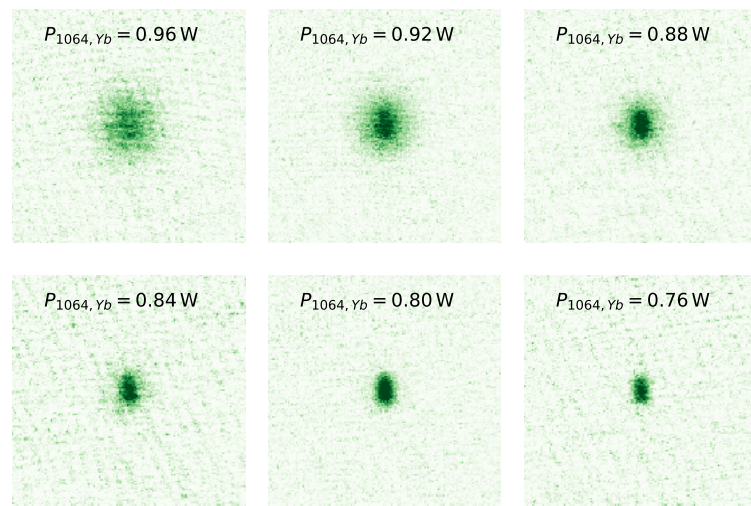
Figure 5.14.: False color absorption images of the ^{170}Yb cloud at different stages of evaporation, showing the transition from an almost purely thermal cloud to a BEC of $2 \cdot 10^4$ atoms with no discernible thermal fraction.

5.3. Combined preparation of Rb and Yb

The previous sections have shown that both species can be cooled to ultracold temperatures and even to quantum degeneracy in our new apparatus with the methods presented. The next step is the creation of an experimental sequence that can achieve this for both species at the same time (or with a time difference that can be bridged by storing one species in a trap for some time) in order to finally create a mixture of Rb and Yb, which forms the starting point for photoassociation experiments.

The separate production chambers for each species allow many preparation steps to be performed independently and in parallel. For example, we can perform microwave evaporation of Rb in the quadrupole trap and simultaneously load an intercombination line MOT of Yb, which would be impossible in a single vacuum chamber due to the huge difference in the magnetic gradients required for these traps.

However, the final evaporation steps in crossed optical traps have to be performed in the science chamber for both species, as performing them in the production chambers would not only increase the demands on the heating tolerable during transport, but also require the atoms to be transfered back into the single beam traps for transport to the science chamber, which is hard to do adiabatically due to the low axial trap frequencies. As all optical traps currently in use operate at 1064 nm, where the trap depth for Rb is about ten times higher than for Yb, simultaneous evaporation in one trap would lead to all Yb being sacrificed while cooling Rb.

When attempting to use two XODTs in the same plane, the two spatially separated XODTs will communicate through their wings. Due to the strong difference in trap depth, this results in the Yb trap – which needs higher intensities to achieve a comparable trap depth – capturing most atoms from the Rb trap. Similarly, attempts at sympathetic cooling are impractical due to the low interspecies scattering rate of the chosen combination of ^{87}Rb and ^{170}Yb and again would result in all Yb atoms being sacrificed due to the relatively low trap depth of Yb, combined with a high heating rate for Rb.

We thus align both tweezers and their crossing beams at different vertical positions in addition to a horizontal offset, so no additional crossings appear along a given beam. At the end of the evaporation, Rb is transferred to the vertical 1d lattice and moved to the plane of the Yb trap using the lattice elevator (see section 4.6.2). This preparation sequence and the merging of both traps will be described in subsection 5.3.1. Finally, subsection 5.3.2 will explore different trapping configurations for the photoassociation experiments.

5.3.1. Mixture

The sequence begins by just loading the Yb MOT, as in the case of ^{170}Yb the cycle time for Yb is significantly longer than that needed for Rb. While the Yb MOT is still loading, the Rb MOT loading and microwave evaporation are performed. Despite this taking place in separate vacuum chambers, the strong magnetic stray fields produced by the quadrupole trap strongly influence the low gradient Yb MOT, so care is taken to compensate for this using the compensation coils of the Yb chamber. To avoid any influence on the particularly
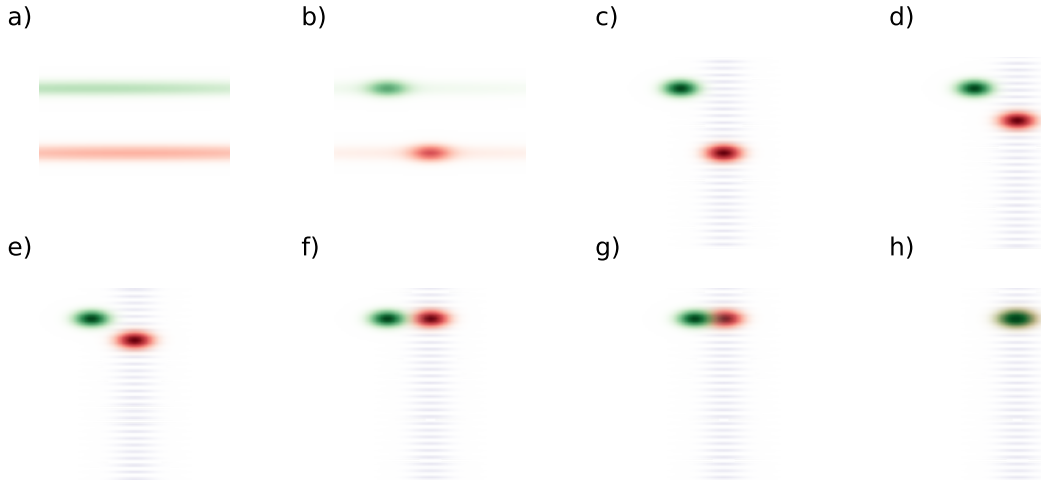
Figure 5.15.: Schematic illustration of the steps for the preparation of an RbYb mixture in the science chamber, showing simulated distributions of Rb (red) and Yb (green) atoms and a Schematic depiction of the vertical lattice beam (light purple). Other (running wave) trapping beams are omitted for clarity. **(a)** Both tweezers moved into science chamber.**(b)** Simultaneous evaporation in separated XODTs.**(c)** Rb is transferred to the vertical lattice.**(d,e)** Rb is elevated in the vertical lattice.**(g,h)** Merging Rb and Yb traps (see Figure 5.16).

sensitive step of transferring the atoms to the tweezer, this step is only performed after the quadrupole field has been turned off and Rb is in the optical trap and on its way to the science chamber.

The following sequence is schematically shown in Figure 5.15. Both species are transferred to the science chamber at approximately the same time, where forced evaporation in the independent XODTs is performed as described in the previous sections. Once evaporative cooling of the Rb atoms is completed, they are transferred to the vertical lattice, which is then translated upwards by $\sim 1\,\mathrm{mm}$ (see section 4.6.2) in order to bring them to the level of the Yb trap. The high density obtained when loading a BEC or a very cold thermal cloud of Rb into the 1D lattice leads to substantial three-body losses. We mitigate this effect and increase the cloud size before the transfer to the lattice by slightly defocussing the Rb tweezer using the translation stage used for the transport, thus spreading the Rb atoms over a larger number of pancake shaped lattice sites.

In addition to the vertical offset, the Yb XODT is also horizontally displaced from the Rb traps by about $0.2\,\mathrm{mm}$, ensuring the Yb cloud is not heated or even moved upwards during translation of the lattice.

As the Yb tweezer beam needs to be on at a substantial power to form the Yb XODT while Rb is being elevated, the Rb atoms experience some amount of compression and heating when they enter the Yb tweezer beam. For this reason, even though relatively low lattice powers are sufficient to hold the atoms against gravity and move them upwards,
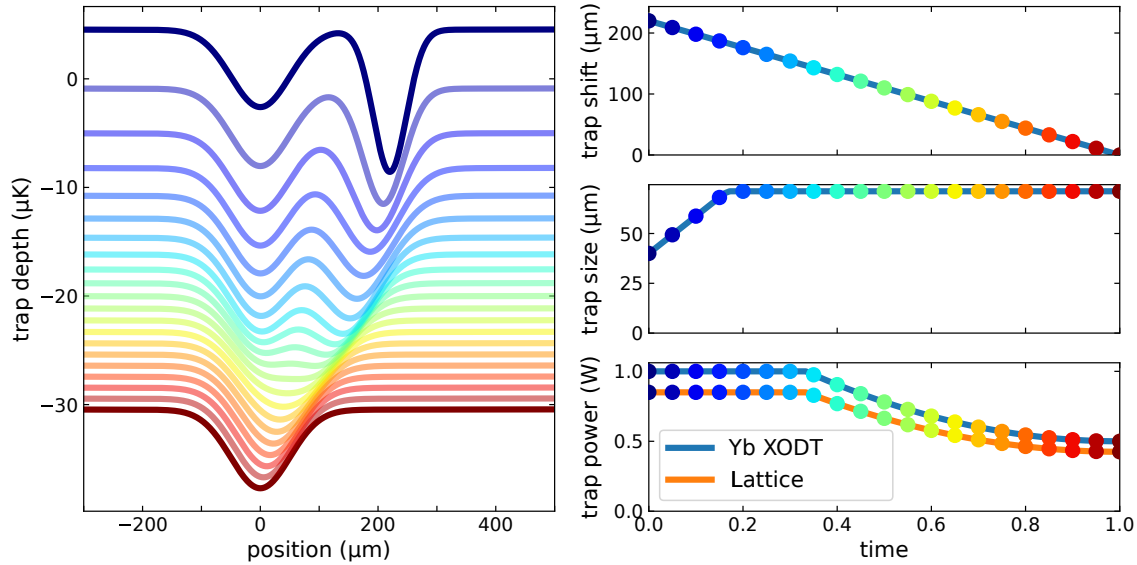
Figure 5.16.: Schematic depiction of the merging process. The left panel shows the evolution of the simulated potential (for Yb, with the potential for Rb differing only by a scaling factor in the trap depth) during the merge, plotted along the direction of the Yb tweezer beam. The individual timesteps are vertically offset, starting from the top, for clarity. For the lattice, the potential is plotted for the intensity maxima. The panels on the right show the evolution of the individual trap parameters during this sequence. The points corresponding to the potentials plotted in the left plot are marked and color coded accordingly.

the lattice power is linearly ramped up on the way up. Unfortunately the controller of the translation stage used here does not allow us to tailor the movement profile for this application beyond specifying maximum acceleration and velocity. Nonetheless, the atom number losses in the elevation step are negligible when it is performed with sufficient lattice beam power – which is required for the next step anyway.

We aim to adjust the timing so that both species are ready to be merged – that is the Yb evaporation has finished and Rb has finished evaporation and arrived at the Yb level – at the same point in time. However, to compensate for small changes during optimization of the evaporation sequences a holding step waiting for the slower of the two evaporation processes is inserted before loading Rb into the lattice.

Merging the traps

After the Rb atoms have been lifted up using the vertical optical lattice, Rb and Yb atoms are both located along the Yb tweezer beam, in crossed dipole traps formed with the vertical lattice beam (for Rb) and the Yb XODT beam (for Yb). As both traps also influence the other species, care has to be taken to merge these traps without causing excessive loss or heating in either species [212–216]. The merging process used is illustrated in Figure 5.16.

In order to quasi-adiabatically[4] merge these traps it is advantageous to first match their trap depths and shapes – or more quantitatively their phase space volume – as closely as possible [216]. This is achieved by increasing the Yb beam size using the trap shaping mechanism described in subsection 4.2.5 to match the waist of the lattice beam. The lattice beam power is chosen to achieve approximately equal trap depths for the lattice and the Yb tweezer beam.

The two traps can then be overlapped by changing the Yb XODT position using its AOM frequency. In order to keep the trap depth constant during the merge and avoid further compression, the powers of both the lattice and the Yb tweezer beam are simultaneously decreased by a quadratic ramp to half their initial power.

If only one of the beams were ramped down to zero power instead or the trap depths and trap shapes are not balanced for the merge, this would lead to the formation of a "shelf" in the potential, from which one species would spill into the other well, leading to a release of potential energy and thus heating for this species [213, 215].

Once the merge is completed, the XODT beam powers and the lattice beam powers are ramped to their final values, depending on the desired trap – a choice which will be discussed in the following sections.

5.3.2. Final trap

Most of the experiments presented in the following chapters where performed in the Yb XODT, without any lattice potentials present, so we will take a closer look at this trap configuration first, before exploring the additional opportunities offered by optical lattices.

Crossed Optical Dipole Trap

To perform experiments in a bulk trap, the optical lattice is ramped off after the merge is completed. For the final trap, the trap depth is still ten times higher for Rb than for Yb. The most important consequence is that this, in combination with the non-negligible heating rate induced by the multi-mode trap laser and the three-body collisions Rb experiences at the high densities in the vertial lattice, makes it hard to get Rb nearly as cold as Yb.

In fact, for a given trap geometry the cloud size for a thermal cloud depends only on the ratio between its temperature and the trap depth, not on the absolute value of the trap depth or the particle mass. While our approach leads to unequal temperatures, it thus still ensures good spatial overlap between the species, at least for sufficiently deep traps.

Following the sequence described above, we typically end up with $3 \cdot 10^5$ Yb atoms at a temperature of $1.5\,\mu\text{K}$ and $2 \cdot 10^5$ Rb atoms at a temperature of $10\,\mu\text{K}$. The calculated trap frequencies along the principal directions of the trap are $\omega_{\text{Yb}} = 2\pi \cdot (80\,\text{Hz}, 250\,\text{Hz}, 260\,\text{Hz})$ and $\omega_{\text{Rb}} = 2\pi \cdot (0.35\,\text{kHz}, 1.1\text{k}\,\text{Hz}, 1.1\,\text{kHz})$, resulting in estimated peak densities of $n_{\text{Yb}} \approx 1 \cdot 10^{13}\,\text{cm}^{-3}$ and $n_{\text{Rb}} \approx 2 \cdot 10^{13}\,\text{cm}^{-3}$ respectively with phase space densities of $\sim 10^{-2}$ for both species. When the trap depth is reduced further, gravitational sag of the Yb cloud becomes an issue. This is illustrated by comparing the position of both clouds for different

---

[4]The process is not strictly adiabatic due to the different contents of each trap, making it irreversible,
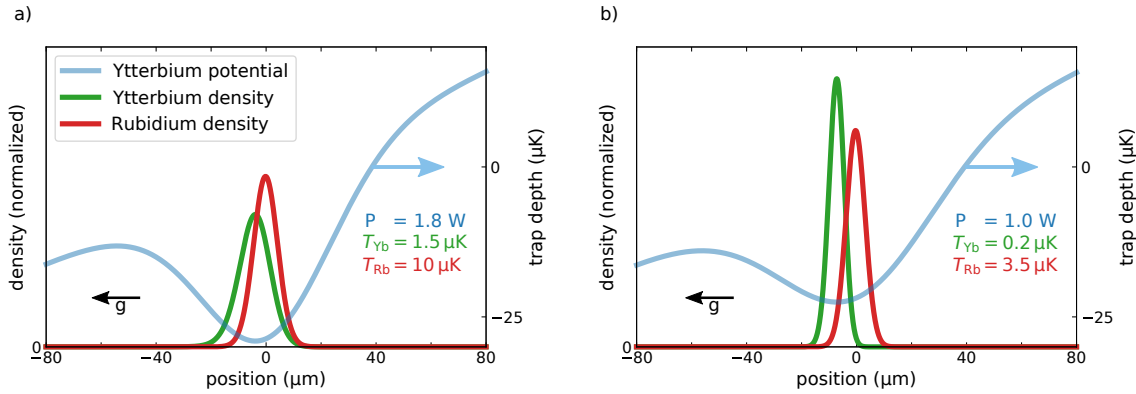
Figure 5.17.: Simulated thermal density profiles for both species (a) for a typical final trap and (b) for reduced trap depths and thus temperatures, plotted along the vertical direction. The sum of trapping and gravitational potential for Yb is also shown for reference.

trap depths as shown in Figure 5.17. The significantly lower trap frequency experienced by Yb, combined with its higher mass, leads to a sag under gravity which is significantly larger than for Rb. In the first situation shown in Figure 5.17a, which corresponds to a typical starting point used for the experiments described in the following chapters, both clouds are still well overlapped, despite the sag of Yb already being noticeable. For the reduced trap depth shown in Figure 5.17b, there is already noticeably less overlap. At the position of the peak of the Rb density, which would give the largest photoassociation rate in our case, the Yb density now almost drops to zero. Gravitational sag thus imposes a lower limit on the temperatures where we can perform photoassociation or interaction experiments in the 1064 nm XODT.

Another consequence of gravity is that the disparity in trap depth between the species becomes even larger at low trap frequencies, as the effective trap depth of Yb is significantly reduced as the trap is tilted by gravity. Attempting to do a final evaporation step after merging the traps is thus doomed to fail, as the trap rapidly loses its ability to hold Yb atoms against gravity while the Rb trap depth is hardly reduced.

While the XODT already provides a good starting point for our photoassociation experiments, optical lattices provide several advantages for the further development of the experiments. We will thus discuss the use of various lattice configurations in the following.

1-dimensional optical lattice

In the simplest configuration, the vertical lattice beam is simply left on after the merge and the horizontal beams are not being used. This trap can be visualized as a vertical stack of pancake shaped traps. The distribution of atoms over the trapping sites is determined by the cloud size at the point of transfer to the lattice, that is at the end of the evaporation ramp for Rb and when the traps are merged for Yb. Tunneling between the lattice sites rapidly decreases with increasing lattice depth (see Equation 5.6). For example the tunneling rate

for Rb is already reduced to below $10\,\mathrm{Hz}$ by a lattice with $s = 14$. In the vertical direction, tunneling is even further suppressed by the fact that gravity shifts the states in neighbouring lattice sites out of resonance [217]. There is thus practically no redistribution of atoms between the lattice sites. A major advantage of this configuration is that the gravitational sag of Yb is prevented by the lattice and the sag experienced at the instant of merging can be compensated for by adjusting the distance the Rb cloud is moved before Yb enters the lattice.

At first glance, the increase in local density due to the lattice will increase photoassociation rates. However a lattice with sufficient depth to suppress tunneling prevents the redistribution of atoms after a possibly selective atom loss. For an imperfect overlap between both species this would mean that only lattice sites with a sufficient density of the other species experience heteronuclear photoassociation, and the total loss is limited by the presence of atoms with no available reaction partner.

Another effect that has to be taken into account when using a 1D (or 2D lattice) is the change in collision behavior due to the additional confinement. In the extreme case of $\hbar\omega_z \gg k_B T$ the lattice dimension is frozen out and only 2D collisions are possible. But the collisional dynamics and thus the photoassociation rates are already altered by the lattice at much higher temperatures [76, 218].

2 and 3-dimensional Lattice

While the addition of more lattice beams to the final trap would significantly increase the local density and thus enhance photoassociation rates where a partner is available, the issue of lattice sites populated by only one species or the depletion of the minority species on a site populated by many atoms, will become worse.

In order to effectively make use of higher dimensional lattices, more advanced preparation techniques than adiabatic loading of the present thermal clouds will thus have to be used. The ideal approach would be to prepare a mixed Mott insulator [219] state, ensuring the population of each site with a heteronuclear pair. While the implementation of this is beyond the scope of this work, we will briefly discuss the concept in section 9.3.

Another perhaps even more important advantage of a 3D lattice as a starting point for photoassociation is the fact that the separated atoms are already present in discrete bound states rather than a continuum, which has important consequences for the line strength of photoassociation lines and especially for 2-photon photoassociation and the prospect of free-bound STIRAP, as we will see in chapter 8 and section 9.5.

6.

Intercombination Line Photoassociation of ^{170}Yb$_2$

Before we embark on the search for RbYb photoassociation lines near the $^2S_{\frac{1}{2}} + {}^3P_1$ asymptote, it is convenient to test our apparatus by performing Yb$_2$ photoassociation near the $^1S_0 + {}^3P_1$ asymptote, which is located at the same energy and thus accessible with the same laser system. This case is experimentally much simpler than the photoassociation of RbYb, as spatial overlap between photoassociation partners is not an issue with homonuclear molecules and there is no need for an elaborate sequence to prepare a mixture.

Also, the positions of a few lines were already known from experiments in the Takahashi group [75, 77], allowing for verification of our results and boosting confidence in the early stages of the search.

Despite this motivation, the investigation of the excited states of Yb$_2$ is not just a toy problem. The theoretical modeling of these states is challenging due to a high number of correlated electrons combined with significant relativistic and spin-orbit effects and subject of continued research [77, 220]. Results of further investigations will prove useful for the investigation of optical Feshbach resonances in Yb [77, 103, 221] and the search for a route to the absolute ground-state [222] of the Yb$_2$ molecule.

Last but not least, photoassociation spectroscopy is a powerful tool to precisely determine the dipole matrix element and thus the radiative lifetime of the excited state [91] using its connection to the C_3 coefficient (see Equation 2.4).

6.1. Experimental procedure

Our Yb$_2$ photoassociation spectroscopy journey was started in the scope of a master thesis [173]. Here the setup for the free-bound laser was established and the first seven of the lines presented in this chapter with binding energies up to $h \cdot 1.3\,\text{GHz}$ were measured in a pure Yb sample. Later additional lines were discovered in the course of the search for RbYb resonances (see chapter 7) – and of course thoroughly checked for any involvement of Rb. This chapter will attempt an analysis of the combined data from these measurements.

Figure 6.1 shows a schematic representation of the PA process. The atomic pair is excited from the scattering state with energy E_{therm} above the ground state potential to one of the bound states of the excited potential, in this case the 0_u^+-potential. A resonance occurs
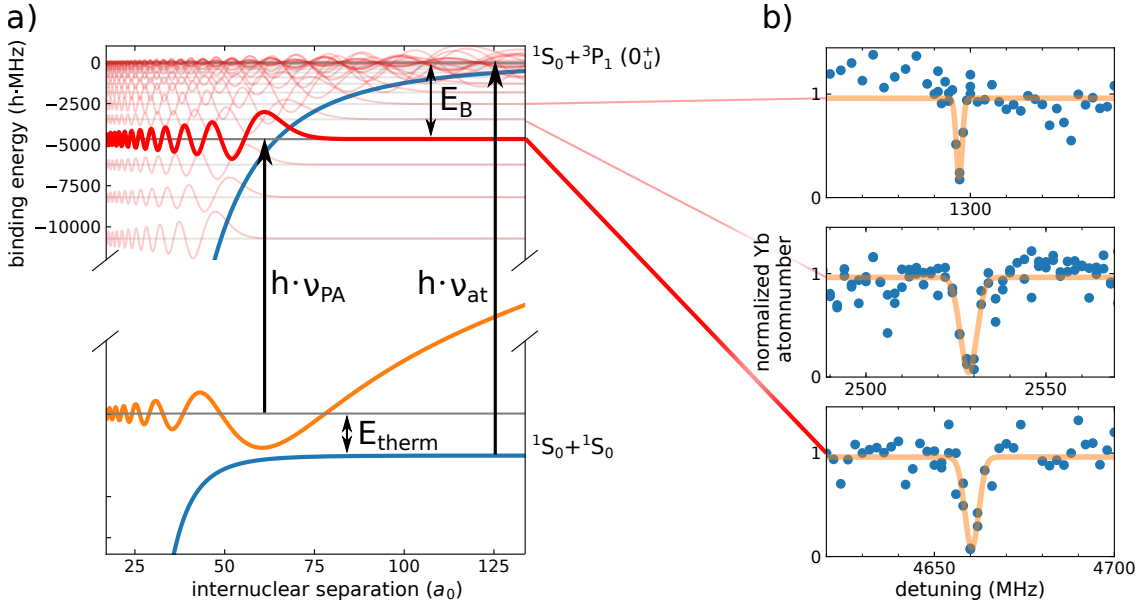
Figure 6.1.: **(a)** Schematic representation of the photoassociation of Yb$_2$ on the ^{2}S$_{\frac{1}{2}}$ + ^{3}P$_1$ asymptote showing the portions of the relevant potentials, wavefunctions and the relevant energies. Note the vast exaggeration of the thermal energy and the break in the y-axis. **(b)** Examples of recorded ^{170}Yb$_2$ photoassociation resonances, each shown with a gaussian fit to guide the eye.

when the detuning of the PA laser frequency ν_{PA} from the atomic line ν_{at} corresponds to the sum of the binding energy E_{B} and the kinetic energy of the unbound pair E_{therm}.

To perform 1-photon PA spectroscopy experiments a sample of ultracold Yb is prepared in an XODT as described in section 5.2 and section 5.3 and then illuminated by the free-bound laser for typically 1 s before the atom number is measured using absorption imaging. This is repeated many times while the laser frequency ν_{PA} is changed, building up spectra like those shown in Figure 6.1b. When the laser is resonant with a photoassociation line, a significant loss in atomnumber is detected.

While the sample is illuminated by the photoassociation laser, the laser frequency is linearly ramped over the stepsize rather than being stepped between the runs. This will increase the signal when the stepsize is larger than the effective transition linewidth and the transition is not aligned to the frequency grid of the scan – which certainly cannot be expected. In this case, sweeping the frequency will increase the worst case signal by a factor on the order of the ratio between stepsize and linewidth.

Despite the relatively low atomic transition linewidth of $\gamma = 2\pi \cdot 182\,\mathrm{kHz}$ and the modest intensities achieved by our free-bound laser, the trap lifetime is severely limited by off-resonant scattering on the atomic transitions when detuned less than $\sim 4\,\mathrm{GHz}$ from the resonance, so PA time and/or intensity need to be reduced significantly when measuring in this region. While this of course also reduces the photoassociation rate, all lines belonging

to the 0_u^+ potential in the scanned range were detected with a good signal level[1].

As most of the data presented here has been extracted from relatively coarse scans (typically 1 MHz resolution), in contrast to the detailed treatment in [77] we make no effort to analyze the detailed lineshapes. The main contribution to our experimental uncertainty thus stems from the determination of the line center and is about 2 MHz. However, a couple of other shifts and uncertainties will be briefly considered in this section.

The first one stems from the fact that the photoassociation process does not start with two separated atoms at zero energy, but with a finite thermal energy E_{therm}. This results in both a shift corresponding to the mean collision energy and a broadening corresponding to the spread of collision energies. This is easy to quantify by measuring the temperature of the sample using a *time of flight* series. For a homonuclear collision the mean collision energy is then given by $E_{\text{therm}} = \frac{3}{2}k_B T \approx h \cdot 0.03$ MHz for typical conditions and in our case the thermal shift of the photoassociation line is thus not relevant at this level of precision.

Light shifts will be introduced by the trapping lasers as well as by the photoassociation laser. The trap laser light shift will be on the order of 0.5 MHz for a typical trap used here. However it is not expected to significantly differ between the photoassociation lines and the atomic line, which is used for calibration, so it will be cancelled to a large degree. The probe lightshift is estimated to be on the order of 0.1 MHz for the worst case, that is the smallest detuning where we operate with full laser power.

For completeness the density shift as estimated by the mean field shift [223]

$$\Delta E_{\text{mf}} = \frac{4\pi\hbar^2\, a\, n\, g^{(2)}(0)}{m} \tag{6.1}$$

is on the order of kHz for the densities experienced here and can thus also be neglected.

Additional effects that need to be considered are the laser stabilization, which due to the beatnote lock to the MOT laser (see section 4.5.1) is accurate at the 0.1 MHz level[2] and Zeeman shifts - which in our case are eliminated to first order by using π-polarization and thus probing the magnetically insensitive transition.

6.2. Yb$_2$ potentials at the ^{2}S$_{\frac{1}{2}}$ + ^{3}P$_1$ asymptote

A schematic overview of the potential energy curves of the ground and the lowest excited states (those corresponding to the ^{1}S$_0$ + ^{3}P$_{0,1,2}$ asymptotes) is shown in Figure 6.2. Note that only Morse potentials approximating the actual potential energy curves [224] are shown and the true potential energy curves will look very different [220].

For our Yb$_2$ photoassociation measurements we are interested in the states corresponding to the atomic states ^{1}S$_0$ + ^{3}P$_1$. Due to the ^{1}S$_0$ ground state only the excited Yb molecule contributes any angular momenta and the resulting molecular states are easy to construct.

---

[1] The lines at detunings smaller than 100 MHz were not attempted.

[2] The quality of the beatnote lock may be subtly degraded by near-orthogonal polarizations of the combined lasers or operation at the edge of a bandpass filter, so careful monitoring is necessary to actually achieve this level of performance.
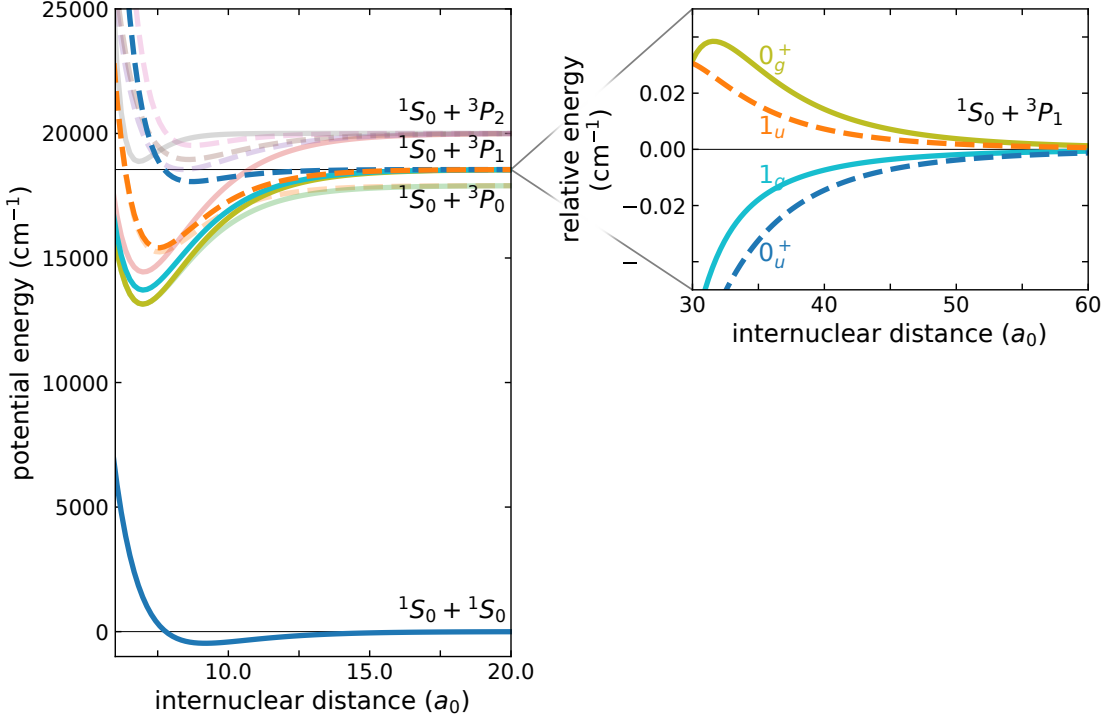
Figure 6.2.: Potential energy curves for the lowest electronic states of the Yb$_2$ molecule. Dashed (solid) lines represent potentials with *ungerade* (*gerade*) symmetry. The ground state and the four potentials corresponding to the $^1S_0 + {}^3P_1$ asymptote are highlighted. Short range potentials are Morse potentials using the spectroscopic constants from [224]. The detail shows the different long range behavior dominated by resonant dipole interaction.

Projecting the atomic total angular momentum $J = 1$ onto the molecular axis to obtain Ω results in either $\Omega = 0$ or $\Omega = 1$.

As both atoms involved are indistinguishable, the excitation is resonantly shared between both of them, leading to molecular states of the form

$$|\Psi_\pm\rangle = \frac{1}{2} \left(|{}^1S_0\rangle_A |{}^3P_1\rangle_B \mp |{}^3P_1\rangle_A |{}^1S_0\rangle_B \right), \tag{6.2}$$

where the subscripts A and B refer to the two atoms and the sign is reversed due to negative parity of the $^3P_1$ state itself. Each angular momentum state thus splits into two states $|\Psi_\pm\rangle$, labeled by their symmetry *gerade* and *ungerade*.

The possible long range states are 0_u^+, 0_g^+, 1_u and 1_g. As we are dealing with indistinguishable bosons, the scattering state necessarily has *gerade* symmetry, meaning photoassociation is dipole allowed only into the *ungerade* states due to the Laporte selection rule [225]. Photoassociation spectroscopy of *gerade* subradiant states has however been demonstrated at very high densities achieved through confinement in a 3D lattice [226] for Yb and in a 1D lattice for Sr [78]. The superradiant transitions to the *ungerade* states on the other hand exhibit twice the atomic linewidth and are thus relatively strong. These are the transitions

we are interested in here.

For all molecular states listed above the long range potential is dominated by the resonant dipole interaction, whose sign and magnitude depends on the symmetry and angular momentum of the state. Its magnitude is twice as large for the $\Omega = 0$ states, as the rotation in the $\Omega = 1$ states causes the interaction to partially average out [226]. It is attractive for the 0_u^+ and 1_g states, while the 0_g^+ and 1_u potentials are repulsive at large separations and only become attractive at short range, where the van der Waals interaction starts to dominate.

These potentials may still support bound states at short separations, but the resulting larger slope leads to a low density of bound states close to dissociation. In addition, these states will have their Condon points at short distances, leading to low overlap with the scattering state. Photoassociation resonances associated with them can thus be expected to be sparse and weak in the range explored here. For these reasons we are mainly interested in the 0_u^+ potential, which is both attractive at long range and superradiant, and thus promises a reasonable density of strong photoassociation resonances.

Due to the low temperature of $T \approx 1\,\mu\text{K}$ of our sample compared to the rotational barrier of $\sim 300\,\mu\text{K}$ [75] for the next lowest allowed partial wave, the d-wave, only s-wave collisions are relevant here. While even under these conditions the observation of photoassociation from higher partial waves has been described for ^{174}Yb due to the presence of a shape resonance [75], there is no such resonance in ^{170}Yb. We thus only observe photoassociation to $J_e = 1$ levels.

6.3. Theoretical modeling of the binding energies

Figure 6.3 shows the measured transition frequencies assigned to the 0_u^+ state together with a fit using the improved LeRoy-Bernstein formula (see section 2.2.5). The frequency range around the state labelled $\Delta\nu' = -20$ was not searched for experimental reasons and the absence of this line from the data does not necessarily indicate a weak transition. While for the first few lines a reasonable agreement can be obtained with the simple LeRoy-Bernstein formula (see section 2.2.5) for a pure C_3 potential [173], the more deeply bound levels are not well described by this model. For this reason the improved LeRoy-Bernstein formula allowing for an additional multipole expansion term is used. In this case the next largest contribution is given by the repulsive C_6 term. The short range parameter γ provided by the improved LeRoy-Bernstein formula is found to not improve the quality of the fit and thus set to zero. This reflects the fact that relative to the well depth which is of the order of 10 THz we are still dealing with very weakly bound levels, which are not very sensitive to the short-range behavior.

The lower panel of Figure 6.3 shows the residuals of the fit, demonstrating the binding energy is reproduced to the $0.1\,\%$ level for the most deeply bound states observed. Nonetheless, the residuals are still significantly larger than the error bars in our data and seem to follow a regular pattern. Possible reasons for deviations are the need for higher expansion terms (in [77] a C_8-term was introduced but claimed to be needed mostly to reproduce the $J = 3$
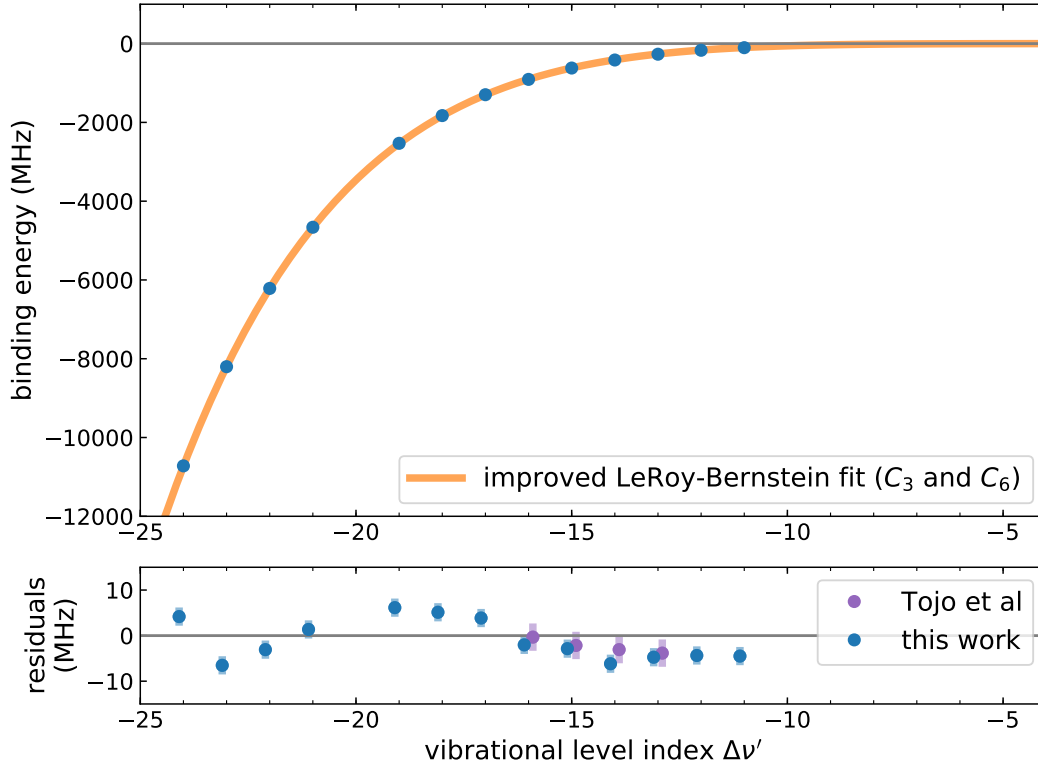
Figure 6.3.: Measured binding energies plotted as a function of the assigned level index. The solid line shows a fit with the improved LeRoy-Bernstein formula by Comparat (see section 2.2.5), with $C_3 = -0.186(1)\,E_h a_0^3$ and $C_6 = 2478(174)\,E_h a_0^6$. The lower panel gives the residuals of this fit. The binding energies measured by Tojo et al. [77] are also shown for reference with an artificial horizontal offset to avoid overlapping symbols.

states), the limitations of the (improved) LeRoy-Bernstein formula, possible perturbation of the 0_u^+ state by nearby levels of the 1_u state [77] or retardation effects [227, 228]. Some of these possibilities will be explored in the following.

It has to be noted that the resonant dipole interaction coefficient of $C_3 = 0.186(1)\,E_h a_0^3$ resulting from this fit – corresponding to a ^{3}P$_1$ lifetime of $\tau = 912(5)$ ns – disagrees with that found by previous experiments [77] ($C_3 = 0.1949(11)\,E_h a_0^3$, $\tau = 869.6(4.5)$ ns) as well as precision lifetime measurements that yielded $\tau = 866.1(7.4)$ ns [229]. Note that the errors given for the C_3 coefficients and derived lifetimes represent only the statistical error of the fit, and do not include errors arising from our choice of model. The likely explanation for the disagreement is thus the limited validity of the extended LeRoy-Bernstein formula for the more deeply bound states that we have observed.

To confirm this we restrict the fit to the levels bound by less than $h \cdot 5$ GHz and obtain a much more satisfactory fit with $C_3 = -0.1942(10)\,E_h a_0^3$ ($\tau = 873(4)$ ns) and residuals at the level of the experimental uncertainty.

Direct potential fit

Instead of using near-dissociation approximations like the LeRoy-Bernstein formula, we can also formulate a model potential and determine the bound states numerically by computing the eigenvalues of Equation 2.6. While this is computationally much more expensive than evaluating a near-dissociation approximation, it is nowadays feasible to perform a non-linear fit of the results of this computation to the experimental data. This is known as a *direct potential fit* [230].

Following the work in [77], we chose the model potential

$$V(r) = \frac{C_6}{r^6} \left(\left(\frac{\sigma}{r} \right)^6 - 1 \right) - \frac{C_3}{r^3} - \frac{C_8}{r^8}, \tag{6.3}$$

where the C_3, C_6 and C_8-terms give the three dominant orders of long-range interaction and the parameter σ allows for an adjustment of the phase arising from the short range potential. Note that this model potential is designed to reproduce the long range behavior only and the short range is likely to be far from correct.

Obviously this approach is a lot more flexible than the near-dissociation expansions. We could use an unlimited number of multipole terms rather than just one or two. If short-range potential energy curves are known from quantum chemistry calculations, they can be included by using a *switching function* that provides a smooth transition between short and long range behavior [231].

It is also straightforward to modify the model potential to take into account further effects. For example if we want to take into account relativistic effects and include retardation in our model [77, 227], the leading C_3 term is multiplied by

$$\cos (kr) + kr \sin (kr), \tag{6.4}$$

where k is the wavenumber. This flexibility is a great advantage of the DPF method.

In addition to the bound state energies this method will also generate approximate vibrational wavefunctions at little extra cost. Figure 6.4 shows the wavefunctions calculated for the states in the relevant energy range using a model potential of the form of Equation 6.3 with binding energies fitted to our experimental data. These wavefunctions may then be used to compute Franck-Condon factors and other properties of the bound states.

To give an overview over the results obtained using different methods, Figure 6.5 shows the residuals for the fit using the improved LeRoy-Bernstein formula and direct potential fits with and without retardation. Although they do not exactly match the experimental energies there is very good agreement between all fits for the states bound by less than $h \cdot 1\,\text{GHz}$. For the more deeply bound levels the direct potential fit gives slightly better results. The residuals are slightly reduced and exhibit less oscillation than for the LeRoy-Bernstein case. Especially the spacing between the two most strongly bound levels observed is reproduced much better by the direct potential fit method.

The fit with retardation results in $C_3 = -0.190(3)\,E_h a_0^3$ ($\tau = 892(13)\,\text{ns}$), giving reasonable agreement with the values mentioned in the previous section. However it is obvious from the residuals that this model still does not completely account for the measured binding energies. While the binding energies observed have been increased by nearly an order
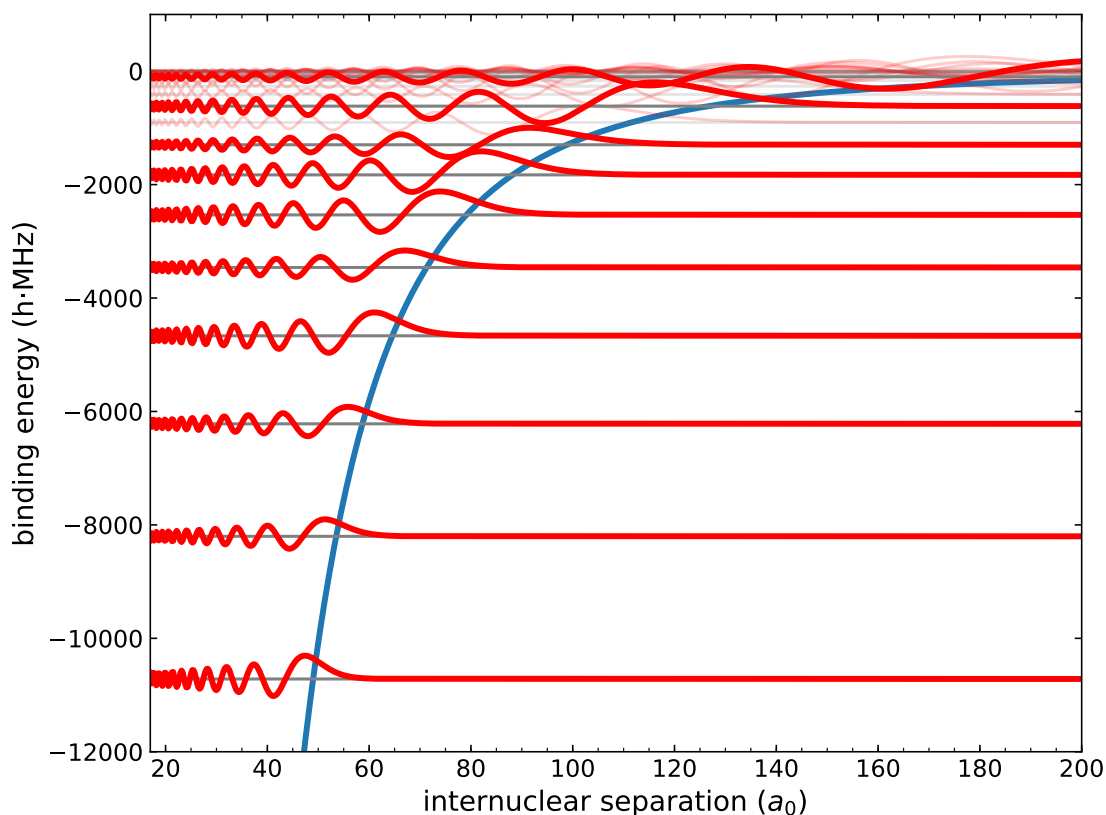
Figure 6.4.: Vibrational wavefunctions of the Yb$_2$ 0_u^+ state in the experimentally probed energy range as obtained by a numerical solution of the Hamiltonian. The model potential is of the form given in Equation 6.3 with the parameters obtained by a direct potential fit. Near the threshold only selected states are shown for clarity.

of magnitude compared to [77], retardation effects are still not readily observable. The fit shows slightly lower residuals, especially for the two most deeply bound levels when including retardation, but this is well within the experimental uncertainty and overwhelmed by effects which are apparently not accounted for by any of the fits.

6.4. Conclusion

Photoassociation resonances up to a binding energy of $h \cdot 10.7$ GHz were measured, extending the range by an order of magnitude compared to the previously known lines in ^{170}Yb and by a factor of five compared to the other more extensively explored isotopes [77].

The data can be explained to a reasonable degree through the improved LeRoy-Bernstein formula – especially when excluding the most deeply bound states. A *direct potential fit* allows a slightly improved description, especially for the most deeply bound states, but still does not account for the variation of the data to the level of the experimental uncertainty. Thus our results hint at the presence of retardation effects, which should become more clear
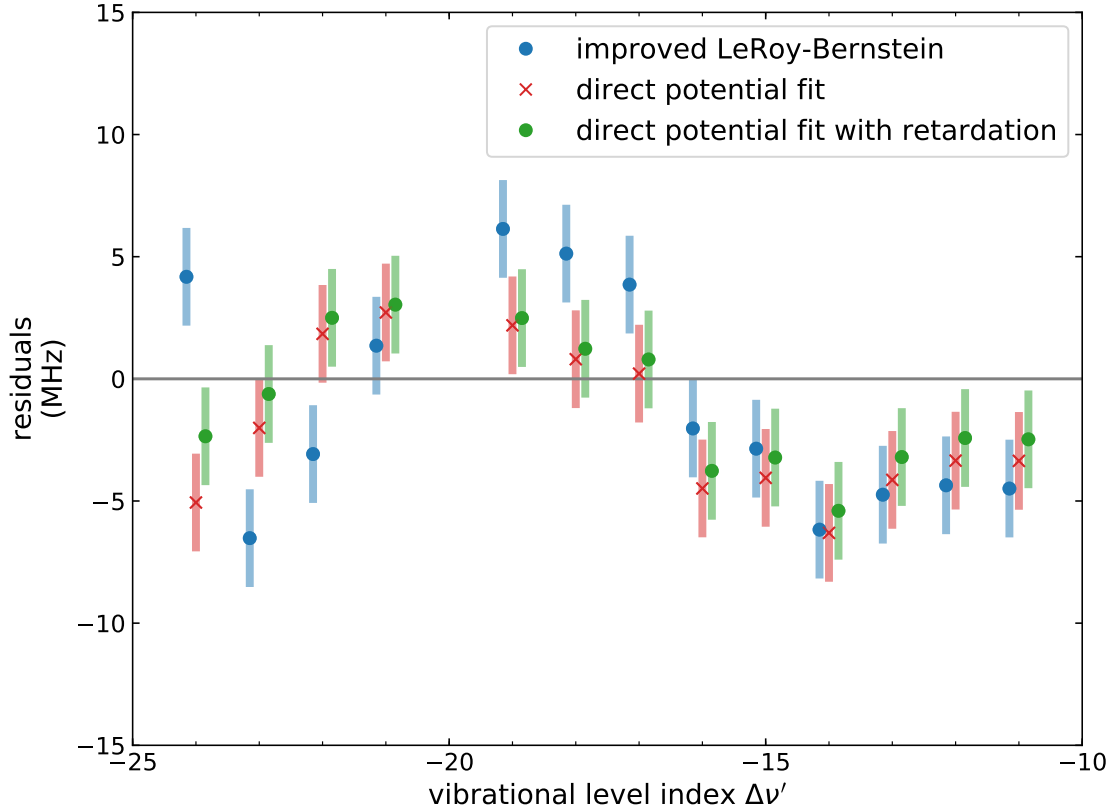
Figure 6.5.: Comparison of the residuals of the measured PA lines when fitted using different methods. The improved LeRoy-Bernstein case corresponds to the fit from Figure 6.3. Data points are offset horizontally for clarity.

following a more thorough investigation including more deeply bound levels.

An analysis of the line strengths and photoassociation rates was not performed as the data was collected under varying conditions regarding atomic density and light intensity.

The results would benefit from a deeper theoretical analysis and the data could be further improved by a measurement campaign involving more detailed scans and analysis of the individual lines as well as the acquisition of more deeply bound lines. The present setup would allow accessing two more lines without major changes and another 3 lines should be reachable by using the diode laser for photoassociation and the fiber laser as a transfer oscillator.

However, even at this stage new knowledge about the bound states of $^{170}Yb_2$ has been gained and most importantly the performance of the apparatus for photoassociation has been validated, boosting confidence when hunting for the photoassociation resonances in RbYb, where both their location and their strength is completely unknown.

7.

Intercombination Line Photoassociation of ^{87}Rb^{170}Yb

Having gotten our feet wet on the photoassociation of Yb$_2$, we now turn towards our main goal, the photoassociation of RbYb. We start by having a closer look at the relevant potentials and the (limited) information that was available to guide our search. The following section describes our search and data analysis methods, before we turn to the results. Finally, the relevant aspects of the discovered resonance are analysed. This includes a determination of the binding energy by taking into account the relevant shifts and an analysis of the Zeeman shift and an attempt to assign quantum numbers to the excited state. A look at the free-bound Franck-Condon factors allows us to judge the potential existence of stronger resonances and possible explanations for the observed linewidths are discussed.

7.1. Excited state molecular potentials in RbYb

Ab initio calculations of the potential curves for the lowest electronic states of the RbYb molecule are shown in figure 7.1 [232]. While the ground state and the states corresponding to Rb excited at the D1 and D2 lines are relatively well understood (in part due to the availability of experimental data), the potential curves corresponding to the $^3P_{0,1,2}$ states of Yb differ greatly among calculations [232–234]. For example, the potentials calculated by Sørensen et al [233] give well depths much smaller than in the potentials by Shandalau et al [232] which are shown in 7.1. In particular, this leads to the disappearance of the avoided crossings in the $^3P_{0,1,2}$ manifold. However, as we will only be probing the long range part of the potential with the short range just contributing a phase, these differences are not critical for our purposes at the moment. In fact photoassociation data may eventually lead to the refinement of these potential energy curves.

7.1.1. Previous PA to the $1^2\Pi_{\frac{1}{2}}$ state

Photoassociation is often performed near the D1 lines of the alkalis [45], as they provide large oscillator strengths and the small value of J leads to relatively simple spectra compared to the D2 lines.

Figure 7.1.: Potential energy curves for the lowest electronic states of the RbYb molecule. The ground state and the three potentials corresponding to the $^2S_{\frac{1}{2}} + {}^3P_1$ asymptote are highlighted. Potentials taken from [232]

Here we consider the molecular state corresponding to excitation near the Rb D1 line and thus to the atomic states $^2P_{\frac{1}{2}} + {}^1S_0$. As the atomic Yb state does not contribute any angular momenta, the only possible molecular state is $1^2\Pi_{\frac{1}{2}}$. Photoassociation spectroscopy has been performed on this potential down to the vibrational state $\Delta\nu' = -28$ which is bound by $E_b = h \cdot 2.2\,\text{THz}$ in the previous incarnation of the RbYb experiment [71]. In particular, the change of the hyperfine splitting with increasing binding energy in this potential was investigated [70].

In the new apparatus described here this asymptote has been used only briefly to confirm overlap between both species. However, it may be called upon again in the future in case photoassociation near the Yb intercombination line proves not to be favorable for the production of ground state molecules.

Figure 7.2.: Binding energies of the least bound states predicted for $C_6 = 4200\, E_H\, a_0$, corresponding to the mean of the values predicted for the two potentials by Porsev et al, by the LeRoy-Bernstein formula. The possible values of $\Delta \nu_D$, which can not be predicted, are on the x-axis. The physical reality for a single isotopologue thus corresponds to the position along a vertical line in the plot. The shaded areas correspond to a $\pm 20\,\%$ error in C_6.

7.1.2. The $^2S_{\frac{1}{2}} + {}^3P_1$ asymptote

In contrast to the $^2P_{\frac{1}{2}} + {}^1S_0$ asymptote discussed previously, no prior experimental data is available for the $^2S_{\frac{1}{2}} + {}^3P_1$ asymptote of RbYb which we will investigate here. Furthermore, little theoretical work has been done on this case till now. However, we can borrow some of the analysis that has been performed on RbSr [235, 236].

Here the construction of the possible states is a little more involved than in the cases where one Yb atom remains in the ground state and does not contribute any angular momenta. Starting from the atomic states $^2S_{\frac{1}{2}} + {}^3P_1$, we can construct molecular states of either doublet or quadruplet character and a total angular momentum of either $\frac{1}{2}$ or $\frac{3}{2}$. The projection $|\Omega|$ of the total angular momentum onto the internuclear axis may thus also take the values $\frac{1}{2}$ or $\frac{3}{2}$.

We then obtain the three short range states $1^4\Pi_{\frac{1}{2}}$, $2^2\Pi_{\frac{3}{2}}$ and $1^4\Pi_{-\frac{1}{2}}$ [232]. The three corresponding long range states are given by $5\left(\Omega = \frac{1}{2}\right)$, $1\left(\Omega = -\frac{1}{2}\right)$ and $2\left(\Omega = \frac{3}{2}\right)$ [232].

7.2. Prior knowledge

To guide our search for photoassociation resonances any information about their possible positions and strengths is beneficial. This section will thus explore what we can deduce from previous studies performed on either RbYb or RbSr.

When predicting the binding energies of the least bound states, which can be done using the *LeRoy-Bernstein formula* (see section 2.2.5), the relevant parameters are the dispersion coefficient of the leading order of the long range interaction, in this case C_6, and the

fractional part of the level index at dissociation $\Delta\nu_D$. In the absence of experimental data it is unfortunately not possible to deduce any information about $\Delta\nu_D$, as this would require a calculation predicting the fractional number of bound states to an accuracy of significantly better than one state. This level of accuracy can be achieved through mass scaling when there is photoassociation data for more than one reduced mass[1], but is not feasible for ab-initio calculations.

We can however obtain some knowledge of the dispersion coefficients, which will give us an idea of the expected density of bound states. Table 7.1 gives an overview of the values of C_6 obtained by different methods.

To some degree they can be obtained from single-atom properties by evaluating the dynamic polarizability of both atoms at imaginary frequencies. This is straight forward for the ground states [237–239] and somewhat more involved for the excited states where downward transitions have to be taken into account. Such calculations have been carried out for RbYb by Porsev et al [240]. The values they obtain for the ground state are in excellent agreement with the experimental values [56]. For the $1^2\Pi_{\frac{1}{2}}$ state on the other hand, their value is larger than the experimentally determined one [72] by one third. They argue this may be caused by the influence of the C_8-term on the apparent C_6 coefficient obtained from the LeRoy-Bernstein formula[2].

Another approach is to use the ab-initio potential energy curves and fit the C_6 coefficient to their long range tails. Although this method is notoriously unreliable [236], it was applied to the published curves [232] for comparison. Fits were performed for internuclear separations $r > 32\,a_0$ and with a simple C_6/r^6 behavior, as the introduction of further orders led to large covariances between the parameters. Unfortunately, the published data only extends to $r = 40\,a_0$, so the validity of this method may be limited. Indeed the values obtained significantly deviate from both the experimental values and those by Porsev et al. Nonetheless, they confirm the rough magnitude of the C_6-coefficient for $^2S_{\frac{1}{2}} + {}^3P_1$.

Figure 7.2 shows the predicted line positions for a given C_6 (the average of the values predicted for the two different potentials by Porsev et al.) for all possible values of $\Delta\nu_D$. The main message from this plot is that we can expect five to six bound states with binding energies less than $h \cdot 10\,\text{GHz}$ and once one line is found, the search range for further lines belonging to the same progression is somewhat narrowed down.

The other important question concerns the expected strength of the photoassociation transitions. Little theoretical work has been done on intercombination line photoassociation in RbYb. For the similar RbSr system however, both experimental data [82, 241, 242] and theoretical calculations [235] on intercombination line photoassociation are available. Indeed these turn out to be rather weak and challenging to observe. According to the calulations in [235], the photoassociation rates decrease by several orders of magnitude for states close to the asymptote. This is in strong contrast to the behavior at the $^2P_{\frac{1}{2}} + {}^1S_0$ asymptote, where rate constants are largest close to the asymptote. While the free-bound Franck-Condon

---

[1]if only the fractional part $\Delta\nu_D$ is required, only a few bound state energies for a single isotopologue needs to be known experimentally

[2]In [72] the improved LeRoy-Bernstein formula was used, but only with the additional short-range parameter γ and no second multipole term.

	Experimental	Porsev et al [240]	Fit
$^2\mathrm{S}_{\frac{1}{2}} + {}^1\mathrm{S}_0$	2837(13) [56]	2837(57)	2263
$^2\mathrm{P}_{\frac{1}{2}} + {}^1\mathrm{S}_0$	5684(98) [72]	7607(114)	4063
$^2\mathrm{S}_{\frac{1}{2}} + {}^3\mathrm{P}_1 \quad |\Omega| = \frac{1}{2}$	-	3955(160)	2383
$\quad\quad\quad |\Omega| = \frac{3}{2}$	-	4466(180)	3749

Table 7.1.: Comparison of the values obtained for the C_6 coefficients of the relevant RbYb asymptotes. All values in units of $E_H\, a_0^6$

factor tends to decrease with increasing binding energy, in the case of the intercombination line transition the transition dipole moment also changes significantly. As the transition is only weakly allowed by mixing of the $^3\mathrm{P}_1$-state with the $^1\mathrm{P}_1$ in free atoms, the transition dipole moment increases when additional perturbations are added by increasing interactions between both electron clouds.

While the atomic intercombination line is significantly stronger in Yb ($\gamma = 2\,\pi \cdot 182\,\mathrm{kHz}$) than in Sr ($\gamma = 2\,\pi \cdot 7.5\,\mathrm{kHz}$), a comparable situation is to be expected in our case. On a positive note, investigations in RbSr [82] have found many lines with single lines having a rate constant several orders of magnitude larger than that of the surrounding transitions, raising hopes of being able to detect at least some photoassociation resonances in RbYb.

7.3. Search for photoassociation resonances

This section will describe our approach to the search for intercombination line photoassociation resonances, the techniques we developed for data analysis and explore the sensitivity for the frequency regions where the search was unsuccessful.

7.3.1. Data analysis

The expected weakness of the transitions, combined with the large search range and the lack of prior information about their location makes the search for these resonances challenging and time consuming. The data recorded for this search spans many days and nights of more or less continuous measurements. During this time, many factors unrelated to photoassociation lead to drifts of the atom numbers on various timescales. Among these are changes in environmental conditions, either on long timescales such as caused by weather or on shorter timescales up to a single shot, such as those from people entering and leaving the lab, drifts in alignment, changes of laser performance over time and many others.

Many of these would be easily mistaken for a resonance and the manual evaluation of such candidates has proven to be both time consuming and prone to errors. We thus attempt to automate and quantify this analysis using the method described in the following.

Our approach is based on so called *gaussian processes*, a tool from machine learning. A very brief description is given here, with a more involved treatment being available in [243].

A *process* is the generalization of a probability distribution from a vector to a function. A *gaussian process* thus represents infinitely many functions, that are defined by a large but finite set of parameters, that follow a normal – or *gaussian* – distribution. In practice these parameters simply represent the values of the function at particular points spanning our region of interest. The nature of the functions is constrained by specifying their covariance matrix or *kernel*. A popular choice, which we also use here, is the so called *radial basis function*, where the functions are the sum of an infinite amount of gaussians with a specified width, called the *lengthscale*.

In adddition to the model, the fitting process can account for a noise term in the data, with the *noise level* specifying the variance of the data that is expected to be due to noise and thus specifying a tradeoff between the same data being explained by a complex model with little noise and a simple model with lots of noise. Both *lengthscale* and *noise level* are so called hyperparameters and may be either specified by the user or optimized by the fitting routine.

Fitting such a *gaussian process* to a set of input data results in both a function representing the most likely fit to the data, as well as errorbars resulting from the width of the distribution fitted for each point. All these calculations are implemented in a number of machine learning libraries such as *scikit-learn* [244] which is used here.
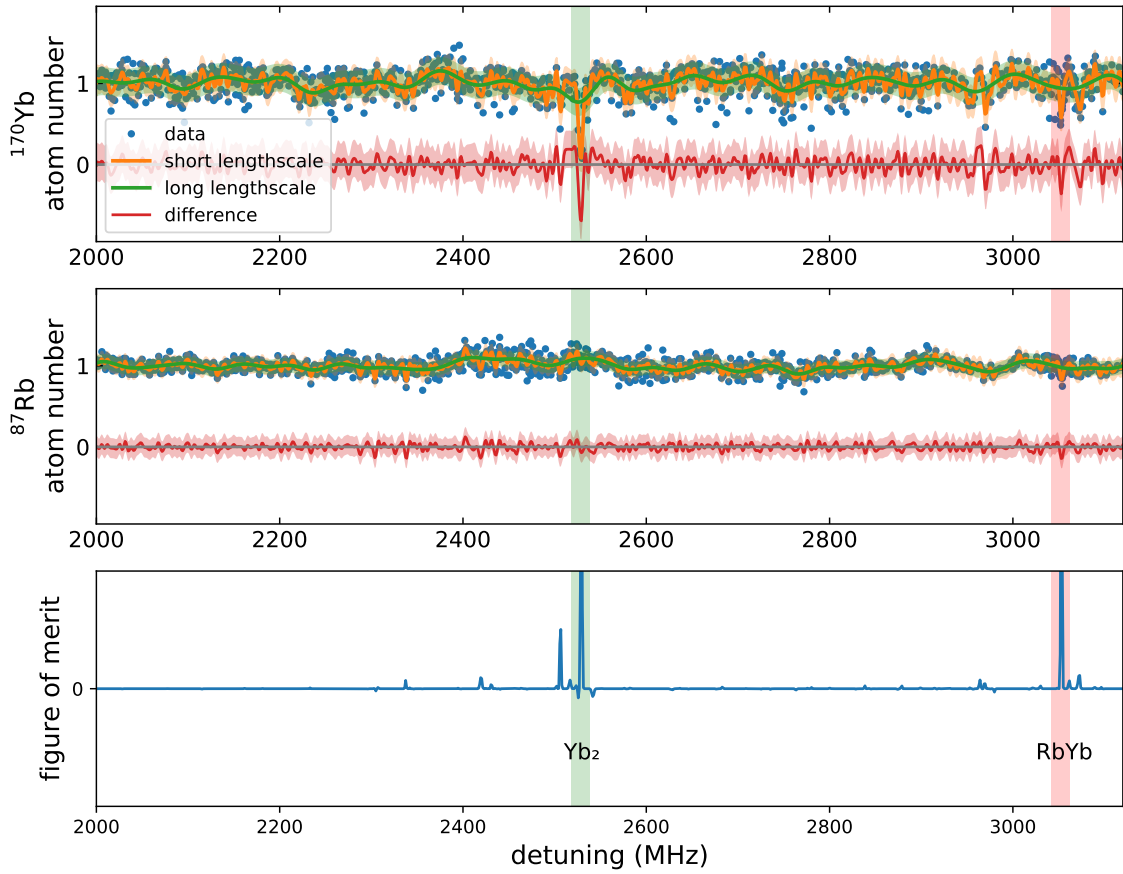
Figure 7.3 illustrates the analysis routine using a small portion of the searched range as an example. First the data for each species is normalized and then fitted using *gaussian processes* with two different lengthscale, one corresponding to the expected transition linewidth, the other larger by a factor of ~ 10, so that it does not follow dips corresponding to potential resonances, but still tracks most fluctuations in atom number that arise from experimental drifts. Taking the difference between these two curves results in a curve reproducing only those changes in atom number that occur on the length scale of interest.

As we are interested mainly in heteronuclear photoassociation resonances and the atom numbers of both species is similar, we expect to observe a simultaneous dip in both datasets. The preprocessed data for both species is thus multiplied, resulting in a quantity that will exhibit a positive peak when both species exhibit a loss. In order to emphasize peaks with respect to the noise while still retaining the sign, we plot the cube of this quantity.

A resonance where only one species experiences loss may result in either a positive or negative peak – or in the particularly unlucky circumstances no peak at all – depending on the fluctuations of the other species at this point. Indeed this method gives a clear signal for both the Yb$_2$ and the RbYb resonance that were found in the range shown in Figure 7.3.

7.3.2. Search range and sensitivity

In the scope of this work, the range from $0.1\,\mathrm{GHz}$ to $11\,\mathrm{GHz}$ – with an unfortunate gap between $3.2\,\mathrm{GHz}$ and $3.7\,\mathrm{GHz}$ – was searched. In this entire range, the only resonance that was found is the one shown in Figure 7.3, which on closer inspection turns out to be a pair of resonances. While of course not as exciting as the actual resonance, we can also gain some information from the range where we did not find any resonances if we take a moment to estimate the sensitivity of our search.

Figure 7.3.: The data analysis routine illustrated on the example of a small portion of the total scan range ranging from $2.0\,\mathrm{GHz}$ to $3.1\,\mathrm{GHz}$. The top two panels show the atom numbers recorded for each species together with the gaussian processes fitted for different length scales and their difference. The lowest panel shows the resulting figure of merit calculated as the cubed product of both differences. The colored backgrounds highlight the $\mathrm{Yb_2}$ and the RbYb photoassociation resonance found in this region.

For most of the search range, transitions with a PA rate constant $K_{\mathrm{PA}} \gtrsim 2 \cdot 10^{-14}\,\mathrm{cm^3/s}$ would have been detected with a high probability. Sensitivity is however strongly degraded for binding energies less than $\sim h \cdot 2\,\mathrm{GHz}$ due to increased off-resonant excitation of the atomic transition – requiring a reduction in photoassociation pulse area by several orders of magnitude – and in the immediate vicinity of $\mathrm{Yb_2}$ resonances (see chapter 6). Sensitivity would also be degraded by a factor of up to four[3] for transitions with an effective linewidth of less than the typical step size of $2\,\pi \cdot 1\,\mathrm{MHz}$. While this could have been avoided by the choice of a smaller step size, e.g. $2\,\pi \cdot 0.2\,\mathrm{MHz}$, the already long scan times would then have increased by a factor of five. Keeping in mind that finding a strong transition would also be more useful for further experiments, the benefit of an increase in search range was deemed to outweigh this potential decrease in sensitivity for weak lines.

---

[3]Assuming their linewidth is no smaller than the atomic linewidth of $2\,\pi \cdot 182\,\mathrm{kHz}$
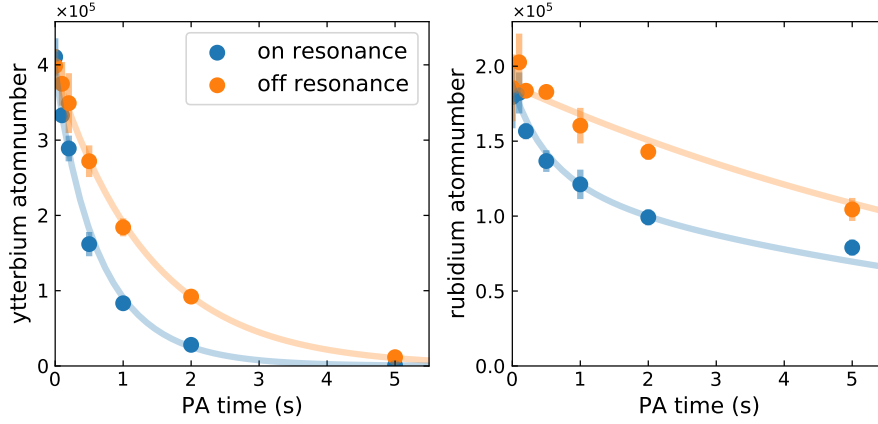
Figure 7.4.: Time evolution of the atom numbers for both species with the photoassociation laser on and off the resonance. The solid lines are a fit of the solution of Equation 7.1.

7.4. Discovery of a pair of resonances

Using the procedures described above, a pair of loss features around 3.1 GHz was located. In measurements in the absence of Rb this feature disappears, ruling out the (remote) possibility of an Rb$_2$ photoassociaton resonance. Despite further extensive search efforts, no other resonances could be located. The following sections will thus deal with the characterization of these two resonances.

7.5. Photoassociation rate

As a first step to characterize the resonance we want to quantify its strength by determining the photoassociation rate constant $K_{\mathrm{PA}}(I)$ for the available photoassociation light intensity, temperature and pair density of the atomic sample. Figure 7.4 shows the evolution of the atom numbers for both species during the photoassociation step with the laser tuned to the photoassociation resonance and detuned just far enough that no photoassociation loss occurs. It is clear that the photoassociation loss in Yb is of a magnitude comparable to that of the loss caused by off-resonant scattering on the atomic transition and the transition is thus rather weak and its exploitation will be challenging. While the Yb atoms are completely eliminated for long times – albeit mostly due to off-resonant excitation and other loss mechanisms unrelated to photoassociation –, the loss in Rb eventually saturates due to the depletion of Yb.

To quantify the observations we use the rate equations for the atomic densities n_{Rb} and n_{Yb} which are given by

$$\dot{n}_{\mathrm{Rb}} = -n_{\mathrm{Rb}} \cdot K_{\mathrm{Rb}} - n_{\mathrm{Rb}} \cdot n_{\mathrm{Yb}} \cdot K_{\mathrm{PA}} \tag{7.1}$$

$$\dot{n}_{\mathrm{Yb}} = -n_{\mathrm{Yb}} \cdot K_{\mathrm{Yb}} - n_{\mathrm{Rb}} \cdot n_{\mathrm{Yb}} \cdot K_{\mathrm{PA}} \tag{7.2}$$
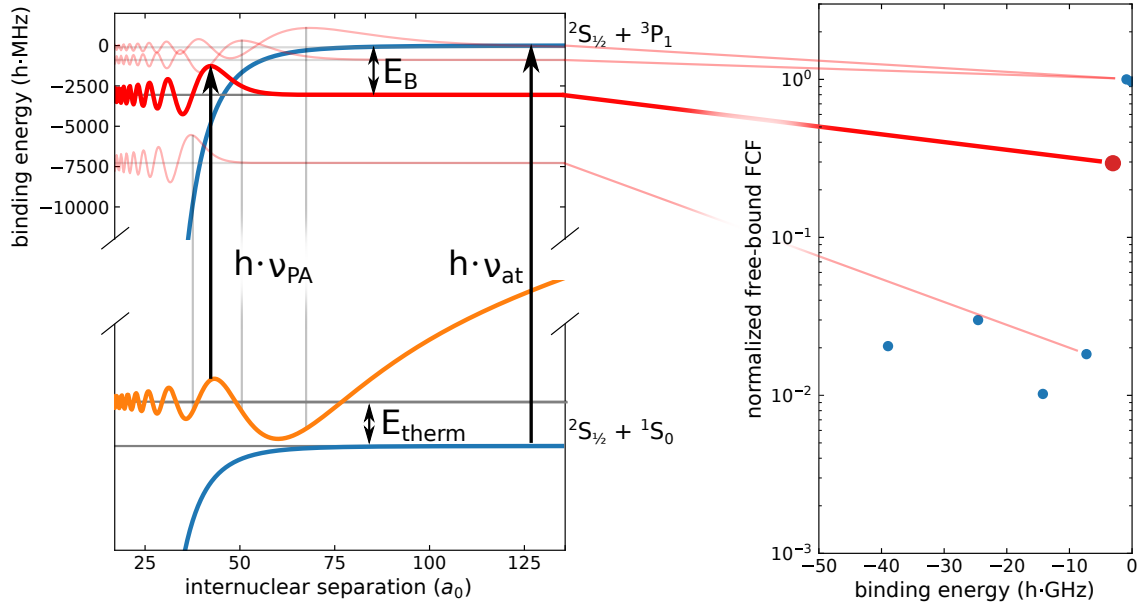
Figure 7.5.: Schematic depiction of the PA process to the observed state in RbYb. Vertical lines indicate the value of the scattering wavefunction at the location of the last lobe in each bound wavefunction. The right panel shows free-bound Franck-Condon factors calculated using these wavefunctions (normalized to the largest value).

with the photoassociation rate constant K_{PA} and the single species loss constants $K_{\mathrm{Rb}}, K_{\mathrm{Yb}}$. Three-body loss terms have been left out as they are not yet relevant at the present densities. The data in Figure 7.4 is fitted by a numerical solution of these equations to extract the rate constants.

From this fit we extract a photoassociation rate constant of $K_{\mathrm{PA}} \approx 5 \cdot 10^{-14}\,\mathrm{cm^3/s}$ per Ytterbium atom. Even considering the difference in atomic linewidths, this is significantly larger than predictions made for RbSr in [235], but nonetheless orders of magnitude lower than typical PA rate constants obtained near the alkali D-line asymptotes.

The single species loss constant of $0.7\,\mathrm{s^{-1}}$ for Yb is an order of magnitude larger than for Rb which is explained by off-resonant scattering. While the PA rate is not saturated and could be increased by increasing the laser intensity, this would also lead to a corresponding increase in the Yb single species loss and would thus not improve the situation.

7.5.1. Free-bound Franck-Condon factors

In addition to the characterisation of the observed line we are of course interested in what we can learn about the possible location and strength of other resonances.

For a closer look at this the relevant wavefunctions were again calculated numerically (see section 6.3) and are shown in Figure 7.5. For both states a Lennard-Jones potential (see subsection 2.2.3) was used as a model potential. For the excited state the value of C_6 was taken from the calculation by Porsev et al (data shown is with $C_6 = 4466\,E_H\,a_0^6$ as calculated
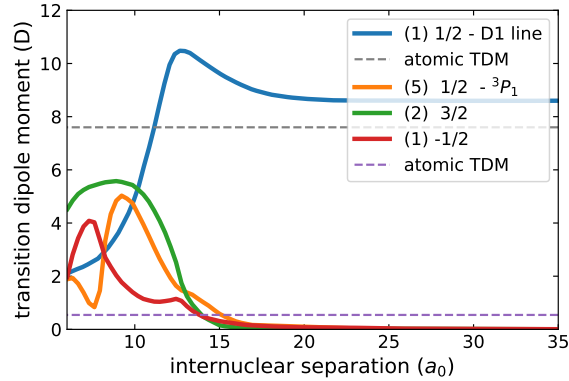
Figure 7.6.: Transition dipole moment curves for the relevant potentials [232, 245]. Dashed lines show experimental values for the atomic transitions [55, 246]. Note the calculations do not include the mixing between $^1P_1$ and $^3P_1$ states, so the TDM for the intercombination line appears to vanish at large separations.

for the $|\Omega| = \frac{3}{2}$ state, but the situation for $|\Omega| = \frac{1}{2}$ is similar) and C_{12} was adjusted so that the binding energy of the observed state is reproduced while approximately maintaining the potential depth of the ab initio potentials. The ground state model potential was based on that in [72], with C_{12} adjusted so that the binding energies of the least bound states and thus the scattering length is reproduced.

Predictions of the location of other resonances can of course be attempted from this if one is prepared to trust the predictions of the C_6 coefficient. Here we are particularly interested in attempting to explain why we have not found any other resonances in our search.

For this model potential the outermost lobe of the bound wavefunction of the observed transition is located almost exactly above an antinode of the scattering wavefunction, indicating a large overlap. Indeed, when calculating the free-bound Franck-Condon factors for the model wavefunctions, this transition is among the strongest.

In contrast, for the next most deeply bound state the lobe is located above a node of the scattering wavefunction indicating low overlap. In fact for all states that are bound more deeply than the observed one, the calculated free-bound Franck-Condon factors are significantly lower. However photoassociation rates may eventually increase again when mixing of the molecular states leads to an increase of the dipole matrix element [235], as shown in Figure 7.6. This only starts having a significant effect at internuclear distances of $\sim 20\,a_0$ [232], which are reached at binding energies of $\sim h \cdot 1\,\text{THz}$ which are neither accessible with our laser system nor feasible to find without further knowledge of the potential.

On the other hand, the Franck-Condon factor increases for the less deeply bound states and is almost an order of magnitude larger for the least bound state predicted to have a binding energy of $h \cdot 0.1\,\text{GHz}$. However, both these states are also significantly closer to the atomic transition. Off-resonant scattering, which already severely limits the spectroscopy at $h \cdot 3.1\,\text{GHz}$, is an order of magnitude stronger at $h \cdot 0.9\,\text{GHz}$ and three orders of magnitude stronger at $h \cdot 0.1\,\text{GHz}$.
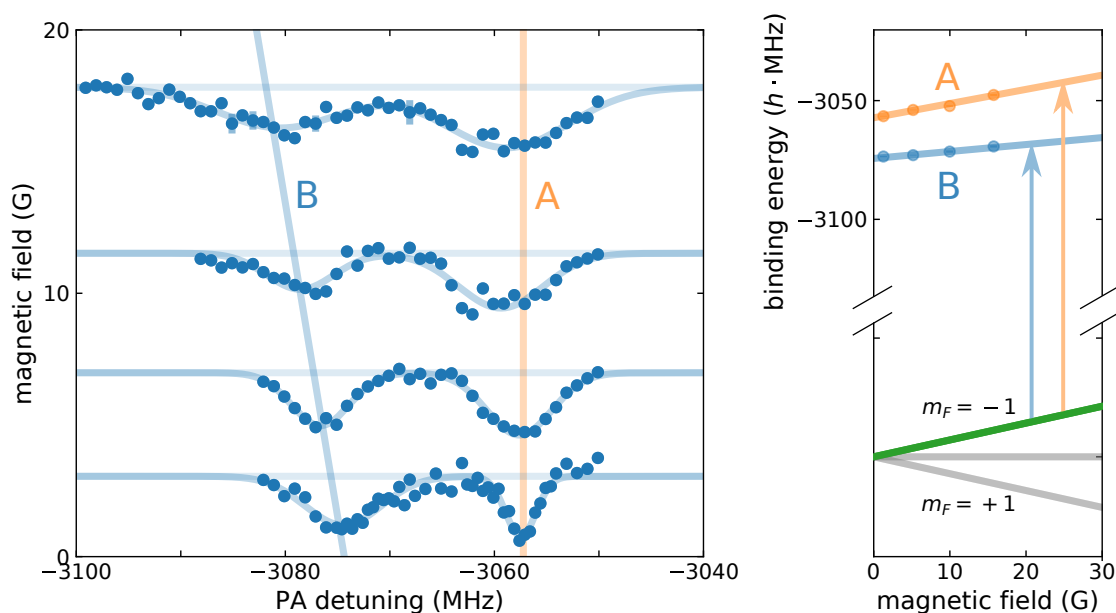
Figure 7.7.: Measurement of the Zeeman shift of the PA transition. The left panel shows the PA spectra obtained at different magnetic fields with gaussian fits. The lines indicate the center of the fitted peaks. The right panel shows the extracted shift when taking into account the shift of the scattering state. [Figure reprinted from Phys. Rev. A 107, 023114 (2023), ©2023 American Physical Society]

To make matters worse, both states are predicted at frequencies in the immediate vicinity of rather strong Yb_2 photoassociation resonances, leading to further losses.

It has to stressed that there is little justification for the shape of the toy potential used here. Its inner turning points are located significantly further outside than those of the ab-initio potentials and the potential depth and thus the number of bound states is only roughly matched to the ab-initio potentials. The validity of the Franck-Condon factors calculated here is thus limited. Further refinement of the potential, ideally based on more spectroscopy data, and possibly incorporating the ab-initio short range potentials may lead to improved predictions, but is unlikely to change the general picture.

7.6. Zeeman shift

Another point of interest is the behavior of the line when applying a magnetic field, as this may help us gain information on the nature of the molecular state involved. Figure 7.7 shows spectra obtained at different magnetic fields which are applied using the bias coils installed in the science chamber. As for all measurements Rb was prepared in the $|F = 1, \ m_F = -1\rangle$ state. The magnetic field values were calibrated using microwave spectroscopy in Rb.

The polarization was undefined for this measurement, so potentially both π and $\sigma_\pm$ transitions contribute to the spectrum. Additionally, when working at low coil currents the

magnetic field is dominated by the ambient field, which does not necessarily have the same orientation as that produced by the coils. The helicity can thus not be expected to be the same for all spectra recorded.

When evaluating the Zeeman shift of the bound state we must keep in mind that the scattering state corresponds to the $|F = 1, \ m_F = -1\rangle$ state of Rb and thus itself shifts with $0.70\,\mathrm{MHz/G}$ [55], which has to be accounted for when determining the shift of the excited state from the measured shifts. The transition at $-3057\,\mathrm{MHz}$ that hardly appears to shift at all thus corresponds to a molecular state with a shift very close or identical to that of the $|F = 1, \ m_F = -1\rangle$ state, while the transition at $-3074\,\mathrm{MHz}$ that appears to shift significantly corresponds to a shift with a much lower shift. The exact shift coefficients are hard to extract from this measurement, as the unresolved splitting may compromise the determination of the line centers. The fits shown yield shift coefficients of $0.6(1)\,\mathrm{MHz/G}$ and $0.3(1)\,\mathrm{MHz/G}$ respectively.

The fit not only serves to determine the magnitude of the shift, but also to extrapolate the transition frequencies from those measured at a finite field to zero field. The zero-field transition frequencies obtained are $-3057.2(3)\,\mathrm{MHz}$ and $-3074.3(3)\,\mathrm{MHz}$. The two peaks obviously remain split even at zero magnetic field. Yet their close proximity and similar strength suggest that they are in fact closely related.

Besides aiding in the determination of the binding energy, we can also hope for the Zeeman splitting to give us some information about the character of the excited state. As the states in question are still very weakly bound, it seems reasonable to argue about their nature in terms of the atomic states. We will adopt the common convention of using lower case letters for the quantum numbers of individual atoms and upper case letters for those of the resulting molecule

The shift coefficients for the Rb states in $f = 1$ are $-m_f \cdot 0.7\,\mathrm{MHz/G}$, while the excited $^3\mathrm{P}_1$ state of Yb shifts with $m_j \cdot 2.1\,\mathrm{MHz/G}$. All combinations of these states will thus shift with multiples of $0.7\,\mathrm{MHz/G}$ and cannot satisfactorily explain the shift of peak B.

To explain the observed shift of state B, we will thus have to take into account the couplings between the atomic angular momenta and the molecular rotation. With both atoms contributing angular momentum, and not a lot being known about these states, the correct coupling scheme is not very clear to start with. We will thus explore the coupling scheme in the following sections.

7.6.1. Assessment of the relevant Hund's cases

In order to correctly analyze the observed state, we first need to determine the applicable Hund's case. This is however less straightforward than in the case of D1 line PA, where only the Rb atom contributed angular momentum and photoassociation spectra in a MOT could be well explained by a Hund's case (e) coupling [67][4]

In general the applicable *Hund's case* depends on the relative energy scales of the electrostatic interaction $|E|$, the spin-orbit coupling $|A|$ and the rotation B. By far the largest

---

[4]Note the Zeeman shift was not analyzed here as measurements where taken in a MOT where a magnetic bias field cannot be applied.

energy scale involved is that of the spin-orbit coupling, with the atomic spin-orbit coupling constants being $a_{\mathrm{Yb}} = 807\,\mathrm{cm}^{-1}$ and $a_{\mathrm{Rb}} = 524\,\mathrm{cm}^{-1}$. This coupling is slightly modified and an additional coupling term between the Rb spin and the Yb orbital angular momentum appears at shorter separations [247]. However it remains by far the largest interaction term at all relevant distances.

This places us in either *Hund's case (c)* or *Hund's case (e)*, depending on the relative magnitude of the rotational and electrostatic energy scales. The rotational energy scale is characterized by the rotational constant (see Equation 2.15) which is approximately $5 \cdot 10^{-4}\,\mathrm{cm}^{-1}$ in our case[5].

The energy scale for the electrostatic interaction or effective anisotropy on the other hand is less straight forward to estimate. It is related to the energy difference to the closest potential curve with a different Λ [248], which in this case will be a Σ potential on the $^3\mathrm{P}_2$ asymptote [232]. As the actual splitting between these potentials is dominated by the spin-orbit coupling, it is necessary to look at the spin-free[6] potential curves, rather than the spin-orbit coupled curves shown in Figure 7.1. These spin-free curves have been determined in [247]. If this interaction were to remain perturbative over the whole range of separations, we could now easily calculate the energy by taking their expectation value for a given vibrational wavefunction. However this interaction becomes dominant at shorter range and obtaining an accurate value would thus necessitate a full quantum chemistry calculation. Instead we estimate the energy scale by evaluating at the classical outer turning point again, where we obtain $|E| \approx 0.02\,\mathrm{cm}^{-1}$. We thus have $|A| \ggg |E| \gg B$, making *Hund's case (c)* the most likely.

7.6.2. Hyperfine coupling

Another important question is how to deal with the nuclear spin of the Rb atom and the resulting hyperfine interactions. The atomic hyperfine splitting of $0.2\,\mathrm{cm}^{-1}$ is larger than the expected effective anisotropy, albeit by only about one order of magnitude. It is thus likely that the Rb electron angular momentum j_{Rb} couples to the nuclear spin i_{Rb} to form f_{Rb} as in an isolated atom.

However, due to the small ratio between the hyperfine coupling and the estimated electrostatic energy scale – and the unreliability of the later one – it is also very possible that a less clean intermediate coupling case is present here.

7.6.3. Explanation of Zeeman effect and zero-field splitting

When applying *Hund's case (c)*, we can indeed make an assignment that appears to explain both the splittings at zero-field and the observed Zeeman shifts. Unfortunately, this assignment would require a change of the total projection quantum number by two, which is not allowed.

---

[5]This value has been calculated using the classical outer turning point, which is slightly larger than the effective distance and will thus be a slight underestimate

[6]spin-free in this context meaning that the spin is uncoupled, not that it is not considered

Within a *Hund's case (e)* coupling scheme there are also a number of possible assignments for the excited state that explain the Zeeman shift, if not the zero-field splitting. However all of these also violate some kind of selection rule.

For completeness, the assignments in both of these cases are discussed in detail in Appendix A.

A possible explanation for the zero-field splitting is provided by a dipolar interaction term between the Rb spin and the Yb atom. Indeed a similar behavior has been observed in the D1 photoassociation of RbYb, where the rotational components of the photoassociation line split into multiple M_R-components [67][7]. This was attributed to the interaction between the Rb magnetic moment and the Yb atom, which in this case is spin-less, but moving relative to the Rb atom –, depending on their relative orientation. In our case, the fact that both atomic states possess a magnetic dipole moment further motivates such a splitting. Applying the expression given for the dipolar interaction in [249] to a model wavefunction calculated using the ab initio potentials gives a value of a few MHz. As this is only a crude estimate of the size of this effect, it cannot be ruled that it is responsible for the observed splitting.

To conclude there is an assignment in *Hund's case (c)* that explains both the splitting between two resonances and the Zeeman shift of the observed states – albeit with an inconsistency in the expected quantum numbers – *Hund's case (e)* can provide explanations for the Zeeman shift, but all these violate selection rules. All of these options require the excited molecule to rotate, which while possible at least raises the question of why no corresponding line with no rotation was observed.

With none of these explanations being convincing, it is perhaps most likely that we are dealing with an intermediate situation that is not well suited to the perturbative treatment inherent to Hund's cases. In the future more experimental data, including Zeeman shift measurements for different initial Rb states and different polarizations of the PA light as well as a full quantum chemistry calculation may be able to give additional insights.

7.7. Linewidth

In addition to the shifts, Figure 7.7 shows a significant broadening of the peaks with increasing magnetic field. When the magnetic fields were calibrated using microwave spectroscopy no additional broadening could be detected, so there is no reason to suspect a technical origin of this broadening. While part of this can be accounted for by the splitting of the Zeeman components as indicated in Figure A.2, this does not account for the fact the individual components do not become resolvable at larger fields.

Remarkably peak B seems to exhibit a minimum in linewidth at a finite field, making it even harder to explain using unresolved splittings. In principle it is possible that there is a change in coupling strength due to the presence of a magnetic background field in the horizontal direction, leading to a change of magnetic field direction as the field is changed.

---

[7]Unfortunately the Zeeman splitting could not be analyzed in this case as the experiments where performed in a MOT.

However as the line is broadening we observe a decrease in PA rate, while changes in coupling strength would lead to the linewidth increasing together with their rate.

For the zero-field FWHM of the peak at $-3057.2(3)$ MHz a value of 3 MHz is extrapolated. Even this linewidth is still an order of magnitude larger than the atomic linewidth. No further reduction of the linewidth was observed when reducing the PA intensity, ruling out saturation broadening.

Radiative decay

Significant broadening of the intercombination line photoassociation resonances has also been observed in RbSr [82]. Here it was argued this could be caused by strong radiative decay to bound states in the electronic ground state.

Recall that for this transition the transition dipole moment strongly increases as the internuclear separation is reduced. This is in strong contrast to the alkali D-lines, for which the transition dipole moment shows a small increase at most and then drops rapidly. So while the Franck-Condon factor for transitions to deeply bound states will be reduced dramatically, the electronic component of the transition strength may overcompensate for this. This is the reason that it is possible in this system to have a bound-bound transition from our excited state to the electronic ground state that has a linewidth that is significantly larger than that of the atomic transition and thus dominates the lifetime and consequently energy width of our state.

If this was indeed the case, and it turned out that the Franck-Condon factors are such that the majority of molecules decay to a single or few bound states, it could provide an interesting prospect for the efficient – if not coherent – production of molecules. Unfortunately we currently have no way of detecting these molecules or knowing to which states their decay would occur.

On the other hand we can estimate the effect by using the transition dipole moment curves calculated by Shundalau and Minko [232] to compute the expectation value for the dipole moment for our vibrational state. As we cannot currently assign the state to one of the three potentials at this asymptote, we repeat this for all of them. We estimate the wavefunction by using the published potential energy curves [232] to get a realistic turning point, connected to an analytic long range expression using a switching function [56] between $30\,a_0$ and $35\,a_0$. The ab initio part is scaled by a factor $1 < a < 1.02$ to approximately reproduce the observed binding energy.

In all potentials the increase in transition dipole moment for this state would be less than $10\,\%$ of the atomic dipole moment. This mechanism thus seems unlikely to significantly affect the state lifetime or transition rates.

Non-radiative decay

Another possible explanation for the observed linewidths is non-radiative decay within the ^3P manifold, for example through predissociation to the $^3P_0$ state. Such decay has for example been encountered in the analysis of Feshbach resonances associated with the $^3P_2$

state [247], where it leads to strongly decayed resonances with lifetimes on the order of microseconds.

Interestingly, the calculations performed for Feshbach resonances in the ^{3}P$_2$ state also show a decay width that is increasing with magnetic field in the same range that is covered by our measurements [247, 250]. If a similar effect is observed for the ^{3}P$_1$ state, this would explain the observed behaviour of the linewidths.

A possible cause for this is the Zeeman effect itself, whose matrix elements for the Yb atom in a l-s-coupled basis are given by [249]:

$$\langle j\,m_j|\,\hat{H}_Z\,|j'\,m_j'\rangle$$

$$= \left[g_s\mu_B(-1)^{2j+l+s-m_j+1}\sqrt{s(s+1)(2s+1)(2j+1)(2j'+1)} \begin{pmatrix} j & 1 & j' \\ -m_j & 0 & m_j \end{pmatrix} \begin{Bmatrix} s & j' & l \\ j & s & 1 \end{Bmatrix} \right.$$

$$\left. + g_l\mu_B(-1)^{j+j'+l+s-m_j+1}\sqrt{l(l+1)(2l+1)(2j+1)(2j'+1)} \begin{pmatrix} j & 1 & j' \\ -m_j & 0 & m_j \end{pmatrix} \begin{Bmatrix} l & j' & s \\ j & l & 1 \end{Bmatrix} \right] B,$$

$$(7.3)$$

where $(:::)$ and $\{:::\}$ are the Wigner 3j and 6j symbols respectively. These are nonzero for $j' = j \pm 1$ if $m_j = m_j'$ and thus lead to mixing between states with different j but equal m_j [249]. For example this effect is the reason the doubly forbidden ^{1}S$_0 \rightarrow {}^3$P$_0$ transition is observable in the bosonic Yb isotopes as the ^{3}P$_0$ state acquires a small ^{3}P$_1$ component through an external magnetic field.

While this effect is small in the atomic case because of the large energy separation between the mixed states, in our case there will be bound states in the molecular potentials dissociating to ^{3}P$_2$ and unbound ^{3}P$_0$ states that are much closer in energy, thus potentially giving a significantly stronger effect. However, involved calculations well beyond the scope of this work will be required to confirm if this is the case. A somewhat similar situation has been described for the ^{3}P$_j$ manifold of the molecular ion HeN$^+$ [251]. Notably this leads to many transitions being broadened to an extent that makes them unobservable and might provide an explanation for the fact that we have only observed transitions to one of the three potential curves.

Unfortunately, unlike the case of radiative decay, non-radiative decay is unlikely to lead to any useful applications.

7.8. f=2 resonances

For further experiments, including the determination of the hyperfine splitting of the ground state (see section 8.7) it would be highly desirable to be able to perform photoassociation for both Rb hyperfine states. So – assuming the two states we observed are indeed of $f = 1$ character – it would be necessary to locate a $f = 2$ transition as well.

When preparing Rb in the $|f = 2,\ m_f = -2\rangle$ state instead, the line was reduced to a

strength consistent with it being caused by imperfections in the state preparation[8] and repopulation of the $f = 1$ states by the trap laser. No $f = 2$ resonance was found within $\pm 100\,\mathrm{MHz}$ of the $f = 1$ resonance. The $|f = 2,\ m_f = -2\rangle$ state was chosen because it can be reached by a single microwave transition from the $|f = 1,\ m_f = -1\rangle$ state and its stretched nature prevents the occurrence of spin relaxation. However, depending on the nature of the PA target state found for $f = 1$, there may be a chance this transition is not allowed from $m_f = -2$. Spin relaxation will then have to be prevented by the application of a sufficiently large bias field.

It has also been suggested in RbSr that resonances lying above the lowest hyperfine asymptote, which in our case corresponds to $f = 1$, may suffer from pre-dissociation that prevents their observation [82]. If this is the case, only levels bound by more than $h \cdot 6.8\,\mathrm{GHz}$ may be observable, explaining our failure to locate this particular state.

A more extensive search for $f = 2$ resonances, involving a larger frequency range and/or different values of m_f will thus be needed in the future.

7.9. Other shifts and binding energies

While the insight to be gained from a single bound state is limited, we are nonetheless interested in the binding energy of the observed states. We thus now turn towards the various shifts influencing the measured resonance positions.

7.9.1. Thermal shift

As the measurements presented here are performed in thermal samples, the mean collision energy, which is given by

$$E_{\mathrm{therm}} = \frac{3}{2}\mu k_B \left(\frac{T_{\mathrm{Rb}}}{m_{\mathrm{Rb}}} + \frac{T_{\mathrm{Yb}}}{m_{\mathrm{Yb}}} \right) \tag{7.4}$$

and is equal to $h \cdot 0.2\,\mathrm{MHz}$ for typical conditions, has to be taken into account when determining the binding energy from the transition frequencies. Thermal broadening does not play a role at the observed linewidths, however.

7.9.2. Light shifts

Another set of shifts that needs to be considered are the light shifts induced by both the trap and the photoassociation laser. The trap light shift is already mostly compensated for in our measurements, as the frequency offsets are calibrated to spectroscopy of the atomic transition performed in the same trap. It is nonetheless useful to know its magnitude so that we can estimate uncertainties from fluctuations in trap power as well as due to slight differences between the light shift experienced by the atomic and photoassociation transitions.

---

[8]by accident the microwave antenna was mounted in a way that produced almost purely π-polarized radiation in a non-obvious way, degrading the Landa-Zener sweep requiring σ_-.
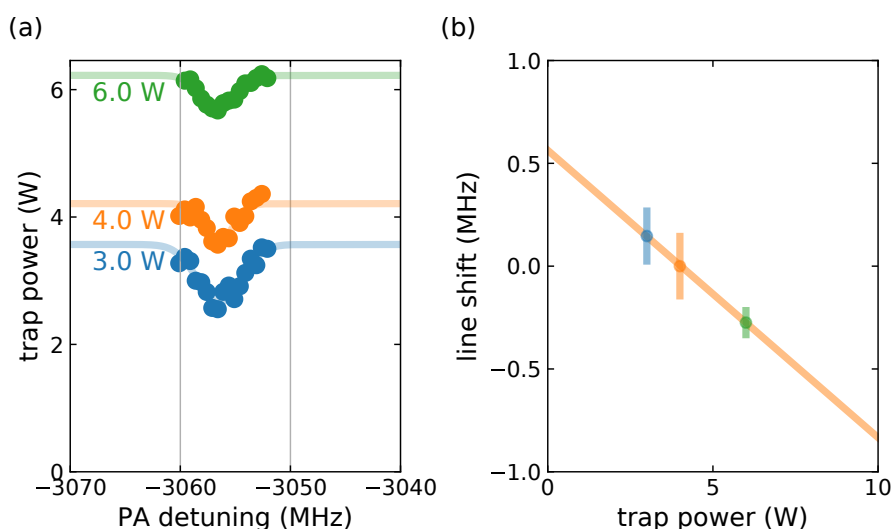
Figure 7.8.: Shift of the transition due to trap induced light shift. In (b) the thermal shift has been compensated for, where a linear fit is used to extract the shift coefficient.

A measurement of the trap light shift is shown in Figure 7.8. The determination of this shift is complicated by the fact that the trap power is inextricably linked to the temperature of the sample and thus the thermal shift. The thermal shift has thus been compensated for by applying Equation 7.4 using temperatures obtained from time-of-flight images in Figure 7.8b. A linear fit yields a shift coefficient of $-0.14(1)\,\mathrm{MHz/W}$ for the trap light shift in the final XODT combination.

7.9.3. Binding energies

Taking into account the effects treated in the previous sections the binding energies of the two states – assuming they can be assigned to the $f = 1$ threshold – are measured to be $3057.0(5)\,\mathrm{MHz}$ and $3074.1(5)\,\mathrm{MHz}$ and are thus split by $17.1(7)\,\mathrm{MHz}$. Taking the C_6 values calculated by Porsev et al, these binding energies correspond to a classical outer turning point of $\sim 45\,a_0$. This is at significantly longer range than the most weakly bound level that was observed for photoassociation near the D1 line with an outer turning point around $35\,a_0$ [67, 68, 70], which is explained by the difference in C_6-coefficients (see Table 7.1) and the lower linewidth allowing for spectroscopy closer to the asymptote. In the electronic ground state, this outer turning point would correspond to a level bound by approximately $h \cdot 2\,\mathrm{GHz}$ [9].

Referring back to section 7.2 this suggests the neighbouring levels at binding energies around $1.2\,\mathrm{GHz}$ and $6\,\mathrm{GHz}$, respectively, though with large uncertainties. Both of these are however close to Yb_2 resonances which could obscure the RbYb resonances.

---

[9]Unfortunately no such level exists, as we will see in chapter 8

7.10. Conclusion

To the best of the authors knowledge this is the first time intercombination line photoassociation has been successfully carried out in an alkali-Yb combination. A pair of states at $-3057.0(5)\,\mathrm{MHz}$ and $-3074.1(5)\,\mathrm{MHz}$ below the $f = 1$ threshold has been found and characterized with regard to photoassociation rate and various shifts. In particular the Zeeman shift was characterized and found to not be consistent with expectations in a simple *Hund's case* interpretation (see Appendix A). Further investigations will thus be required to determine the true nature of the excited states.

While the observed lines are weak, the PA rates are consistent with theoretical predictions for photoassociation rate in the similar RbSr system. Free-bound Franck-Condon factors were calculated for a model potential and give a possible explanation for the failure to discover any of the other lines belonging to the same potential in the spectral range covered by our search.

We conclude that it is unlikely that another resonance providing larger PA rates can be found in the $^{87}\mathrm{Rb}^{170}\mathrm{Yb}$ system. Remaining options for improving the PA rate will thus require improvements to the apparatus, either to increase the Rb density or to manipulate the scattering wavefunction by external confinement, Feshbach resonances, or non-resonant light [252]. Alternatively, one could switch to a different isotopologue (see section 2.4) in hopes of finding a happy coincidence in Franck-Condon factors occurring farther away from the atomic resonance.

8.

2-Photon-Photoassociation: the $X^2\Sigma_{\frac{1}{2}}$ ground state of ^{87}Rb^{170}Yb

We can now make use of the free-bound transition discovered in the previous chapter to explore the ground state by means of 2-photon photoassociation. Here an additional laser field, the bound-bound laser is used to couple the vibrational level in the electronically excited state to a vibrational level of the electronic ground state. In the context of the production of ground state molecules, this serves as an intermediate step, stabilizing the molecule in a state with a lifetime that is much larger than that of the electronically excited state[1]. From there it can usually be transferred into the absolute ground state using an additional pair of lasers. But even on its own, spectroscopy of the bound states of the electronic ground state provides insights into the scattering behaviour of the atom pair as well as useful information for the prediction of magnetic Feshbach resonances.

This chapter will briefly introduce the knowledge that has previously been acquired about the RbYb ground state, much of it coming from 2-photon photoassociation experiments utilizing the Rb D1 line. After this, 2-photon photoassociation measurements using the intercombination line free-bound resonance discovered in chapter 7 will be presented and discussed.

8.1. The $X^2\Sigma_{\frac{1}{2}}$ ground state of RbYb

For the molecular ground state derived from the atomic states $^2S_{\frac{1}{2}} + {}^1S_0$, again only the electronic state of Rb is contributing any angular momentum, so the corresponding molecular state has to be $X^2\Sigma_{\frac{1}{2}}$ in short range terms or $X\left(\Omega = \frac{1}{2}\right)$ in the long-range nomenclature. The vibrational levels of this state have already been explored by 2-photon photoassociation performed near the Rb D1 line in a dual-species MOT [72, 253]. Theoretical analysis of the obtained data together with ab initio potentials has yielded relatively precise figures for the dispersion coefficients, the scattering lengths and the position of the bound states near the asymptote. Table 8.1 shows the resulting predictions for the binding energies of the least bound states in ^{87}Rb^{170}Yb. The difference in binding energy between the $F = 1$

---

[1]While in theory it would be possible to go directly to the absolute ground state, the extremely low Franck-Condon factors involved make this infeasible in practice.
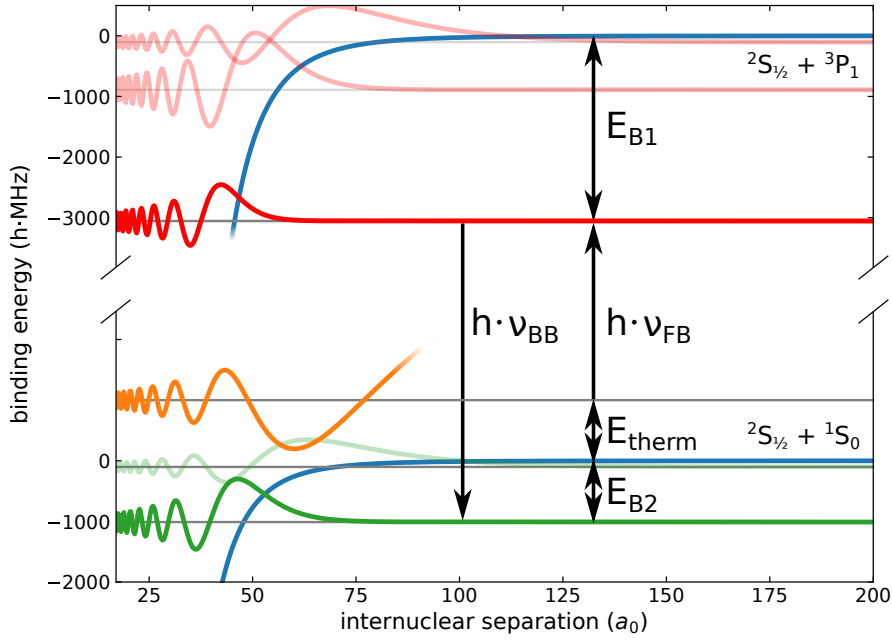
Figure 8.1.: Schematic depiction of the two photon PA, showing the ground and excited state potentials and example vibrational wavefunctions for the scattering state (orange, again the thermal energy is greatly exaggerated), the electronically excited vibrational state (red) and the weakly bound state in the electronic ground state (green).

and $F = 2$ states is also listed, as this quantity has relevance for the strength of certain magnetic Feshbach resonances and would thus be a desirable result of our measurements.

Unfortunately the available experimental data covers a broad range in binding energies only for the isotopologue ^{87}Rb^{176}Yb, so the validity of predictions for the other isotopologues hinges on the applicability of simple Born-Oppenheimer mass scaling. However, this scaling can be expected to hold to a very high degree due to the large mass and the absence of any other electronic states coupling to the groundstate potential [60, 254].

As these measurements where performed on the broad Rb D1 line and using a free-running laser with the detunings determined by a wavemeter (or a beatnote for a few weakly bound levels), they carry uncertainties of tens to hundreds of MHz.

8.2. 2-photon-photoassociation using the intercombination line

Experiments for 2-photon PA proceed in a similar way to those for the free-bound transition described in the previous chapter, with the addition of the bound-bound laser. In all experiments described here, both the free-bound and the bound-bound laser are kept on for the entire interaction time in order to maximize the observed signal. All data shown in this chapter was acquired using the free-bound resonance at $-3057\,\text{MHz}$, but similar results

| $\Delta\nu'$ | ν | binding energy | | hyperfine | experimental $F = 1$ |
		$F = 1$	$F = 2$	splitting	binding energy
-1	65	-0.103 GHz	-0.103 GHz	0.2 MHz	0.113(15) GHz
-2	64	-1.019 GHz	-1.017 GHz	1.1 MHz	1.029(16) GHz
-3	63	-3.675 GHz	-3.673 GHz	2.5 MHz	
-4	62	-9.018 GHz	-9.013 GHz	4.5 MHz	
-5	61	-17.997 GHz	-17.990 GHz	7.2 MHz	
-6	60	-31.564 GHz	-31.554 GHz	10.5 MHz	
-7	59	-50.665 GHz	-50.650 GHz	14.4 MHz	

Table 8.1.: Predicted $R = 0$ binding energies for the seven least bound states of ^{87}Rb^{170}Yb $X^2\Sigma_{\frac{1}{2}}$ ground state [56, 255]. The two most weakly bound states have previously been observed by 2-photon photoassociation spectrosopy near the D1 line [56, 72].

could also be obtained using the line at -3074 MHz.

Keeping the free-bound laser on resonance and scanning the bound-bound laser as described in the first case in the previous section, the two least bound states $\Delta\nu' = -1$ and $\Delta\nu' = -2$ could be observed. Typical spectra for both transitions are shown in Figure 8.2 together with fits of Equation 2.23 – which for this case reduces to a Lorentzian – , integrated over the thermal distribution. In both cases the lineshape and width is dominated by the thermal energy. The bound-bound beam was generated using either the AOM (see section 4.5.2) or the EOM (see section 4.5.2) setups for the $\Delta\nu' = -1$ and $\Delta\nu' = -2$ states respectively

Attempts at observing the next two states $\Delta\nu' = -3$ and $\Delta\nu' = -4$ using the diode laser failed. For the $\Delta\nu' = -3$ this is likely caused by excessive off-resonant excitation (see
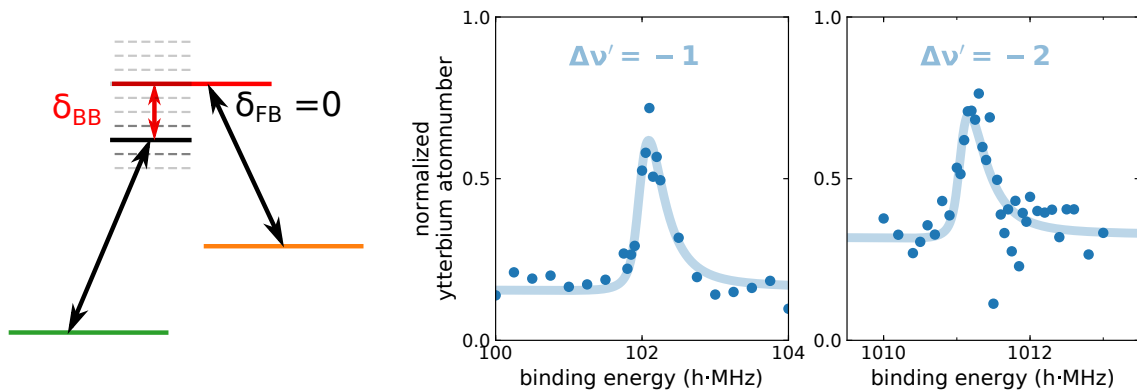
Figure 8.2.: Level scheme for the 2-photon photoassociation measurement when only the bound-bound laser is scanned and the lineshapes observed for the two least bound states. The lines are fits of Equation 2.23 integrated over the thermal distribution. [Figure reprinted from Phys. Rev. A 107, 023114 (2023), ©2023 American Physical Society]
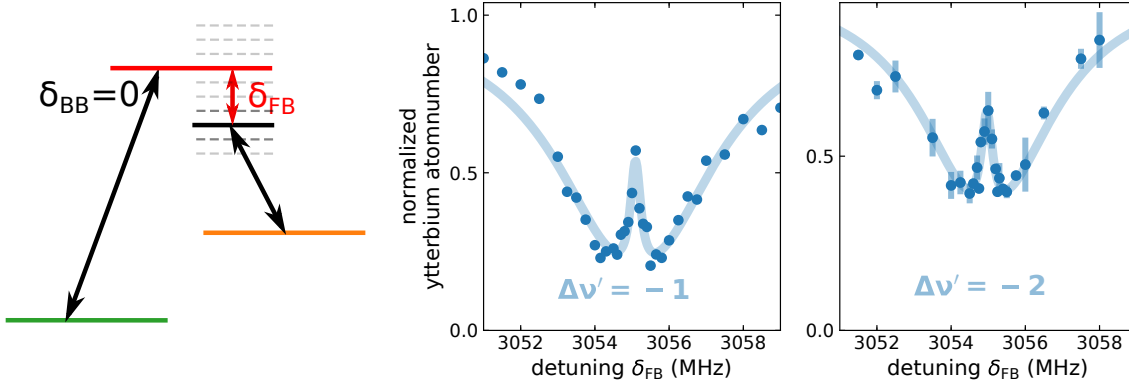
Figure 8.3.: Level scheme for the 2-photon photoassociation measurement for the *dark resonance* measurement with $\delta_{BB} = 0$ and variable δ_{FB}, and the corresponding lineshapes obtained for the two observed states. The lines are fits of Equation 2.23 integrated over the thermal distribution. [Figure reprinted from Phys. Rev. A 107, 023114 (2023), ©2023 American Physical Society]

section 8.4). For $\Delta\nu' = -4$, reasons might include an unfavorable Franck-Condon factor or insufficient performance of the diode laser phase lock. To test the latter theory, we attempted to observe the $\Delta\nu' = -2$ state using the diode laser instead of the AOM and indeed obtained a broader, noisy signal with reduced contrast compared to the measurements with the AOM, where the coherence between both beams can be assumed to be perfect for our purposes. While the beatnote measurement presented in section 4.5.2 shows a narrow carrier peak, this peak might only contain a small portion of the laser power which is not sufficient to observe a clear signal. Further investigation and improvement of this system will thus be needed in the future.

8.3. Dark resonance spectroscopy

Another way of observing two-photon photoassociation once the position of both bound states is known is to scan the free-bound detuning δ_{FB} while keeping the bound-bound detuning fixed at $\delta_{BB} = 0$.

For low values of Ω_{BB} – corresponding to the dark state or interference picture –, this results in the classic dark resonance lineshape [110], where the free-bound lineshape is modified by a sharp central dip. Such measurements are shown in Figure 8.3. Again the data is fitted with Equation 2.23, integrated over the thermal distribution of scattering energies.

When Ω_{BB} is large compared to the effective linewidth, this corresponds to the light shift picture and two distinct peaks that are separated by the generalized Rabi frequency are observed. This is the Autler-Townes splitting, which is commonly used for the measurement of Franck-Condon factors [73]. Mainly due to the limited bound-bound laser power – not least because of off-resonant scattering which will be discussed in the following section –

this regime could not be accessed in our experiment.

The dark resonance method, in addition to providing an attractive plot, has the advantage of containing information about both the free-bound and the bound-bound transition in a single scan. For the data shown, the values extracted from the fit are $\Omega_{\mathrm{FB}} \approx 2\,\pi \cdot 1\,\mathrm{kHz}$ and $\Omega_{\mathrm{BB}} \approx 2\,\pi \cdot 1\,\mathrm{MHz}$ for both transitions, with a free-bound laser power of $0.5\,\mathrm{mW}$ and bound-bound laser powers of $0.1\,\mathrm{mW}$ for the $\Delta\nu' = -1$ state and $0.02\,\mathrm{mW}$ for the $\Delta\nu' = -2$ state.

8.4. Off-resonant excitation

As the only free-bound transition known so far for our system is relatively weak and close to the asymptote, the measurements presented here are plagued by off-resonant excitation of the atomic transition.

In fact, for the $\Delta\nu' = -3$ state the bound-bound laser frequency will be detuned from the atomic resonance by only $\sim 0.6\,\mathrm{GHz}$. Even worse, when light to address the $\Delta\nu' = -2$ state is generated using the EOM, the third sideband at $3 \cdot f_{\mathrm{EOM}} = 3.03\,\mathrm{GHz}$ is detuned from the atomic resonance by only $\sim 0.02\,\mathrm{GHz}$ and thus creates troublesome excitation rates already at very low powers.

This strongly limits the usable intensities for the bound-bound laser and thus the achievable Rabi frequencies and will likely prevent the efficient photoassociation in a pump and dump scheme as well as any coherent processes under the current experimental conditions. For further experiments a stronger free-bound transition or laser frequencies that are farther detuned from the atomic line would thus be highly desirable.
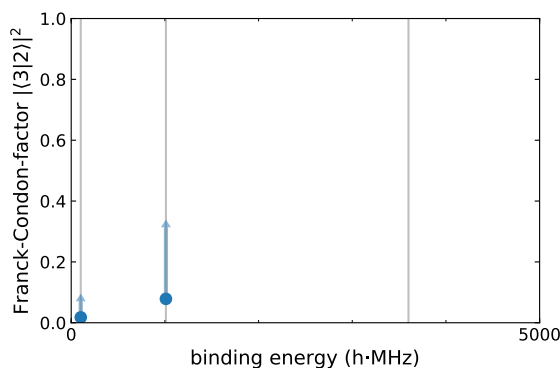
8.5. Franck-Condon factors

We will now attempt to quantify the coupling strength of the observed bound-bound transitions. As the states we are dealing with here are still very weakly bound, it is reasonable to assume that their dipole matrix elements are still close to the atomic value.

From the fits shown in the previous section, the bound-bound Rabi frequency Ω_{BB} can be estimated. Combined with the intensity I_{PA} of the photoassociation light calculated using the measured beamwaist, this gives a value of the bound-bound Franck-Condon factor

$$f_{\mathrm{c}} = \left(\frac{\Omega_{\mathrm{BB}}}{\Omega_{\mathrm{at}}}\right)^2 \qquad , \text{where} \qquad \Omega_{\mathrm{at}} = \gamma\sqrt{\frac{I_{\mathrm{PA}}}{2\,I_{\mathrm{sat}}}}, \tag{8.1}$$

where I_{sat} and γ are the atomic saturation intensity and natural linewidth. The Franck-Condon factors thus obtained for the two states observed in the experiment are plotted in Figure 8.4 as a function of binding energy.

As the actual intensity at the location of the atoms can be assumed to be somewhat lower than the calculated intensity, e.g. due to imperfect alignment, this can be seen as a lower bound on the Franck-Condon factors.

Figure 8.4.: Estimates of bound-bound Franck-Condon factors extracted from the measurements shown in Figure 8.3.

The bound-bound Franck-Condon factors depend sensitively on the number of bound states and thus the short range behavior of both potentials. As this is unknown for the excited state, no attempt to model the FCFs using calculated wavefunctions is made in this case.

While the sum of the observed FCFs is already substantial, there still is room for more states with appreciable FCFs and the two observed states show an increasing trend.

Similarly the reflection approximation – predicting large FCF between states that have outer turning points at a similar separation – would predict the maximum FCF to occur near the $\Delta\nu' = -3$ state.

While the FCFs for $\Delta\nu' = -3$ and/or $\Delta\nu' = -4$ might still turn out to be small due to an unfortunate placement of the wavefunctions nodes, at present it is likely that the failure to detect additional states may be due to the experimental issues described previously rather than due to weak transitions.

8.6. Shifts and binding energies

As is the case for the 1-photon photoassociation, there are a variety of factors influencing the apparent photoassociation detuning. This section will explore their contributions and finally determine the binding energies of the two observed states.

8.6.1. Zeeman shifts

For both observed states the Zeeman shift was determined by measurements similar to those used on the free-bound transition (see section 7.6) to be less than $0.1\,\mathrm{MHz/G}$. It can thus be assumed that the states probed in the ground states, like the scattering state, are of $|F = 1, \ m_F = -1\rangle$-character. The fact that no transitions with a different magnetic moment were observed indicates that the bound-bound laser does not induce a significant coupling between the Rb Zeeman or hyperfine states. It also implies the excited state does not have a significant $|f = 1, m_f = 0\rangle$

8.6.2. Thermal energy

In all the experiments presented here, the atoms are only weakly trapped with $\hbar\omega_{\mathrm{trap}} \ll k_B T$ and the scattering state $|1\rangle$ is thus a continuum with thermally distributed energies rather than a well defined single state. As discussed in the previous chapter the mean collision energy is on the order of $h \cdot 0.2\,\mathrm{MHz}$ for typical experimental conditions. This gives rise to an asymmetrical broadening of the observed lines that is obvious in Figure 8.2 and somewhat more subtle in Figure 8.3. In the latter case it also prevents us from extracting the true lifetime of our dark state – which hopefully will be much longer than that corresponding to the thermal linewidth – from the measured spectra.

While it is merely annoying at present, this thermal spread of energies poses a significant obstacle to the implementation of coherent techniques like STIRAP (see section 9.5) and will have to be overcome for future experiments.

8.6.3. Light shifts

The light shifts due to the trapping light can be expected to cancel to a large degree, as the electronic states in the scattering and in the final bound state will experience almost identical polarizability at the trapping wavelength. While the trap light shift is different for the electronically excited state (see subsection 7.9.2), this does not influence the measured binding energies.

The dark resonance is also insensitive to probe light shifts from either of the two probe fields [256][2]. Unlike in the free-bound measurements light shifts are thus not a relevant source of uncertainty in 2-photon photoassociation measurements.

8.6.4. Binding energies

The main results of our measurements are of course the binding energies of the vibrational states. Taking into account the thermal shifts, the measured binding energies are $E_B(\Delta\nu' = -1) = h \cdot 101.9(1)\,\mathrm{MHz}$ and $E_B(\Delta\nu' = -2) = h \cdot 1011.0(1)\,\mathrm{MHz}$. This is in reasonable agreement with the predicted binding energies of $h \cdot 103\,\mathrm{MHz}$ and $h \cdot 1019\,\mathrm{MHz}$ (see Table 8.1), especially considering the experimental error bars of the data used to build the model are in the range between $7\,\mathrm{MHz}$ and $257\,\mathrm{MHz}$.

A more detailed analysis of the binding energies – similar to that previously performed on the D1 line data [56] – would require data involving either more bound states or more isotopologues to make use of the more precise binding energies obtained. Such data would for example allow for a precision test of Born-Oppenheimer mass scaling in the RbYb system and further refinement of the model potentials.

---

[2]Note this only holds true for the photoassociation transition itself and the light shifts caused by the nearby atomic transition may still significantly influence a STIRAP sequence [82].

8.7. Hyperfine splitting of the ground state

For further experiments the change of the hyperfine splitting with increasing binding energy in the ground state is of considerable interest, as this interaction represents one of the main coupling terms of interest for magnetic Feshbach resonances [40].

For the states accessible with our laser system this shift is expected to be on the order of a few Megahertz according to predictions by Borkowski et al [56] shown in the last column of Table 8.1 and would thus be easily resolvable in our measurements. At present this measurement is prevented by the absence of a known free-bound transition originating from the $F = 2$ state of Rb. There is however no reason to believe that such a transition can not be found in a more extensive search.

On the other hand experiments in RbSr have been successful in performing this measurement using the same hyperfine state for the one-photon transition and changing the hyperfine state on the bound-bound transition [241]. Once the diode laser setup is fully implemented for two-photon photoassociation, this route may be an option if no suitable $F = 2$ free-bound transition can be located. However it remains to be seen whether the strength of the bound-bound transition is sufficient to achieve a clear signal in this case, as so far no such coupling could be observed.

8.8. Conclusion

Using the free-bound transition discovered in chapter 7, 2-photon photoassociation to the two least bound states of the ground state was successfully observed, both by scanning just the bound-bound laser and in the dark-resonance configuration where the free-bound detuning is scanned while keeping the two-photon detuning at zero. In both cases the linewidth of the resonance is limited by the thermal energy distribution of the initial sample. The observation of 2-photon photoassoiation constitutes further confirmation that the resonance discovered in chapter 7 is indeed an RbYb photoassociation resonance.

The binding energies of the two observed states were determined to be $E_B(\Delta\nu' = -1) = h \cdot 101.9(1)\,\mathrm{MHz}$ and $E_B(\Delta\nu' = -2) = h \cdot 1011.0(1)\,\mathrm{MHz}$, two orders of magnitude more precise than the values obtained in previous measurements utilizing the Rb D1 line. This improved precision will allow the detailed investigation of for example the hyperfine splitting of the ground state in future experiments. This will provide important information on the coupling strength of certain Feshbach resonances, while the measured binding energies allow precise prediction of their locations.

Last but not least the observation of a dark resonance opens the perspective of coherent free-bound photoassociation as a route towards ground state molecules, although this will require certain improvements to the apparatus. These aspects will be discussed in detail in the next chapter.

9.

Outlook

This chapter aims to give a roadmap towards the goal of producing RbYb molecules in the absolute ground state. The first sections deal with improvements that can be made to get to a better starting point for photoassociation and especially for the effective production of molecules by photoassociation. A section on magnetic Feshbach resonances introduces a technique that may serve as an alternative to photoassociation or to complement it. Finally, the route from the weakly bound molecules produced by these techniques to the absolute ground state will be sketched.

9.1. Improved transport

The optical transport from the production chambers to the science chambers repeatedly proved to be a bottleneck in the operation of the experiment. Especially for Yb the transport performance depends critically on the axial trap frequency and thus beam quality of the trapping laser and suffers from even slight degradations of the components operated at high power. The need to first load the atoms into a single beam trap that necessarily has weak confinement along one direction and later transfer to a crossed trap is also limiting the phase space trajectory, especially for the Yb isotopes with low intraspecies scattering lengths

In the long term it might thus be desirable to make this step more robust. One approach would be the use of an optical lattice travelling with the atoms. While having a retroreflector on a second, synchronized translation stage [257] would be an option, this would require additional translation stages of similar working distance, adding considerable cost and complexity. Another approach to realizing a moving lattice is to independently vary the frequency of two counterpropagating beams derived from the same source using AOMs. However, in contrast to the lattice elevator described in section 4.6.2, the translation distance is much larger than the Rayleigh range here, so the beam divergence may not be neglected here.

Transport over a similar distance to the one required here has recently been demonstrated [258] by a running optical lattice formed by the interference of a weakly focussed Gaussian and a Bessel beam. A similar scheme could potentially be implemented here, with a stationary, weakly focussed beam counter-propagating to the tweezer beam. As the lattice is translated by controlling AOM frequencies, in our case the existing translation stages

could be used to keep the focus of the tightly focussed beam aligned with the location of
the atoms.

Formation of an optical lattice would however require the use of a spectrally narrow laser
source. While the commercial amplifier used for the Rb tweezer is supposedly designed
for this, our current homebuilt amplifier designs would be severely limited in their output
power by SBS (see section 3.1.3).

9.2. A more balanced trap

It has become obvious in the course of this thesis that the large difference in trap depth
between Rb and Yb makes the preparation of a cold mixture unnecessarily difficult. A high
phase space density is however a requirement for efficient association, as well as for many
applications of ultracold polar molecules.

One of the next steps is thus the implementation of a trapping scheme that will be able
to provide similar trap depths for both species by introducing trapping beams at additional
wavelengths.

Suitable wavelengths include 532 nm, which is attractive for Yb and repulsive for Rb,
allowing its use as second wavelength in a bichromatic trap [62, 65, 259] to balance the
trap depths. Generation of high powers at this wavelength is straightforward by frequency
doubling of 1064 nm light and a reasonably large detuning from all atomic transitions ensures
low scattering rates.

Another possibility would be a trap between the Rb D1 and D2 lines around 790 nm. This
would allow the Rb polarizability to be tuned from strongly repulsive to strongly attractive,
while it remains attractive for Yb. Useful conditions would include the Rb-blind or tune-
out wavelength, where only Yb would be affected by the beam as well as a wavelengths
where both species experience either equal trap depths or equal trapping frequencies. This
flexibility comes at the cost of the close proximity to strong Rb transitions, leading to high
scattering rates and thus short trap lifetimes for practical trap depths. A similar scheme
could be realized around 420 nm [260] at the cost of much less accessible laser wavelengths.

Finally, a trap that is close to the Yb intercombination line at 556 nm would allow large
trap depth for Yb with little effect on Rb [69, 70], again associated with larger scattering
rates for Yb.

Any of these schemes could allow the production of samples with more balanced temper-
atures for both species, eventually opening the possibility of producing a double species
Bose-Einstein condensate or in the case of the fermionic Yb isotopes a Bose-Fermi gas. In
addition to greatly enhancing densities and free-bound photoassociation rates this would
significantly decrease the mean collision energy, allowing for higher resolution spectroscopy
and eventually even the use of coherent techniques such as STIRAP (see section 9.5).
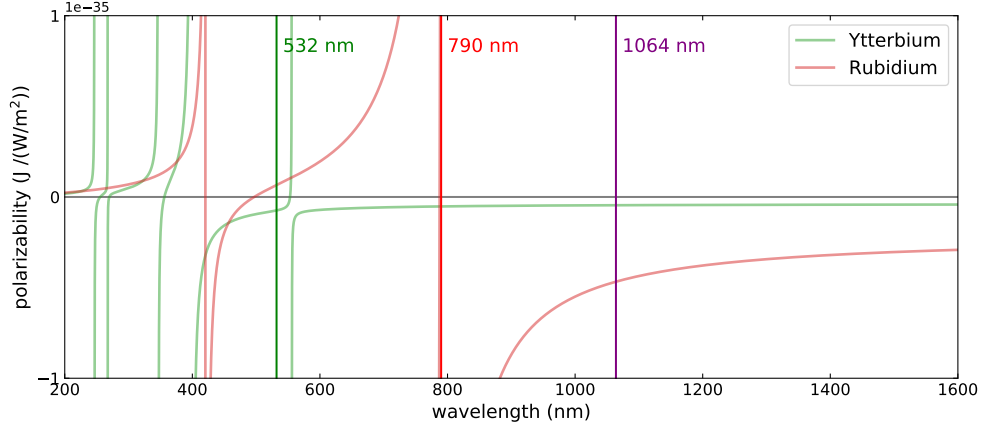
Figure 9.1.: Plot of the trap depth per intensity for both species as a function of trap wavelength. The new wavelengths 532 nm and 790 nm and the current trap wavelength of 1064 nm are marked by vertical lines.

9.3. Optical Lattices and the Mott-Insulator phase

Improvements to PA rates can not only be achieved by increasing the phase space density, but also by increasing the local density and changing their energy spectrum. A three dimensional optical lattice with atoms prepared in the lowest band would greatly benefit the 2-photon photoassociation process by providing a discrete trap induced bound state rather than a continuum of scattering states as a starting point [76, 81]. This would eliminate the thermal broadening of the two photon resonance and any associated challenges. Additionally, the lattice confinement leads to an enhancement of the local density and thus also improves the free-bound transition.

The apparatus is already equipped with a 3D lattice setup (see [180], subsection 4.6.2 and subsection 5.1.6). However due to the relatively high temperature of the samples until now this capability could not yet be fully exploited. The improvements to the preparation sequence described in the previous section will enable loading of the lattice ground states and thus allow the exploitation of the described benefits.

Mott Insulator

Even greater improvements could be attained if, rather than having the atoms delocalized over the entire lattice in a superfluid state or having a thermal distribution of atom numbers localized to individual sites, it could be ensured that each (or most) lattice site is occupied by exactly one atom of each species. The preparation of a Mott insulator state [261] provides a way to achieve this goal and thus provides an ideal starting point for photoassociation [262]. A short introduction to this state will thus be given here: Atoms in the ground state of an optical lattice in the tight-binding limit are well described by the *Bose-Hubbard-Hamiltonian*

given by

$$\hat{H} = -J \sum_{<i,j>} \hat{a}_i^\dagger \hat{a}_j + \frac{U}{2} \sum_i \hat{n}_i(\hat{n}_i - 1) \tag{9.1}$$

where $<i,j>$ denotes the summation over nearest neighbours, $\hat{a}_i^\dagger$ and $\hat{a}_j$ are the creation and annihilation operator for an atom at lattice site i combining to form $\hat{n}_i = \hat{a}_i^\dagger \hat{a}_i$ as the number operator for lattice site i, J is the tunneling matrix element and U the on-site interaction. The external confinement and the chemical potential have been omitted here for clarity.

The values of U and J can be obtained as overlap integrals between the wavefunctions of localized atoms in the lattice, the *Wannier* functions. With increasing lattice depth s, the tunneling J decreases exponentially as the barriers between sites increase in height, while U increases as $s^{\frac{3}{4}}$ due to the increased confinement on each lattice site.

For low values of $\frac{U}{J}$, the ground state of the system is the superfluid state, where each atom is delocalized over the entire lattice. For sufficiently high values of $\frac{U}{J}$, the onsite interaction becomes dominant and atoms are localized to individual lattice sites in a manner that minimizes the interaction energy. This is the Mott insulator state, where each lattice site has a well defined occupation number. In practical experiments, a harmonic external confinement potential usually leads to shells with Mott insulating zones of increasing occupation number towards the center of the trap, separated by superfluid zones.

When sites with one atom of each species are energetically favorable compared to having sites with only one species, the ground state will be a mixed Mott insulator [263]. Such a mixed Mott insulator is the ideal starting point for photoassociation. In addition to the advantages of a three dimensional optical lattice described in the previous section, it can ensure that the majority of lattice sites is populated by exactly one atom of each species, so that they can then be converted into molecules with high efficiency and are protected from collisional losses after conversion.

For this approach to work to its full potential, the Mott insulator regime has to be achieved for both species. In the case of Yb, this will be somewhat challenging – although calculations indicate it will be possible – with the current lattice setup due to its low polarizability at 1064 nm. An upgrade to multiple fiber amplifiers instead of a single system for all lattice axes, thus providing higher powers in spite of the challenges involved in high power narrow line amplification (see section 3.1.3) would allow achieving this goal more easily.

The isotope combination has to be chosen so that the mixed Mott insulator with one atom of each species is energetically favorable with respect to having sites with two atoms of either species. This will be the case for the combination of ^{87}Rb and ^{170}Yb (see section 2.4) used in the experiments described in this thesis. For other isotopologues with less favourable interspecies scattering length, magnetic Feshbach resonances (see section 9.6) could be exploited to achieve this condition.

In other groups the Mott insulating phase has been experimentally achieved for both Rb [264] and Yb [265, 266] and different two species Mott insulator phases have been explored

in mixtures of different Yb isotopes [219]. Our desired mixed Mott insulator phase in an RbYb mixture has however not been demonstrated yet.

9.4. Further intercombination line photoasssociation spectroscopy

With the upgrade described in the previous section, the experiment will become sensitive to even weaker free-bound transitions and potentially give access to more deeply bound vibrational states of the excited potential.

Locating more bound states is necessary to obtain a good understanding of the excited potential and may result in the discovery of a more favorable free-bound transition. While as described in section 7.5 it is unlikely that a significantly stronger transition than the one reported here can be found, the use of a more deeply bound vibrational state will significantly reduce off-resonant excitation of the atomic line, and may thus still improve overall performance.

Finding free-bound transitions associated with the $F = 2$ state of the Rb atom will enable the measurement of the hyperfine splitting in the electronic ground state potential, which will give information helpful for the search for magnetic Feshbach resonances (see section 9.6). Finally, exploring other isotopologues may result in the discovery of a more favorable free-bound transition.

Extension of two-photon photoassociation can also be expected to be both relatively straightforward and worthwhile. As detailed in chapter 8, the range of accessible vibrational levels of the $X^2\Sigma$ ground state could be greatly increased by improvements to the diode laser setup. Extending this spectroscopy to more deeply bound vibrational levels of the electronic ground state will allow further refinement of the molecular potential curve for this state.

9.5. STIRAP

Once optimal starting conditions for photoassociation have been established as described in the previous sections, it may be possible to further improve the performance by use of more sophisticated schemes for the photoassociation itself.

In **STI**mulated **R**aman **A**diabatic **P**assage or STIRAP [46] the dark state we observed in chapter 8 is exploited to transfer atoms from one state - in this case the scattering state - to a bound state in the electronic ground state while avoiding any population of the electronically excited state and the associated decoherence.

Ideally, the first photoassociation step would be performed using free-bound STIRAP sequences as demonstrated for Sr_2 [81, 82]. This would allow an efficient, coherent and reversible transfer from atom pairs to molecules. The reversibility is of particular advantage, as it allows detection of the molecules by converting them back into atoms and using the existing detection schemes.
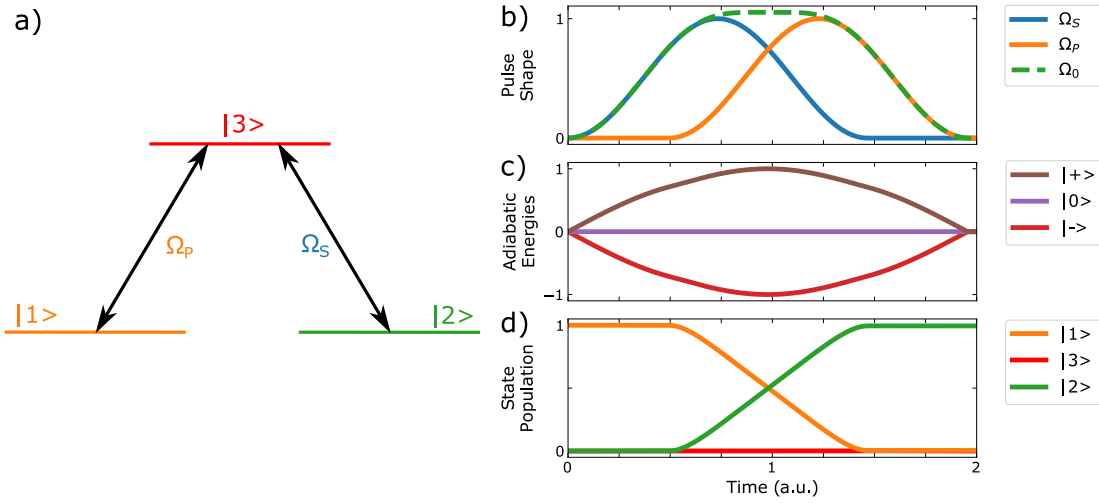
Figure 9.2.: Schematic depiction of a STIRAP sequence **(a)** level scheme with the pump coupling Ω_P and the Stokes coupling Ω_S. **(b)** The counterintuitive pulse sequence for Stokes and Pump beam. The dashed line shows the rms Rabi frequency, which stays constant during the actual transfer. **(c)** time dependence of the energies of the adiabatic states $|-\rangle$, $|0\rangle$ and $|-\rangle$. **(d)** evolution of the population of the states $|1\rangle$, $|2\rangle$ and $|3\rangle$ during the transfer, clearly showing the practically complete transfer to state $|2\rangle$ without any intermediate population appearing in $|3\rangle$.

The corresponding Λ-level scheme with the pump coupling Ω_P between the initial and the intermediate state and the Stokes coupling Ω_S between the intermediate and the final state is illustrated in Figure 9.2a. In the rotating wave approximation the corresponding Hamiltonian is given by

$$\hat{H}_{\mathrm{RWA}} = \frac{\hbar}{2} \begin{pmatrix} 0 & 0 & \Omega_{\mathrm{P}} \\ 0 & 2\delta & \Omega_{\mathrm{S}} \\ \Omega_{\mathrm{P}} & \Omega_{\mathrm{S}} & 2\Delta \end{pmatrix} \tag{9.2}$$

where $\Omega_{\mathrm{P}}(t)$ and $\Omega_{\mathrm{S}}(t)$ are the Rabi frequencies on the pump and stokes transition, Δ is the one photon detuning and δ is the two photon detuning. After introducing the two mixing angles θ and ϕ defined by

$$\tan \theta(t) = \frac{\Omega_{\mathrm{P}}(t)}{\Omega_{\mathrm{S}}(t)} \qquad \text{and} \qquad \tan 2\phi(t) = \frac{\sqrt{\Omega_{\mathrm{P}}(t)^2 + \Omega_{\mathrm{S}}(t)^2}}{\Delta} \tag{9.3}$$

the following adiabatic eigenstates are obtained:

$$\begin{aligned} |0\rangle &= & \cos\theta & & |1\rangle & - & \sin\theta & & |2\rangle & & \\ |+\rangle &= & \sin\theta\sin\phi & & |1\rangle & + & \cos\theta\sin\phi & & |2\rangle & + & \cos\phi\,|3\rangle \\ |-\rangle &= & \sin\theta\cos\phi & & |1\rangle & + & \cos\theta\cos\phi & & |2\rangle & - & \sin\phi\,|3\rangle \end{aligned} \tag{9.4}$$

where the time dependence of the mixing angles has been omitted for clarity. It is obvious that the state $|0\rangle$ can be smoothly moved from the initial state $|1\rangle$ to the final state $|2\rangle$ by

varying the mixing angle θ. Figure 9.2b shows a typical set of pulses with a $\cos^2$-pulseshape. Note that for a transfer from $|1\rangle$ to $|2\rangle$, the Stokes pulse coupling $|2\rangle$ and $|3\rangle$ actually has to precede the pump pulse, which couples $|1\rangle$ and $|3\rangle$. This counter-intuitive pulse ordering is characteristic for STIRAP.

The evolution of the adiabatic state energies during this sequence is illustrated in Figure 9.2c. While the energy of the $|0\rangle$-state remains at zero, the energies of the other two states are given by

$$E_\pm = \frac{\Delta \pm \sqrt{\Delta^2 + \Omega_P^2 + \Omega_S^2}}{2} \tag{9.5}$$

This lifting of the degeneracy corresponds to the Autler-Townes splitting induced by the driving fields. The non-overlapping parts of the pulses thus serve to establish a sufficient energy splitting between these states, which then allows the change of the mixing angle to be performed adiabatically. The system remains in the $|0\rangle$-state which, as shown in Figure 9.2d, is transformed from $|1\rangle$ to $|2\rangle$ and never acquires a component of the lossy state $|3\rangle$ during the actual transfer. The transfer efficiency for such a pulse sequence is approximately given by [267]

$$P = \exp\left(-\frac{\pi^2 \gamma}{\Omega_0^2 \tau} - \left(\frac{\delta^2 \gamma}{2\,\Omega_0^2} + \frac{D}{2}\right)\tau\right). \tag{9.6}$$

The first term represents the adiabacity condition where γ is the decay rate of the lossy state, τ is the duration of the transfer and $\Omega_0^2 = \Omega_P^2 + \Omega_S^2$ is the reduced Rabi frequency. The second term, which is often omitted in applications dealing with discrete states where it can be kept at zero, gives the lineshape as a function of the two-photon detuning δ and the third term represents the influence of a finite relative linewidth D between the two lasers.

In contrast to applications dealing with discrete states, in free-bound STIRAP the thermal energy distribution of the scattering state means the resulting averaging over the two-photon lineshape has to be taken into account. Under the current experimental conditions, where both the natural linewidth of the excited state and the thermal energy are orders of magnitude larger than the achievable free-bound Rabi frequency, this leads to a vanishingly small transfer efficiency. The use of repeated low efficiency pulses has been proposed for this situation [268], but the need to remove the transferred molecules – either by hiding them in a dark state or by physical removal from the interaction zone – will make the production of cold and dense samples challenging using this method.

The main challenges to be overcome for the successful use of free-bound STIRAP are thus the thermal energy distribution of the scattering state and the currently very low Rabi frequencies achieved on the free-bound transition[1]. The improvements described in the previous sections will thus be a significant step towards the implementation of a free-bound STIRAP.

---

[1]The fact that only the reduced Rabi frequency Ω_0 appears in Equation 9.6 suggests that only one laser needs to have a large Rabi frequency for an effective transfer. On closer inspection, the derivation in [267] only holds if Ω_0 is constant over the entire transfer, necessitating equal peak Rabi frequencies for both transitions, and an efficient transfer is not possible with dissimilar Rabi frequencies.
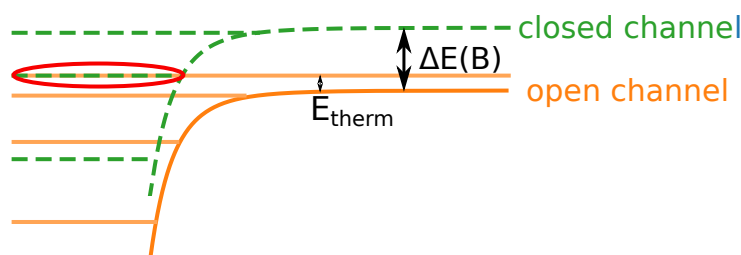
Figure 9.3.: Schematic depiction of a magnetic Feshbach resonance. The scattering state (open channel, orange solid lines) is tuned into resonance with a bound state (closed channel, blue dashed lines) by exploiting the different Zeeman shifts of both states.

While the prospect of a coherent transfer is alluring, it has to be noted that the use of STIRAP for the initial association step is by no means a requirement. Indeed the recent all optical production of absolute ground state Sr_2 molecules uses an initial photoassociation pulse followed by spontaneous decay [269]. The main advantages of the STIRAP route are the high efficiency [81] and its reversibility, meaning that there is a straightforward way to convert molecules back into atom pairs for detection using the established imaging schemes for atoms. In the end a scheme relying on π pulses and or spontaneous decay – or even using magnetoassociation, which will be discussed in the next section, rather than photoassociation – may prove to be experimentally favorable.

9.6. Magnetic Feshbach resonances

In addition to photoassociation or optical Feshbach resonances, magnetically tuneable Feshbach resonances [270] remain an option for the first association step and may also prove useful for manipulating the scattering behaviour of mixtures, potentially enabling the use of isotopologues with unfavorable interspecies background scattering lengths (see section 2.4).

In a magnetic Feshbach resonance, schematically depicted in Figure 9.3, a magnetic field is applied to tune the energy of a bound state – the closed channel – into resonance with the scattering state of typically a different hyperfine state – the open channel. If a coupling between these channels exists, this allows use of the resonance to tune the scattering length and, by adiabatic ramping over the resonances, the association of atom pairs into weakly bound molecules.

The scattering length as a function of magnetic field will exhibit a pole at the resonance. This way, by tuning the field to either side of the resonance, (almost) arbitrary attractive or repulsive scattering lengths can be accessed. The large absolute value of the scattering length close to the resonance leads to high three-body loss rates. This loss provides a convenient signal for the spectroscopy of magnetic Feshbach resonances.

In the case of for example bi-alkali mixtures, the spin-spin interaction provides a strong coupling – corresponding to the large difference between the singlet and triplet potential energy curves – between these channels for states of equal L and M_F. If, as in our case, a spin singlet ground state is involved, there is no such strong coupling term. There are

however a number of weaker couplings which we will briefly explore in this section, following the treatment in [42].

For this we consider the Hamiltonian for a pair of ground state atoms

$$\hat{H} = -\frac{\hbar^2}{2\mu}\nabla_R^2 + V(R) + \hat{H}_{\text{Rb}} + \hat{H}_{\text{Yb}} + \hat{H}' \tag{9.7}$$

where the terms $\hat{H}_{\text{Rb}}$ and $\hat{H}_{\text{Yb}}$ represent the internal state of isolated atoms and the perturbation term $\hat{H}'$ – which contains the relevant coupling terms – is given by [42]

$$\hat{H}' = \underbrace{\Delta\zeta_{\text{Rb}}(R)\hat{i}_{\text{Rb}}\cdot\hat{s}}_{\text{Mechanism I}} + \underbrace{\Delta\zeta_{\text{Yb}}^{\text{iso}}(R)\hat{i}_{\text{Yb}}\cdot\hat{s}}_{\text{Mechanism II}} + \underbrace{\sqrt{6}\Delta\zeta_{\text{Yb}}^{\text{dip}}(R)T^2(C)\cdot T^2(\hat{i}_{\text{Yb}},\hat{s})}_{\text{Mechanism III}} + \dots \tag{9.8}$$

where each perturbation term corresponds to a possible coupling mechanism associated with a distance dependent modification $\Delta\zeta(R)$ of the hyperfine coupling constant of one of the atoms and T^2 denotes a second order tensor.

Mechanism I arises from the influence of the Yb atom deforming the Rb electron cloud and thus slightly changing the hyperfine coupling constant. This leads to a coupling between states of different F and thus allows the association of atoms with $F = 1$ into a molecular state with $F = 2$.

This interaction was the first to be proposed as leading to Feshbach resonances in such systems [40, 41]. A search for resonances of this type in RbYb was subsequently conducted in the previous iteration of this experiment [69], with the main effort concentrating on the isotopologue ^{85}Rb^{171}Yb. Less exhaustive searches were also performed for ^{85}Rb^{172}Yb and ^{85}Rb^{174}Yb. All of these remained fruitless. However the experimentally accessible fields limited these searches to only a few level crossings. As the coupling strength increases with the square of the magnetic field for low[2] fields, these resonances also had to be expected to be relatively weak. The use of ^{85}Rb without use of Feshbach resonances to control scattering behaviour dictated relatively low atomic densities, leading to a reduced detection sensitivity. A new search with possibly increased magnetic field capabilities, and improved atomic densities could thus be worthwhile.

Since the previous unsuccessful search for MFR in RbYb [71], the observation of MFR in RbSr [43] has confirmed this type of coupling can indeed lead to observable Feshbach resonances. Additionally, the precise spectroscopy of the bound levels of the electronic ground states developed in this thesis will allow measurements of the hyperfine splitting in the $^2\Sigma$ ground state (see section 8.7) and thus confirm the magnitude of this coupling and possibly increase confidence in a further search.

The observations in RbSr also included resonances induced by two other coupling mechanisms. The second observed mechanism stems from hyperfine coupling between the Yb nuclear spin and the Rb valence electron spin. This thus applies only to the fermionic Yb isotopes ^{171}Yb and ^{173}Yb, which are the only Yb isotopes with non-zero nuclear spin. A resonance based on this coupling type II [42] has also recently been observed in the CsYb system [44]. Finally, there are anisotropic interaction terms between the electron spin and

_____
[2]from a theorists perspective

either nuclear spin, only one of which is shown in Equation 9.8 by way of example, resulting in the third coupling mechanism. Resonances based on these other coupling mechanisms have not been explored in the previous RbYb measurements, and might prove a worthwhile target.

9.6.1. Feshbach resonances in electronically excited states

Another approach that has recently been investigated theoretically is the use of the long-lived $^3P_0$ *clock* state of Yb rather than the $^1S_0$ ground state. This enables additional coupling mechanisms and promises resonances that are both stronger and more dense in magnetic field [247] than what is available in the ground state. However, much like was the case with $^2S_{\frac{1}{2}} + {}^3P_1$ photoassociation resonances, the current knowledge of the potentials involved is not sufficient for the prediction of resonances and will have to be improved either by photoassociation or by Feshbach spectroscopy.

9.7. Rovibrational ground state

Once molecules have been prepared in a bound state of the electronic ground state, they can be transferred to the rovibrational ground state using a further STIRAP step [48]. This technique was first demonstrated for Cs_2 [271] and then successfully applied to the heteronuclear molecules KRb [49], RbCs [50, 51], NaK [52] and NaRb [53]. In all of these cases the initial weakly bound molecule was obtained by means of a magnetic Feshbach resonance. The STIRAP transfer to the ground state is however independent of the method used to reach this intermediate state, and photoassociation has the potential to access more deeply bound levels, and may thus even provide an advantage. Very recently, the all optical production of ground state Sr_2 molecules by means of a photoassociation pulse followed by spontaneous decay to a weakly bound molecular state and successive STIRAP has been reported [269].

As the choice of excited potential used for this step is independent of the choice for the first step, the $1^2\Pi_{\frac{1}{2}}$ state could be used again here, making use of the much greater amount of experimental data and theoretical understanding of this potential. In [72], a pair of transitions with wavelengths conveniently located in the telecommunication regions around $1.3\,\mu m$ and $1.5\,\mu m$ has been proposed. These spectral regions are advantageous because of the excellent availability of a wide variety of laser sources and components. In particular extremely widely tunable ECDLs with kHz linewidths based on butterfly gain chips have been demonstrated [272]. In combination with a high bandwidth stabilization system based on a ULE cavity and wideband fiber EOMs to allow tunability of the laser with respect to the cavity modes [273, 274], these would be an attractive choice for this application.

In order to identify suitable transitions, extensive spectroscopy of deeply bound vibrational states will be required, as the current predictions are based on a toy potential and the level spacing is on the order of THz for the relevant states. However, the precise 2-photon spectroscopy developed in this thesis allows highly sensitive detection of light shifts on weakly bound ro-vibrational states of the electronic ground state and will immensely benefit

the search for any transitions originating from these states..

9.8. Experiments with ground state molecules

One of the first experiments with ground state molecules will naturally be the determination of the magnitude of their electric dipole moment. To orient the molecules and make the electric dipole moment observable in the lab frame, the capability to apply a stable and uniform electric field of a strength on the order of 10^4 V/cm will have to be added [14].

After these characterisations have been completed, the experiment will provide a playground for the exploration of dipolar quantum gases as discussed in the introduction. The specific systems that can be implemented here will depend to a large degree on the density and order the molecules can be prepared in.

10.

Summary

In the scope of this thesis, an apparatus for the stable and reliable production of ultracold mixtures of Rb and Yb has been developed and demonstrated.

Due to the use of long distance optical transport, many of the cooling steps for each species can be performed in separate vacuum chambers, allowing them to be performed in parallel and vastly improving optical access to both the production and the science chamber. The separation will allow the reconfiguration of the science chamber for further experiments, for example by installing electrodes or high-field magnetic coils, without breaking vacuum in the production chambers.

Bose-Einstein condensation of each species was demonstrated and ultracold thermal mixtures of both species are routinely produced. The achieved densities compare favorably with those in previous experiments while several hours of hands off operation now allow for extensive spectroscopy to be performed.

A variety of optical traps including an optical lattice allow experiments to be performed under a variety of trapping conditions. Several laser systems with precise, tuneable frequency stabilisation near the narrow $^1\mathrm{S}_0$-$^3\mathrm{P}_1$ intercombination line of Yb were implemented – among them a novel fiber amplifier design – and used for several photoassociation experiments.

Homonuclear $^{170}\mathrm{Yb}_2$ photoassociation resonances up to a binding energy of $h \cdot 10.7\,\mathrm{GHz}$ were measured, extending the range by an order of magnitude compared to the previously known lines in $^{170}\mathrm{Yb}$ and by a factor of five compared to the other more extensively explored isotopes. Although the physics of the Yb dimer are interesting in their own right, these investigations primarily laid the groundwork for the next step.

Working towards the long standing goal of the production of ground state RbYb molecules, extensive photoassociation spectroscopy was performed in a mixture of $^{87}\mathrm{Rb}$ and $^{170}\mathrm{Yb}$ over detunings ranging from $0.1\,\mathrm{GHz}$ to $11\,\mathrm{GHz}$. This search yielded a single pair of resonances around $3\,\mathrm{GHz}$ detuning. To the best of the authors knowledge this is the first time the narrow intercombination line transition of Yb has been used for photoassociation of an Yb-alkali dimer. Relevant shift mechanisms were investigated and the corresponding binding energies were determined to be $h \cdot 3057.0(5)\,\mathrm{MHz}$ and $h \cdot 3074.1(5)\,\mathrm{MHz}$. The photoassociation rate constant was measured to be $K_{\mathrm{PA}} \approx 5 \cdot 10^{-14}\,\mathrm{cm}^3/\mathrm{s}$ under the current conditions and paths for further improvement were identified, for example through use of an optical lattice.

Building on these results, the technique of two-photon photoassociation was used to obtain binding energies for the two most weakly bound vibrational states of the electronic ground state as $E_B(\Delta\nu' = -1) = h \cdot 101.9(1)\,\mathrm{MHz}$ and $E_B(\Delta\nu' = -2) = h \cdot 1011.0(1)\,\mathrm{MHz}$,

with a precision two orders of magnitude higher than that of previous measurements. This sensitive probe paves the way for further investigations of the $^2\Sigma$ ground state of the RbYb molecule and will be invaluable in future spectroscopy. Furthermore, the observation of dark resonances involving these states indicates a successful coherent coupling between atoms and molecules, potentially enabling the coherent photoassociation by free-bound STIRAP in the future.

Finally, various improvements to the apparatus have been suggested. Various topics for further investigations have been pointed out and the path towards production of RbYb molecules in the absolute ground state has been outlined.

A.

Attempts at a *Hund's case (c) or (e)* explanation of the observed spectra

This appendix presents possible interpretations for the observed spectra in two different Hund's cases.

A.1. Interpretation in Hund's case (c)

Having identified *Hund's case (c)* as a likely coupling scheme in subsection 7.6.1), we will now attempt to establish the relevant effective Hamiltonian and use it to explain our observed spectra.

The angular momenta coupling scheme for this variation of *Hund's case (c)* is illustrated in Figure A.1. Here the atomic angular momenta f_{Rb} and j_{Yb} couple to form F_{a} (in analogy to the usual J_{a}). The projection of F_{a} onto the nuclear axis then gives Ω_{F}, which in turn couples to the end-over-end rotation N to form the total angular momentum J. In a
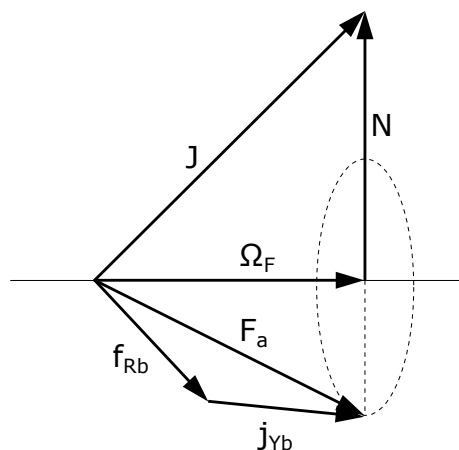
Figure A.1.: Schematic diagram of the most likely angular momentum coupling scheme for the state in question. The atomic f_{Rb} and j_{Yb} form F_a, which precesses around the internuclear axis as indicated by the dashed circle, resulting in the projection Ω_F. In turn Ω_F couples to the end-over-end rotation of the nuclei N to form the total angular momentum J.

magnetic field the state then splits into the Zeeman levels labeled by $M_J = -J.. + J$.

The expected Zeeman shift in case (c) is given by [226]

$$E_Z(B) = \mu_B M_J g_{F_a} \frac{\Omega_F^2}{J(J+1)} B \tag{A.1}$$

resulting in no Zeeman shift for a $|\Omega_F| = 0$ molecule – where the magnetic moment is entirely averaged out – and a shift coefficient decreasing with increasing J, but increasing with $|\Omega_F|$, for the $|\Omega_F| = 1, 2$ states. As we observe a shift of both states, a $|\Omega_F| = 1$ or $|\Omega_F| = 2$ assignment seems likely. As Ω_F is also the projection of J onto the internuclear axis, J has to be equal to or larger than $|\Omega_F|$.

The *Lande g factor* for F_a can be obtained by applying a formula familiar from atomic physics, yielding [1]

$$\begin{aligned} g_{F_a} = \quad & g_{j_{\text{Yb}}} \frac{F_a(F_a+1) - f_{\text{Rb}}(f_{\text{Rb}}+1) + j_{\text{Yb}}(j_{\text{Yb}}+1)}{2F_a(F_a+1)} \\ + \quad & g_{f_{\text{Rb}}} \frac{F_a(F_a+1) - j_{\text{Yb}}(j_{\text{Yb}}+1) + f_{\text{Rb}}(f_{\text{Rb}}+1)}{2F_a(F_a+1)} \\ = \quad & \frac{1}{2} \quad \text{for } f_{\text{Rb}} = j_{\text{Yb}} = 1, F_a = 1, 2 \end{aligned} \tag{A.2}$$

In order to explain the observed zero field splittings, we are also interested in additional terms of the effective Hamiltonian. The rotational energy in *Hund's case (c)* is given by [275]

$$E_{\text{rot}} = B_\nu \cdot \left[J(J+1) - \Omega_F^2 \right], \tag{A.3}$$

where the Ω_F^2 term appears because the end-over-end rotation N^2 is not a good quantum number and the corresponding expectation value is obtained by subtraction of the atomic angular momentum F_a^2 from the total angular momentum J^2.

We can now attempt to use these to explain our experimentally observed spectra: Because a larger Zeeman shift is observed for the higher energy state, while the Zeeman splitting decreases with increasing J, it is likely that the states differ in $|\Omega_F|$. If we assign the two observed transitions to $|\Omega_F| = 1$ and $|\Omega_F| = 2$, each with their respective lowest total angular momentum $J = 1$ and $J = 2$, we obtain the energies shown in Figure A.2.

This assignment provides an explanation for the zero field splitting, which would be equal to B_ν for the proposed assignment, and reproduces the Zeeman splitting behaviour reasonably well - especially considering the only free parameter is the rotational constant B_ν, whose value is very close to that estimated from the binding energy and the long-range potential.

The existence of a $|\Omega_F| = 2$ state means we are in $F_a = 2$. A possible explanation for the fact that no $\Omega = 0$ state is observed in this progression is given by the possibility of the potential leading to a strong broadening of the $F_a = 2$, $\Omega = 0$ state due to predissociation,

---

[1]Note the shift given by Equation A.2 and Equation A.1 agrees with the somewhat more involved derivation in [275].
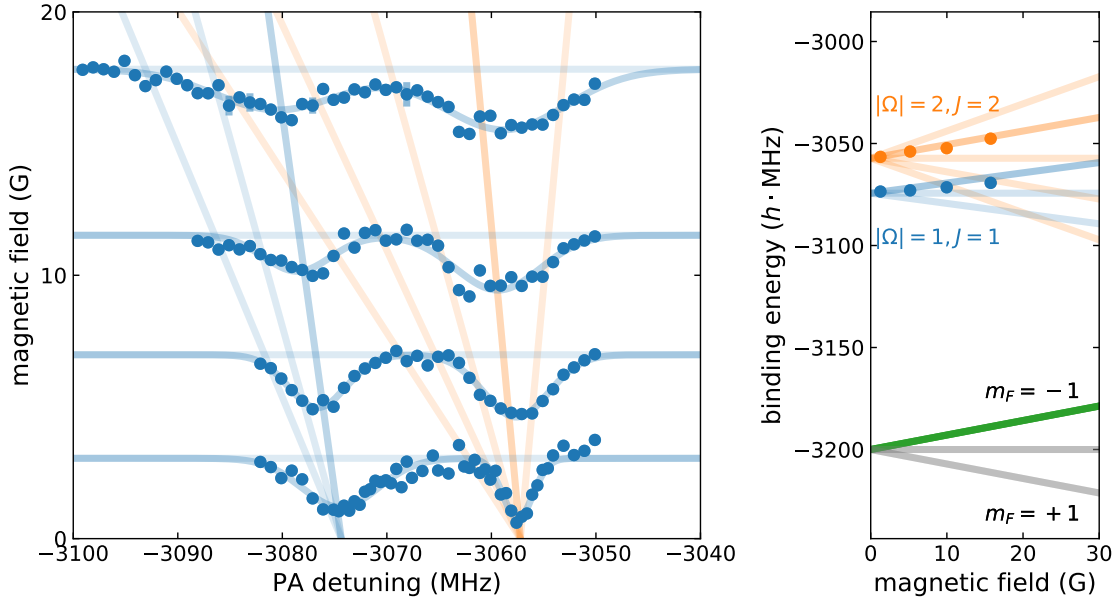
Figure A.2.: Zeeman shift of the PA transition as shown in Figure 7.7, but with the energies and shifts of the suggested *Hund's case (c)* states. The Zeeman states corresponding most closely to the center of mass of the observed spectra are highlighted.

while this is only possible as a higher order process mediated by Coriolis coupling for $|\Omega| = 1,\ 2$ [251].

However, as the value we obtain for g_F is positive (unlike $g_f = -\frac{1}{2}$ for an isolated $f_{\mathrm{Rb}} = 1$ atom), the highlighted state in Figure A.2, which closely corresponds to the center of mass of the observed peaks, actually is the $M_J = +1$ state rather than the $M_J = -1$ state as expected from our scattering state.

Because of this inconsistency and the very limited amount of information available, it has to be stressed that this by no means constitutes a definite assignment of the observed states.

A.2. Attempts at an *Hund's case (e)* explanation

It is of course possible that the analysis in subsection 7.6.1 does not reflect the true situation and another coupling scheme is more appropriate for this state. For example, it might be better described by *Hund's case (e)*. While every effort has been made to explain the observed Zeeman coefficients in a *Hund's case (e)* picture, this remained unsuccesful. For completeness these attempts will be summarized in this section. In the scheme shown in Figure A.3, the Yb total angular momentum j_{Yb} couples to the molecular rotation N to form a new quantum number J. This is analogous to *Hund's case (e)* except for the exclusion of the Rb spin as coupling between the Rb spin and the molecular rotation is assumed to be weak. This separation of the Rb spin allows us to preserve the positive shift
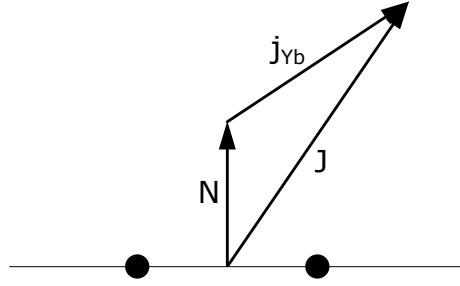
Figure A.3.: Schematic diagram of the a possible *Hund's case (e)*-type coupling scheme. The atomic angular momentum j_{Yb} couples to the end-over-end rotation N to form the total angular momentum J. The Rb angular momentum does not couple to either the Yb angular momentum or the rotation.

for the states associated with the $|f = 1, m_f = -1\rangle$ state, which seems necessary to explain the observations.

In this scenario the Yb magnetic moment in the lab frame is reduced, reflected by the g-factor of

$$g_J = g_{j_{\mathrm{Yb}}} \frac{J(J+1) - N(N+1) + j_{\mathrm{Yb}}(j_{\mathrm{Yb}}+1)}{2J(J+1)}. \tag{A.4}$$

The expected shift coefficients in this case are then given by

$$\frac{dE}{dB} = \mu_B g_{f,Rb}(f_{\mathrm{Rb}})m_f + \mu_B g_J(j_{\mathrm{Yb}}, J, N)m_J. \tag{A.5}$$

Within this coupling scheme we will now explore possible assignments for our two states that approximately reproduce the observed shifts.

1st option

For $N = 1$ and $J = 2$ we get $g_J = \frac{g_j}{2}$ and our first set of candidates

$$A : |f = 1, m_f = -1\rangle_{\mathrm{Rb}} + |J = 2, M_J = 0\rangle_{\mathrm{Yb}} \qquad\qquad 0.7\,\mathrm{MHz/G}$$

$$B : |f = 1, m_f = 0\rangle_{\mathrm{Rb}} + |J = 2, M_J = 1\rangle_{\mathrm{Yb}} \qquad\qquad 0.35\,\mathrm{MHz/G}$$

While the first state preserves the hyperfine state and projection of the Rb atom as well as the projection M_J, the second state requires a change in both of these projections and results in a change in the total projection $M_F = m_f + m_J$ of two, which is not allowed by the dipole selection rules.

If this were the case, PA rates on the second state should improve greatly when Rb is prepared in $|f = 1, m_f = 0\rangle_{\mathrm{Rb}}$ before the photoassociation. This would however require a sufficient magnetic bias field or a 3d lattice to prevent spin relaxation. Furthermore a $N = 1$

state will have the same parity as the $l = 0$ scattering state and such a transition would thus only be allowed from a higher partial wave.

2nd option

Again assuming $N = 1$ another possibility is

$$A : |f = 2, m_f = -2\rangle_{\text{Rb}} + |J = 2, M_J = 2\rangle_{\text{Yb}} \qquad 0.7\,\text{MHz/G}$$

$$B : |f = 2, m_f = -1\rangle_{\text{Rb}} + |J = 2, M_J = 1\rangle_{\text{Yb}} \qquad 0.35\,\text{MHz/G}$$

This time the total projection does not change, but there is a large change in the individual projections and most importantly we need to change the hyperfine state of the Rb atom. While not impossible, this is very unlikely as the transition dipole moment on the Rb atom will be very small.

This case would mean that the state observed is in fact an $f = 2$ state with a binding energy of $E_B \approx h \cdot 9.9\,\text{GHz}$. A significantly stronger transition could then be expected when starting with Rb in $f = 2$.

3rd option

Finally, if we assume $N = 2$ and $J = 2$, we have $g_J = \frac{g_j}{6}$ and

$$A : |f = 1, m_f = -1\rangle_{\text{Rb}} + |J = 2, M_J = -1\rangle_{\text{Yb}} \qquad 0.35\,\text{MHz/G}$$

$$B : |f = 1, m_f = -1\rangle_{\text{Rb}} + |J = 2, M_J = 0\rangle_{\text{Yb}} \qquad 0.7\,\text{MHz/G}$$

This case does not require a change in the hyperfine state or projection of the Rb atom and has the correct parity, so it appears much more likely than the previous two from this perspective. However, photoassociation to a $N = 2$ state should not be possible from a s-wave scattering state.

This explanation would thus require some coupling mechanism between different N (or l in the scattering state). This is not out of the question as dipole-dipole interactions can couple partial waves with $\Delta l = 2$, giving rise to d-wave Feshbach resonances [276, 277].

However, as the transition from our excited state to the previously known $N = 0$ ground state levels was observed in the 2-photon-photoassociation experiments, it is very unlikely that the excited state has $N = 2$ character.

Conclusion

We find that all of the possible *case (e)* combinations that explain the observed shifts violate a selection rule. Combined with the consideration in subsection 7.6.1, a *Hund's case (e)* type coupling can thus be considered to be very unlikely.

A.3. Conclusion

We have attempted an explanation of the observed spectra in the framework of both *Hund's case (c)*, as suggested by the relative interaction strengths analyzed in subsection 7.6.1 and in *Hund's case (e)*. Unfortunately, while both cases can account for the Zeeman shift and *case (c)* even provides an explanation for the zero-field splitting, all suffer from inconsistencies in the assigned quantum numbers and selection rules. For a full understanding, future investigations beyond the scope of this thesis will be needed. These could include measurements in different Rb Zeeman states and with different light polarizations or full electronic structure and coupled-channel calculations.

Acknowledgements

Many people have – directly or indirectly – helped make this work possible. In particular my thanks go to:

- Richarda Niemann for the first night shift on the new machine, many after work beers and lots of good music, braving storms, boggy fields and cold water, lots of writing motivation and much more!

- All the bachelor or master students who contributed to the experiment over the years

- *Team Rydberg* for being good lab neighbours and for flourishing mutual disaster tourism.

- Simon Cornish for putting up with an incomplete postdoc during the final writing and submission phase. All of QLM for a warm welcome and especially the Friday seminar regulars for distraction from it all.

- Matthew Frye for insightful discussions on molecules.

- Bastian and Richarda for careful reading of this thesis.

- And my family for their love and support.

Publications

The following peer-reviewed publications have appeared on work described in this thesis:

[129]
TF, B. Pollklesener, and A. Görlitz.
A single-stage 1112 nm fiber amplifier with large gain for laser cooling of ytterbium. Applied Physics B, 124(12):1–7, 2018.
The author developed the concept, designed, built and characterized the amplifier, participated in the MOT measurements and prepared the manuscript.
Section 3.3 and Figure 5.10 reproduce parts of this paper with minor editing.
[167]
C. Sillus, TF, B. Pollklesener, and A. Görlitz.
Active position stabilization of an atomic cloud in a narrow-line magneto-optical trap using a Raspberry Pi. Review of Scientific Instruments, 92(3):033204, 2021.
The author participated in the development of the concept and the stabilization system, characterization of the system and editing of the manuscript.
Section 4.2.3 describes the system developed here, but no content of the paper is directly reproduced here.

The following article on the work described here has been submitted for publication in a peer-reviewed journal after the completion of this manuscript:

TF, B. Pollklesener, C. Sillus, and A. Görlitz.
Intercombination line photoassociation spectroscopy of $^{87}\text{Rb}^{170}\text{Yb}$.
arXiv preprint arXiv:2212.00913. [now published in Phys. Rev. A 107, 023114 (2023)]
The author led the development of the required laser systems, the data taking and analysis as well as the preparation of the manuscript. This preprint contains material from chapter 7 and chapter 8 of this thesis.

Eidesstattliche Erklärung

Ich versichere an Eides Statt, dass die Dissertation von mir selbständig und ohne unzulässige fremde Hilfe unter Beachtung der „Grundsätze zur Sicherung guter wissenschaftlicher Praxis an der Heinrich-Heine-Universität Düsseldorf" erstellt worden ist.

Durham, den 5. Dezember 2022

_____
Tobias Franzen

Bibliography

[1] EL Raab, M Prentiss, Alex Cable, Steven Chu, and David E Pritchard. Trapping of neutral sodium atoms with radiation pressure. Physical Review Letters, 59(23):2631, 1987.

[2] Kendall B Davis, M-O Mewes, Michael R Andrews, Nicolaas J van Druten, Dallin S Durfee, DM Kurn, and Wolfgang Ketterle. Bose-Einstein condensation in a gas of sodium atoms. Physical Review Letters, 75(22):3969, 1995.

[3] Mike H Anderson, Jason R Ensher, Michael R Matthews, Carl E Wieman, and Eric A Cornell. Observation of Bose-Einstein condensation in a dilute atomic vapor. Science, 269(5221):198–201, 1995.

[4] Immanuel Bloch, Jean Dalibard, and Wilhelm Zwerger. Many-body physics with ultracold gases. Reviews of Modern Physics, 80(3):885, 2008.

[5] Oliver Morsch and Markus Oberthaler. Dynamics of Bose-Einstein condensates in optical lattices. Reviews of Modern Physics, 78:179–215, Feb 2006.

[6] R Wynands and S Weyers. Atomic fountain clocks. Metrologia, 42(3):S64–S79, jun 2005.

[7] BJ Bloom, TL Nicholson, JR Williams, SL Campbell, M Bishof, X Zhang, W Zhang, SL Bromley, and J Ye. An optical lattice clock with accuracy and stability at the 10^{-18} level. Nature, 506(7486):71–75, 2014.

[8] Masao Takamoto, Feng-Lei Hong, Ryoichi Higashi, and Hidetoshi Katori. An optical lattice clock. Nature, 435(7040):321–324, 2005.

[9] Savas Dimopoulos, Peter W Graham, Jason M Hogan, and Mark A Kasevich. Testing general relativity with atom interferometry. Physical Review Letters, 98(11):111102, 2007.

[10] Jeffrey B Fixler, GT Foster, JM McGuirk, and MA Kasevich. Atom interferometer measurement of the Newtonian constant of gravity. Science, 315(5808):74–77, 2007.

[11] TL Gustavson, P Bouyer, and MA Kasevich. Precision rotation measurements with an atom interferometer gyroscope. Physical Review Letters, 78(11):2046, 1997.

[12] Iulia M Georgescu, Sahel Ashhab, and Franco Nori. Quantum simulation. Reviews of Modern Physics, 86(1):153, 2014.

[13] Andrew J Daley, Immanuel Bloch, Christian Kokail, Stuart Flannigan, Natalie Pearson, Matthias Troyer, and Peter Zoller. Practical quantum advantage in quantum simulation. Nature, 607(7920):667–676, 2022.

[14] T Lahaye, C Menotti, L Santos, M Lewenstein, and T Pfau. The physics of dipolar bosonic quantum gases. Reports on Progress in Physics, 72(12):126401, nov 2009.

[15] Renate Landig, Lorenz Hruby, Nishant Dogra, Manuele Landini, Rafael Mottl, Tobias Donner, and Tilman Esslinger. Quantum phases from competing short- and long-range interactions in an optical lattice. Nature, 532(7600):476–479, 2016.

[16] Mikhail Baranov, K Góral, L Santos, M Lewenstein, et al. Ultracold dipolar gases–a challenge for experiments and theory. Physica Scripta, 2002(T102):74, 2002.

[17] Jürgen Stuhler, Axel Griesmaier, Tobias Koch, Marco Fattori, Tilman Pfau, Stefano Giovanazzi, Paolo Pedri, and Luis Santos. Observation of dipole-dipole interaction in a degenerate quantum gas. Physical Review Letters, 95(15):150406, 2005.

[18] A. Frisch. Dipolar quantum gases of erbium. PhD thesis, University of Innsbruck, Jul 2014.

[19] Mingwu Lu, Nathaniel Q Burdick, Seo Ho Youn, and Benjamin L Lev. Strongly dipolar Bose-Einstein condensate of dysprosium. Physical Review Letters, 107(19):190401, 2011.

[20] Andrea Micheli, GK Brennen, and Peter Zoller. A toolbox for lattice-spin models with polar molecules. Nature Physics, 2(5):341–347, 2006.

[21] Alexey V Gorshkov, Salvatore R Manmana, Gang Chen, Eugene Demler, Mikhail D Lukin, and Ana Maria Rey. Quantum magnetism with polar alkali-metal dimers. Physical Review A, 84(3):033619, 2011.

[22] Philip D Gregory, Jacob A Blackmore, Sarah L Bromley, Jeremy M Hutson, and Simon L Cornish. Robust storage qubits in ultracold polar molecules. Nature Physics, 17(10):1149–1153, 2021.

[23] Rahul Sawant, Jacob A Blackmore, Philip D Gregory, Jordi Mur-Petit, Dieter Jaksch, Jesús Aldegunde, Jeremy M Hutson, M R Tarbutt, and Simon L Cornish. Ultracold polar molecules as qudits. New Journal of Physics, 22(1):013027, jan 2020.

[24] R. V. Krems. Cold controlled chemistry. Physical Chemistry Chemical Physics, 10:4079–4092, 2008.

[25] N Balakrishnan. Perspective: Ultracold molecules and the dawn of cold controlled chemistry. The Journal of chemical physics, 145(15):150901, 2016.

[26] Hyungmok Son, Juliana J Park, Yu-Kun Lu, Alan O Jamison, Tijs Karman, and Wolfgang Ketterle. Control of reactive collisions by quantum interference. Science, 375(6584):1006–1010, 2022.

[27] Kai K. Voges, Philipp Gersema, Torsten Hartmann, Silke Ospelkaus, and Alessandro Zenesini. Hyperfine dependent atom-molecule loss analyzed by the analytic solution of few-body loss equations. Phys. Rev. Research, 4:023184, Jun 2022.

[28] Bhuvanesh Sundar, Bryce Gadway, and Kaden RA Hazzard. Synthetic dimensions in ultracold polar molecules. Scientific reports, 8(1):1–7, 2018.

[29] Goulven Quéméner and John L Bohn. Shielding $^2\Sigma$ ultracold dipolar molecular collisions with electric fields. Physical Review A, 93(1):012704, 2016.

[30] Jesús Pérez-Ríos, Felipe Herrera, and Roman V Krems. External field control of collective spin excitations in an optical lattice of $^2\Sigma$ molecules. New Journal of Physics, 12(10):103007, 2010.

[31] Mohit Verma, Andrew M. Jayich, and Amar C. Vutha. Electron electric dipole moment searches using clock transitions in ultracold molecules. Physical Review Letters, 125:153201, Oct 2020.

[32] Mallikarjun Karra, Ketan Sharma, Bretislav Friedrich, Sabre Kais, and Dudley Herschbach. Prospects for quantum computing with an array of ultracold polar paramagnetic molecules. The Journal of chemical physics, 144(9):094301, 2016.

[33] NJ Fitch and MR Tarbutt. Laser-cooled molecules. Advances in Atomic Molecular and Optical Physics, Vol 54, 70:157–262, 2021.

[34] DJ McCarron, MH Steinecker, Y Zhu, and D DeMille. Magnetic trapping of an ultracold gas of polar molecules. Physical Review Letters, 121(1):013202, 2018.

[35] Lawrence W Cheuk, Loïc Anderegg, Benjamin L Augenbraun, Yicheng Bao, Sean Burchesky, Wolfgang Ketterle, and John M Doyle. Λ-enhanced imaging of molecules in an optical trap. Physical Review Letters, 121(8):083201, 2018.

[36] Loïc Anderegg, Lawrence W Cheuk, Yicheng Bao, Sean Burchesky, Wolfgang Ketterle, Kang-Kuen Ni, and John M Doyle. An optical tweezer array of ultracold molecules. Science, 365(6458):1156–1158, 2019.

[37] S Truppe, HJ Williams, M Hambach, L Caldwell, NJ Fitch, EA Hinds, BE Sauer, and MR Tarbutt. Molecules cooled below the Doppler limit. Nature Physics, 13(12):1173–1176, 2017.

[38] HJ Williams, L Caldwell, NJ Fitch, S Truppe, J Rodewald, EA Hinds, BE Sauer, and MR Tarbutt. Magnetic trapping and coherent control of laser-cooled molecules. Physical Review Letters, 120(16):163201, 2018.

[39] Thorsten Köhler, Krzysztof Góral, and Paul S Julienne. Production of cold molecules via magnetically tunable Feshbach resonances. Reviews of Modern Physics, 78(4):1311, 2006.

[40] Daniel A Brue and Jeremy M Hutson. Prospects of forming ultracold molecules in 2 Σ states by magnetoassociation of alkali-metal atoms with yb. Physical Review A, 87(5):052709, 2013.

[41] Piotr S. Żuchowski, J. Aldegunde, and Jeremy M. Hutson. Ultracold RbSr Molecules can be formed by Magnetoassociation. Physical Review Letters, 105:153201, Oct 2010.

[42] BC Yang, Matthew D Frye, A Guttridge, Jesus Aldegunde, Piotr S Żuchowski, Simon L Cornish, and Jeremy M Hutson. Magnetic Feshbach resonances in ultracold collisions between Cs and Yb atoms. Physical Review A, 100(2):022704, 2019.

[43] Vincent Barbé, Alessio Ciamei, Benjamin Pasquiou, Lukas Reichsöllner, Florian Schreck, Piotr S Żuchowski, and Jeremy M Hutson. Observation of Feshbach resonances between alkali and closed-shell atoms. Nature Physics, 14(9):881–884, 2018.

[44] Tobias Franzen, Alexander Guttridge, Kali E. Wilson, Jack Segal, Matthew D. Frye, Jeremy M. Hutson, and Simon L. Cornish. Observation of magnetic Feshbach resonances between Cs and ^{173}Yb. Phys. Rev. Research, 4:043072, 2022.

[45] Kevin M Jones, Eite Tiesinga, Paul D Lett, and Paul S Julienne. Ultracold photoassociation spectroscopy: Long-range molecules and atomic scattering. Reviews of Modern Physics, 78(2):483, 2006.

[46] K. Bergmann, H. Theuer, and B. W. Shore. Coherent population transfer among quantum states of atoms and molecules. Reviews of Modern Physics, 70:1003–1025, Jul 1998.

[47] Silke Ospelkaus, A Pe'Er, K-K Ni, JJ Zirbel, B Neyenhuis, S Kotochigova, PS Julienne, J Ye, and DS Jin. Efficient state transfer in an ultracold dense gas of heteronuclear molecules. Nature Physics, 4(8):622–626, 2008.

[48] K Winkler, F Lang, G Thalhammer, P vd Straten, R Grimm, and J Hecker Denschlag. Coherent optical transfer of Feshbach molecules to a lower vibrational state. Physical Review Letters, 98(4):043201, 2007.

[49] K-K Ni, S Ospelkaus, MHG De Miranda, A Pe'Er, B Neyenhuis, JJ Zirbel, S Kotochigova, PS Julienne, DS Jin, and Jun Ye. A high phase-space-density gas of polar molecules. Science, 322(5899):231–235, 2008.

[50] Tetsu Takekoshi, Lukas Reichsöllner, Andreas Schindewolf, Jeremy M Hutson, C Ruth Le Sueur, Olivier Dulieu, Francesca Ferlaino, Rudolf Grimm, and Hanns-Christoph Nägerl. Ultracold dense samples of dipolar RbCs molecules in the rovibrational and hyperfine ground state. Physical Review Letters, 113(20):205301, 2014.

[51] Peter K Molony, Philip D Gregory, Zhonghua Ji, Bo Lu, Michael P Köppinger, C Ruth Le Sueur, Caroline L Blackley, Jeremy M Hutson, and Simon L Cornish. Creation of ultracold Rb 87 Cs 133 molecules in the rovibrational ground state. Physical Review Letters, 113(25):255301, 2014.

[52] Jee Woo Park, Sebastian A Will, and Martin W Zwierlein. Ultracold dipolar gas of fermionic Na23 K40 molecules in their absolute ground state. Physical Review Letters, 114(20):205302, 2015.

[53] Mingyang Guo, Bing Zhu, Bo Lu, Xin Ye, Fudong Wang, Romain Vexiau, Nadia Bouloufa-Maafa, Goulven Quéméner, Olivier Dulieu, and Dajun Wang. Creation of an ultracold gas of ground-state dipolar Na 23 Rb 87 molecules. Physical Review Letters, 116(20):205303, 2016.

[54] Y. Ralchenko, A.E. Kramida, J. Reader, and NIST ASD Team. NIST Atomic Spectra Database (version 3.1.5). `http://physics.nist.gov/asd3`, Zugriff am 15.06.2010, 2008.

[55] Daniel Steck. Rubidium 87 D Line Data. https://steck.us/alkalidata/, 01 2003.

[56] Mateusz Borkowski, Piotr S. Żuchowski, Roman Ciuryło, Paul S. Julienne, Dariusz Kędziera, Łukasz Mentel, Paweł Tecmer, Frank Münchow, Cristian Bruni, and Axel Görlitz. Scattering lengths in isotopologues of the RbYb system. Physical Review A, 88:052708, Nov 2013.

[57] Alexander Guttridge, Matthew D Frye, BC Yang, Jeremy M Hutson, and Simon L Cornish. Two-photon photoassociation spectroscopy of CsYb: Ground-state interaction potential and interspecies scattering lengths. Physical Review A, 98(2):022707, 2018.

[58] Richard Roy, Rajendra Shrestha, Alaina Green, Subhadeep Gupta, Ming Li, Svetlana Kotochigova, Alexander Petrov, and Chi Hong Yuen. Photoassociative production of ultracold heteronuclear YbLi* molecules. Physical Review A, 94(3):033413, 2016.

[59] William Dowd, Richard J Roy, Rajendra K Shrestha, Alexander Petrov, Constantinos Makrides, Svetlana Kotochigova, and Subhadeep Gupta. Magnetic field dependent interactions in an ultracold Li–Yb (3P2) mixture. New Journal of Physics, 17(5):055007, 2015.

[60] Alessio Ciamei, Jacek Szczepkowski, Alex Bayerle, Vincent Barbé, Lukas Reichsöllner, Slava M Tzanova, Chun-Chia Chen, Benjamin Pasquiou, Anna Grochola, Pawel Kowalczyk, et al. The RbSr $^2\Sigma^+$ ground state investigated via spectroscopy of hot and ultracold molecules. Physical Chemistry Chemical Physics, 20(41):26221–26240, 2018.

[61] Alexander Batär. Erzeugung und Charakterisierung ultrakalter Rubidium-und Ytterbiumatome-Auf dem Weg zu einem gemischten Quantengas. PhD thesis, Ph. D. thesis, Heinrich-Heine-Universität, Düsseldorf, 2005.

[62] Varun D Vaidya, J Tiamsuphat, SL Rolston, and JV Porto. Degenerate Bose-Fermi mixtures of rubidium and ytterbium. Physical Review A, 92(4):043604, 2015.

[63] Sören Erik Dörscher. Creation of ytterbium quantum gases with a compact 2D-/3D-MOT setup. PhD thesis, Universität Hamburg, 2013.

[64] Sven Tassy. Sympathetische Kühlung von Ytterbium mit Rubidium. PhD thesis, Ph. D. thesis, Heinrich-Heine-Universität, Düsseldorf, 2007.

[65] Florian Baumer. Isotope dependent interactions in a mixture of ultracold atoms. PhD thesis, Ph. D. thesis, Heinrich-Heine-Universität, Düsseldorf, 2010.

[66] F. Baumer, F. Münchow, A. Görlitz, S. E. Maxwell, P. S. Julienne, and E. Tiesinga. Spatial separation in a thermal mixture of ultracold ^{174}Yb and ^{87}Rb atoms. Physical Review A, 83:040702, Apr 2011.

[67] Nils Nemitz. Production and spectroscopy of ultracold YbRb* molecules. PhD thesis, Ph. D. thesis, Heinrich-Heine-Universität, Düsseldorf, 2008.

[68] N Nemitz, F Baumer, F Münchow, S Tassy, and A Görlitz. Production of heteronuclear molecules in an electronically excited state by photoassociation in a mixture of ultracold Yb and Rb. Physical Review A, 79(6):061403, 2009.

[69] Cristian Bruni. Exploring strategies for the production of ultracold RbYb molecules in conservative traps. PhD thesis, Heinrich-Heine-Universität Düsseldorf, 2015.

[70] C. Bruni and A. Görlitz. Observation of hyperfine interaction in photoassociation spectra of ultracold RbYb. Physical Review A, 94:022503, Aug 2016.

[71] Christian Bruni. Aufbau und Charakterisierung eines optischen Gitters für Ytterbium. Diplomarbeit, AG Görlitz, Universität Düsseldorf, 2008.

[72] Frank Münchow. 2-Photon-Photoassociation spectroscopy in a mixture of Ytterbium and Rubidium. PhD thesis, HHU Düsseldorf, 2012.

[73] C. Bruni, F. Münchow, and A. Görlitz. Optical Autler–Townes spectroscopy in a heteronuclear mixture of laser-cooled atoms. Applied Physics B, 123(1):6, Jan 2017.

[74] Fabian Wolf. Interactions of Yb and Rb in a crossed dipole trap. Master Thesis, Universität Düsseldorf, 2013.

[75] Satoshi Tojo, Masaaki Kitagawa, Katsunari Enomoto, Yutaka Kato, Yosuke Takasu, Mitsutaka Kumakura, and Yoshiro Takahashi. High-resolution photoassociation spectroscopy of ultracold ytterbium atoms by using the intercombination transition. Physical Review Letters, 96(15):153201, 2006.

[76] T. Zelevinsky, M. M. Boyd, A. D. Ludlow, T. Ido, J. Ye, R. Ciuryło, P. Naidon, and P. S. Julienne. Narrow line photoassociation in an optical lattice. Physical Review Letters, 96:203201, May 2006.

[77] M Borkowski, R Ciuryło, PS Julienne, S Tojo, K Enomoto, and Y Takahashi. Line shapes of optical Feshbach resonances near the intercombination transition of bosonic ytterbium. Physical Review A, 80(1):012715, 2009.

[78] Bart H McGuyer, Mickey McDonald, Geoffrey Z Iwata, Marco G Tarallo, Wojciech Skomorowski, Robert Moszynski, and Tanya Zelevinsky. Precise study of asymptotic physics with subradiant ultracold molecules. Nature Physics, 11(1):32–36, 2015.

[79] M Borkowski, A A Buchachenko, R Ciuryło, P S Julienne, H Yamada, K Yuu, K Takahashi, Y Takasu, and Y Takahashi. Probing non-newtonian gravity by photoassociation spectroscopy. Journal of Physics: Conference Series, 810:012014, feb 2017.

[80] Max Kahmann, Eberhard Tiemann, Oliver Appel, Uwe Sterr, and Fritz Riehle. Photoassociation spectroscopy of Ca 40 measured with kilohertz accuracy near the 3P1 + 1S0 asymptote and its Zeeman effect. Physical Review A, 89(2):023413, 2014.

[81] Alessio Ciamei, Alex Bayerle, Chun-Chia Chen, Benjamin Pasquiou, and Florian Schreck. Efficient production of long-lived ultracold Sr2 molecules. Physical Review A, 96(1):013406, 2017.

[82] Alessio Ciamei. Taming ultracold RbSr and Sr$_2$. PhD thesis, Universiteit van Amsterdam, 2018.

[83] H. Lefebvre-Brion and R.W. Field. The Spectra and Dynamics of Diatomic Molecules: Revised and Enlarged Edition. Elsevier Science, 2004.

[84] J.M. Brown and A. Carrington. <u>Rotational Spectroscopy of Diatomic Molecules</u>. Cambridge Molecular Science. Cambridge University Press, 2003.

[85] B. Judd. <u>Angular Momentum Theory for Diatomic Molecules</u>. Elsevier Science, 2012.

[86] Robert J Le Roy. Determining equilibrium structures and potential energy functions for diatomic molecules, 2011.

[87] V Aquilanti, S Cavalli, and G Grossi. Hund's cases for rotating diatomic molecules and for atomic collisions: angular momentum coupling schemes and orbital alignment. <u>Zeitschrift für Physik D Atoms, Molecules and Clusters</u>, 36(3):215–219, 1996.

[88] Jonathan Tennyson, Lorenzo Lodi, Laura K McKemmish, and Sergei N Yurchenko. The ab initio calculation of spectra of open shell diatomic molecules. <u>Journal of Physics B: Atomic, Molecular and Optical Physics</u>, 49(10):102001, 2016.

[89] Edmund R Meyer. <u>Structure and spectroscopy of candidates for an electron electric dipole moment experiment</u>. PhD thesis, University of Colorado at Boulder, 2010.

[90] G. W. King and J. H. van Vleck. Dipole-dipole resonance forces. <u>Phys. Rev.</u>, 55:1165–1172, Jun 1939.

[91] H Wang, J Li, XT Wang, CJ Williams, PL Gould, and WC Stwalley. Precise determination of the dipole matrix element and radiative lifetime of the K39 4p state by photoassociative spectroscopy. <u>Physical Review A</u>, 55(3):R1569, 1997.

[92] WI McAlexander, ERI Abraham, NWM Ritchie, CJ Williams, HTC Stoof, and RG Hulet. Precise atomic radiative lifetime via photoassociative spectroscopy of ultracold lithium. <u>Physical Review A</u>, 51(2):R871, 1995.

[93] Daniel Comparat. Improved LeRoy–Bernstein near-dissociation expansion formula, and prospect for photoassociation spectroscopy. <u>Journal of Chemical Physics</u>, 120(3):1318–1329, 2004.

[94] Jean Dalibard. Collisional dynamics of ultra-cold atomic gases. In <u>Bose-Einstein Condensation in Atomic Gases</u>, pages 321–349. IOS Press, 1999.

[95] John R. de Laeter, John Karl Böhlke, P. De Bièvre, H. Hidaka, H. S. Peiser, K. J. R. Rosman, and P. D. P. Taylor. Atomic weights of the elements. Review 2000 (IUPAC technical report). <u>Pure and Applied Chemistry</u>, 75(6):683–800, 2003.

[96] Masaaki Kitagawa, Katsunari Enomoto, Kentaro Kasa, Yoshiro Takahashi, Roman Ciuryło, Pascal Naidon, and Paul S. Julienne. Two-color photoassociation spectroscopy of ytterbium atoms and the precise determinations of s-wave scattering lengths. <u>Physical Review A</u>, 77:012719, Jan 2008.

[97] GF Gribakin and VV Flambaum. Calculation of the scattering length in atomic collisions using the semiclassical approximation. <u>Physical Review A</u>, 48(1):546, 1993.

[98] 1PA Ruprecht, MJ Holland, K Burnett, and Mark Edwards. Time-dependent solution of the nonlinear Schrödinger equation for Bose-condensed trapped neutral atoms. <u>Physical Review A</u>, 51(6):4704, 1995.

[99] Curtis Charles Bradley, CA Sackett, and RG Hulet. Bose-Einstein condensation of lithium: Observation of limited condensate number. <u>Physical Review Letters</u>, 78(6):985, 1997.

[100] Jacob L Roberts, Neil R Claussen, Simon L Cornish, Elizabeth A Donley, Eric A Cornell, and Carl E Wieman. Controlled collapse of a Bose-Einstein condensate. <u>Physical Review Letters</u>, 86(19):4211, 2001.

[101] N. R. Claussen, S. L. Cornish, J. L. Roberts, E. A. Cornell, and C. E. Wieman. 85Rb BEC near a Feshback resonance. <u>AIP Conference Proceedings</u>, 551(1):325–336, 2001.

[102] A. Marte, T. Volz, J. Schuster, S. Dürr, G. Rempe, E. G. M. van Kempen, and B. J. Verhaar. Feshbach resonances in rubidium 87: Precision measurement and analysis. Physical Review Letters, 89:283202, Dec 2002.

[103] K Enomoto, K Kasa, M Kitagawa, and Y Takahashi. Optical Feshbach resonance using the intercombination transition. Physical Review Letters, 101(20):203201, 2008.

[104] Fabian Türck. Microwave spectroscopy in an ultracold mixture of Yb and Rb atoms. Master Thesis, Universität Düsseldorf, 2018.

[105] Caroline L. Blackley, C. Ruth Le Sueur, Jeremy M. Hutson, Daniel J. McCarron, Michael P. Köppinger, Hung-Wen Cho, Daniel L. Jenkin, and Simon L. Cornish. Feshbach resonances in ultracold ^{85}Rb. Physical Review A, 87:033611, Mar 2013.

[106] Thomas Volz, Stephan Dürr, Sebastian Ernst, Andreas Marte, and Gerhard Rempe. Characterization of elastic scattering near a Feshbach resonance in ^{87}Rb. Physical Review A, 68:010702, Jul 2003.

[107] John L Bohn and Paul S Julienne. Semianalytic theory of laser-assisted resonant cold collisions. Physical Review A, 60(1):414, 1999.

[108] R Ciuryło, Eite Tiesinga, and Paul S Julienne. Stationary phase approximation for the strength of optical Feshbach resonances. Physical Review A, 74(2):022710, 2006.

[109] John L. Bohn and P. S. Julienne. Semianalytic treatment of two-color photoassociation spectroscopy and control of cold atoms. Physical Review A, 54:R4637–R4640, Dec 1996.

[110] Michael Fleischhauer, Atac Imamoglu, and Jonathan P Marangos. Electromagnetically induced transparency: Optics in coherent media. Reviews of Modern Physics, 77(2):633, 2005.

[111] Stephen E Harris, JE Field, and A Imamoğlu. Nonlinear optical processes using electromagnetically induced transparency. Physical Review Letters, 64(10):1107, 1990.

[112] JR Kuklinski, U Gaubatz, Foek T Hioe, and K Bergmann. Adiabatic population transfer in a three-level system driven by delayed laser pulses. Physical Review A, 40(11):6741, 1989.

[113] Nikolay V Vitanov, Andon A Rangelov, Bruce W Shore, and Klaas Bergmann. Stimulated raman adiabatic passage in physics, chemistry, and beyond. Reviews of Modern Physics, 89(1):015006, 2017.

[114] R. Grimm, M. Weidemüller, and Y.B. Ovchinnikov. Optical dipole traps for neutral atoms. Adv. at. mol. opt. phys, 42(95):130, 2000.

[115] Wolfgang Ketterle and N.J. Van Druten. Evaporative cooling of trapped atoms. volume 37 of Advances In Atomic, Molecular, and Optical Physics, pages 181–236. Academic Press, 1996.

[116] Thomas J. Kane and Robert L. Byer. Monolithic, unidirectional single-mode Nd:YAG ring laser. Optics Letters, 10(2):65–67, Feb 1985.

[117] N. M. Sampas, E. K. Gustafson, and R. L. Byer. Long-term stability of two diode-laser-pumped nonplanar ring lasers independently stabilized to two Fabry–Perot interferometers. Optics Letters, 18(12):947–949, Jun 1993.

[118] R. Y. Chiao, C. H. Townes, and B. P. Stoicheff. Stimulated Brillouin Scattering and Coherent Generation of Intense Hypersonic Waves. Physical Review Letters, 12:592–595, May 1964.

[119] E.P. Ippen and R.H. Stolen. Stimulated Brillouin scattering in optical fibers. Applied Physics Letters, 21(11):539–541, 1972.

[120] V. I. Kovalev and R. G. Harrison. Suppression of stimulated Brillouin scattering in high-power single-frequency fiber amplifiers. Optics Letters, 31(2):161–163, Jan 2006.

[121] Henry Fernandes Passagem, Ricardo Colín-Rodríguez, Paulo Cesar Ventura da Silva, Nadia Bouloufa-Maafa, Olivier Dulieu, and Luis Gustavo Marcassa. Formation of ultracold molecules induced by a high-power single-frequency fiber laser. Journal of Physics B: Atomic, Molecular and Optical Physics, 50(4):045202, jan 2017.

[122] Carlos R. Menegatti, Bruno S. Marangoni, Nadia Bouloufa-Maafa, Olivier Dulieu, and Luis G. Marcassa. Trap loss in a rubidium crossed dipole trap by short-range photoassociation. Physical Review A, 87:053404, May 2013.

[123] J. D. Miller, R. A. Cline, and D. J. Heinzen. Photoassociation spectrum of ultracold Rb atoms. Physical Review Letters, 71:2204–2207, Oct 1993.

[124] T. Lauber, J. Küber, O. Wille, and G. Birkl. Optimized Bose-Einstein-condensate production in a dipole trap based on a 1070-nm multifrequency laser: Influence of enhanced two-body loss on the evaporation process. Physical Review A, 84:043641, Oct 2011.

[125] Rudiger Paschotta, Johan Nilsson, Anne C Tropper, and David C Hanna. Ytterbium-doped fiber amplifiers. IEEE Journal of quantum electronics, 33(7):1049–1056, 1997.

[126] Rüdiger Paschotta. Encyclopedia of Laser Physics and Technology. Wiley-VCH, 2008.

[127] Bastian Pollklesener. tbd. PhD thesis, HHU Düsseldorf, 2023.

[128] Rissanen Joona. PyFiberAmp simulation library.

[129] Tobias Franzen, Bastian Pollklesener, and Axel Görlitz. A single-stage 1112 nm fiber amplifier with large gain for laser cooling of ytterbium. Applied Physics B, 124(12):1–7, 2018.

[130] N. Kostylev, C. R. Locke, M. E. Tobar, and J. J. McFerran. Spectroscopy and laser cooling on the 1S0 - 3P1 line in Yb via an injection-locked diode laser at 1111.6 nm. Applied Physics B, 118(4):517–525, Mar 2015.

[131] S. C. Burd, D. T. C. Allcock, T. Leinonen, J. P. Penttinen, D. H. Slichter, R. Srinivas, A. C. Wilson, R. Jördens, M. Guina, D. Leibfried, and D. J. Wineland. VECSEL systems for the generation and manipulation of trapped magnesium ions. Optica, 3(12):1294–1299, Dec 2016.

[132] Yan Feng, Luke Taylor, and Domenico Bonaccini Calia. Multiwatts narrow linewidth fiber Raman amplifiers. Optics Express, 16(15):10927–10932, Jul 2008.

[133] A Guttridge, SA Hopkins, SL Kemp, D Boddy, R Freytag, MPA Jones, MR Tarbutt, EA Hinds, and SL Cornish. Direct loading of a large Yb MOT on the transition. Journal of Physics B: Atomic, Molecular and Optical Physics, 49(14):145006, 2016.

[134] S. Uetake, A. Yamaguchi, S. Kato, and Y. Takahashi. High power narrow linewidth laser at 556 nm for magneto-optical trapping of ytterbium. Applied Physics B, 92(1):33–35, Jul 2008.

[135] Dmitrii A Grukh, Andrei S Kurkov, Vladimir M Paramonov, and Evgenii M Dianov. Effect of heating on the optical properties of Yb3+-doped fibres and fibre lasers. Quantum Electronics, 34(6):579, 2004.

[136] Hoon Jeong, Hyoyeong Park, Seungtaek Kim, Jongseok Kim, Chulsoo Byun, and Cheolho Kim. Output power improvement in an Yb-doped fiber laser with an additional unpumped Yb-doped fiber. Optical Review, 19(2):86–88, Mar 2012.

[137] Joona Koponen, Mikko Söderlund, Hanna J. Hoffman, Dahv A. V. Kliner, Jeffrey P. Koplow, and Mircea Hotoleanu. Photodarkening rate in Yb-doped silica fibers. Applied Optics, 47(9):1247–1256, Mar 2008.

[138] Benoît Gouhier, Germain Guiraud, Sergio Rota-Rodrigo, Jian Zhao, Nicholas Traynor, and Giorgio Santarelli. 25W single-frequency, low noise fiber MOPA at 1120nm. Optics Letters, 43(2):308–311, Jan 2018.

[139] Mridu P. Kalita, Shaif ul Alam, Christophe Codemard, Seongwoo Yoo, Alexander J. Boyland, Morten Ibsen, and Jayanta K. Sahu. Multi-watts narrow-linewidth all fiber Yb-doped laser operating at 1179 nm. Optics Express, 18(6):5920–5925, Mar 2010.

[140] CJ Mackechnie, WL Barnes, DC Hanna, and JE Townsend. High power ytterbium (Yb3+)-doped fibre laser operating in the 1.12 μm region. Electronics Letters, 29(1):52–53, 1993.

[141] A S Kurkov, V M Paramonov, and O I Medvedkov. Ytterbium fiber laser emitting at 1160 nm. Laser Physics Letters, 3(10):503, 2006.

[142] Andrei S Kurkov and Evgenii M Dianov. Moderate-power cw fibre lasers. Quantum Electronics, 34(10):881, 2004.

[143] J. E. Gray and D. W. Allan. A Method for Estimating the Frequency Stability of an Individual Oscillator. In 28th Annual Symposium on Frequency Control, pages 243–246, May 1974.

[144] Carl Hippler. Ein selbstgebauter Ytterbium-Faserverstärker mit 25 W Ausgangsleistung bei 1064 nm zur Realisierung eines optischen Gitters für ultrakalte RbCs-Moleküle. Master's thesis, TU München, 2013.

[145] C. Barnard, P. Myslinski, J. Chrostowski, and M. Kavehrad. Analytical model for rare-earth-doped fiber amplifiers and lasers. IEEE Journal of Quantum Electronics, 30(8):1817–1830, Aug 1994.

[146] S Höfer, A Liem, J Limpert, H Zellmer, A Tünnermann, S Unger, S Jetschke, H-R Müller, and I Freitag. Single-frequency master-oscillator fiber power amplifier system emitting 20 w of power. Optics Letters, 26(17):1326–1328, 2001.

[147] F.M. Gardner. Phaselock Techniques. Wiley, 2005.

[148] John Daniel Kraus. Antennas. McGraw-Hill Companies, 2 sub edition, 1988.

[149] G. Santarelli, A. Clairon, S.N. Lea, and G.M. Tino. Heterodyne optical phase-locking of extended-cavity semiconductor lasers at 9 Ghz. Optics Communications, 104(4):339–344, 1994.

[150] Thomas J Kane, Alan C Nilsson, and Robert L Byer. Frequency stability and offset locking of a laser-diode-pumped nd: Yag monolithic nonplanar ring oscillator. Optics Letters, 12(3):175–177, 1987.

[151] A Castrillo, E Fasci, G Galzerano, G Casa, P Laporta, and L Gianfrani. Offset-frequency locking of extended-cavity diode lasers for precision spectroscopy of water at 1.38 μm. Optics Express, 18(21):21851–21860, 2010.

[152] P.C.D. Hobbs. Building Electro-Optical Systems: Making It all Work. Wiley Series in Pure and Applied Optics. Wiley, 2009.

[153] Takayuki Sugeta, Tsuneo Urisu, Seizo Sakata, and Yoshihiko Mizushima. Metal-semiconductor-metal photodetector for high-speed optoelectronic circuits. Japanese Journal of Applied Physics, 19(S1):459, 1980.

[154] Tomoyuki Uehara, Kenichiro Tsuji, Kohei Hagiwara, and Noriaki Onodera. Optical beat-note frequency stabilization between two lasers using a radio frequency interferometer in the gigahertz frequency band. Optical Engineering, 53(12):1 – 6, 2014.

[155] Scott A. Diddams, Kerry Vahala, and Thomas Udem. Optical frequency combs: Coherently uniting the electromagnetic spectrum. Science, 369(6501), 2020.

[156] Nicolas Von Bandel, Mikhaël Myara, Mohamed Sellahi, Tahar Souici, Rémi Dardaillon, and Philippe Signoret. Time-dependent laser linewidth: beat-note digital acquisition and numerical analysis. Optics Express, 24(24):27961–27978, Nov 2016.

[157] Robert W. Stewart, Louise Crockett, Dale Atkinson, Kenneth Barlee, David Crawford, Iain Chalmers, Mike Mclernon, and Ethem Sozer. A low-cost desktop software defined radio design environment using matlab, simulink, and the rtl-sdr. IEEE Communications Magazine (1979-present), 53(9):64–71, 2015.

[158] Mark A. Wickert and McKenna R. Lovejoy. Hands-on software defined radio experiments with the low-cost rtl-sdr dongle. In 2015 IEEE Signal Processing and Signal Processing Education Workshop (SP/SPE), pages 65–70, 2015.

[159] J. Huckans, W. Dubosclard, E. Maréchal, O. Gorceix, B. Laburthe-Tolra, and M. Robert de Saint-Vincent. Note on the reflectance of mirrors exposed to a strontium beam, 2018.

[160] Sven Kroboth. Laserkühlung von Ytterbiumatomen. Diplomarbeit, AG Görlitz, Universität Stuttgart, 2002.

[161] Bastian Pollklesener. Aufbau eines Lasersystems zur Laserkühlung von Ytterbium. Bachelor Thesis, Universität Düsseldorf, 2014.

[162] X. Baillard, A. Gauguet, S. Bize, P. Lemonde, Ph. Laurent, A. Clairon, and P. Rosenbusch. Interference-filter-stabilized external-cavity diode lasers. Optics Communications, 266(2):609–613, 2006.

[163] M. Gilowski, Ch. Schubert, M. Zaiser, W. Herr, T. Wübbena, T. Wendrich, T. Müller, E.M. Rasel, and W. Ertmer. Narrow bandwidth interference filter-stabilized diode laser systems for the manipulation of neutral atoms. Optics Communications, 280(2):443–447, 2007.

[164] Cornell P. Gonschior, Karl-Friedrich Klein, Matthias Menzel, Tong Sun, and Kenneth T. Grattan. Investigation of single-mode fiber degradation by 405-nm continuous-wave laser light. Optical Engineering, 53(12):1 – 7, 2014.

[165] F Riehle. Use of optical frequency standards for measurements of dimensional stability. Measurement Science & Technology, 9(7):1042, 1998.

[166] W. Zhang, M. J. Martin, C. Benko, J. L. Hall, J. Ye, C. Hagemann, T. Legero, U. Sterr, F. Riehle, G. D. Cole, and M. Aspelmeyer. Reduction of residual amplitude modulation to $1 \cdot 10^{-6}$ for frequency modulation and laser stabilization. Optics Letters, 39(7):1980–1983, Apr 2014.

[167] C. Sillus, T. Franzen, B. Pollklesener, and A. Görlitz. Active position stabilization of an atomic cloud in a narrow-line magneto-optical trap using a Raspberry Pi. Review of Scientific Instruments, 92(3):033204, 2021.

[168] Richard Roy, Alaina Green, Ryan Bowler, and Subhadeep Gupta. Rapid cooling to quantum degeneracy in dynamically shaped atom traps. Physical Review A, 93:043403, Apr 2016.

[169] Kurt L. Haller and Philip C. D. Hobbs. Double-beam laser absorption spectroscopy: shot noise-limited performance at baseband with a novel electronic noise canceler. In Bryan L. Fearey, editor, Optical Methods for Ultrasensitive Detection and Analysis: Techniques and Applications, volume 1435, pages 298 – 309. International Society for Optics and Photonics, SPIE, 1991.

[170] E A Khazanov. Compensation of thermally induced polarisation distortions in Faraday isolators. Quantum Electronics, 29(1):59–64, jan 1999.

[171] Torsten Kemmerling. Setup of an Optical Lattice at 1064nm for Ultracold Rubidium Atoms. Master Thesis, Universität Düsseldorf, 2019.

[172] S. Schiller, A. Görlitz, A. Nevsky, S. Alighanbari, S. Vasilyev, C. Abou-Jaoudeh, G. Mura, Tobias Franzen, U. Sterr, S. Falke, C. Lisdat, Ernst-Maria Rasel, A. Kulosa, S. Bize, J. Lodewyck, G. Tino, N. Poli, M. Schioppa, K. Bongs, Y. Singh, P. Gill, G. Barwood, Y. Ovchinnikov, J. Stuhler, W. Kaenders, C. Braxmaier, R. Holzwarth, A. Donati, S. Lecomte, D. Calonico, and F. Levi. Towards Neutral-atom Space Optical Clocks (SOC2): Development of high-performance transportable and breadboard optical clocks and advanced subsystems. In 2012 European Frequency and Time Forum, 2012.

[173] Richarda Niemann. Photoassociation Spectroscopy at the Intercombination Line of Ytterbium. Master Thesis, Universität Düsseldorf, 2019.

[174] Rachel Houtz, Cheong Chan, and Holger Müller. Wideband, efficient optical serrodyne frequency shifting with a phase modulator and a nonlinear transmission line. Optics Express, 17(21):19235–19240, 2009.

[175] DMS Johnson, JM Hogan, S-W Chiow, and MA Kasevich. Broadband optical serrodyne frequency shifting. Optics Letters, 35(5):745–747, 2010.

[176] E. Kirilov, M. Mark, M. Segl, and H. Nägerl. Compact, robust, and spectrally pure diode-laser system with a filtered output and a tunable copy for absolute referencing. Applied Physics B, 119:233–240, 2014.

[177] Jaroslaw Labaziewicz, Philip Richerme, Kenneth R. Brown, Isaac L. Chuang, and Kazuhiro Hayasaka. Compact, filtered diode laser system for precision spectroscopy. Optics Letters, 32(5):572–574, Mar 2007.

[178] J. F. Kelly and A. Gallagher. Efficient electro-optic modulator for optical pumping of Na beams. Review of Scientific Instruments, 58(4):563–566, 1987.

[179] KG Libbrecht and John L Hall. A low-noise high-speed diode laser current controller. Review of Scientific Instruments, 64(8):2133–2135, 1993.

[180] Bastian Pollklesener. Setup of an optical lattice for rubidium and ytterbium. Master Thesis, Universität Düsseldorf, 2016.

[181] Aviv Keshet and Wolfgang Ketterle. A distributed, graphical user interface based, computer control system for atomic physics experiments. Review of Scientific Instruments, 84(1):015105, 2013.

[182] analysis and calibration of absorptive images of bose-einstein condensate at nonzero temperatures.

[183] Michael Erhard. Experimente mit mehrkomponentigen Bose-Einstein-Kondensaten. PhD thesis, Universität Hamburg, 2004.

[184] C. F. Ockeloen, A. F. Tauschinsky, R. J. C. Spreeuw, and S. Whitlock. Detection of small atom numbers through image processing. Physical Review A, 82:061606, Dec 2010.

[185] Wolfgang Petrich, Michael H. Anderson, Jason R. Ensher, and Eric A. Cornell. Behavior of atoms in a compressed magneto-optical trap. Journal of the Optical Society of America B: Optical Physics, 11(8):1332–1335, Aug 1994.

[186] Marshall T DePue, S [Lukman Winoto], D.J Han, and David S Weiss. Transient compression of a MOT and high intensity fluorescent imaging of optically thick clouds of atoms. Optics Communications, 180(1):73 – 79, 2000.

[187] J. Dalibard and C. Cohen-Tannoudji. Laser cooling below the Doppler limit by polarization gradients: simple theoretical models. Journal of the Optical Society of America B: Optical Physics, 6(11):2023–2045, Nov 1989.

[188] Wolfgang Ketterle, Kendall B Davis, Michael A Joffe, Alex Martin, and David E Pritchard. High densities of cold atoms in a dark spontaneous-force optical trap. Physical Review Letters, 70(15):2253, 1993.

[189] N. Radwell, G. Walker, and S. Franke-Arnold. Cold-atom densities of more than 10^{12} cm^{-3} in a holographically shaped dark spontaneous-force optical trap. Physical Review A, 88:043409, Oct 2013.

[190] Alan L. Migdall, John V. Prodan, William D. Phillips, Thomas H. Bergeman, and Harold J. Metcalf. First observation of magnetically trapped neutral atoms. Physical Review Letters, 54:2596–2599, Jun 1985.

[191] G. Modugno, G. Ferrari, G. Roati, R. J. Brecha, A. Simoni, and M. Inguscio. Bose-Einstein condensation of potassium atoms by sympathetic cooling. Science, 294(5545):1320–1322, 2001.

[192] Y-J Lin, Abigail R Perry, Robert L Compton, Ian B Spielman, and James V Porto. Rapid production of Rb87 Bose-Einstein condensates in a combined magnetic and optical potential. Physical Review A, 79(6):063631, 2009.

[193] DS Naik and C Raman. Optically plugged quadrupole trap for Bose-Einstein condensates. Physical Review A, 71(3):033617, 2005.

[194] David E. Pritchard. Cooling neutral atoms in a magnetic trap for precision spectroscopy. Physical Review Letters, 51:1336–1339, Oct 1983.

[195] T. Bergeman, Gidon Erez, and Harold J. Metcalf. Magnetostatic trapping fields for neutral atoms. Physical Review A, 35:1535–1546, Feb 1987.

[196] M. D. Barrett, J. A. Sauer, and M. S. Chapman. All-optical formation of an atomic Bose-Einstein condensate. Physical Review Letters, 87:010404, Jun 2001.

[197] K. M. O'Hara, M. E. Gehm, S. R. Granade, and J. E. Thomas. Scaling laws for evaporative cooling in time-dependent optical traps. Physical Review A, 64:051403, Oct 2001.

[198] Isidor Isaac Rabi. Space quantization in a gyrating magnetic field. Physical Review, 51(8):652, 1937.

[199] Clarence Zener and Ralph Howard Fowler. Non-adiabatic crossing of energy levels. Proceedings of the Royal Society of London. Series A, Containing Papers of a Mathematical and Physical Character, 137(833):696–702, 1932.

[200] Jan R. Rubbmark, Michael M. Kash, Michael G. Littman, and Daniel Kleppner. Dynamical effects at avoided level crossings: A study of the Landau-Zener effect using Rydberg atoms. Physical Review A, 23:3107–3117, Jun 1981.

[201] G. Breit and I. I. Rabi. Measurement of nuclear spin. Physical Review, 38:2082–2083, Dec 1931.

[202] S Bize, Y Sortais, M. S Santos, C Mandache, A Clairon, and C Salomon. High-accuracy measurement of the 87Rb ground-state hyperfine splitting in an atomic fountain. Europhysics Letters (EPL), 45(5):558–564, mar 1999.

[203] NW Ashcroft and ND Mermin. Solid State Physics. Saunders, 1976.

[204] Thomas R Carver. Mathieu's functions and electrons in a periodic lattice. American Journal of Physics, 39(10):1225–1230, 1971.

[205] Maksims Arzamasovs and Bo Liu. Tight-binding tunneling amplitude of an optical lattice. European Journal of Physics, 38(6):065405, oct 2017.

[206] Gregory H. Wannier. The structure of electronic excitation levels in insulating crystals. Physical Review, 52:191–197, Aug 1937.

[207] Phillip L. Gould, George A. Ruff, and David E. Pritchard. Diffraction of atoms by light: The near-resonant Kapitza-Dirac effect. Physical Review Letters, 56:827–830, Feb 1986.

[208] Bryce Gadway, Daniel Pertot, René Reimann, Martin G. Cohen, and Dominik Schneble. Analysis of Kapitza-Dirac diffraction patterns beyond the Raman-Nath regime. Optics Express, 17(21):19173–19180, Oct 2009.

[209] S. Burger, F. S. Cataliotti, C. Fort, F. Minardi, M. Inguscio, M. L. Chiofalo, and M. P. Tosi. Superfluid and dissipative dynamics of a Bose-Einstein condensate in a periodic optical potential. Physical Review Letters, 86:4447–4450, May 2001.

[210] J Hecker Denschlag, J E Simsarian, H Häffner, C McKenzie, A Browaeys, D Cho, K Helmerson, S L Rolston, and W D Phillips. A Bose-Einstein condensate in an optical lattice. Journal of Physics B: Atomic, Molecular and Optical Physics, 35(14):3095–3110, jul 2002.

[211] Thomas H. Loftus, Tetsuya Ido, Martin M. Boyd, Andrew D. Ludlow, and Jun Ye. Narrow line cooling and momentum-space crystals. Physical Review A, 70:063413, Dec 2004.

[212] S. Händel, T. P. Wiles, A. L. Marchant, S. A. Hopkins, C. S. Adams, and S. L. Cornish. Magnetic merging of ultracold atomic gases of ^{85}Rb and ^{87}Rb. Physical Review A, 83:053633, May 2011.

[213] Lee R Liu, Jonathan D Hood, Yichao Yu, Jessie T Zhang, Kenneth Wang, Y-W Lin, Till Rosenband, and K-K Ni. Molecular assembly of ground-state cooled single atoms. Physical Review X, 9(2):021039, 2019.

[214] Kunpeng Wang, Xiaodong He, Ruijun Guo, Peng Xu, Cheng Sheng, Jun Zhuang, Zongyuan Xiong, Min Liu, Jin Wang, and Mingsheng Zhan. Preparation of a heteronuclear two-atom system in the three-dimensional ground state in an optical tweezer. Physical Review A, 100(6):063429, 2019.

[215] Ralph Vincent Brooks, Stefan Spence, Alexander Guttridge, Alexandros Chantif Alampounti, Ana Rakonjac, Lewis McArd, Jeremy M Hutson, and S L Cornish. Preparation of one 87Rb and one 133Cs atom in a single optical tweezer. New Journal of Physics, 2021.

[216] P Hommelhoff, W Hänsel, T Steinmetz, T W Hänsch, and J Reichel. Transporting, splitting and merging of atomic ensembles in a chip trap. New Journal of Physics, 7:3–3, jan 2005.

[217] G. Nenciu. Dynamics of band electrons in electric and magnetic fields: rigorous justification of the effective hamiltonians. Reviews of Modern Physics, 63:91–127, Jan 1991.

[218] D. S. Petrov and G. V. Shlyapnikov. Interatomic collisions in a tightly confined Bose gas. Physical Review A, 64:012706, Jun 2001.

[219] Seiji Sugawa, Kensuke Inaba, Shintaro Taie, Rekishu Yamazaki, Makoto Yamashita, and Yoshiro Takahashi. Interaction and filling-induced quantum phases of dual Mott insulators of bosons and fermions. Nature Physics, 7(8):642–648, 2011.

[220] Paweł Tecmer, Katharina Boguslawski, Mateusz Borkowski, Piotr S Żuchowski, and Dariusz Kędziera. Modeling the electronic structures of the ground and excited states of the ytterbium atom and the ytterbium dimer: A modern quantum chemistry perspective. International Journal of Quantum Chemistry, 119(18):e25983, 2019.

[221] TL Nicholson, S Blatt, BJ Bloom, JR Williams, JW Thomsen, J Ye, and Paul S Julienne. Optical Feshbach resonances: Field-dressed theory and comparison with experiments. Physical Review A, 92(2):022709, 2015.

[222] Jeremy M Sage, Sunil Sainis, Thomas Bergeman, and David DeMille. Optical production of ultracold polar molecules. Physical Review Letters, 94(20):203001, 2005.

[223] T. Akatsuka, M. Takamoto, and H. Katori. Optical lattice clocks with non-interacting bosons and fermions. Nature Physics, 4(12):954–959, 2008.

[224] Yixuan Wang and Michael Dolg. Pseudopotential study of the ground and excited states of Yb2. Theoretical Chemistry Accounts, 100(1):124–133, 1998.

[225] Otto Laporte and William F Meggers. Some rules of spectral structure. JOSA, 11(5):459–463, 1925.

[226] Yosuke Takasu, Yutaka Saito, Yoshiro Takahashi, Mateusz Borkowski, Roman Ciuryło, and Paul S Julienne. Controlled production of subradiant states of a diatomic molecule in an optical lattice. Physical Review Letters, 108(17):173002, 2012.

[227] William J. Meath. Retarded interaction energies between like atoms in different energy states. Journal of Chemical Physics, 48(1):227–235, 1968.

[228] Mette Machholm, Paul S Julienne, and Kalle-Antti Suominen. Calculations of collisions between cold alkaline-earth-metal atoms in a weak laser field. Physical Review A, 64(3):033425, 2001.

[229] Kyle Beloy, Jeffrey A Sherman, Nathan D Lemke, Nathan Hinkley, Christopher W Oates, and Andrew D Ludlow. Determination of the 5 d 6 s 3 d 1 state lifetime and blackbody-radiation clock shift in yb. Physical Review A, 86(5):051404, 2012.

[230] Jenning Y Seto, Robert J Le Roy, Jean Verges, and Claude Amiot. Direct potential fit analysis of the $X^1\Sigma_g^+$ state of Rb 2: Nothing else will do! Journal of Chemical Physics, 113(8):3067–3076, 2000.

[231] Liesbeth M. C. Janssen, Gerrit C. Groenenboom, Ad van der Avoird, Piotr S. Żuchowski, and Rafał Podeszwa. Ab initio potential energy surfaces for NH($^3\Sigma^-$)–NH($^3\Sigma^-$) with analytical long range. Journal of Chemical Physics, 131(22):224314, 2009.

[232] MB Shundalau and AA Minko. Ab initio multi-reference perturbation theory calculations of the ground and some excited electronic states of the RbYb molecule. Computational and Theoretical Chemistry, 1103:11–16, 2017.

[233] Lasse Kragh Sørensen, Stefan Knecht, Timo Fleig, and Christel M Marian. Four-component relativistic coupled cluster and configuration interaction calculations on the ground and excited states of the RbYb molecule. The Journal of Physical Chemistry A, 113(45):12607–12614, 2009.

[234] SN Tohme and M Korek. Electronic structure and rovibrational calculation of the low-lying states of the RbYb molecule. Chemical Physics, 410:37–44, 2013.

[235] Adrien Devolder, Eliane Luc-Koenig, Osman Atabek, Michèle Desouter-Lecomte, and Olivier Dulieu. Proposal for the formation of ultracold deeply bound RbSr dipolar molecules by all-optical methods. Physical Review A, 98(5):053411, 2018.

[236] Piotr S. Żuchowski, R. Guérout, and O. Dulieu. Ground- and excited-state properties of the polar and paramagnetic RbSr molecule: A comparative study. Physical Review A, 90:012507, Jul 2014.

[237] J. Mitroy and M. W. J. Bromley. Semiempirical calculation of van der waals coefficients for alkali-metal and alkaline-earth-metal atoms. Physical Review A, 68:052714, Nov 2003.

[238] Ilya G. Kaplan. Intermolecular Interactions: Physical Picture, Computational Methods and Model Potentials. Wiley, 1 edition, 2006.

[239] MS Safronova, SG Porsev, and Charles W Clark. Ytterbium in quantum gases and atomic clocks: van der waals interactions and blackbody shifts. Physical Review Letters, 109(23):230802, 2012.

[240] SG Porsev, MS Safronova, A Derevianko, and Charles W Clark. Relativistic many-body calculations of van der waals coefficients for Yb-Li and Yb-Rb dimers. Physical Review A, 89(2):022703, 2014.

[241] Alex Bayerle. Ultracold strontium and rubidium: mixtures, quantum gases and molecules. PhD thesis, Universiteit van Amsterdam, 2017.

[242] Vincent Barbé. Ultracold RbSr: Optical and magnetic spectroscopy, Feshbach resonances and molecular structure. PhD thesis, Universiteit van Amsterdam, 2018.

[243] Christopher K. I. Williams Carl Edward Rasmussen. Gaussian Processes for Machine Learning. Adaptive computation and machine learning. MIT Press, 2006.

[244] F. Pedregosa, G. Varoquaux, A. Gramfort, V. Michel, B. Thirion, O. Grisel, M. Blondel, P. Prettenhofer, R. Weiss, V. Dubourg, J. Vanderplas, A. Passos, D. Cournapeau, M. Brucher, M. Perrot, and E. Duchesnay. Scikit-learn: Machine learning in Python. Journal of Machine Learning Research, 12:2825–2830, 2011.

[245] MB Shundalau. Private communication.

[246] CJ Bowers, D Budker, ED Commins, D DeMille, SJ Freedman, A-T Nguyen, S-Q Shang, and M Zolotorev. Experimental investigation of excited-state lifetimes in atomic ytterbium. Physical Review A, 53(5):3103, 1996.

[247] Bijit Mukherjee, Matthew D Frye, and Jeremy M Hutson. Feshbach resonances and molecule formation in ultracold mixtures of Rb and Yb (^{3}P) atoms. Physical Review A, 105(2):023306, 2022.

[248] B.H. Bransden and C.J. Joachain. Physics of Atoms and Molecules. Pearson Education, 2003.

[249] Maykel L González-Martínez and Jeremy M Hutson. Sympathetic cooling of fluorine atoms with ultracold atomic hydrogen. Physical Review A, 88(5):053420, 2013.

[250] Bijit Mukherjee and Matthew D Frye. Personal communication.

[251] Pavel Soldán and Jeremy M Hutson. Near-dissociation states and coupled potential curves for the HeN+ complex. The Journal of chemical physics, 117(7):3109–3119, 2002.

[252] Rosario González-Férez and Christiane P Koch. Enhancing photoassociation rates by nonresonant-light control of shape resonances. Physical Review A, 86(6):063420, 2012.

[253] Frank Münchow, Cristian Bruni, Maximilian Madalinski, and Axel Görlitz. Two-photon photoassociation spectroscopy of heteronuclear YbRb. Physical Chemistry Chemical Physics, 13(42):18734–18737, 2011.

[254] Jesse J Lutz and Jeremy M Hutson. Deviations from born-oppenheimer mass scaling in spectroscopy and ultracold molecular physics. Journal of Molecular Spectroscopy, 330:43–56, 2016.

[255] Mateusz Borkowski. Private communication.

[256] Y Stalgies, I Siemers, B Appasamy, and PE Toschek. Light shift and fano resonances in a single cold ion. JOSA B, 15(10):2505–2514, 1998.

[257] Thomas Middelmann, Stephan Falke, Christian Lisdat, and Uwe Sterr. Long-range transport of ultracold atoms in a far-detuned one-dimensional optical lattice. New Journal of Physics, 14(7):073020, 2012.

[258] Till Klostermann, Cesar R Cabrera, Hendrik von Raven, Julian F Wienand, Christian Schweizer, Immanuel Bloch, and Monika Aidelsburger. Fast long-distance transport of cold cesium atoms, 2022.

[259] Kali E Wilson, Alexander Guttridge, Jack Segal, and Simon L Cornish. Quantum degenerate mixtures of Cs and Yb. Physical Review A, 103(3):033306, 2021.

[260] CD Herold, VD Vaidya, Xiao Li, SL Rolston, JV Porto, and MS Safronova. Precision measurement of transition matrix elements via light shift cancellation. Physical Review Letters, 109(24):243003, 2012.

[261] H. A. Gersch and G. C. Knollman. Quantum cell model for bosons. Physical Review, 129:959–967, Jan 1963.

[262] D Jaksch, V Venturi, J Ignacio Cirac, Carl J Williams, and P Zoller. Creation of a molecular condensate by dynamically melting a Mott insulator. Physical Review Letters, 89(4):040402, 2002.

[263] MG Moore and HR Sadeghpour. Controlling two-species Mott-insulator phases in an optical lattice to form an array of dipolar molecules. Physical Review A, 67(4):041603, 2003.

[264] Markus Greiner, Olaf Mandel, Tilman Esslinger, Theodor W Hänsch, and Immanuel Bloch. Quantum phase transition from a superfluid to a Mott insulator in a gas of ultracold atoms. Nature, 415(6867):39–44, 2002.

[265] Takeshi Fukuhara, Seiji Sugawa, Masahito Sugimoto, Shintaro Taie, and Yoshiro Takahashi. Mott insulator of ultracold alkaline-earth-metal-like atoms. Physical Review A, 79(4):041604, 2009.

[266] Martin Miranda, Ryotaro Inoue, Naoki Tambo, and Mikio Kozuma. Site-resolved imaging of a bosonic Mott insulator using ytterbium atoms. Physical Review A, 96(4):043626, 2017.

[267] L. P. Yatsenko, V. I. Romanenko, B. W. Shore, and K. Bergmann. Stimulated Raman adiabatic passage with partially coherent laser fields. Physical Review A, 65:043409, Apr 2002.

[268] Elena Kuznetsova, Marko Gacesa, Philippe Pellegrini, Susanne F Yelin, and Robin Côté. Efficient formation of ground-state ultracold molecules via STIRAP from the continuum at a Feshbach resonance. New Journal of Physics, 11(5):055028, 2009.

[269] KH Leung, E Tiberi, B Iritani, I Majewska, R Moszynski, and T Zelevinsky. Ultracold ^{88}Sr$_2$ molecules in the absolute ground state. New Journal of Physics, 23(11):115002, 2021.

[270] Cheng Chin, Rudolf Grimm, Paul Julienne, and Eite Tiesinga. Feshbach resonances in ultracold gases. Reviews of Modern Physics, 82(2):1225, 2010.

[271] Johann G Danzl, Elmar Haller, Mattias Gustavsson, Manfred J Mark, Russell Hart, Nadia Bouloufa, Olivier Dulieu, Helmut Ritsch, and Hanns-Christoph Nägerl. Quantum gas of deeply bound ground state molecules. Science, 321(5892):1062–1066, 2008.

[272] Shayne Bennetts, Gordon D McDonald, Kyle S Hardman, John E Debs, Carlos CN Kuhn, John D Close, and Nicholas P Robins. External cavity diode lasers with 5khz linewidth and 200nm tuning range at 1.55 μm and methods for linewidth measurement. Optics Express, 22(9):10642–10654, 2014.

[273] Alexander Nevsky, Soroosh Alighanbari, Q-F Chen, Ingo Ernsting, Sergey Vasilyev, Stephan Schiller, Geoffrey Barwood, Patrick Gill, Nicola Poli, and Guglielmo M Tino. Robust frequency stabilization of multiple spectroscopy lasers with large and tunable offset frequencies. Optics Letters, 38(22):4903–4906, 2013.

[274] PD Gregory, PK Molony, MP Köppinger, A Kumar, Z Ji, B Lu, AL Marchant, and SL Cornish. A simple, versatile laser system for the creation of ultracold ground state molecules. New Journal of Physics, 17(5):055006, 2015.

[275] Mickey Patrick McDonald. High precision optical spectroscopy and quantum state selected photodissociation of ultracold ^{88} Sr$_2$ molecules in an optical lattice. PhD thesis, Columbia University, 2016.

[276] Yue Cui, Chuyang Shen, Min Deng, Shen Dong, Cheng Chen, Rong Lü, Bo Gao, Meng Khoon Tey, and Li You. Observation of broad d-wave Feshbach resonances with a triplet structure. Physical Review Letters, 119(20):203402, 2017.

[277] Q Beaufils, A Crubellier, T Zanon, B Laburthe-Tolra, E Maréchal, L Vernac, and O Gorceix. Feshbach resonance in d-wave collisions. Physical Review A, 79(3):032706, 2009.

[278] The figures in this thesis make heavy use of the symbols provided in *ComponentLibrary* by Alexander Franzen, `http://www.gwoptics.org/ComponentLibrary/`